

Characterization of Proteins with Intrinsic Disorder in Solution and in Lipid Monolayers

Dissertation

zur Erlangung des Doktorgrades der Naturwissenschaften

(Dr. rer. nat.)

der

Naturwissenschaftlichen Fakultät II

Chemie, Physik und Mathematik

der Martin-Luther-Universität

Halle-Wittenberg

vorgelegt von

Frau Anna Katharina Weyrauch

geboren am 03.09.1985 in Kaiserslautern

1. Gutachter: Prof. Dr. Dariush Hinderberger

2. Gutachter: Prof. Dr. Oliver P. Ernst

Tag der Verteidigung: 13.12.2018

Contents

Abbreviations and Symbols	vii
1. Abbreviations	vii
2. Physical Constants	ix
3. Symbols (EPR)	x
4. Symbols (Membranes)	xii
5. Symbols (HPRG)	xii
1. Introduction	1
1.1. Intrinsically Disordered Proteins	1
1.2. Model Systems	2
1.2.1. Example of an IDP: α -Synuclein	2
1.2.1.1. The Synucleins – a Historical Background	3
1.2.1.2. Structure of α -Synuclein	4
1.2.1.3. Functions of α -Synuclein	4
1.2.1.4. Membrane-bound Structure of α -Synuclein	6
1.2.2. Example of an IDR: Histidine-Proline-rich Glycoprotein	6
1.2.2.1. Structure of HPRG	7
1.2.2.2. Functions of HPRG	7
1.3. Methods and Theory	11
1.3.1. Electron Paramagnetic Resonance	11
1.3.1.1. Basics of EPR Spectroscopy	11
1.3.1.2. The Spin Hamiltonian	13
1.3.1.3. Electron Zeeman Interaction	14
1.3.1.4. Nuclear Zeeman Interaction	14
1.3.1.5. Hyperfine Interaction	15
1.3.1.6. Nuclear Quadrupole Interaction	16

1.3.1.7. Zero-Field Splitting	16
1.3.1.8. Weak Coupling between Electron Spins	17
1.3.1.9. Electron Dipole-Dipole Interaction	17
1.3.1.10. Relaxation and Bloch Equations	18
1.3.1.11. Rotational Diffusion	20
1.3.1.12. CW-EPR Spectroscopy	21
1.3.1.13. Pulsed EPR-Methods	22
1.3.1.14. 4-Pulse DEER	24
1.3.2. Biological Membranes	29
1.3.2.1. Lipid Monolayers	30
1.3.2.2. Compression Isotherms	32
1.3.2.3. Adsorption Isotherms	33
2. Scope	37
2.1. α -Synuclein	37
2.2. HPRG	38
3. Results and Discussion	39
3.1. α -Synuclein	39
3.1.1. Electron Paramagnetic Resonance	39
3.1.1.1. Membrane-bound State of α -Synuclein	41
3.1.1.2. Membrane-bound State of α -Synuclein (Influence of Lig- and X)	60
3.1.2. Film Balance Measurements	74
3.1.2.1. Adsorption of α -Synuclein to the Air/Water-Interface	75
3.1.2.2. Compression Isotherms of Phospholipids	76
3.1.2.3. Adsorption of α -Synuclein to Phospholipid Monolayers	81
3.1.2.4. Adsorption of α -Synuclein to Phospholipid Monolayers (Influence of Ligand X)	86
3.2. HPRG	89
3.2.1. Cobalt Affinity Chromatography	89
3.2.2. Preparative Gel Electrophoresis	92
3.2.3. Recovery	95

3.2.4. Mass Spectrometry	95
3.2.4.1. Purity	96
3.2.4.2. Amino Acid Sequence	96
3.2.4.3. Molecular Weight	98
3.2.4.4. Glycosylation Pattern	99
3.2.5. CD Spectroscopy	102
4. Conclusion and Outlook	105
4.1. α -Synuclein	105
4.2. HPRG	107
5. Material and Methods	109
5.1. Materials	109
5.1.1. Chemicals	109
5.1.2. Biological Reagents	110
5.1.3. Phospholipids	110
5.1.4. Reagents and Buffer Compositions	111
5.2. Methods (α -Synuclein)	113
5.2.1. Electron Paramagnetic Resonance	113
5.2.1.1. X-Band CW-EPR Spectroscopy	113
5.2.1.2. Q-Band CW-EPR Spectroscopy	113
5.2.1.3. Pulsed X-Band EPR Spectroscopy	114
5.2.1.4. Simulation of CW-EPR Spectra	115
5.2.1.5. EPR Sample Preparation	116
5.2.2. Film Balance Measurements	119
5.2.2.1. Detection of Compression Isotherms	119
5.2.2.2. Detection of Adsorption Isotherms	120
5.2.2.3. Preparation of Samples for the Ligand Measurements	121
5.3. Methods (HPRG)	122
5.3.1. Determination of Protein Concentration	122
5.3.1.1. UV/Vis-Spectroscopy	122
5.3.1.2. BCA Assay	123
5.3.2. Polyacrylamide Gel Electrophoresis	124

5.3.3. Cobalt Affinity Chromatography	125
5.3.4. Preparative Gel Electrophoresis	126
5.3.5. Mass Spectrometry	130
5.3.6. Circular Dichroism	132
References	135
A. Appendix	157
A.1. α -Synuclein	157
A.1.1. Influence of Ligand X - X-Band CW-EPR - 1st Series	157
A.1.2. Influence of Ligand X - X-Band CW-EPR - 2nd Series	161
A.1.3. Influence of Ligand X - X-Band CW-EPR - 3rd Series	165
A.1.4. Influence of Ligand X - X-Band CW-EPR - Simulation Parameters	166
A.1.5. Influence of Ligand X - Q-Band CW-EPR - 1st Series	167
A.1.6. Influence of Ligand X - Q-Band CW-EPR - 2nd Series	171
A.1.7. Influence of Ligand X - Q-Band CW-EPR - 3rd Series	175
A.1.8. Influence of Ligand X - Q-Band CW-EPR - Simulation Parameters	176
A.1.9. Influence of Ligand X - DEER Time Traces	177
A.1.10. Scaling of Δ_{eff}	179
A.1.11. Fatty acid distribution of Porcine Brain Lipids	180
A.1.12. Epi-Fluorescence Microscopy	180
A.2. HPRG	183
A.2.1. Alternative Purification Approaches of HPRG	183
A.2.2. Mass Spectrometry Data	185
B. Acknowledgements	199
C. Scientific Contributions	201
C.1. Publications	201
C.2. Oral Contributions	201
C.3. Poster Contributions	201
D. Curriculum Vitae	202
E. Eidesstattliche Erklärung	203

Abbreviations and Symbols

1. Abbreviations

A ₂₈₀	Absorption at 280 nm
AD	Alzheimer's Disease
AEC	Anion Exchange Chromatography
APS	Ammonium Persulfate
BCA	Bicinchoninic Acid
<i>BCSG1</i>	Breast Cancer-specific Gene 1
BSA	Bovine Serum Albumin
C1q	Complement Component 1q
CD	Circular Dichroism
CD36	Cluster of Differentiation 36
cDNA	Complementary Deoxyribonucleic Acid
CLESH	CD36 LIMP-II Emp Sequence Homology
Comp.	Components / Composition
CW	Continuous Wave
DEER	Double Electron-Electron Resonance
DMSO	Dimethyl Sulfoxide
DTT	Dithiothreitol
<i>E. coli</i>	Escherichia coli
EPR	Electron Paramagnetic Resonance
ESE	Electron Spin Echo
ESI	Electrospray Ionization
ESR	Electron Spin Resonance
GlcNAc	N-Acetylglucosamine

Hex	Hexose
HexNac	N-Acetylhexosamine
HPLC	High Performance Liquid Chromatography
HPRG	Histidine-Proline-rich Glycoprotein
HRG	Histidine-rich Glycoprotein
HRR	Histidine-rich Region
IC	Immune Complex
IDP	Intrinsically Disordered Protein
IDR	Intrinsically Disordered Region
IgG	Immunoglobulin G
IMAC	Immobilized Metal Ion Affinity Chromatography
LC-MS	Liquid Chromatography–Mass Spectrometry
LUV	Large Unilamellar Vesicle
MALDI	Matrix-Assisted Laser Desorption/Ionization
MIP	Maximum Insertion Pressure
MS	Mass Spectrometry
MS/MS	Tandem Mass Spectrometry
MTS	S-(1-oxyl-2,2,5,5-tetramethyl-2,5-dihydro-1H-pyrrol-3-yl) methylnmethanesulfonylthioate
MWCO	Molecular Weight Cut-Off
N1/N2	Cystatin-like Domains 1 and 2, respectively
NAC	Non-A β -Component of AD Amyloid
NACP	Non-A β -Component of AD Amyloid Precursor
NeuAc	N-Acetylneuraminic Acid (Sialic Acid)
NMR	Nuclear Magnetic Resonance
NTA	Nitrilotriacetic Acid
PAGE	Polyacrylamide Gel Electrophoresis
<i>PARK1</i>	Gene coding α -Synuclein; Synonym of <i>SNCA</i>
PBS	Phosphate Buffered Saline
PC	Phosphatidylcholine
PD	Parkinson's Disease
PE	Phosphatidylethanolamine
PELDOR	Pulsed Electron-Electron Double Resonance

PG	Phosphatidylglycerole
POPC	1-Palmitoyl-2-oleoyl- <i>sn</i> -glycero-3-phosphocholine
POPG	1-Palmitoyl-2-oleoyl- <i>sn</i> -glycero-3-phosphoglycerole
POPS	1-Palmitoyl-2-oleoyl- <i>sn</i> -glycero-3-phosphoserine
PRR	Proline-rich Region
PS	Phosphatidylserine
RNA	Ribonucleic Acid
RP-HPLC	Reversed-Phase High Performance Liquid Chromatography
RT	Room Temperature
SDS	Sodium Dodecyl Sulfate
SEC	Size Exclusion Chromatography
SM	Sphingomyeline
SNCA	Gene coding α -Synuclein
SNR	Signal-to-Noise Ratio
SUV	Small Unilamellar Vesicle
SV	Synaptic Vesicle
TFA	Trifluoroacetic Acid
TOC	Total Organic Carbon
TOF	Time of Flight
TSP	Thrombospondin
w/o	without
WT	Wildtype

2. Physical Constants

g_e	Landé Factor of the free Electron	2.002319304
h	Planck's constant	$6.626070040 \cdot 10^{-34}$ Js
\hbar	Reduced Planck's constant	$1.054571800(13) \cdot 10^{-34}$ Js
k_B	Boltzmann Constant	$1.38064852(79) \cdot 10^{-23}$ JK ⁻¹
μ_0	Vacuum Permeability	$1.2566370614 \cdot 10^{-6}$ VsA ⁻¹ m ⁻¹
μ_B	Bohr Magneton	$9.274009994(57) \cdot 10^{-24}$ JT ⁻¹
μ_N	Nuclear Magneton	$5.050783699(31) \cdot 10^{-27}$ JT ⁻¹
R	Universal Gas Constant	$8.3144598(48)$ JK ⁻¹ mol ⁻¹

3. Symbols (EPR)

a_{iso}	Isotropic Hyperfine Coupling Constant
A	Hyperfine Tensor
B	Magnetic Field Vector
B_0	Static Magnetic Field
B_0	Center Field
B_1	Microwave Field
B_m	Oscillating Magnetic Field (Field Modulation)
$B(t)$	Background Factor (DEER)
d	Dimensionality
D	Dipole-Dipole Coupling Tensor
D_G	Zero-Field Interaction Tensor
D_r	Rotational Diffusion Tensor
E	Energy
$F(t)$	Form Factor (DEER)
g	Anisotropic g -Tensor
g	Landé Factor
g_{iso}	Isotropic g -Value
H_0	Static Spin Hamiltonian
I	Nuclear Spin Vector
I	Nuclear Spin I
J	Exchange Coupling Tensor
k	Spin Density
m	Mass
m_I	Nuclear Spin Quantum Number
m_s	Electron Spin Quantum Number
M	Macroscopic Magnetization
M_0	Macroscopic Magnetization in Thermal Equilibrium
M	Spin Multiplicity
$\langle n \rangle$	Number of Coupled Spins
N	Population Number

P	Nuclear Quadrupole Tensor
r	Radius
S	Electron Spin Vector
S	Electron Spin
S_G	Group Spin
T	Dipolar Coupling Tensor
t	Time
t_d	Dead Time
T	Temperature
T_1	Longitudinal/Spin-Lattice Relaxation Time
T_2	Transversal/Spin-Spin Relaxation Time
T_m	Phase Memory Time
V	Volume
β	Flip Angle
γ	Gyromagnetic Ratio
Δ	Modulation Depth
λ	Inversion Efficiency
μ	Magnetic Moment
ν	Frequency
τ	Interpulse Delay
τ_c	Rotational Correlation Time
τ_p	Microwave Pulse Length
ω_1	Nutation Frequency
ω_a	Observer Frequency
ω_b	Pump Frequency
ω_l	Larmor Frequency
ω_{dd}	Dipolar Coupling Frequency
ω_{mw}	Microwave Frequency
Ω	Resonance Offset

4. Symbols (Membranes)

A	Surface
c	Concentration
G	Free Enthalpy
p	Pressure
G	Gaseous-Analogous State
LC	Liquid-Condensed State
LE	Liquid-Expanded State
S	Solid State

Γ	Gibbs Adsorption Isotherm
π	Surface Pressure
σ	Surface Tension

5. Symbols (HPRG)

ϵ	Molar Absorption Coefficient
d	Path Length

1. Introduction

1.1. Intrinsically Disordered Proteins

It has been as early as in 1894 that Emil Fischer proposed the famous “lock-and-key” model to describe the specific interaction between a substrate and an enzyme [1]. This model, as well as the newer “induced fit” model [2], were the basis for the central dogma of structural biology: in order to fulfill its biological function a protein needs to fold correctly in its unique three-dimensional shape [3, 4]. Since the first X-ray crystallographic structure of myoglobin at atomic resolution was published in the late 1950s [5], this model was further verified.

However, this so-called structure-function paradigm was shaken in the late 1980s to the late 1990s. More data were published upon proteins that had either unstructured regions or were fully disordered, but still exerted biological functions [3, 6, 7].

Computational studies indicated that about 40% of human proteins have at least a long (> 30 amino acid residues) disordered region (intrinsically disordered region, IDR), and about 25% of the proteins are fully disordered (intrinsically disordered protein, IDP) [8, 9].

IDPs are characterized by the lack of a well-defined three-dimensional structure. This is due to the absence of so-called order-promoting amino acid residues (Cys, Trp, Tyr, Ile, Phe, Val, Leu, His, Thr, and Asn). These amino acid residues would form the hydrophobic core of a folded protein. Analogue, IDPs are rich in polar disorder-promoting residues (Asp, Met, Lys, Arg, Ser, Gln, Pro, Glu). Summarized, IDPs possess a low mean hydrophobicity and a high net charge [6, 10].

Due to the intrinsic disorder, IDPs as well as IDRs possess a high intramolecular flexibility leading them to the ability to interact with multiple ligands [11, 12]. Therefore, IDPs have a large role in acting as hubs in protein interaction networks [13]. Functions

include i.a. the regulation of transcription and translation as well as cell division and signal transduction [12, 14]. Upon interaction with their binding partner, IDPs often fold into a more ordered structure, i.e. coupled folding and binding [14]. It is this flexibility and the resulting capability of interacting with different ligands that intrinsic disorder is prevalent in proteins that are associated with cancer and neurodegenerative diseases. Mutations of genes or misfolding in general can lead to the breakdown of the protein interaction network due to the malfunctioning hub protein or in the case of neurodegenerative diseases to formation of insoluble aggregates like it is observed in Alzheimer's disease, Parkinson's disease and Huntington's disease [15, 16].

1.2. Model Systems

1.2.1. Example of an IDP: α -Synuclein

α -Synuclein is the probably most famous and most studied intrinsically disordered protein due to its contribution to Parkinson's disease (PD). PD is the second most common neurodegenerative disorder after Alzheimer's disease (AD) and the most common movement disorder characterized by tremor, rigidity, bradykinesia, and postural instability [17, 18]. From a neurological point of view it is defined by the loss of dopaminergic neurons in the *substantia nigra pars compacta* of the mid-brain, however other parts of the brain can also be affected. Another characteristic of the disease is the presence of the so-called Lewy bodies and Lewy neurites in neurons of the affected brain regions [19–21].

First described in 1912, only little was known about the composition of Lewy bodies and Lewy neurites until 1997. In that year a missense mutation was discovered in a gene that was previously mapped to the human protein α -Synuclein (*SNCA* gene, also termed as *PARK1* in the literature due to the link to PD). This mutation leads to an Ala to Thr substitution at the amino acid position 53 (A53T). The A53T substitution was found in a large family of Italian descent (the Contursi kindred) and in Greek families that had a strong PD phenotype [22–24].

At the same time Spillantini et al. [25, 26] tested an antibody against a peptide corresponding to amino acid residues 116–131 of human α -Synuclein. They could show a strong staining of Lewy bodies and Lewy neurites indicating that α -Synuclein is a

major component. It was discovered that the Lewy bodies are intraneuronal inclusions and consist mainly of abnormal β -sheet rich aggregates of α -Synuclein, ubiquitin, and neurofilaments that cause the eventual neuronal cell death [25–28].

Up to now several more missense mutations of *SNCA/PARK1* have been identified to cause an autosomal-dominant inherited form of PD. Whereas usually elderly people are affected by the sporadic forms of PD, mutations in *SNCA/PARK1* lead to an early-onset of the disease (≤ 50 years) [29]. These missense mutations include: A30P [30], E46K [31], H50Q [32], G51D [33, 34] A53E [35], and A53V [36]. Moreover, duplication and triplication of the whole *SNCA/PARK1* locus can lead to familial PD [37, 38]. Here the clinical phenotype of the *SNCA* multiplication is strongly dependent on the gene dosage and thus the expression level of α -Synuclein in the brain [29, 39]. Recently two more missense mutations of *SNCA* were discovered, but those may rather be associated with sporadic PD [40, 41].

1.2.1.1. The Synucleins – a Historical Background

Maroteaux et al. [42] used an antiserum against cholinergic vesicles from the electric organ of the pacific electric ray *Torpedo californica*. They isolated a protein that was localized to the nucleus and the presynaptic nerve terminal, thus terming the protein as Synuclein. Following experiments however did not show the nuclear localization of the protein, but the original given name was kept. During the following years several proteins were isolated out of brain tissues that were related to the Synuclein of *Torpedo californica*. Due to the homology of these proteins the family of the Synucleins was discovered:

Uéda et al. [43] isolated the cDNA of a 140 amino acid protein. They termed it as the “non- $A\beta$ -component of AD amyloid precursor” (NACP). A 35 amino acid peptide of this protein “non- $A\beta$ -component of AD amyloid” (NAC) had been found in some purified AD amyloid preparations. Jakes et al. [44] isolated two proteins from adult brain. One of these proteins was a 140 amino-acid protein identical to the earlier described NACP, and was subsequently termed as α -Synuclein. The other 134 amino acid protein was highly homologous to a phosphoprotein (phosphoneuroprotein 14) isolated from rat brain [45], which was termed as β -Synuclein. Ji et al. [46] discovered the *Breast Cancer-specific Gene 1 BCSG1* due to high expression levels in breast cancer tissue. The predicted



Figure 1.1. – Schematic structure of human α -Synuclein. The protein is arranged into the N-terminal domain, whose repeats are responsible for membrane binding. The NAC region is responsible for the aggregation into insoluble fibrils found in the Lewy bodies of PD. The acidic C-terminal domain remains disordered upon binding to negatively charged membranes. Based upon [48].

amino acid sequence of *BCSG1* is homologous to NACP, and therefore it was termed as γ -Synuclein.

All members of the Synuclein family are small abundant brain proteins with a molecular mass of about 14 kDa. They all share a similar structure; the structure of α -Synuclein will be discussed in particular. It is worth to note that only α -Synuclein was shown to cause PD.

1.2.1.2. Structure of α -Synuclein

α -Synuclein consists of three different regions. The amino-terminal part of the protein (approximately amino acids 1–95) is composed of an imperfect 11 amino acid residue repeat motif that bears the consensus sequence KTKEGV. This motif is repeated seven times. Due to the high content of lysine residues the amino-terminal region is positively charged at physiological pH-values. This region also comprises the 35 amino acid NAC, a very hydrophobic region, which was already described earlier (amino acids 60–95). The C-terminal domain (amino acids 96–140) is negatively charged [47] (Fig. 1.1).

1.2.1.3. Functions of α -Synuclein

Although it is known that α -Synuclein can misfold into insoluble aggregates, the precise physiological function remains unknown.

All members of the Synuclein family are highly expressed in the brain [49]. α -Synuclein in particular was localized to the presynaptic terminal in proximity to synaptic vesicles [42] indicating that it may have a synaptic function. Potential functions may include synaptic plasticity and thus be important in learning processes and memory functions [50]. This was indeed discovered in the song learning process of male zebra finches. The

gene expression of the human homologue of NAC(P), Synelfin, is significantly changed during the critical period for song learning [51].

It had also been shown by Jenco et al. [52] that α -Synuclein as well as β -Synuclein inhibit selectively phospholipase D2. This phospholipase D isoform can localize to the plasma membrane where it may have a role of signal-induced cytoskeletal regulation and/or endocytosis. Therefore, α -Synuclein may regulate vesicular transport processes [17, 49, 53]. More recent studies indicate that α -Synuclein can sense and also generate membrane curvature – two processes that are needed for exocytosis or endocytosis [54, 55]. A potential role for α -Synuclein in synaptic vesicle (SV) endocytosis and exocytosis has also been shown more recently [56–58].

The presynaptic localization may also regulate neurotransmitter release [59]. The result of a recent study shows that α -Synuclein can accelerate the kinetics of exocytosis by dilating the exocytotic fusion pore. It can thus affect the release event of neurotransmitters [60, 61].

It is also worth to note that there have been conflicting publications in the past regarding the potential binding of α -Synuclein to synaptic vesicles. Several biochemical preparations revealed that α -Synuclein may rather be in close proximity to synaptic vesicles, but not directly bound to them [50, 51, 62, 63]. However, Vargas et al. [58] stated that this may be due to experimental conditions with Synucleins detaching of the membrane when ionic conditions are low. By preserving physiological salt conditions during the experiment this detaching should not be the case. They could indeed show that the majority of α -Synuclein was associated with synaptic vesicles throughout the presynaptic terminal [58]. Another characteristic of α -Synuclein in SV-binding is its affinity for curved membranes, especially vesicles around 40 – 50 nm in diameter, the exact size of a synaptic vesicle [54, 64].

Another prominent characteristic of α -Synuclein is the 11 amino acid residue motif in the N-terminal region. This motif is also a feature of the exchangeable apolipoproteins that are known to interact with lipids [65]. Davidson et al. [66] hypothesized that also α -Synuclein should interact with phospholipids. They demonstrated that α -Synuclein indeed interacts with synthetic membranes composed of negatively charged lipids. Upon this interaction the previously IDP increases its helicity from 3 % to approximately 80 %, i.e. a transition from a random coil to an α -helical conformation. Moreover,

affinity is higher for vesicles that have a smaller diameter, as already mentioned before regarding the interaction of α -Synuclein and synaptic vesicles. Since the membrane-bound structure is crucial for this work, it will be addressed in the following section.

1.2.1.4. Membrane-bound Structure of α -Synuclein

α -Synuclein was found to be intrinsically disordered in solution, but can adopt more ordered structures upon binding to negatively charged membranes [66]. Upon this interaction the N-terminal region with its 11-residue motif interacts with the phospholipids, whereas the C-terminal domain remains free in solution and is still unstructured [67]. Interestingly Eliezer et al. [67] detected a slight propensity for a helical structure in the N-terminal region already in the free α -Synuclein in solution.

Early NMR studies of α -Synuclein bound to SDS-micelles showed a break in the α -helix, with α -Synuclein arranging into two anti-parallel helices, the so-called horseshoe model [68]. In this model, the two α -helices are connected by a short linker around the amino acid residues 38–44. It has been pointed out that this break could also be due to the usage of SDS-micelles having a diameter of about 5 nm. Therefore, they are about ten times smaller compared to a synaptic vesicle so that the smaller diameter may force the protein into this broken helix-form [69]. Several contradicting NMR as well as EPR studies have been published in the past regarding this issue. Some could find the broken helix even when working with SUVs [70–72], whereas other groups detected α -Synuclein as a single, extended α -helix [73–76]. Finally Robotta et al. [77] stated that α -Synuclein can also be found in the broken form on larger vesicles and that the protein exists in a superposition of both, broken and extended form.

1.2.2. Example of an IDR: Histidine-Proline-rich Glycoprotein

The Histidine-Proline-rich Glycoprotein (HPRG), which is also known as Histidine-rich protein (HRG), is a plasma protein that can be found in all vertebrates [78, 79]. Human HPRG was first isolated and characterized in 1972 [80] due to its affinity for carboxymethylcellulose. In a subsequent study the concentration was found to be 100-150 mg/l [81], whereas in rabbit serum a concentration of 900 mg/l was shown [82]. HPRG is a member of the cystatin superfamily, a class of cysteine protease inhibitors [83]. Together with fetuins and kininogen it forms the subgroup cystatin type 3, which

are disulfide-bonded, multi-domain plasma glycoproteins that are mainly produced in the liver [84–86]. Interesting to note is that only kininogen was shown to possess cysteine protease inhibitor activity.

1.2.2.1. Structure of HPRG

As shown in Fig. 1.2 human HPRG is arranged into multiple domains and is stabilized by presumably six disulfide bonds. Besides the two Cystatin-like N-terminal regions (termed N1 and N2), HPRG possesses a central histidine-rich region (HRR), in which half of the protein's histidine residues are located [79]. The HRR is flanked by two proline-rich regions (termed PRR1 and PRR2) and PRR2 is finally followed by the C-terminal domain. Both, the HRR and the two PRRs, are assumed to be intrinsically disordered so that the full length protein is not crystallisable and hence not accessible to characterization by means of X-ray crystallography. However, the two Cystatin-like N-terminal domains are assumed to possess more ordered structures, so that the N2 domain of the rabbit HPRG has been crystallized in 2014 [87]. In general, the overall structure of HPRG is similar in several mammalian species with a protein chain length of around 500 amino acid residues, leading to a molecular weight of about 70 kDa for the fully glycosylated protein [78, 79, 88]. Furthermore, the HRR of HPRG contains repeats of the sequence GHHPH, whose number differ also among mammalian species, for example human HPRG contains 12 of those repeats, whereas in rabbit 19 repeats can be found (Fig. 1.4). Where in human HPRG the protein is assumed to be stabilized by six disulfide bonds, the rabbit HPRG is assumed to be stabilized by five disulfide bonds [89], see Fig. 1.3.

1.2.2.2. Functions of HPRG

HPRG can interact with a variety of ligands, however the exact physiological role is still unknown. HPRG seems to be involved in the blood coagulation and fibrinolysis system, the regulation of angiogenesis, as well as the immune system.

Subsequent analysis of HPRG after the first isolation in 1972 [80] showed a high affinity for heparin. Antithrombin, important for the inhibition and thus regulation of blood coagulation, also binds heparin with a high affinity. Indeed, Koide et al. [90] showed that the N-terminal sequences of both proteins, where the putative heparin-binding

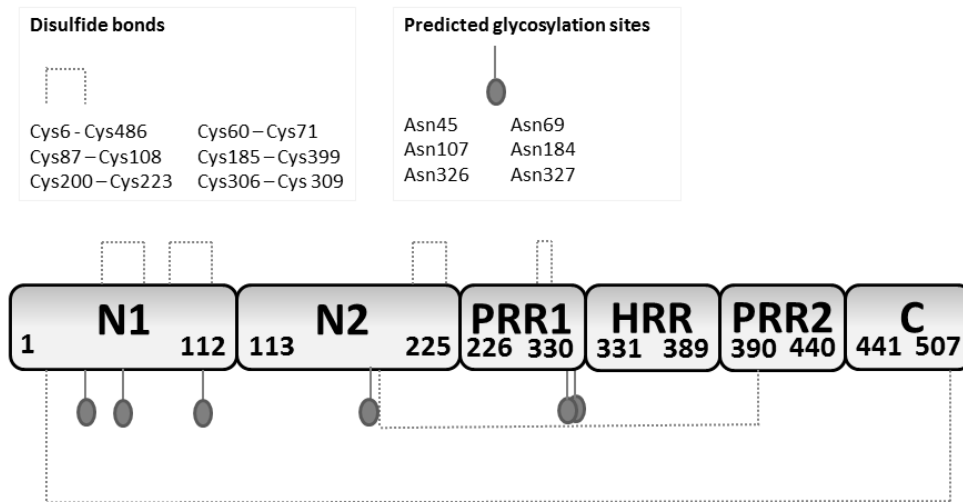


Figure 1.2. – Schematic structure of the multiple domains of human HPRG. Also shown are the predicted glycosylation sites and the disulfide bridges. It is worth to note that according to [79] human HPRG is assumed to contain eight disulfide bonds, however the arrangements of the last two are not certain. Modified according to [88, 89].

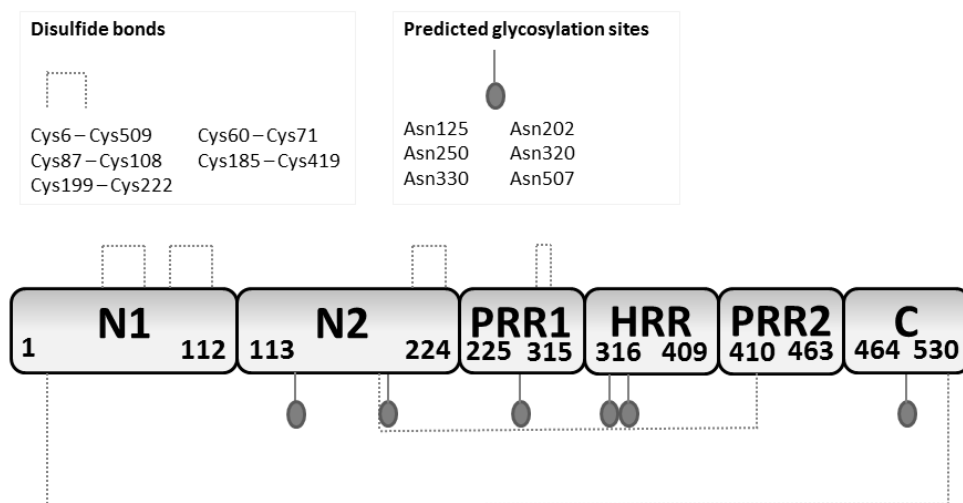


Figure 1.3. – Schematic structure of the multiple domains of rabbit HPRG. Also shown are the predicted glycosylation sites and the disulfide bridges. Modified according to [88, 89].

HRR Repeats in Rabbit HPRG (NCBI Reference Sequence: XP_008264798.1)

HHPHGPPPHGHHPHGPPPHGHHPHGPPPHGHPPHGPPPHGHPPHGPPPH
 GHPPHGPPPHGHPPHGPPPHGHPPHGPPPHGHPPHGPPPHGHPPHG

HRR Repeats in Human HPRG (NCBI Reference Sequence: NP_000403.1)

DLHPHKHHSHEQHPHGHHPHAHHPHEHDTHRQHPHGHHPHGHHPHGHH
 PHGHHPHGHHPH

Figure 1.4. – Comparison of the repeat motif in the HRR of rabbit and human HPRG, respectively. Note that the repeats in the rabbit HPRG are based on a more recently published sequence because the sequence published in 1996 is probably incorrect [82, 89].

site is located, are homologous to each other. Upon interaction with heparin, HPRG prevents the interaction of heparin and antithrombin, resulting in the neutralization of the anticoagulant activity of heparin and antithrombin [78, 79].

The interaction of HPRG and fibrinogen was demonstrated by Leung in 1986 [91]. It was shown that upon interaction HPRG became incorporated into fibrin clots. This incorporation had no effect on the conversion of fibrinogen to fibrin. It rather affected the final structure of the fibrin gels leading to more, but thinner fibrils.

Another ligand of the fibrinolytic system is plasminogen, whose lysine-binding sites are involved in the regulation of fibrinolysis. When HPRG and plasminogen interact, the effective concentration of plasminogen in the blood is reduced by 50 %. Besides, this interaction also interferes with the interaction of plasminogen and fibrin, which leads to a delay in fibrinolysis. HPRG has an antifibrinolytic effect [92]. It is also worth to note that HPRG itself is very sensitive to plasmin cleavage [93].

HPRG is also active in the modulation and regulation of angiogenesis, the formation of new blood vessels. Angiogenesis is very important for several physiological processes, including normal development and wound healing. However, it may also lead to the growth and proliferation of tumors, thus it needs to be controlled. An inhibitor for angiogenesis are the thrombospondins (TSPs) TSP-1 and TSP-2. The antiangiogenic

effect of those TSPs is mediated by binding of a peptide sequence (properdin-like type I repeats) to the receptor CD36 (type B scavenger receptor), which can be found on the surface of many cell types [94–96]. HPRG itself contains two regions with a homology to the TSP-1 binding site of the CD36 receptor, which are known as CLESH-1 motifs. Therefore, HPRG can bind to the properdin-like type I repeats of TSP-1 and interfere with the binding of TSP-1 to CD36, which leads to the neutralization of the antiangiogenic effect of TSP-1 [79, 95]. A similar effect can be found in vasculostatin, which is the soluble antiangiogenic domain of the *Brain angiogenesis inhibitor 1*. In this case the HPRG also binds via the CLESH-motif to vasculostatin and inhibits its antiangiogenic activity [94].

An important process for the normal immune response is the formation of antigen-antibody complexes, which are also known as immune complexes (ICs). These ICs need to be cleared effectively from the circulation, otherwise they may be deposited in target tissues which in turn can cause a severe tissue injury and lead to several diseases [88, 97]. HPRG has been shown to interact with human C1q and IgG which inhibit the formation of insoluble ICs [97].

Another prominent feature of HPRG is the high content of histidines within the central histidine-rich region. HPRG is able to interact with divalent metal ions and heme.

It has been reported that human HPRG can interact with up to 10 molecules of heme bound per HPRG (K_d about 1.5 μM) [98]. It was postulated that the amount of heme that can be bound to human HPRG correlates with the number of the tandem repeat motifs in the HRR. The 12 tandem repeats in the human HPRG can thus bind about 10 heme molecules [99]. With a few tandem repeats more in the HRR, it was assumed that rabbit HPRG has around 20-30 binding sites for heme [100].

Due to the many histidines within the HRR, HPRG can also bind to divalent metal ions like Cu^{2+} , Zn^{2+} , Ni^{2+} , and Co^{2+} . About 10 divalent metal ions can be bound to 1 molecule of rabbit HPRG with a dissociation constant of about 1 μM [101].

The interaction of HPRG with divalent metal ions is also physiologically very important and is often connected with several functions stated above. For example upon binding of Zn^{2+} , HPRG can undergo a conformational change, which in turn increases the affinity of HPRG for heparin [102, 103]. Upon binding of Zn^{2+} or when the histidines are protonated at low local pH-values (e.g. in conditions of ischemia or hypoxia), HPRG

becomes positively charged and can strongly interact with negatively charged ligands, like heparan sulphate or also bacterial membranes [103–105].

1.3. Methods and Theory

1.3.1. Electron Paramagnetic Resonance

Electron Paramagnetic Resonance (EPR) spectroscopy, also known as Electron Spin Resonance (ESR), is a magnetic resonance technique, based on the interaction between electromagnetic radiation and the magnetic moments of electrons. The intrinsic magnetic moment of the electron, called electron spin, was discovered in 1922 by Stern and Gerlach [106].

With this technique paramagnetic systems containing unpaired electrons, e.g. radicals or some transition metal ions, can be investigated. Biological samples, like proteins, are diamagnetic. Hence, it is necessary to introduce an EPR-active compound to the sample. This can either be achieved through the so-called *spin probing* method, in which paramagnetic ligands are added to the sample and the interaction between the ligand and the protein is observed. Another method is the *spin labeling* technique, where a stable radical is bound covalently to the protein of interest.

Information that is obtained via an EPR experiment comprises structure and dynamics of the micro-environment of the spin label/spin probe. Additionally, if more than one EPR-active compound is available, distances can be measured between individual electron spins.

1.3.1.1. Basics of EPR Spectroscopy

Electrons are negatively charged particles with an intrinsic angular momentum, the electron spin $\hbar\mathbf{S}$. For a charged particle with the mass m , the electron spin gives rise to a magnetic moment $\boldsymbol{\mu}$, which is directed opposite to the electron spin:

$$\boldsymbol{\mu}_e = -g_e\mu_B\mathbf{S} , \quad (1.1)$$

where μ_B is the Bohr magneton and g_e is the Landé-factor. The Landé-factor has a value of 2.0023 for a free electron.

In an external magnetic field $\mathbf{B} = [0, 0, B_z]$, the electron spin can only adopt two states: parallel or anti-parallel with respect to the external magnetic field. The component of the spin in direction of the magnetic field \mathbf{B}_0 is defined as z -direction:

$$S_z = m_S \hbar . \quad (1.2)$$

The spin quantum number m_S for $S = \frac{1}{2}$ adopts the values $-\frac{1}{2}$ and $+\frac{1}{2}$. Since the electron spin is oriented along the z -axis, the respective magnetic moment $\boldsymbol{\mu}_e$ is also oriented along z :

$$\mu_{e,z} = -g_e \cdot \mu_B \cdot m_S . \quad (1.3)$$

The energy of a magnetic moment oriented along the z -axis is defined as:

$$E = -\mu_{e,z} \cdot B_0 = g_e \cdot \mu_B \cdot m_S \cdot B_0 . \quad (1.4)$$

Both spin orientations $m_S = -\frac{1}{2}$ and $m_S = +\frac{1}{2}$ are degenerated without an external magnetic field. However, when an external magnetic field is applied, the so-called *Zeeman Splitting* occurs (Fig. 1.5):

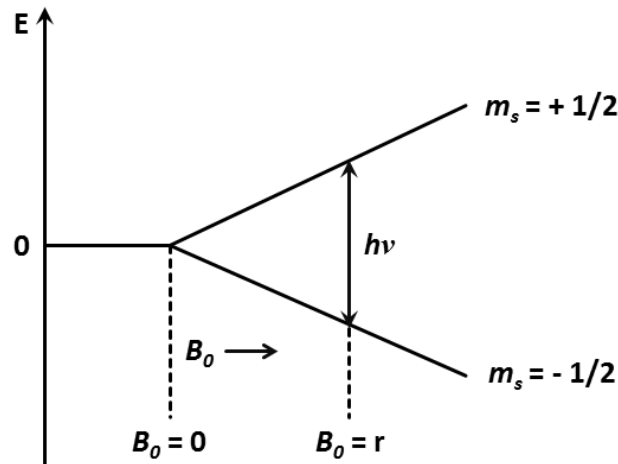


Figure 1.5. – Zeeman splitting of the states of the electron spin in a homogeneous magnetic field B_0 . The lower $m_S = -\frac{1}{2}$ -level is oriented parallel with respect to the external magnetic field, whereas the upper $m_S = +\frac{1}{2}$ -level is oriented anti-parallel. At the resonance field $B_0 = r$ a transition from the lower to the upper level can occur. Modified according to [107].

The energy for both states is defined as:

$$E_{m_S=+\frac{1}{2}} = \frac{1}{2} \cdot g_e \cdot \mu_B \cdot B_0 \quad (1.5)$$

and

$$E_{m_S=-\frac{1}{2}} = -\frac{1}{2} \cdot g_e \cdot \mu_B \cdot B_0 \quad , \quad (1.6)$$

where the energy difference between the two states - the resonance condition - is then

$$\Delta E = g_e \cdot \mu_B \cdot B_0 \quad . \quad (1.7)$$

Upon electromagnetic irradiation (in the case of EPR microwaves) a transition from the lower level $m_S = -\frac{1}{2}$ to the upper level $m_S = +\frac{1}{2}$ is induced once the resonance condition is fulfilled.

The population of the two energy levels in the ground state is given by a Boltzmann factor

$$\frac{N_{m_S = +\frac{1}{2}}}{N_{m_S = -\frac{1}{2}}} = e^{-\frac{\Delta E}{k_B T}} \quad , \quad (1.8)$$

where k_B is the Boltzmann constant. The population of the lower level is higher than that of the upper level. Hence a transition from the lower to the upper level is observed at resonance conditions. By measuring EPR spectra at low temperatures, the sensitivity will be increased.

The magnetic field experienced by the unpaired electron will differ from \mathbf{B} due to different interactions, like interactions with other electrons or surrounding nuclei. The different types of interactions and the different energetic contributions can be described with the *Spin Hamiltonian* [108, 109].

1.3.1.2. The Spin Hamiltonian

The static *Spin Hamiltonian* [110] of an electron spin S and nuclei spin I can be described as

$$H_0 = H_{EZ} + H_{ZFS} + H_{HF} + H_{NZ} + H_{NQ} + H_{NN} \quad . \quad (1.9)$$

The Hamiltonian only includes interactions where spins are involved: interactions of spins with the external magnetic field (electron and nuclear Zeeman terms) H_{EZ} and H_{NZ} , respectively, as well as the zero-field splitting H_{ZFS} , the hyperfine interaction H_{HF} between electron spins and nuclear spins, the nuclear quadrupole interaction H_{NQ} and interactions between pairs of nuclear spins H_{NN} [109].

1.3.1.3. Electron Zeeman Interaction

The electron Zeeman interaction is the dominant term of the Hamiltonian in a system with $S = \frac{1}{2}$ in a static magnetic field. It describes the interaction of the unpaired electron and the external magnetic field B_0 which leads to the Zeeman splitting:

$$H_{EZ} = \frac{\mu_B \mathbf{B}^T \mathbf{g} \mathbf{S}}{\hbar} . \quad (1.10)$$

\mathbf{S} is the spin vector operator and \mathbf{g} is a symmetric tensor with three principal values g_{xx} , g_{yy} , and g_{zz} and three Euler angles describing their orientation in a molecular coordinate system. The superscript “T” indicates transposing of the respective vector/matrix. The rotation of molecules in solution is fast, hence the \mathbf{g} -matrix is averaged out and an isotropic g -factor can be calculated as the trace of the g -matrix:

$$g_{\text{iso}} = \frac{1}{3}(g_{xx} + g_{yy} + g_{zz}) . \quad (1.11)$$

The value of g is of great importance for EPR spectroscopy. For a free electron one EPR line would be observed at $g = g_e = 2.0023$. However, if the electron is located in a molecule, one observes coupling between electrostatic and magnetic interactions, the so-called spin-orbit coupling. Hence the g -value deviates from that of the free electron so that information about the electronical state, the binding situation and the geometry of the molecule can be obtained [110]. Organic radicals, like nitroxides, which are also used in this work, have a small spin-orbit coupling so that the measured g -values are usually close to the g -value of the free electron [111].

1.3.1.4. Nuclear Zeeman Interaction

The interaction of a nuclear spin I and the external magnetic field is described by the nuclear Zeeman interaction:

$$H_{\text{NZ}} = -\frac{\mu_N g_N \mathbf{B}^T \mathbf{I}}{\hbar}, \quad (1.12)$$

where \mathbf{I} is the nuclear spin vector. The nuclear Zeeman interactions can be considered isotropic in most EPR experiments and have little influence on the EPR spectrum [109].

1.3.1.5. Hyperfine Interaction

The interaction between an electron spin and a nuclear spin splits the absorption spectrum into $M = 2NI + 1$ lines, where N is the number of magnetic equivalent nuclei and I is the nuclear spin (see Fig. 1.6).

The hyperfine interaction is described as:

$$H_{\text{HF}} = \mathbf{S}^T \mathbf{A} \mathbf{I}, \quad (1.13)$$

where \mathbf{A} is the hyperfine tensor, which can be written as the sum of the isotropic Fermi contact interaction H_{F} and the anisotropic electron-nuclear dipolar coupling H_{DD} .

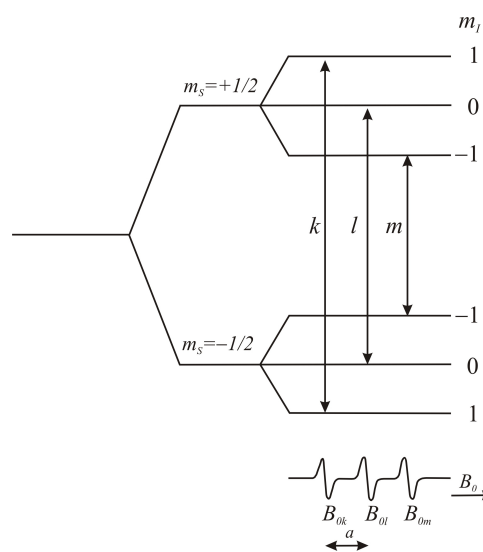


Figure 1.6. – Energy levels of a system with an unpaired electron that couples with a magnetic nucleus of spin $I = 1$. The resulting EPR spectrum consists of three absorption lines. The selection rules in EPR spectroscopy are $\Delta m_s = \pm 1$ and $\Delta m_I = 0$. Taken from [107].

The Fermi contact interaction is defined as:

$$H_F = a_{\text{iso}} \mathbf{S}^T \mathbf{I} , \quad (1.14)$$

where a_{iso} is the isotropic hyperfine coupling constant. The isotropic hyperfine coupling often only considers the contribution of s -orbitals because they are centered at the nucleus. The name *contact interaction* arises from the fact that the unpaired electron and the nucleus interact through direct contact with each other. However, the unpaired electron is often located in a p , d , or f -orbital. The spin density at the nucleus is then induced indirectly through polarization mechanisms [109, 110]. When the molecules are rotating fast in solution, only the Fermi contact interaction contributes to the hyperfine interaction.

The anisotropic dipole-dipole coupling is defined as:

$$H_{\text{DD}} = \mathbf{S}^T \mathbf{T} \mathbf{I} , \quad (1.15)$$

with the dipolar coupling tensor \mathbf{T} .

1.3.1.6. Nuclear Quadrupole Interaction

When the spin of a nucleus is ≥ 1 the charge-distribution is non-spherical and is described by a nuclear electrical quadrupole moment. The interaction of this charge-distribution with the electrons and nuclei in close vicinity is described as:

$$H_{\text{NQ}} = \mathbf{I}^T \mathbf{P} \mathbf{I} , \quad (1.16)$$

where \mathbf{P} is the traceless nuclear quadrupole tensor.

1.3.1.7. Zero-Field Splitting

Zero-field splitting is caused by the dipolar interaction of several unpaired electrons, e.g. transition metals or lanthanide ions, which leads to a group spin of $S_G > \frac{1}{2}$. Even without an external magnetic field a splitting is observed, which is termed as *fine structure*. A symmetric and traceless zero-field interaction tensor \mathbf{D}_G is added to the spin Hamiltonian:

$$H_{ZFS} = \mathbf{S}_G^T \mathbf{D}_G \mathbf{S}_G . \quad (1.17)$$

1.3.1.8. Weak Coupling between Electron Spins

If two unpaired electrons are strongly coupled to each other they are described by a group spin $S_G > \frac{1}{2}$. If two electrons are only weakly coupled, they may be regarded as two individual coupled spins with an exchange coupling tensor \mathbf{J} and a dipole-dipole coupling tensor \mathbf{D} . The complete Hamiltonian of such a system is described as:

$$H_0(S_1, S_2) = H_0(S_1) + H_0(S_2) + H_{exch} + H_{dd} . \quad (1.18)$$

The exchange coupling of two spins S_1 and S_2 , also termed as *Heisenberg exchange coupling*, is defined as:

$$H_{exch} = \mathbf{S}_1^T \mathbf{J} \mathbf{S}_2 , \quad (1.19)$$

and is important when orbitals of two spins overlap strongly so that the two unpaired electrons can be exchanged. In solution such an exchange can occur when two spins are very close to each other, e.g. in biradicals, or upon collisions.

1.3.1.9. Electron Dipole-Dipole Interaction

The interaction between two electrons through space is defined as:

$$H_{dd} = \mathbf{S}_1^T \mathbf{D} \mathbf{S}_2 . \quad (1.20)$$

If the interactions of both the spins with the external magnetic field are isotropic and dominant, then the two spins are oriented parallel to the external magnetic field, the so-called high-field approximation. If this is the case the anisotropy of the \mathbf{g} -tensor can be neglected and the Electron-Zeeman interaction is much stronger than the hyperfine interaction. \mathbf{D} is then defined as

$$\mathbf{D} = \frac{\mu_0}{4\pi\hbar} \frac{g_1 g_2 \mu_B^2}{r_1^3} \begin{pmatrix} -1 & & \\ & -1 & \\ & & 2 \end{pmatrix} = \begin{pmatrix} -\omega_{dd} & & \\ & -\omega_{dd} & \\ & & 2\omega_{dd} \end{pmatrix} , \quad (1.21)$$

where r_1 is the vector connecting the two electron spins (see Fig. 1.7) and ω_{dd} is the dipolar coupling frequency.

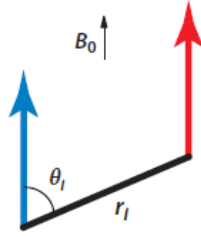


Figure 1.7. – Distance vector r_1 connecting two coupled electron spins. The angle θ_1 describes the angle of the vector r_1 with respect to the external magnetic field. Scheme from [112].

1.3.1.10. Relaxation and Bloch Equations

Detection of an EPR signal is not based upon only one spin. It is rather based upon an ensemble of different electron spins which leads to a macroscopic magnetization \mathbf{M} , the net magnetic moment per unit volume, which at thermal equilibrium is defined as:

$$\mathbf{M}_0 = \frac{1}{V} \sum \boldsymbol{\mu}_s . \quad (1.22)$$

If a static external magnetic field \mathbf{B}_0 is applied, the resulting macroscopic magnetization \mathbf{M}_0 is oriented along the z -axis. Upon absorption of microwave irradiation the relative populations of the spins in the lower and the higher energy levels are changed and thus the magnetization is forced out of thermal equilibrium conditions [111]. The torque on each of the magnetic moments is given as follows:

$$\frac{d\mathbf{M}}{dt} = \gamma \mathbf{M} \times \mathbf{B}_0 , \quad (1.23)$$

with the gyromagnetic ratio $\gamma = g\mu_B/\hbar$. This leads to a precession of \mathbf{M} around the z -axis, which can be described by the following equations [113]:

$$\frac{dM_x}{dt} = \omega_l M_y , \quad (1.24)$$

$$\frac{dM_y}{dt} = -\omega_l M_x , \quad (1.25)$$

$$\frac{dM_z}{dt} = 0 , \quad (1.26)$$

with the Larmor frequency $\omega_l = g_e \mu_B B_0 / \hbar$.

After the magnetization is forced out of equilibrium, the spins will start to interact with the surrounding lattice, which bring the system back to the equilibrium towards z , the so-called longitudinal or spin-lattice relaxation T_1 . This relaxation process is also called *spin flip* because the value of m_S changes its sign. Interactions of the spins with each other leads to the loss of coherence and thus a dephasing in the xy -plane, the so-called transversal or spin-spin-relaxation T_2 , a so-called *spin flip-flop* process.

This two relaxation effects can be described as follows [111]:

$$\frac{dM_x}{dt} = \omega_l M_y - \frac{M_x}{T_2} , \quad (1.27)$$

$$\frac{dM_y}{dt} = -\omega_l M_x - \frac{M_y}{T_2} , \quad (1.28)$$

$$\frac{dM_z}{dt} = \frac{M_z^0 - M_z}{T_1} . \quad (1.29)$$

To detect an EPR signal it is necessary to apply an additional field B_1 of the microwave frequency ω_{mw} . Then the Bloch equations can be obtained as [113]:

$$\frac{dM_x}{dt} = \omega_l M_y - \omega_1 \sin(\omega_{mw} t) M_z - \frac{M_x}{T_2} , \quad (1.30)$$

$$\frac{dM_y}{dt} = -\omega_l M_x + \omega_1 \cos(\omega_{mw} t) M_z - \frac{M_y}{T_2} , \quad (1.31)$$

$$\frac{dM_z}{dt} = \omega_1 [\sin(\omega_{mw} t) M_x - \cos(\omega_{mw} t) M_y] + \frac{M_z^0 - M_z}{T_1} . \quad (1.32)$$

For the sake of simplicity a rotating frame is assumed that rotates around the z -axis with the frequency ω_{mw} [113]:

$$\frac{dM_{x'}}{dt} = -\Omega M_{y'} - \frac{M_{x'}}{T_2} , \quad (1.33)$$

$$\frac{dM_{y'}}{dt} = \Omega M_{x'} + \omega_1 M_z - \frac{M_{y'}}{T_2} , \quad (1.34)$$

$$\frac{dM_{z'}}{dt} = -\omega_1 M_{y'} + \frac{M_z^0 - M_z}{T_1} , \quad (1.35)$$

with the resonance offset $\Omega = \omega_l - \omega_{mw}$.

1.3.1.11. Rotational Diffusion

It is of great importance in EPR spectroscopy to obtain information about the dynamics of the nitroxide radical. The motion is usually expressed as the rotational correlation time τ_c , the time the molecule needs to rotate about 1 radian [114]. If a molecule in solution is unhindered and thus can rotate very fast with respect to the EPR timescale, i.e. fast tumbling, the anisotropic parameters are averaged out. The spectra are isotropic and consist of sharp, narrow lines. Fast tumbling is often observed for small molecules in solutions of low viscosity [111].

However, when molecules are larger, e.g. labeled proteins, or the solutions are of higher viscosity, a slower tumbling is observed. The spectra will be anisotropic since in this case the anisotropic parameters are not averaged out. In a frozen sample no tumbling occurs and therefore, a powder spectrum is obtained. EPR spectra of a nitroxide radical at different temperatures are shown in Fig. 1.8.

The rotational correlation time τ_c can be obtained by spectral simulation of the experimental EPR spectra. The rotational correlation time τ_c in the slow motion regime (spectrum c in Fig. 1.8) can be calculated from:

$$\tau_c = \frac{1}{6D_r} , \quad (1.36)$$

where D_r is the rotational diffusion tensor.

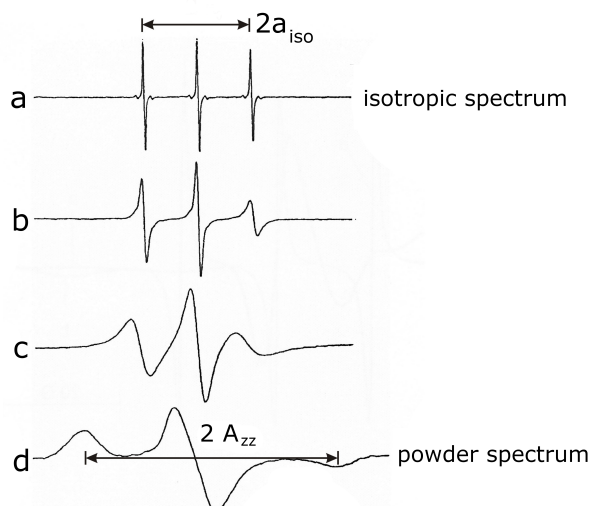


Figure 1.8. – EPR spectra of di-tert-butyl nitroxide at different temperatures. (a) 25°C, (b) -25 °C, (c) -80 °C, (d) - 150 °C. The isotropic hyperfine coupling constant $2a_{\text{iso}}$ describes the distance between the low field and the high field peak in the spectrum of a freely rotating molecule. In the immobilized powder spectrum the outer extrema separation can be described by the $2A_{zz}$ -value. Modified according to [115].

1.3.1.12. CW-EPR Spectroscopy

In *continuous wave* (CW) EPR spectroscopy the microwave frequency is kept constant while the magnetic field is swept in order to detect the electronic transitions. In this work multi-frequency CW-EPR measurements were carried out. Due to historical background the microwave frequencies are divided into different bands, e.g. X-band at about 9.5 GHz, Q-band at about 34 GHz, and W-band at about 95 GHz. The letter nomenclature was used at the time during the second world war to classify the microwave bands for the use of radar technology [107].

In EPR, some magnetic parameters, like the g -values, are dependent on the magnetic field. At X-band the g -values are superimposed, whereas at higher frequencies the individual g_{xx} , g_{yy} , and g_{zz} -values can be obtained. To some extent these values are accessible at Q-band, and can be well separated especially at W-band.

To optimize the SNR, a field modulation is applied by adding a small oscillating magnetic field B_m to the external magnetic field B . The frequency of the oscillating magnetic field is 100 kHz, see Fig. 1.9. When the external magnetic field is swept from B_a to B_b the

detector output increases from i_a to i_b , where the resulting output also oscillates with 100 kHz so that the first derivative of the absorption spectrum is obtained [111]. The SNR is therefore optimized because the detector only detects signals with the same output modulation frequency and thus background noise can be eliminated.

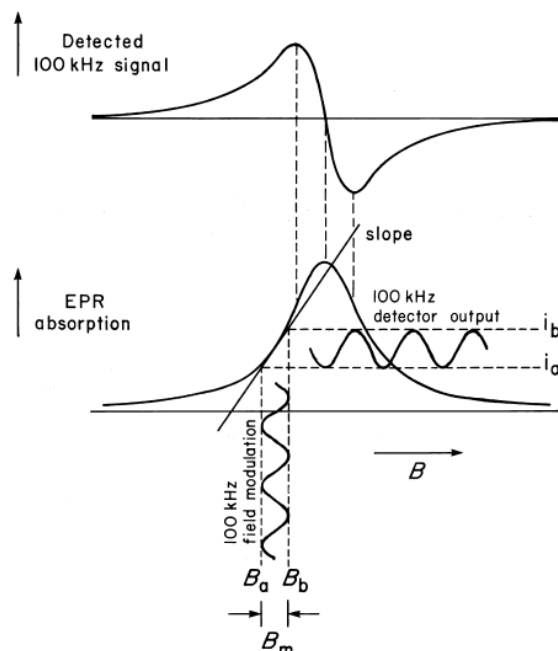


Figure 1.9. – Scheme of the field modulation of the static magnetic field with an additional oscillating magnetic field (100 kHz) to increase the SNR in CW-EPR spectroscopy. Taken from [107].

1.3.1.13. Pulsed EPR-Methods

Instead of continuous microwave irradiation, pulsed EPR applies short microwave pulses. In thermal equilibrium the macroscopic magnetization is aligned along the z -axis. If a microwave pulse B_1 of the length τ_p is applied along the x -axis in the rotating frame, the macroscopic magnetization flips around the y -axis in the xy -plane with the frequency ω_l . By choosing τ_p the so-called flip angle β can be changed

$$\beta = \omega_l \tau_p . \quad (1.37)$$

When the flip angle along the x -axis is $\beta = 90^\circ$ the pulse is termed as $(\frac{\pi}{2})_x$ -pulse, a flip

angle of $\beta = 180^\circ$ is then termed as $(\pi)_x$ -pulse. A fundamental pulse sequence was introduced in 1950 by Erwin Hahn [116] and is termed the *Hahn echo*: $\pi/2 - \tau - \pi - \tau - \text{Echo}$. The Hahn echo will be discussed more precisely in the following part, see Fig. 1.10.

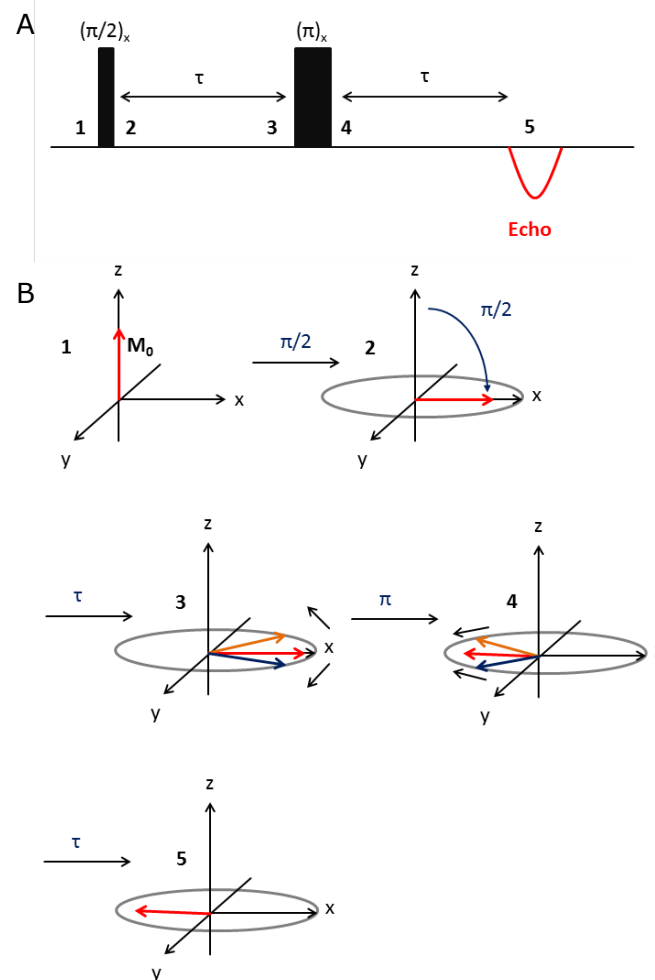


Figure 1.10. – (A) Pulse sequence of the Hahn Echo $\pi/2 - \tau - \pi - \tau - \text{Echo}$ [116]. (B) shows how the applied microwave pulses affect the magnetization vector \mathbf{M} during the Hahn Echo sequence. First, \mathbf{M} is in thermal equilibrium and therefore aligned along the z -axis (1). Upon a $(\pi/2)_x$ -pulse along the x -axis (2) \mathbf{M} flips in the xy -plane, where it starts to dephase during time τ (3). Then a $(\pi)_x$ -pulse is applied and the different dephased spin packets are mirrored at the y -axis (4) and after another time τ they unify again and give rise to the Hahn Echo (5).

At first the macroscopic magnetization is in the thermal equilibrium and thus aligned along the z -axis parallel with respect to the external magnetic field (point 1 in Fig. 1.10). If a $(\pi/2)_x$ -pulse is applied, the magnetization will be flipped so that it is rotating around the y -axis in the xy -plane (point 2 in Fig. 1.10). The different spin packets will precess around the y -axis with their own respective Larmor frequencies, i.e. some precess faster than others, which finally leads to a fanning out and dephasing of the spin packets (point 3 in Fig. 1.10).

When a $(\pi)_x$ -pulse is applied the magnetization is mirrored at the y -axis, so that the faster precessing and the slower precessing spin packets are unified again after another time τ , giving rise to the so-called *Electron Spin Echo (ESE)*, also known as *Primary Echo* (points 4 and 5, respectively, in Fig. 1.10).

The echo amplitude is a function of the evolution time τ between the pulses. If the echo is measured with respect to τ , the decay of the amplitude is [113]

$$E(\tau) = E_0 \cdot e^{\left(\frac{-2\tau}{T_m}\right)}, \quad (1.38)$$

with the phase memory time T_m . T_m can be described as the time that an echo needs to fall to $1/e$ of its maximum after the pulse has ended [107].

Usually, the pulses do only possess a narrow excitation bandwidth so that only the spins around the resonance frequency ω_{mw} are excited. These are called A-spins. Spins that are not affected by the pulse are termed as B-spins. It is possible to measure ESE-detected spectra similar to CW-EPR, however in this case the absorption spectrum is obtained. The magnetic field is swept so that the amplitude of the echo is determined with respect to the magnetic field. Due to short T_2 relaxation times at room temperature it is necessary to use frozen samples. The optimal temperature for nitroxides is about 50 K [117].

1.3.1.14. 4-Pulse DEER

The dipolar interaction between two electron spins is correlated to the interspin distance, see Ch. 1.3.1.9, p. 17. By measuring DEER (double electron-electron resonance), also known as PELDOR (pulsed electron-electron double resonance), it is possible to determine the dipolar coupling of two interacting electrons and thus the respective distance and their relative orientation can be extracted in optimum cases. Distances that can

be measured with this technique are in the range of about 1.6 - 6 nm for membrane proteins and up to 10 nm for deuterated soluble proteins [112].

The first DEER measurement was performed in 1984 by Milov et al. [118]. However, the applied 3-pulse sequence had the problem of a dead time so that the most interesting part of the signal in the beginning at $t = 0$ was not accessible. This problem could be circumvented by the introduction of a 4-pulse sequence in 2000 by Pannier et al. [119]. This 4-pulse DEER sequence is also used in this work and will be explained in the following part (see Fig. 1.11).

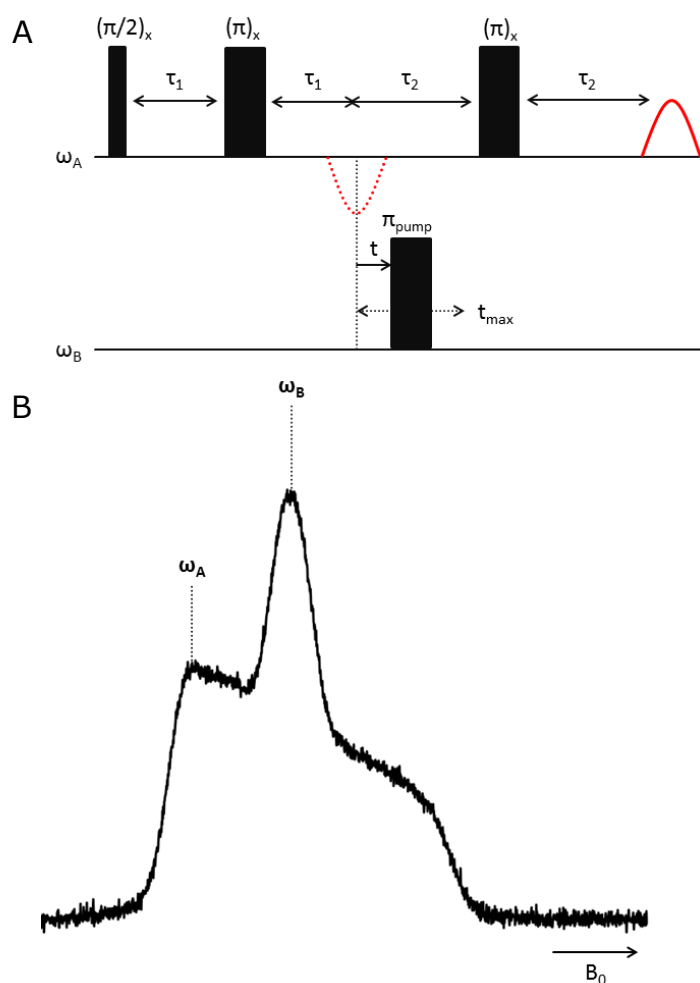


Figure 1.11. – (A) 4-Pulse DEER Sequence as introduced by Pannier et al. [119]. Scheme according to [117]. (B) Electron Spin Echo at X-band frequency of a nitroxide radical shows the observer and pump positions ω_A and ω_B , respectively.

In a 4-pulse DEER experiment, 3 pulses at the observer frequency (ω_A) are used to create a refocused primary echo with fixed interpulse delays τ_1 and τ_2 , respectively. Then an inversion pulse is applied at the pump frequency (ω_B) at variable times t with respect to the first observer echo [112]. The complete pulse sequence is $\pi/2(\nu_{obs}) - \tau_1 - \pi(\nu_{obs}) - t_d - \pi(\text{pump}) - (\tau_1 + \tau_2 - t_d) - \pi(\nu_{obs}) - \tau_2 - \text{Echo}$.

The excitation bandwidth of the pulses do not overlap as already stated. Hence the observer pulse should only excite the A-spins and the pump pulse the B-spins. If two electron spins are coupled, then inversion of the B-spins at the time t is also affecting the local field of the A-spins and thus the echo amplitude will be modulated. Upon measuring the echo amplitude with respect to time t the coupling of the electrons, ω_{dd} , can be determined and the interspin distance becomes accessible.

Not all of the electron spins B coupled to the spins A are excited with the pump pulse, which has typically a pulse length of 12 ns at X-band frequency. This fraction $\lambda < 1$ is termed as *inversion efficiency* and has a value of about ≈ 0.5 for nitroxide labels at X-band frequencies [112]. The echo amplitude as a function of time t and ω_{dd} are defined as [120]:

$$V(t, \theta, r) = 1 - \lambda[1 - \cos(\omega_{dd}(\theta, r)t)] \quad , \quad (1.39)$$

$$\omega_{dd}(\theta, r) = (3\cos^2\theta - 1) \frac{2\pi \cdot 52.04}{r^3} [\text{MHz nm}^3] \quad . \quad (1.40)$$

The dependence of the angle θ with respect to ω_{dd} is shown in Fig. 1.12. The vector connecting the two spins can vary from an orientation parallel ($\theta = 0^\circ$) to perpendicular ($\theta = 90^\circ$) with respect to the external magnetic field. If molecules are randomly oriented, the dipolar interaction will be zero and at the magic angle ($\theta = 54.7^\circ$) it vanishes [121]. If molecules rotate fast, the dipolar interaction is averaged out. However, in case of slowly rotating molecules or molecules in frozen samples, a superposition of spectra of randomly oriented molecules will be obtained. This resulting spectrum is called Pake pattern, see Fig. 1.12. The Pake pattern consists of two lines, that are separated by ω_{dd} [121].

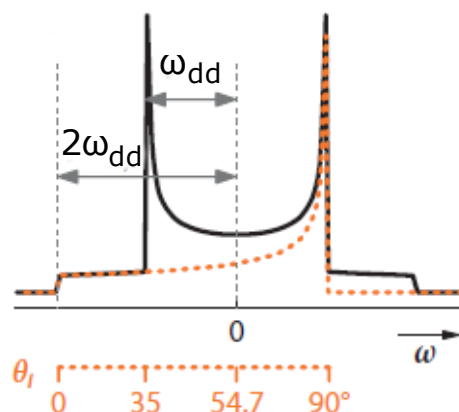


Figure 1.12. – Pake pattern obtained upon Fourier Transformation of the modulation of the echo as a function of time. The dependence of the angle θ with respect to the dipolar coupling frequency ω_{dd} is shown. Taken from [112].

When the pump frequency is set to the maximum of the nitroxide ESE spectrum at X-band frequencies (ω_B in Fig. 1.11) and therefore a λ -value of ≈ 0.5 is obtained, the orientation of the molecule with respect to the external magnetic field can be neglected. The mean distances can then be extracted mainly from the dipolar frequency at ($\theta = 90^\circ$) [112].

The assumption that the spin pairs are isolated is incorrect since the electron spin also interacts with other spins of the sample. Hence, the “pump-pulse dependent echo amplitude” has to be split into an intramolecular part, i.e. spin within the same nano-object, and the intermolecular part, which is termed as the DEER background. The intramolecular part is known as form factor $F(t)$, whereas the background factor is termed as $B(t)$ [112]:

$$V(t) = F(t)B(t) . \quad (1.41)$$

When the dead-time-free 4p-DEER experiment is used, $V(t)$ can be normalized to $V(0) = 1$ [122]. Separation of the background factor $B(t)$ is also dependent on the dimensionality. When the nanoobjects are homogeneously distributed and when longitudinal relaxation of the A and B spins can be neglected, $B(t)$ is an exponentially decaying function [122]:

$$B(t) = e^{(-kt^{\frac{d}{3}})} , \quad (1.42)$$

with k = spin density and d = dimensionality.

A homogeneous distribution usually has $d = 3$ dimensions. However, when proteins are reconstituted in a liposome, i.e. a lipid bilayer, $d = 2$ may apply because lipid bilayers can be regarded as 2-dimensional surfaces.

Upon Fourier transformation of the background-corrected modulation of the echo as a function of time, which is also termed as *time trace*, a distribution of different dipole-dipole coupling frequencies is obtained. Due to the proportionality of ω_{dd} to r^3 the respective interspin distance can be obtained.

For extracting the respective distances, the form factor $F(t)$ needs to be converted into a distribution of distances, which is an ill-posed problem. Ill-posed problems imply that a small change in $F(t)$ can lead to large changes in $P(r)$. Tikhonov regularization, which is included in the DEERAnalysis software package [122] overcomes this problem.

It is also possible to obtain the number of coupled spins as defined in [122]:

$$\langle n \rangle = 1 - \frac{\ln(1 - \Delta)}{\lambda} , \quad (1.43)$$

with the modulation depth Δ of the DEER time trace (see Fig. 1.13B), which resembles the signal decay at $t \rightarrow \infty$

Fig. 1.13 shows the different data sets that are obtained from a 4-pulse DEER experiment.

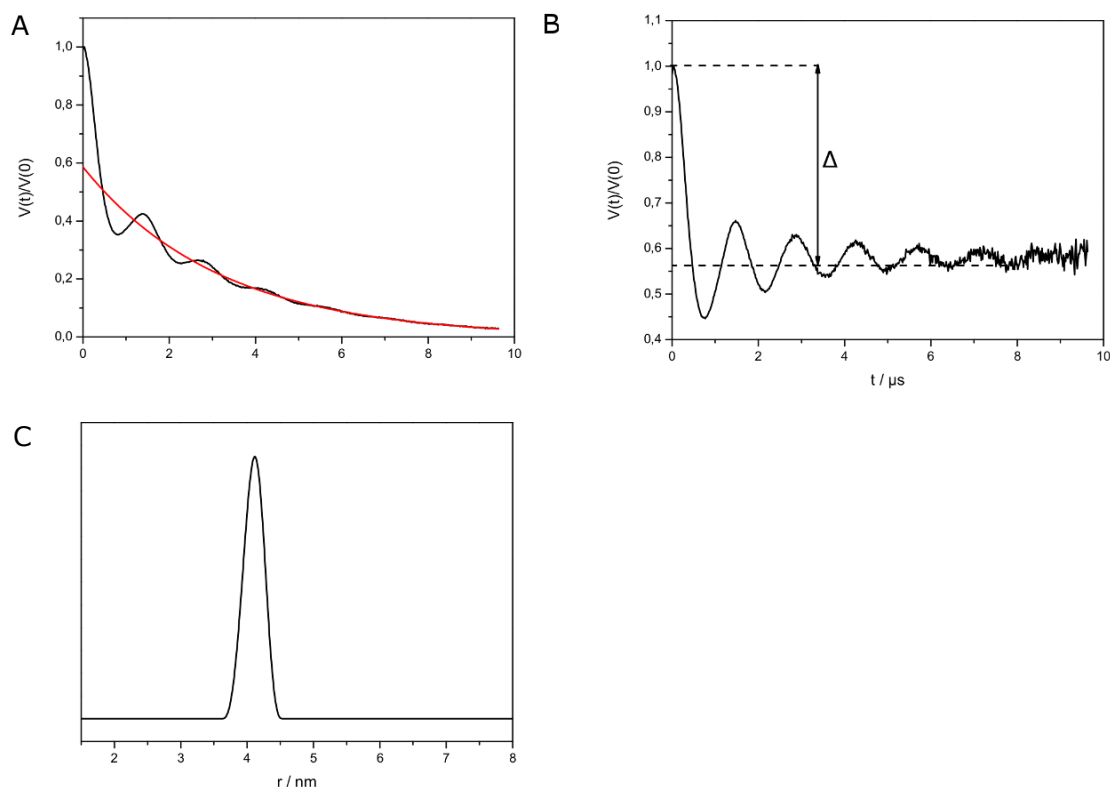


Figure 1.13. – (A) Raw data of a 4-pulse DEER experiment. The (normalized) experimental data set is shown in black, the red curve resembles the background fit. (B) Form factor $F(t)$ and the modulation depth Δ which is related to the number of coupled spins (Eq. 1.43). (C) Determined distance distribution. Modified according to [112].

1.3.2. Biological Membranes

Biological cell membranes have an essential role in living organisms. They provide a barrier that separates the interior of cells, or organelles within the cells, from the outside. Important functions include the control of the exchange of molecules, cell adhesion, and cell signaling [123, 124]. Biological membranes can be described by the fluid-mosaic model, which has been introduced in 1972 by Singer and Nicholson [125] and which has been updated ever since [123]. According to this model, membranes consist of a phospholipid bilayer and membrane proteins. Due to the high mobility of the lipids and the proteins, the membrane in general behaves like a two-dimensional fluid. Membrane proteins can either be peripheral bound to the membrane or they can

span the membrane as an integral protein dependent on the amino acid sequence. Thus, charged and/or polar amino acids are located in the extra-membrane domain, whereas nonpolar and neutral residues are located in the membrane-spanning domains.

The most common type of phospholipids found in biological cell membranes are the glycerophospholipids. They consist of a phosphoglycerol backbone attached to a polar head group and two fatty acid tails. Different phospholipids vary in the composition of their head groups and their hydrophobic chains, see Fig. 1.15.

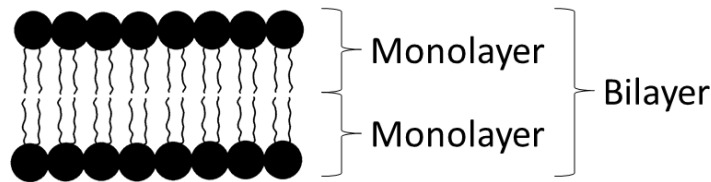


Figure 1.14. – Biological membranes are about 4 to 5 nm thick and consist of a phospholipid bilayer, i.e. it is composed of two phospholipid monolayers. Phospholipids are a class of amphipathic molecules with a hydrophilic head group and hydrophobic fatty acid tails. Due to this amphipathic character the phospholipids arrange in a manner that the polar head group is in contact with the surrounding aqueous phase, whereas the hydrophobic fatty acid tails form a hydrophobic core. This arrangement leads to the formation of closed vesicular structures [126]. Sketch modified according to [124].

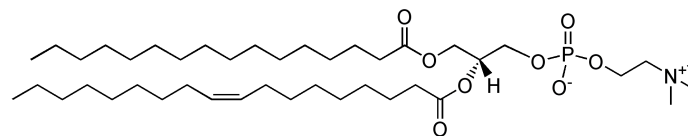
A good means to study membranes and their interaction with proteins is to work with model systems, e.g. in this work the following systems have been used:

Lipid Monolayers resemble one leaflet of a phospholipid bilayer on an aqueous surface

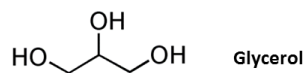
Liposomes closed spherical vesicles made up of a lipid bilayer

1.3.2.1. Lipid Monolayers

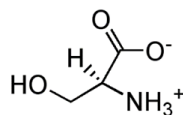
A lipid monolayer can be generated by spreading a lipid, which is usually dissolved in an organic solvent like chloroform/methanol, on an aqueous subphase. After evaporation of the organic solvent, the hydrophilic head groups of the lipids will be solubilized in the polar subphase, whereas the hydrophobic fatty acid tails will point towards the



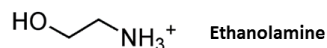
(a) – Structure of the phosphatidylcholine POPC



Glycerol

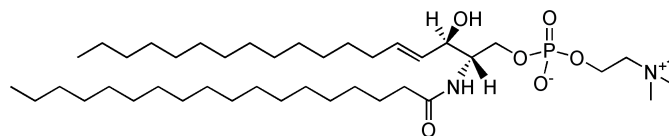


Serine



Ethanolamine

(b) – Structure of alternative head groups



(c) – Structure of Sphingomyelin

Figure 1.15. – (a) Structure of phosphatidylcholine POPC. The phosphoglycerol backbone is esterified with the two fatty acids palmitic acid and oleic acid. The polar head group is the positively charged choline. Full chemical name of POPC is: 1-palmitoyl-2-oleoyl-*sn*-glycero-3-phosphocholine. (b) Alternative head groups include i.a. glycerol, serine, and ethanolamine. (c) Structure of Sphingomyelin. Sphingomyelin (a sphingophospholipid) has a sphingosine backbone instead of a glycerol backbone. The phosphate group is esterified with a choline.

(hydrophobic) air. Such amphiphilic membrane lipids will not dissolve in the aqueous subphase and form thus an insoluble surface film termed as *Langmuir film*.

To study monolayers at the air/water-interface the surface pressure π is measured, which is related to the surface tension σ . π is the difference of the surface tension of pure water ($\sigma_0 = 72.8 \text{ mN/m}$ at 20°C) and the surface tension σ of the lipid monolayer:

$$\pi = \sigma_0 - \sigma \quad (1.44)$$

The surface tension in general is defined as the partial derivative of the free enthalpy G

with respect to the surface A at constant temperature T and pressure p :

$$\sigma = \left(\frac{\partial G}{\partial A} \right)_{p,T} . \quad (1.45)$$

In general two different types of monolayer experiments can be used:

Compression Isotherms π is measured as a function of the area per molecule

Adsorption Experiments π is measured as function of time

Both experiments have been performed with the *Wilhelmy plate* method, as seen in Fig. 1.16.

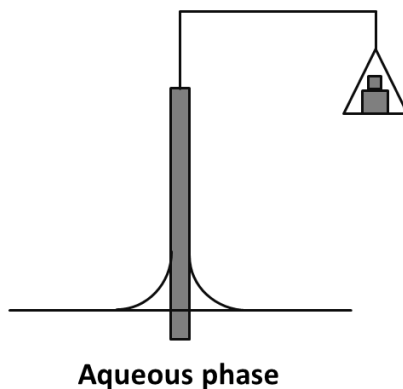


Figure 1.16. – Sketch of a Wilhelmy plate. The Wilhelmy plate measures the surface tension and therefore the surface pressure. Due to the contact to the aqueous sub-phase the plate gets wetted and experiences 1) a pulling force into the sub-phase because of surface tension and gravity, and 2) an upward force due to buoyancy of the displaced water. This can be observed in an increase of weight and thus measured by a pair of scales. Modified according to [124].

1.3.2.2. Compression Isotherms

Upon measuring the change of the surface pressure as a function of the area per molecule in a so-called *Langmuir film trough* at a constant temperature, the compression isotherm can be obtained. By minimizing the area between two barriers, the lipid

molecules of the monolayer are forced to align themselves. If the density of the lipid is higher, then the surface tension of the lipid monolayer decreases and the resulting surface pressure increases. A scheme of a compression isotherm of a phospholipid is shown in Fig. 1.17.

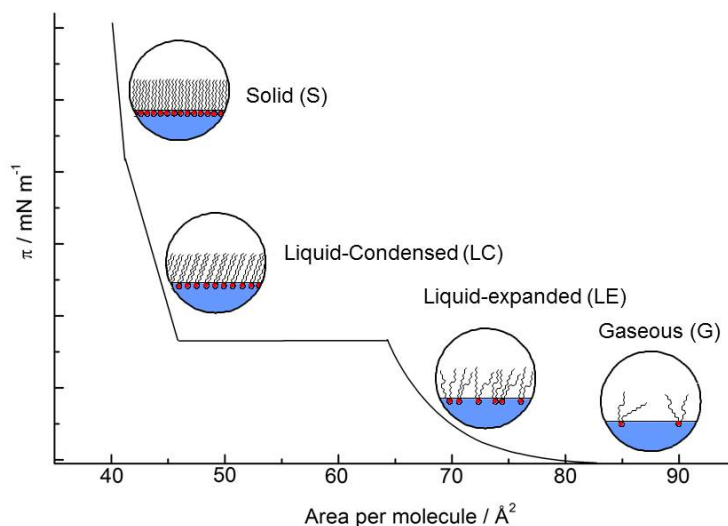


Figure 1.17. – Scheme of a compression isotherm of a phospholipid at the air/water-interface. Shown are the different phase transitions that occur upon minimizing the surface area. In the LE-phase fatty acid chains of the lipids are predominantly in the gauche-conformation state. Upon compression they are forced to straighten up (LC-phase) and finally in the crystalline state they are all-trans configured with limited space and also limited compressibility. Upon further compression, the monolayer will collapse. If lipids with unsaturated fatty acid chains are compressed there will be only the phase transition from the gas-analogous to the liquid expanded state at 20 °C. Further compression will directly lead to the collapse of the monolayer [124]. Scheme modified according to [127].

1.3.2.3. Adsorption Isotherms

The adsorption of an amphiphilic, soluble molecule to an aqueous subphase (water or buffer) can be observed by using a film trough with a constant area. If the protein is surface-active, it will displace the water molecules from the surface into the aqueous subphase. The surface pressure π and therefore the surface tension σ will change upon this interaction. At some point, an equilibrium of the molecules with the bulk phase

will be reached. The resulting saturation concentration Γ is defined as:

$$\Gamma = \frac{n_s - n_b}{A} , \quad (1.46)$$

where n_s are the moles at the surface, n_b are the moles in the bulk phase and A is surface area.

The *Gibbs adsorption isotherm* is defined as:

$$\Gamma = - \frac{1}{RT} \left(\frac{d\sigma}{d \ln c} \right) , \quad (1.47)$$

where R is the gas constant, T is the temperature, σ is the surface tension, and c is the concentration.

Another approach in this work was to spread a phospholipid monolayer to different surface pressures π . After the stabilization of the film, the protein has been injected into the aqueous subphase (buffer) underneath the monolayer and the changes in the surface pressure π have been observed. To compare the different measurements it is necessary to inject the same amount of protein into the aqueous subphase.

If the surface pressure π increases, the protein inserts into the phospholipid monolayer. Upon injection of the protein at different surface pressures the so-called maximum insertion pressure MIP can be obtained, up to which a protein can insert into the phospholipid monolayer [128], see Fig. 1.18.

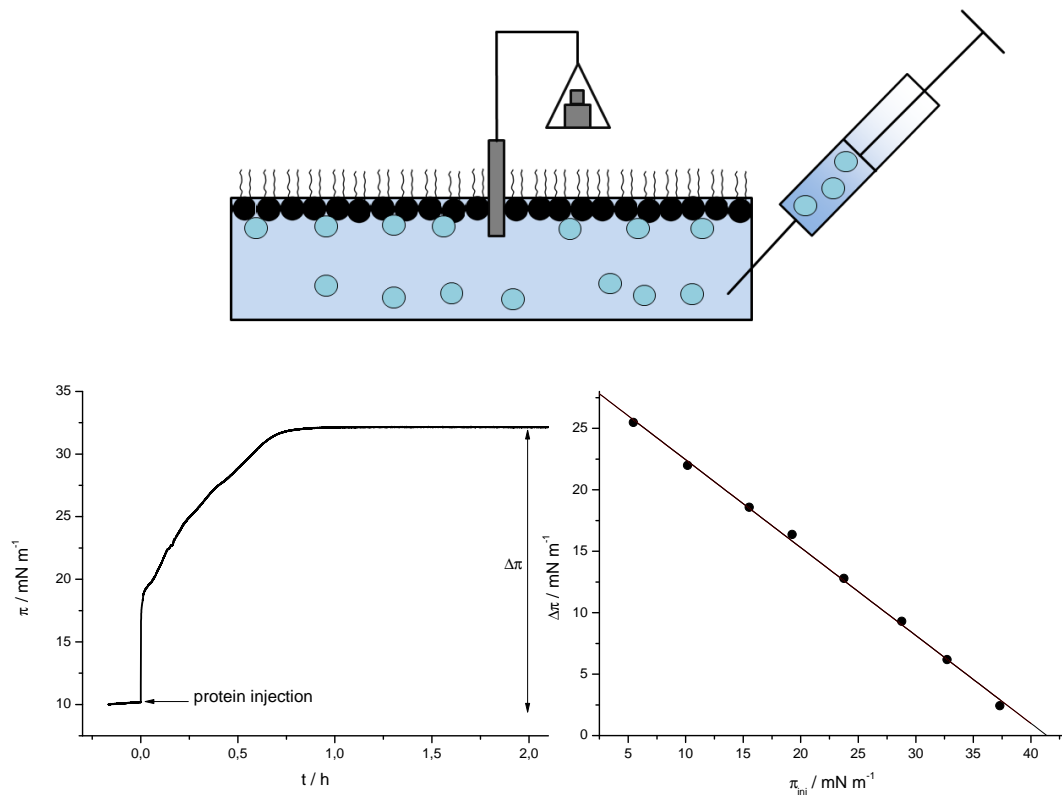


Figure 1.18. – Determination of the maximum insertion pressure. The phospholipid monolayer is spread up to different surface pressures π_{ini} . After stabilizing of the monolayer the molecule to be observed (e.g. a protein) is injected into the aqueous surface underneath the phospholipid monolayer. If the protein is surface-active, the π will increase. At some point, a saturation behavior will be observed and the respective surface pressure will be read out at this point. Upon plotting $\Delta\pi = \pi - \pi_{\text{ini}}$ against π_{ini} , a linear plot is obtained and the maximum insertion pressure can be read out at the interception of the plot with the x -axis.

Since lipid membranes in organisms consist of a bilayer it is necessary to compare phospholipid monolayers and bilayers. It has been shown that the behavior of a monolayer at a lateral surface pressure of about 30 mN/m is similar to that of the bilayer [129]. That is, membrane-bound proteins usually show MIPs at values about 30 mN/m.

2. Scope

2.1. α -Synuclein

α -Synuclein can be assigned to the class of intrinsically disordered proteins. As already stated in the introduction part of this work, this class does not possess a folded structure. In the case of α -Synuclein the protein is intrinsically disordered without a folded structure in solution. However, it can adopt a more ordered structure upon binding to negatively charged membranes. In cooperation with the R. Konrat group of the University of Vienna this membrane-bound state was studied. Via the EPR-technique (X-band CW-EPR, Q-band CW-EPR, as well as 4p-DEER) six single-cysteine mutants were examined upon binding to liposomes composed of the negatively charged lipid POPG. The cysteines were within different positions along the protein chain in order to cover a wide range of different regions. Since single-cysteine mutants were used, it was possible to look at the intermolecular environment and to ask whether there was a self-assembly of the protein on the liposomes. This was achieved by measuring DEER. By conducting CW-EPR experiments, the rotational dynamics of the corresponding spin label was examined. The main purpose of the examination of the membrane-bound state was to check how the protein is affected upon addition of a small molecule of therapeutic interest. Due to patent protection the structure of this molecule is unknown and moreover will be termed as “Ligand X”.

Moreover, the affinity of α -Synuclein to different lipids was examined since early and recent publications are based on measurements of POPG liposomes or SDS micelles [68–77]. Because there are publications about the interaction of α -Synuclein with synaptic vesicles, also a lipid composition of a synaptic vesicle was used. These measurements were carried out via the film balance technique, especially adsorption experiments.

2.2. HPRG

The initial scope of this project was to purify the rabbit HPRG protein according to literature. HPRG is a glycoprotein and therefore can not be purified according to standard expression protocols due to *E. coli*'s incapability to glycosylate. Early purification approaches were based upon phosphocellulose columns that yielded also in several co-purified proteins [130, 131]. More recent purification strategies consisted of metal chelate affinity chromatography and then size exclusion chromatography or anion exchange chromatography, respectively [87, 130]. However, my initial finding was, when metal chelate affinity chromatography was carried out, a large amount of serum albumin also eluted from the column. Serum albumin could not be successfully removed via the above named chromatographic steps. Hence another purification strategy was needed in order to obtain a pure protein because serum albumin can also bind to most of the components (e.g. divalent metal ions) that should be added as spin probes to HPRG for further EPR measurements.

3. Results and Discussion

3.1. α -Synuclein

3.1.1. Electron Paramagnetic Resonance

The aim of this part of the work was to study the membrane-bound structure of different spin-labeled single cysteine mutants of α -Synuclein and how it was affected by addition of a small molecule of medical interest.

Proteins are diamagnetic, hence it is necessary to introduce an EPR-active compound into the molecule, the so-called spin label. Most often the pyrrolidin derivate MTS (S-(1-oxyl-2,2,5,5-tetramethyl-2,5-dihydro-1H-pyrrol-3-yl)methylmethanesulfonothioate) is used. Due to the methyl groups, this nitroxide spin label is sterically protected and thus considered as a stable radical. Because of its affinity for thiol groups, MTS is suitable for labeling the cysteine residues of a protein.

WT α -Synuclein does not contain any cysteine residues so that *site-directed mutagenesis* had to be carried out. *Site-directed mutagenesis* and subsequent labeling of cysteine residues is termed as *site-directed spin labeling* and was introduced by Altenbach et al. in 1989 [132]. A scheme of the labeling reaction of a cysteine residue with MTS is shown in Fig. 3.1.

The biochemical nomenclature for protein mutants is that at first the amino acid of the WT is listed, then the position of the respective amino acid followed by the substituted amino acid. For example in this work α -Synuclein A19C was measured. In the WT sequence there was an alanine at the position 19, whereas in the protein mutant, a cysteine was introduced.

The six spin-labeled single cysteine mutants α -Synuclein A19C, α -Synuclein G41C, α -Synuclein A53C, α -Synuclein K80C, α -Synuclein E104C, and α -Synuclein S129C as well as the POPG liposomes (100 nm diameter) were provided in collaboration with

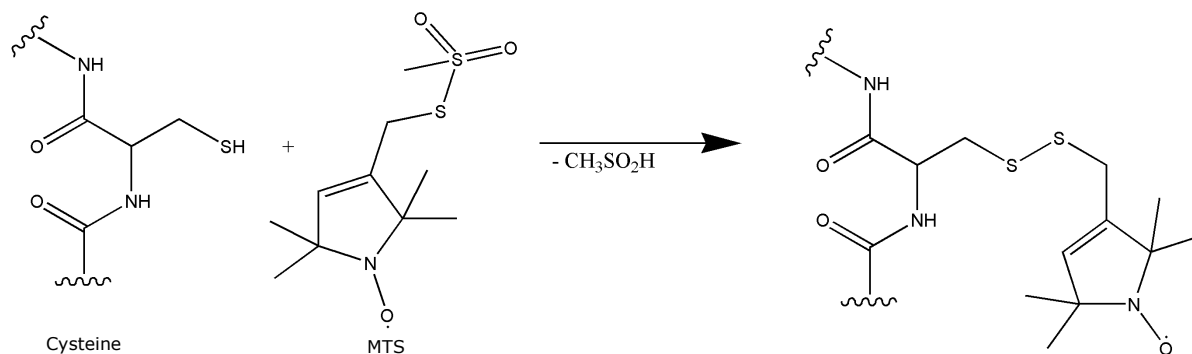


Figure 3.1. – Scheme of a spin labeling reaction of a cysteine residue.

University of Vienna (Research group of Prof. R. Konrat). The different positions of the cysteine residues covered a wide range of the protein's amino acid chain, see Fig. 3.2.

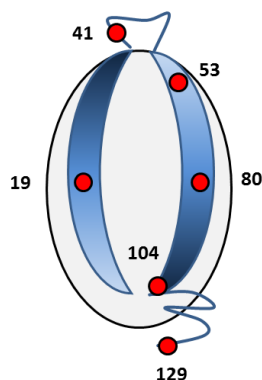


Figure 3.2. – Cartoon of the horseshoe structure of α -Synuclein bound to an ellipsoidal micelle [133]. Shown are the two helices of the protein as well as the linker region, which connects the two helices. The C-terminal domain remains unbound and unstructured. The red dots indicate the spin labeling positions used in this work. Modified according to [133].

At first, an initial measurement was carried out to obtain optimum experimental conditions, especially to check if for a certain concentration of protein and liposome an appropriate EPR spectrum could be obtained. RT multi-frequency CW-EPR measurements were carried out at about 9.43 GHz (X-band CW-EPR spectroscopy) and at about 34 GHz (Q-band CW-EPR spectroscopy). In the next step pulsed X-band measurements were carried out to obtain information about the dipolar coupling (DEER measurements) and therefore to obtain information about a possible self-assembly of α -Synuclein on

the liposome. Pulsed X-band measurement were carried out at cryogenic temperatures, so that it was necessary to add an amount of 20 % glycerol to the sample as a cryoprotectant. The measurements were conducted with a protein concentration of 0.24 mM α -Synuclein, 1.6 mg/ml POPG (2 mM) in 20 mM phosphate, 100 mM NaCl, pH 7.4 as stated in Ch. 5, p. 109.

It should be noted that when speaking of the membrane-bound state of an α -Synuclein mutant, for example A19C, not the membrane-bound state of the protein in general is addressed. The MTS label is used to analyze the membrane-bound state of a certain *labeling position*, in this case how strong is the position 19 interacting with the liposome.

3.1.1.1. Membrane-bound State of α -Synuclein

X-Band CW-EPR Fig. 3.3 illustrates the spectra of 0.24 mM α -Synuclein and 2 mM POPG in buffer. Preliminary analysis of the experimental spectra (black curves) shows that the N-terminal part, especially α -Synuclein A19C and G41C, are strongly bound to the liposome. This can be observed in the relatively broad central peak and a few more freely rotating components. A53C and K80C are less strongly bound to the liposome and more freely rotating components are visible. E104C and S129C are little bound to the liposome and show a high percentage of freely rotating components, which is in accordance with the literature, that when the protein is bound to a membrane, the C-terminal domain starting from about amino acid 100 is still intrinsically disordered and remains in solution [67]. Moreover, it has been stated that the two helices of the horseshoe structure (see Fig. 3.2), have different binding affinities for membranes. The first helix contains more cationic residues, like lysines, than the second helix so that the electrostatic interaction of the second helix may be weaker[134].

In order to extract more information from the experimental CW-EPR spectra, spectral simulation as stated in the experimental part (see Ch. 5.2.1.4, p. 115) was done. The respective simulations of the measurement of 0.24 mM α -Synuclein and 2 mM POPG in buffer are shown in red in Fig. 3.3.

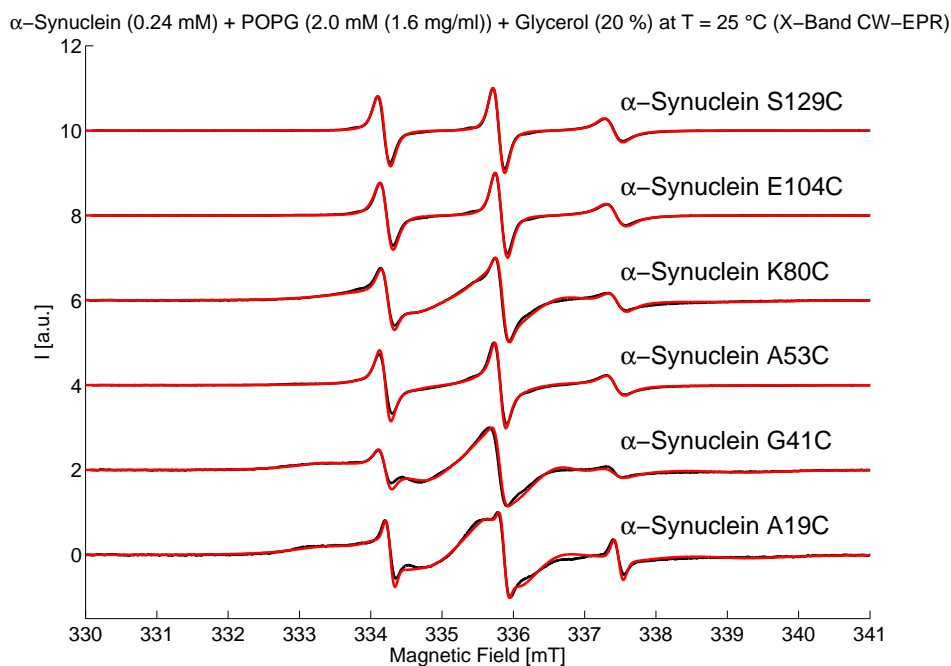


Figure 3.3. – Experimental spectra (black) and simulations (red) of 0.24 mM α -Synuclein and 2 mM POPG in buffer (X-band CW-EPR).

A CW-EPR spectrum consists of several components of different dynamic behavior which have to be taken into account during spectral simulations. Fig. 3.4 shows the three components, which form the X-band CW-EPR spectrum of α -Synuclein A19C. An immobilized slowly rotating component, a more fast rotating intermediate component, and a rather freely, fast rotating component with different contributing percentages, are detectable. The spectrum of α -Synuclein G41C also needed to be simulated with three components.

When comparing different simulated EPR spectra, it is necessary to take a close look on the contributing percentages of each component. Where in α -Synuclein A19C the slow component is the one with the highest contribution, in case of α -Synuclein G41C it is the intermediate one, which has a dominant role. α -Synuclein A53C and K80C are composed of only the intermediate and the fast component. The intermediate component is the one of the highest contribution. α -Synuclein E104C and S129C consist only of the fast component. Percentages and the respective rotational correlation times

are listed in Tab. 3.1.

The component of the highest percentage will be referred as *main component* in this work and most of the data analysis is focused on the main components.

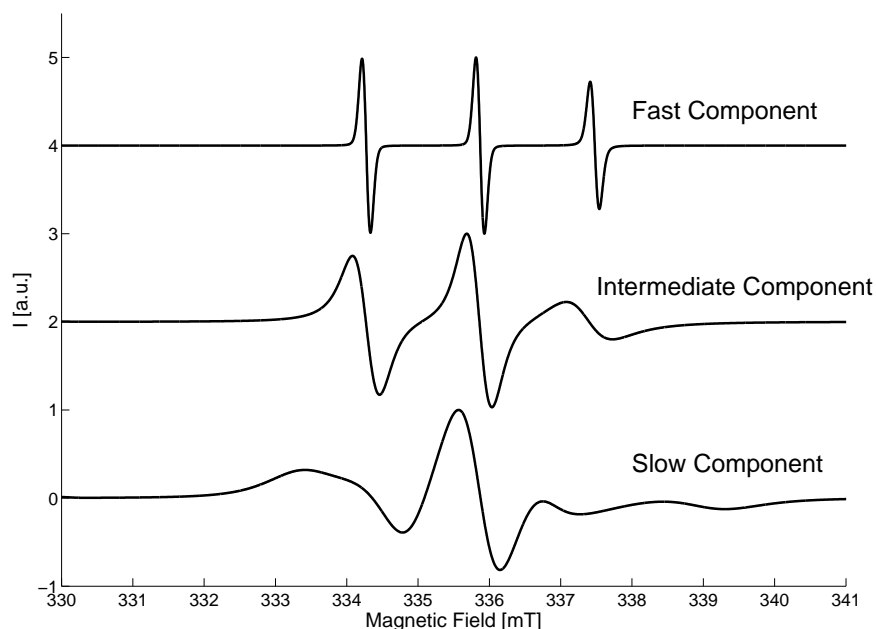


Figure 3.4. – Different components of a X-band CW-EPR spectrum.

0.24 mM α -Synuclein + 2 mM POPG in 20 mM Phosphate + 20% Glycerol (X-band CW-EPR)			
	Slow Comp. [%] / τ_c [ns]	Intermediate Comp. [%] / τ_c [ns]	Fast Comp. [%] / τ_c [ns]
α -Synuclein A19C	83 / 6.822	15 / 1.672	2 / 0.092
α -Synuclein G41C	10 / 6.360	80 / 5.778	10 / 0.852
α -Synuclein A53C	0 / -	60 / 3.852	40 / 0.699
α -Synuclein K80C	0 / -	86 / 3.868	14 / 0.604
α -Synuclein E104C	0 / -	0 / -	100 / 0.902
α -Synuclein S129C	0 / -	0 / -	100 / 0.749

Table 3.1. – Contributing percentages and rotational correlation times τ_c of the different components extracted from spectral simulation (X-band CW-EPR). The slow component is relatively strongly immobilized, thus rotating rather slow, whereas the intermediate and the fast components are rotating fast.

The nitroxide spin label is sensitive to changes in the microenvironment, especially to changes in the polarity. Changes in polarity can be reported by the g -values and the hyperfine interaction. Upon a more polar environment, the unpaired electron is more likely located close to the nitrogen nucleus of the nitroxide spin label due to the zwitterionic structure, see Fig. 3.5. This leads to stronger hyperfine interactions so that the coupling constant a increases [135, 136]. Moreover, due to the negative charge at the oxygen atom, hydrogen bonds can be formed more easily so that the g -values get smaller [135, 136].

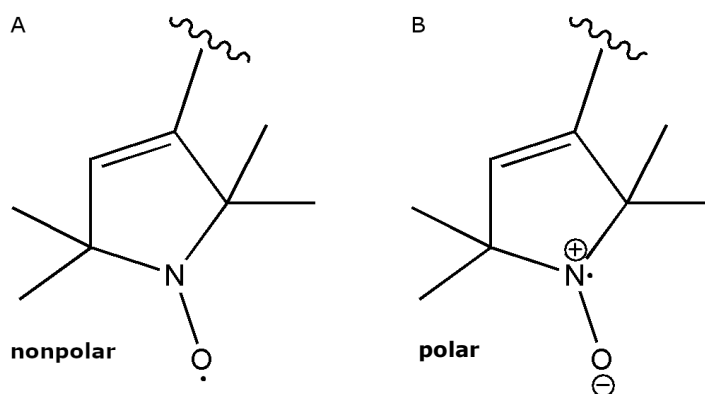


Figure 3.5. – Mesomeric structures of the nitroxide spin label MTS in a nonpolar (A) and a polar (B) environment. In a polar environment the unpaired electron is more likely located close to the nitrogen nucleus. In a nonpolar environment the unpaired electron is more likely located close to the oxygen.

The different simulation parameters of the X-band CW-EPR of 0.24 mM α -Synuclein and 2 mM POPG in buffer are listed in Tab. 3.2.

0.24 mM α -Synuclein + 2 mM POPG in 20 mM Phosphate + 20 % Glycerol (X-band CW-EPR)			
	g_{iso}	a_{iso} [MHz]	τ_c [ns]
α -Synuclein A19C	2.0057	45.0	6.822
α -Synuclein G41C	2.0056	45.4	5.778
α -Synuclein A53C	2.0057	45.5	3.852
α -Synuclein K80C	2.0056	45.4	3.868
α -Synuclein E104C	2.0058	45.3	0.902
α -Synuclein S129C	2.0058	45.3	0.749

Table 3.2. – X-band CW-EPR simulation parameters of 0.24 mM α -Synuclein and 2 mM POPG in buffer. Determined from the spectral simulation were the values of g_{iso} and the isotropic coupling constant a_{iso} as well as the rotational correlation time τ_c .

The values of g_{iso} at X-Band frequencies are of the same magnitude so that no precise conclusion can be drawn whether the environment of the spin label is more polar or nonpolar. However, a_{iso} seems to be more affected. α -Synuclein A19C shows the lowest value for the coupling constant indicating that the protein, i.e. this position near the N-terminus, is indeed strongly bound to the liposome and the spin label is probably at least slightly incorporated into the membrane. The coupling constant for α -Synuclein G41C is higher compared to that for A19C, which can be explained by a strong binding to the membrane as confirmed by the high τ_c -value. However, this labeling position does probably possess a bit more motional freedom and may face towards the solvent. It has to be noted that this labeling position is within the hypothesized linker region of the horseshoe structure of a membrane-bound α -Synuclein and therefore may be more flexible compared to the A19C labeling position. The labeling positions in the second helix of the horseshoe structure (Fig. 3.2, p. 40) all show similar values for a_{iso} , indicating a slightly more polar environment compared to α -Synuclein A19C. Information about the binding of α -Synuclein to the liposome can also be obtained from a plot of the rotational correlation time τ_c obtained from the spectral simulations against the respective labeling position (see Fig. 3.6).

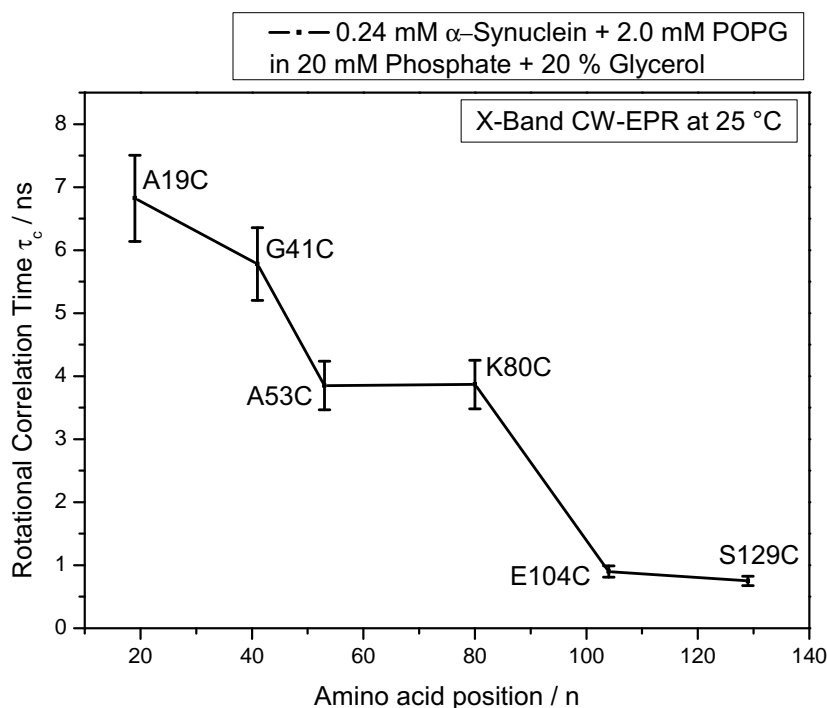


Figure 3.6. – Plot of τ_c against corresponding labeling position of 0.24 mM α -Synuclein and 2 mM POPG in buffer (X-band).

α -Synuclein A19C is strongly bound to the liposome as indicated by the relatively high τ_c . α -Synuclein G41C is a equally strong/a bit less bound, when taking the error bars of τ_c into account. The error bars were determined from the spectral simulation by changing the values of the diffusion tensor until a visible change could be observed. The error was found to be about 10 % for all CW-EPR spectra, in X-band and Q-band spectra, respectively.

α -Synuclein A53C and K80C show rotational correlation times in the same range, but are significantly reduced compared to α -Synuclein A19C an G41C. α -Synuclein E104C and S129C contain only the fast component as proved by a low τ_c -value. Both these labeling positions are within the C-terminal domain, which is unstructured and remains in solution even when the N-terminal domain is bound to the liposome. Therefore the spin label exhibits a large flexibility explaining why the fast rotating component is the only one contributing to the EPR spectrum.

Q-Band CW-EPR The samples of 0.24 mM α -Synuclein and 2 mM POPG in buffer were measured in a Q-band CW-EPR experiment at about 34 GHz (black curve in Fig. 3.7).

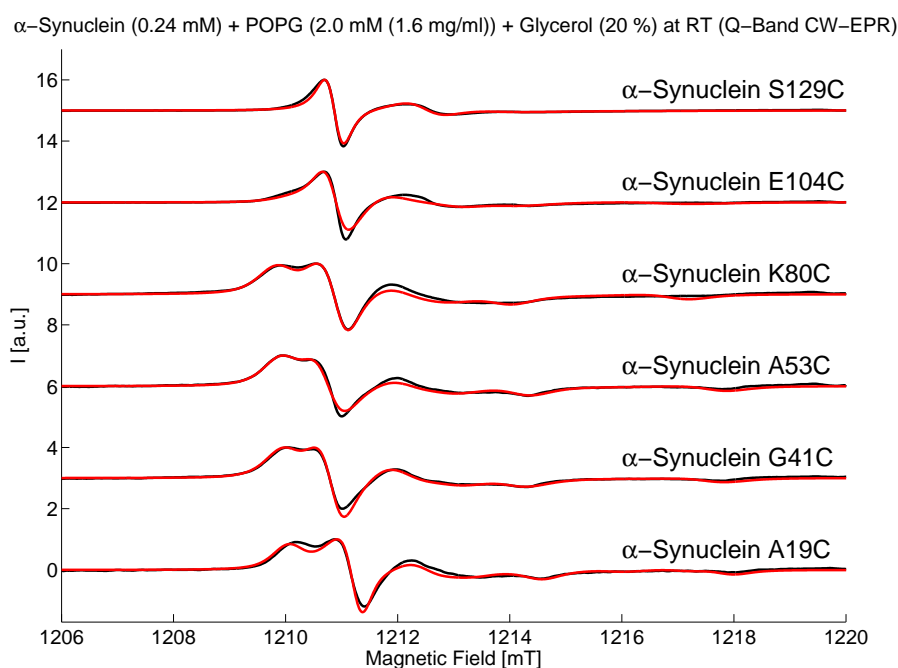


Figure 3.7. – Experimental spectra (black) and simulation (red) of 0.24 mM α -Synuclein and 2 mM POPG in buffer (Q-band CW-EPR).

Interesting observations can be made upon checking the different spectra. The peaks are becoming more broad compared to the experimental spectra at X-band frequencies. Moreover, at Q-band frequencies the g -anisotropy is partially resolved. The g_{xx} -value can be determined as well as the g_{zz} - and the A_{zz} -values as demonstrated in Fig. 3.8. However, the latter parameters were not always properly resolved in the experimental spectra in this work. Q-band spectra were measured at RT, whereas most often the EPR parameters described above are determined from frozen spectra [137]. The fact that an immobilized spectrum could be obtained, where these parameters are resolved, as shown exemplary in Fig. 3.8 for α -Synuclein A19C, is another indication for the strong interaction of α -Synuclein with the liposome.

In Fig. 3.8 another significant difference regarding the shape of α -Synuclein E104C and S129C compared to the other mutants can be observed especially in the low-field peak. This difference is likely to arise from the difference in polarity since the C-terminal domain remains in solution.

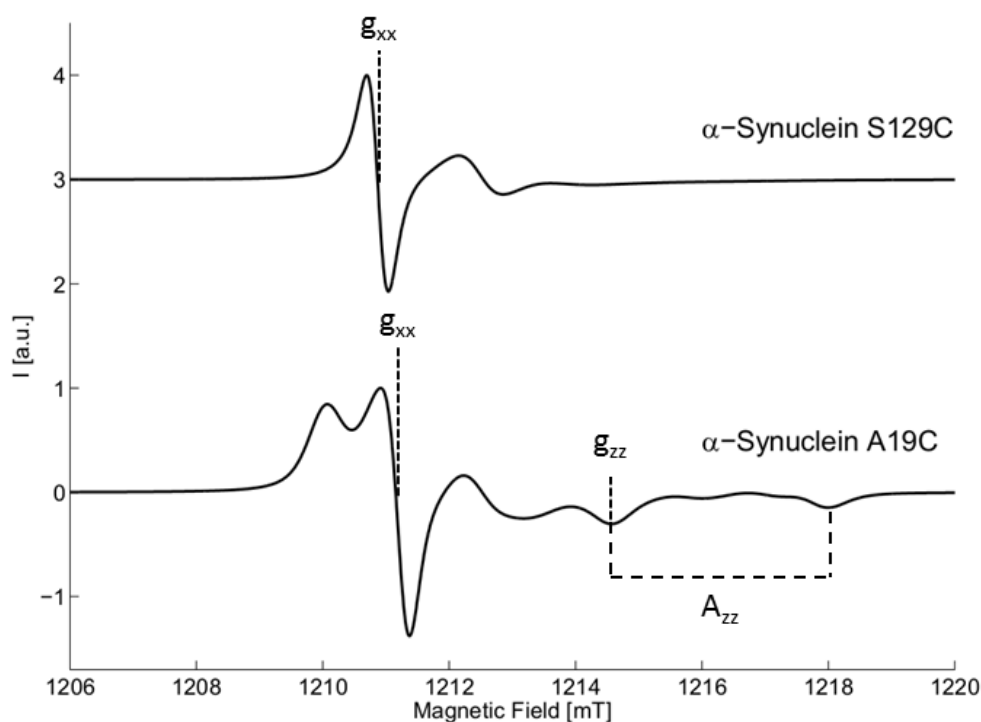


Figure 3.8. – Two simulated Q-band CW-EPR spectra of α -Synuclein (A19C and S129C) at RT. In Q-band CW-EPR spectra the g -anisotropy is already partially resolved. g_{xx} , g_{zz} , and A_{zz} can be determined as demonstrated. Modified according to [137]

The Q-band CW-EPR spectra were simulated with the EasySpin program package (red curve in Fig. 3.7). For the simulations at Q-band frequencies two components were taken into account for α -Synuclein A19C (see Fig. 3.9), which are termed as slow component and fast component. All simulations of the α -Synuclein mutants, except S129C, were composed of these two components with different contributing percentages. S129C was only composed of the fast one, see Tab. 3.3. Interestingly, E104C had to be simulated with two components, however with a much higher percentage of the fast component. This again indicates that E104C is stronger bound to the liposome or at least in the border region where the C-terminal unbound domain begins.

The simulation parameters are listed in Tab. 3.4.

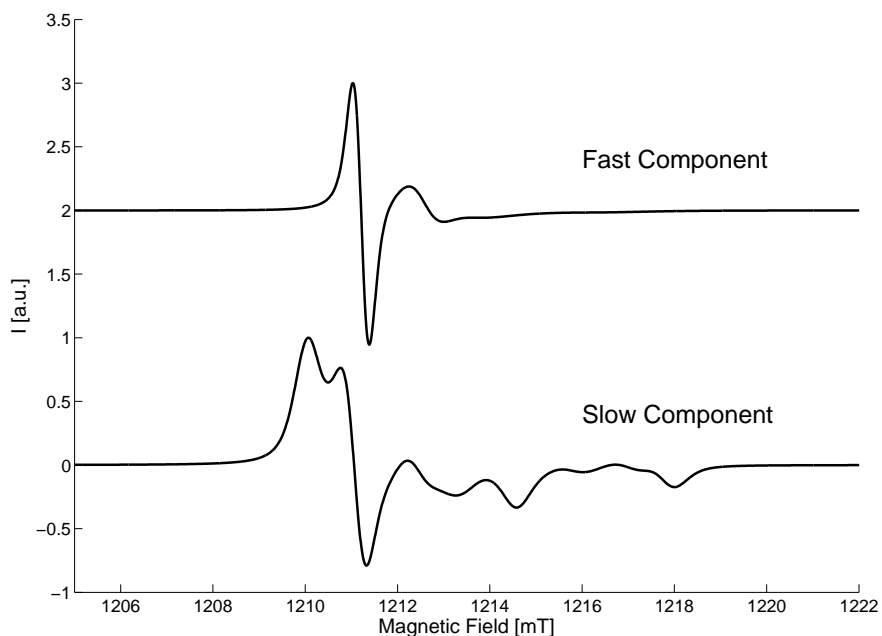


Figure 3.9. – Different components of a Q-band CW-EPR spectrum.

0.24 mM α -Synuclein + 2 mM POPG in 20 mM Phosphate + 20 % Glycerol (Q-band CW-EPR)		
	Slow Comp. [%] / τ_c [ns]	Fast Comp. [%] / τ_c [ns]
α -Synuclein A19C	88 / 132.283	12 / 2.740
α -Synuclein G41C	85 / 29.518	15 / 4.240
α -Synuclein A53C	90 / 47.947	10 / 20.999
α -Synuclein K80C	90 / 48.178	10 / 2.664
α -Synuclein E104C	26 / 20.999	74 / 8.012
α -Synuclein S129C	0 / -	100 / 1.877

Table 3.3. – Contributing percentages and rotational correlation times τ_c of the different components extracted from spectral simulation (Q-band CW-EPR). The slow component is relatively strongly immobilized, thus rotating rather slow, the fast component is rotating more fast. Data analysis is mostly focused on the main components with the highest percentage because a better comparison between the different α -Synuclein mutants is possible.

0.24 mM α -Synuclein + 2 mM POPG in 20 mM Phosphate + 20 % Glycerol (Q-band CW EPR)				
	g_{xx}	g_{zz}	A_{zz} [MHz]	τ_c [ns]
α -Synuclein A19C	2.0090	2.0026	96.0	132.283
α -Synuclein G41C	2.0090	2.0025	101.5	29.518
α -Synuclein A53C	2.0090	2.0025	100.0	47.947
α -Synuclein K80C	2.0090	(2.0028)	(90.0)	48.178
α -Synuclein E104C	2.0084	(2.0025)	(95.0)	8.012
α -Synuclein S129C	2.0084	(2.0025)	(109.0)	1.877

Table 3.4. – Q-band CW-EPR simulation parameters of 0.24 mM α -Synuclein and 2 mM POPG in buffer. As already stated, the g_{xx} , g_{zz} , and A_{zz} -values, respectively, can be determined at the Q-band frequency. However, this was only the case for the labeling positions that are strongly bound to the liposome. If a parameter could not be determined properly from the spectrum, the respective value is marked by brackets.

The extracted values g_{xx} are again within the same magnitude, however α -Synuclein E104C and α -Synuclein S129C differ from the values obtained for the other labeling positions. Changes in polarity can be better extracted from the A_{zz} -values. Again, α -Synuclein A19C has one of the lower values. Also in Q-band A_{zz} of α -Synuclein G41C is

higher indicating a more polar environment, which may be due to the position 41 being within the linker region of the horseshoe structure. A_{zz} -values of α -Synuclein K80C, E104C, and S129C have to be interpreted with caution because the respective spectral features were not always properly resolved at RT measurements for these labeling positions. But it is obvious that the relative high value for S129C accounts for a polar environment.

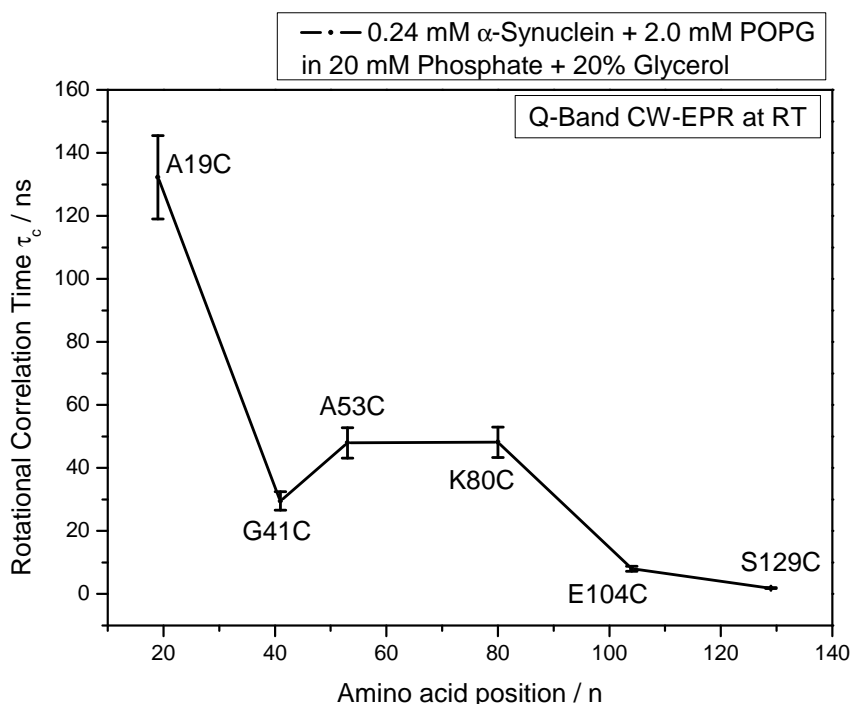


Figure 3.10. – Plot of τ_c against corresponding labeling position of 0.24 mM α -Synuclein + 2 mM POPG in buffer (Q-band).

The rotational correlation time τ_c of the main components obtained from the spectral simulations is plotted against the respective labeling position (see Fig. 3.10). τ_c -values in Q-band have higher values compared to the X-band values. Again the value for α -Synuclein A19C is much higher compared to the other labeled positions, which was to be expected for a strong binding to the liposome. In contrast to the X-band CW measurement, τ_c of α -Synuclein G41C is lower than the values of A53C and K80C. This may stem from this mutant being within the linker region (amino acids 42–44 [134]) of the horseshoe structure of the protein so that it might be conformationally more

flexible. α -Synuclein A53C and K80C again have similar rotational correlation times. As expected α -Synuclein E104C and S129C have a low τ_c -value because the spin label can rotate more fast.

Influence of Glycerol Q-band CW-EPR measurements revealed considerable broader peaks compared to the measurements at X-band frequencies. Out of interest, an additional measurement was conducted with the same amounts of α -Synuclein and POPG as in the initial measurement to check if this broadening behavior is due to the use of 20 % glycerol as cryoprotectant, which was used in the pulsed-EPR measurements. This test measurements were only conducted in CW-EPR experiments at X-band and Q-band frequencies.

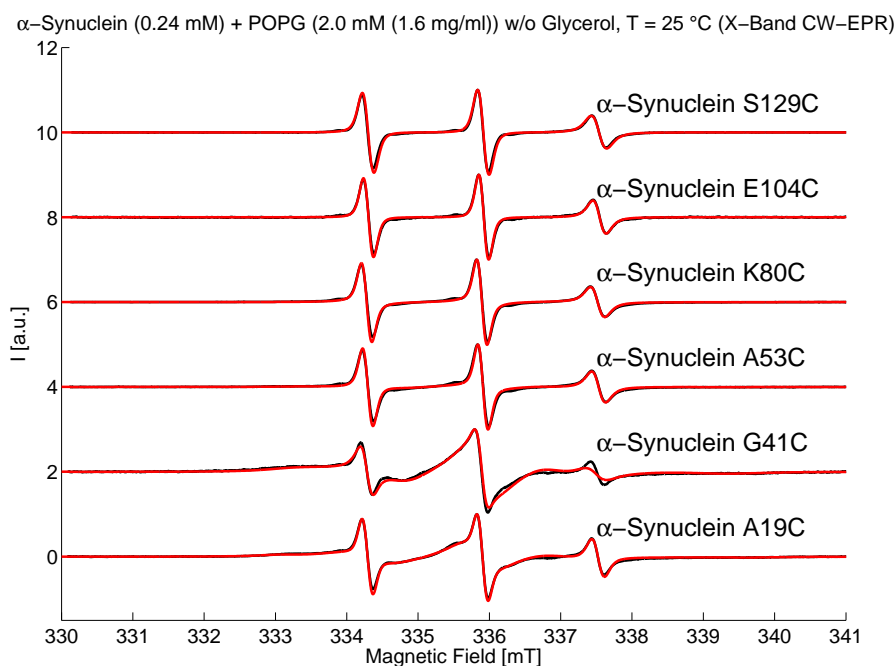


Figure 3.11. – Experimental spectra (black) and simulation (red) of 0.24 mM α -Synuclein and 2 mM POPG w/o glycerol in buffer (X-band CW-EPR).

Fig. 3.11 shows the spectra of 0.24 mM α -Synuclein and 2 mM POPG without glycerol in buffer at X-band frequencies. Preliminary analysis of the experimental spectra (black

curves) shows that the N-terminal part is strongly bound to the liposome. The central peak is relatively broad in the case of α -Synuclein A19C and G41C, respectively. However, a difference between Fig. 3.3 and Fig. 3.11 is that all the labeling positions that are located in the second helix of the predicted horseshoe structure nearly look the same in the measurements without glycerol, indicating a large amount of freely rotating components.

To extract more precise information, the measured CW-EPR spectra were simulated (red curves in Fig. 3.11). The several components for spectral simulation are listed in Tab. 3.5.

0.24 mM α -Synuclein + 2 mM POPG in 20 mM Phosphate w/o Glycerol (X-band CW EPR)			
	Slow Comp. [%] / τ_c [ns]	Intermediate Comp. [%] / τ_c [ns]	Fast Comp. [%] / τ_c [ns]
α -Synuclein A19C	20 / 21.198	65 / 3.591	15 / 0.282
α -Synuclein G41C	10 / 10.499	75 / 6.360	15 / 0.833
α -Synuclein A53C	0 / -	40 / 5.250	60 / 0.385
α -Synuclein K80C	0 / -	30 / 2.497	70 / 0.417
α -Synuclein E104C	0 / -	0 / -	100 / 0.372
α -Synuclein S129C	0 / -	0 / -	100 / 0.426

Table 3.5. – Contributing percentages and rotational correlation times τ_c of the different components extracted from spectral simulation (X-Band CW-EPR w/o glycerol).

α -Synuclein A19C and G41C could be simulated with three components, however in the case of α -Synuclein A19C the contributing percentages have shifted so that the intermediate component is now the dominant one. Interestingly, α -Synuclein G41C seems not to be that strongly affected by the absence of glycerol since the percentages of the components as well as the τ_c of the intermediate and the fast component remain nearly the same. Percentages of α -Synuclein A53C and K80C shifted so that the fast component and not the intermediate one contributing the most. α -Synuclein E104C and S129C consist of only the freely rotating fast component.

The parameters extracted from simulation of the main component of the spin label g_{iso} , a_{iso} , and τ_c are listed in Tab. 3.6.

0.24 mM α -Synuclein + 2 mM POPG in 20 mM Phosphate w/o Glycerol (X-band CW EPR)			
	g_{iso}	a_{iso} [MHz]	τ_c [ns]
α -Synuclein A19C	2.0058	45.4	3.591
α -Synuclein G41C	2.0056	45.4	6.360
α -Synuclein A53C	2.0058	45.5	0.385
α -Synuclein K80C	2.0058	45.5	0.417
α -Synuclein E104C	2.0058	45.5	0.372
α -Synuclein S129C	2.0057	45.5	0.426

Table 3.6. – X-band CW-EPR simulation parameters of 0.24 mM α -Synuclein and 2 mM POPG w/o glycerol in buffer. Determined from the spectral simulation were the values of g_{iso} and the coupling constant a_{iso} as well as the rotational correlation time τ_c .

The values of g_{iso} of Tab. 3.6 are of the same magnitude so that no precise conclusion can be drawn whether the environment of the spin label is more polar or nonpolar. No significant changes are also visible in the a_{iso} -value. Values of the rotational correlation time are significantly reduced compared to the measurement with 20 % glycerol. Glycerol is a rather viscous liquid so that it may reduce the ability of the spin label to rotate fast in solution. However, it is interesting that α -Synuclein G41C seems not to be affected at all by the addition or removal of glycerol.

Plotting the rotational correlation times against the corresponding labeling position (see Fig. 3.12), α -Synuclein A19C and G41C show a relative high τ_c of the main component indicating the strong binding that was already observed at preliminary visual analysis of the EPR spectra. The main component of α -Synuclein G41C even has a higher τ_c than A19C. However, since the magnitude is the same as of the measurement with glycerol, this position seems not to be affected by the absence of glycerol. In the measurement with glycerol a motional freedom due to being within the linker region of the horseshoe structure was suggested and that this position may face towards the solvent. However, upon facing to the solvent the removal of glycerol should then at least show a small effect. Another explanation for this effect may be that position G41C is not faced towards the solvent, it may rather face the lipid membrane and be close to a polar amino acid, which in return will affect the a_{iso} -value of the X-band measurements. One has also to bear in mind that there are two postulated membrane-bound structures of α -Synuclein as explained in the introduction part of this work. In the extended bound form of α -

Synuclein, G41C may be a bit stronger bound so that maybe a superposition of both forms are observed here, which shows up in G41C being not affected by glycerol. As already seen in the visual interpretation of the X-band CW-EPR spectra, the labeling positions of the second helix show a large motional freedom and therefore very low rotational correlation times.

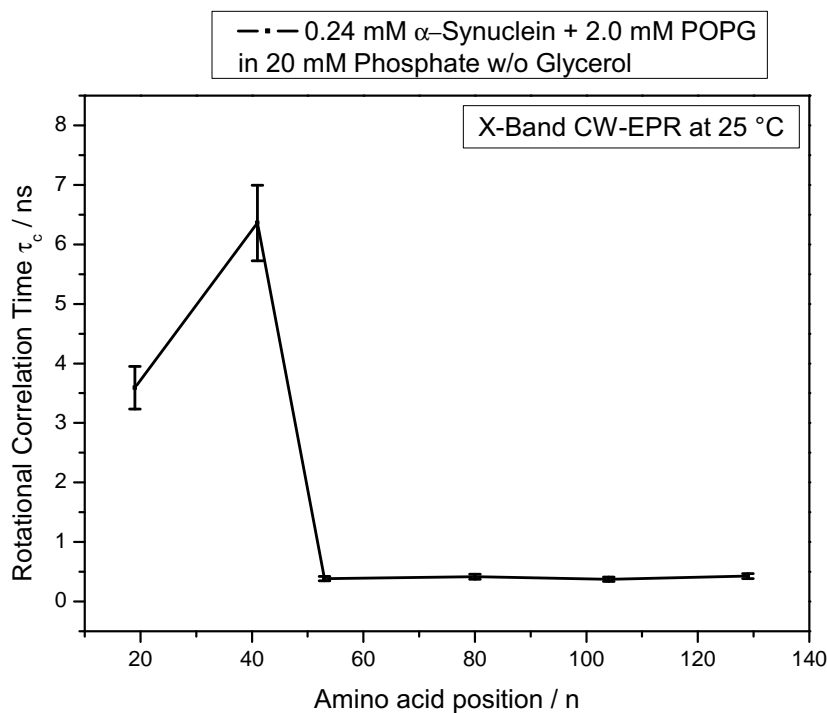


Figure 3.12. – Plot of τ_c against corresponding labeling position of 0.24 mM α -Synuclein and 2 mM POPG w/o glycerol in buffer (X-band).

The samples of 0.24 mM α -Synuclein and 2 mM POPG without glycerol in buffer were also measured in a CW-EPR experiment at Q-Band frequencies (black curve in Fig. 3.13). Compared to the measurements with additional glycerol as cryoprotectant, the spectra consist of much more motional freedom and resemble those of the X-band CW-EPR spectra.

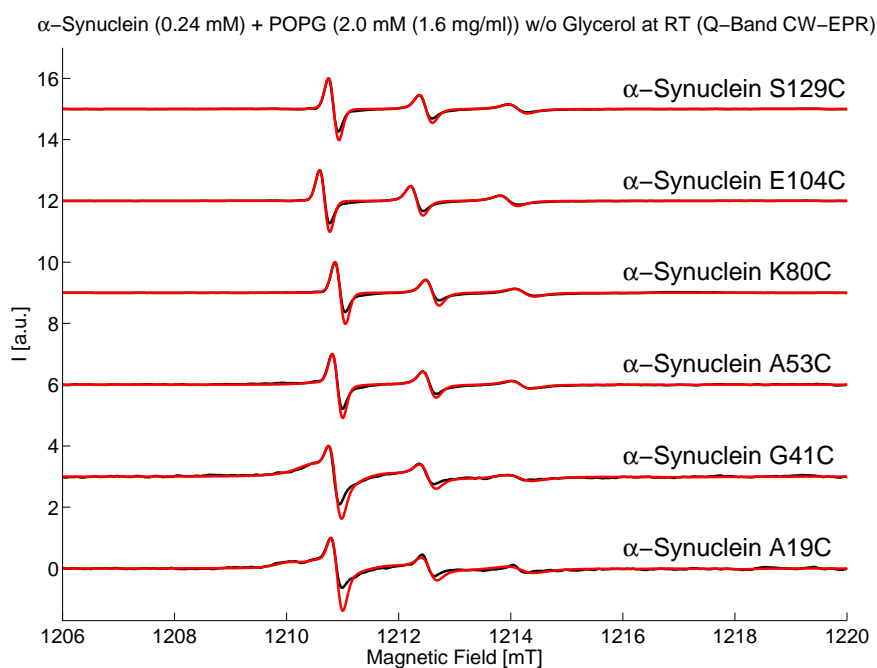


Figure 3.13. – Experimental spectra (black) and simulation (red) of 0.24 mM α -Synuclein and 2 mM POPG w/o glycerol in buffer (Q-band CW-EPR).

0.24 mM α -Synuclein + 2 mM POPG in 20 mM Phosphate w/o Glycerol (Q-band CW EPR)			
	Slow Comp. [%] / τ_c [ns]	Intermediate Comp. [%] / τ_c [ns]	Fast Comp. [%] τ_c [ns]
α -Synuclein A19C	50 / 166.667	30 / 4.873	20 / 0.528
α -Synuclein G41C	0 / -	80 / 4.524	20 / 0.614
α -Synuclein A53C	0 / -	40 / 5.700	60 / 0.375
α -Synuclein K80C	0 / -	0 / -	100 / 0.371
α -Synuclein E104C	0 / -	0 / -	100 / 0.295
α -Synuclein S129C	0 / -	0 / -	100 / 0.318

Table 3.7. – Contributing percentages and rotational correlation times τ_c of the different components extracted from spectral simulation (Q-band CW-EPR).

The components used for the simulation are listed in Tab. 3.7. The parameters obtained from spectral simulation are listed in Tab. 3.8. α -Synuclein A19C is simulated with three components, whereas α -Synuclein G41C and A53C are simulated with the intermediate

and the fast component, the other α -Synuclein labeling positions consist only of the fast rotating component.

0.24 mM α -Synuclein + 2 mM POPG in 20 mM Phosphate w/o Glycerol (Q-band CW EPR)			
	g_{iso}	a_{iso} [MHz]	τ_c [ns]
α -Synuclein A19C	2.0058	46.3	166.667
α -Synuclein G41C	2.0058	46.5	4.524
α -Synuclein A53C	2.0058	46.2	0.375
α -Synuclein K80C	2.0058	46.3	0.371
α -Synuclein E104C	2.0058	46.3	0.295
α -Synuclein S129C	2.0058	46.3	0.318

Table 3.8. – Q-band CW-EPR simulation parameters of 0.24 mM α -Synuclein + 2 mM POPG w/o glycerol in buffer.

No significant changes are observable in g_{iso} and a_{iso} so that no conclusion can be drawn on the polarity of the environment of the spin label. Finally τ_c is plotted against the labeling position and again α -Synuclein A19C is stronger bound to the liposome than G41C. The other labeling positions consist mainly of freely rotating components, see Fig. 3.14.

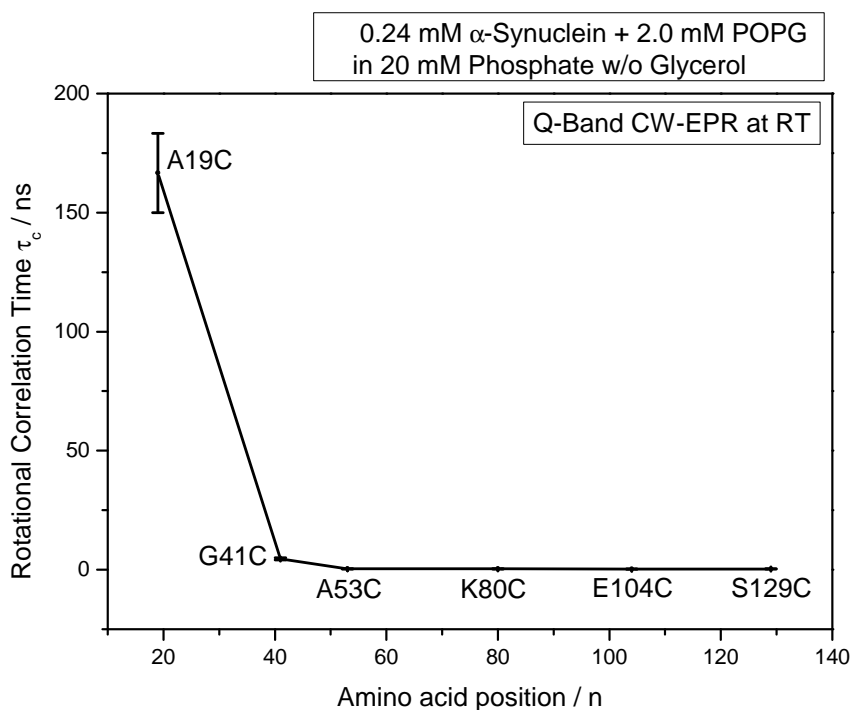


Figure 3.14. – Plot of τ_c against corresponding labeling position of 0.24 mM α -Synuclein + 2 mM POPG w/o glycerol in buffer (Q-band).

For a better comparison Fig. 3.15 shows the τ_c -values of X-band and Q-band CW-EPR measurements with and without glycerol, respectively. The plot demonstrates what has already been explained earlier. α -Synuclein G41C is only little affected by the removal of glycerol. Major differences are observed for the labeling positions that are strongly bound to the liposome. α -Synuclein E104C and S129C also show little changes due to the position at the unbound C-terminal domain.

In general, upon addition of 20 % glycerol to the sample the contrast of τ_c is increased so that a better comparison especially of the weaker bound labeling positions is possible.

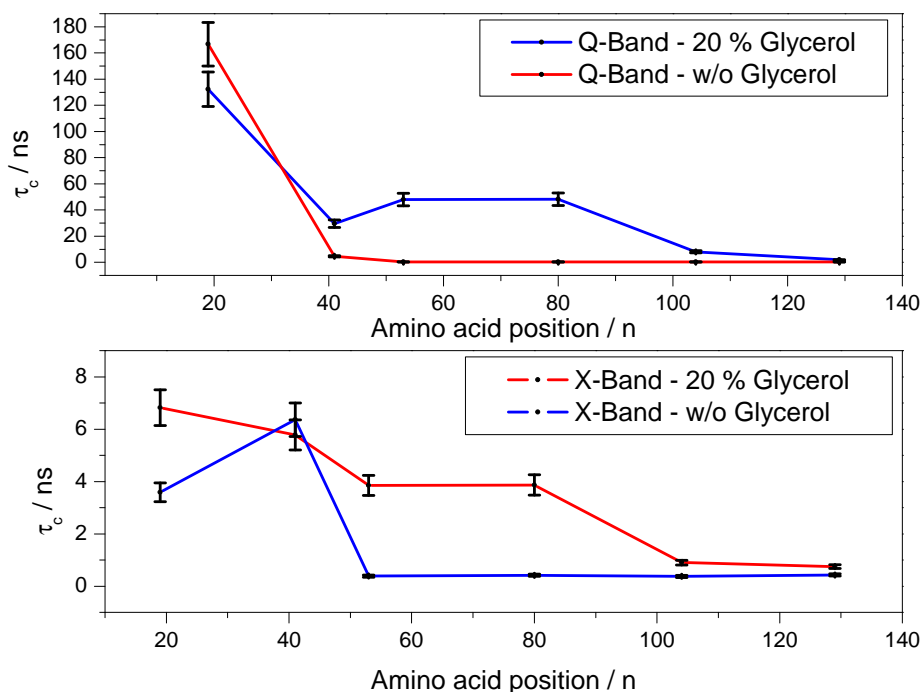


Figure 3.15. – Comparison of X-band and Q-band measurements with and without 20 % glycerol.

X-Band 4p-DEER 4p-DEER measurements were carried out to gain information about the dipolar interaction between electron spins. Because in this work single cysteine mutants of α -Synuclein were used, the intermolecular environment is addressed and therefore if there is a self-assembly of the protein on the liposome into multimeric structures.

DEER measurements were conducted as explained in Ch. 5.2.1.3, p. 114. DEER time traces were analyzed with the DEERAnalysis software package [122]. The DEER time traces after background correction are shown in Fig. 3.16. No clear modulations are present in all time traces indicating a broad distribution.

DEER time traces were analyzed by an effective modulation depth Δ_{eff} , which was read out at background positions between 600ns - 1000ns, for α -Synuclein S129C it was read out at positions 1000ns - 1800ns. Maxima and minima values of the respective Δ_{eff} were used for calculating the average value and the error bars. The number of coupled spins were calculated with Eq. 1.43 on p. 28. λ for the spectrometer used in this work was determined to be 0.52 by measuring a rigid model biradical.

Parameters obtained from analyses of the DEER time traces are listed in Tab. 3.9. Analyses of the time traces was conducted with a dimensionality of 3 for the α -Synuclein labeling positions, which are located in the weaker bound second helix of the postulated horseshoe-structure as well as for the still in solution remaining C-terminal domain. For the α -Synuclein labeling positions that are strongly bound to the liposome (α -Synuclein A19C and G41C) the background was fitted with 2 dimensions, a value that can be used for proteins bound to a membrane [138]. When Δ_{eff} is plotted against the respective labeling position, the plot shows a similar distribution as already shown for the plot of the rotational correlation time τ_c of X-band CW-EPR measurements (see Fig. 3.6, p. 45). The strongly bound N-terminal part of the protein is therefore confirmed again. The number of coupled spins especially for the strongly bound N-terminal domain of the protein indicates the formation of dimeric structures on the liposome. A similar result for formation of dimeric structures were also obtained by Drescher et al. [139].

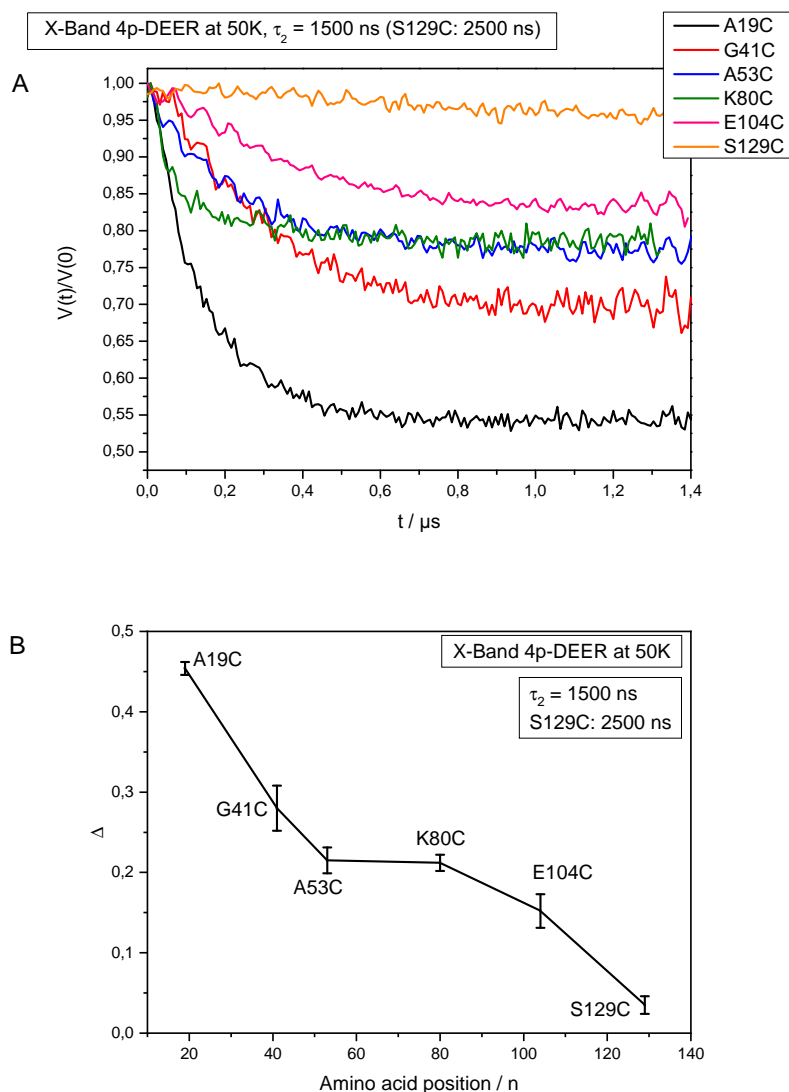


Figure 3.16. – (A) DEER time traces of 0.24 mM α -Synuclein + 2 mM POPG (B) Plot of Δ_{eff} against the respective labeling position.

0.24 mM α -Synuclein + 2 mM POPG in 20 mM Phosphate + 20 % Glycerol (4p-DEER)			
	Dimensions	Δ_{eff}	Coupled Spins
α -Synuclein A19C	2	0.454	2.16
α -Synuclein G41C	2	0.280	1.63
α -Synuclein A53C	3	0.215	1.46
α -Synuclein K80C	3	0.212	1.46
α -Synuclein E104C	3	0.152	1.32
α -Synuclein S129C	3	0.035	1.07

Table 3.9. – DEER parameters of 0.24 mM α -Synuclein + 2 mM POPG in 20 mM phosphate. The coupled spins were calculated with Eq. 1.43 and a λ -value of 0.52.

3.1.1.2. Membrane-bound State of α -Synuclein (Influence of Ligand X)

To elucidate the influence of a small molecule of therapeutic interest (the structure is unknown due to patent protection), similar measurements of X-band CW-EPR, Q-band CW-EPR, and 4p-DEER measurements were carried out and compared to the membrane-bound state without the ligand. The sample concentrations of this measurement were changed to 0.2 mM α -Synuclein and 1.5 mM POPG (see Ch. 5.2.1.5, p. 116) in agreement with the collaboration partner. Different ligand concentrations were examined regarding its influence on the membrane-bound state of α -Synuclein. The concentrations of the ligand were within the range from equimolar with respect to α -Synuclein (0.2 mM), 0.1 mM, 0.05 mM, down to 0.01 mM.

For the lower ligand concentrations of 0.05 and 0.01 mM the stock solution had to be diluted (see Ch. 5.2.1.5, p. 116), otherwise this low concentrations could not have been pipetted properly. Three test series were conducted. Since the ligand was dissolved in DMSO, the low concentrations of series 1 and 2 were diluted with DMSO, whereas series 3 was diluted with the α -Synuclein buffer. This was done in order to check if the solvent affected the obtained results because DMSO can denature proteins at higher concentrations [140]. The focus of data analyses will be on the general trends rather than the mean values of the extracted parameters. α -Synuclein S129C has not been measured because it did not show any dipolar coupling at all in the initial EPR measurement.

For a better comparison, the results of X-band CW, Q-band CW, and 4p-DEER will be discussed simultaneously for every α -Synuclein labeling position. Data analysis will be focused on the rotational correlation times of X-band and Q-band CW-EPR, a_{iso} of X-band CW-EPR, and Δ_{eff} of X-band 4p-DEER. A_{zz} -values of Q-band CW-EPR will not be interpreted because they are not always resolved properly in the spectra to guarantee an adequate analysis of the experimental spectra. It must also be pointed out that due to spectrometer issues some measurements of the first series had to be measured with a pump pulse length of 32 ns in 4p-DEER. The respective modulation depths had to be scaled. Further explanation regarding this matter is found in Ch. A.1.10, p. 179.

To examine the influence of the Ligand X on the membrane-bound state of the protein, X-band CW-EPR at 25 °C had been carried out. Corresponding experimental spectra and their simulations are shown in the Appendix, see Figs. A.1–A.5, pp. 157 (Series 1), Figs. A.6–A.10, pp. 161 (Series 2), and Fig. A.11, pp. 165 (Series 3). Contributing percentages

of the different components used for spectral simulation are given in the Appendix, see p. 160 (Series 1), p. 164 (Series 2), and p. 165 (Series 3).

Spectra of Q-band CW-EPR at RT as well as the simulations can be found in the Appendix, see Figs. A.12–A.16, p. 167 (Series 1), Figs. A.17–A.21, p. 171 (Series 2), and Fig. A.22, p. 175 (Series 3). Contributing percentages of the different components used for spectral simulation are shown in the Appendix, see p. 170 (Series 1), p. 174 (Series 2), and p. 175 (Series 3).

The 4p-DEER time traces can be found in Ch. A.1.9, p. 177.

The extracted simulation parameters a_{iso} , g_{iso} , and τ_c of X-band CW-EPR spectroscopy are shown on p. 166, g_{xx} , g_{zz} , A_{zz} , and τ_c of Q-band CW-EPR spectroscopy are shown on p. 176.

Parameters determined from analysis of the DEER time traces are shown in Tab. 3.10. Values are listed for all three measurement series in one column and are separated by a line. Note that series 3 consisted only of measurements with the low ligand concentrations (0.05 and 0.01 mM).

0.2 mM α -Synuclein A19C + 1.5 mM POPG + Ligand X in 20 mM Phosphate + 20 % Glycerol (4p-DEER)			
α -Synuclein A19C	Dimensions	Δ_{eff}	Coupled Spins
0 mM Ligand X	2	0.289 0.390 -	1.65 1.92 -
0.01 mM Ligand X	2	0.501 0.415 0.431	2.33 2.01 2.03
0.05 mM Ligand X	2	0.372 0.674 0.393	1.89 3.04 1.93
0.1 mM Ligand X	2	0.146 0.275 -	1.30 1.61 -
0.2 mM Ligand X	2	0.204 0.245 -	1.44 1.54 -

Table 3.10. – DEER parameters of 0.2 mM α -Synuclein A19C and 1.5 mM POPG + Ligand X in buffer. The coupled spins were calculated using Eq. 1.43 and a λ -value of 0.52. Values are listed for all three measurement series in one column and are separated by a line.

Results from the different EPR measurements regarding the influence of Ligand X on α -Synuclein A19C are shown in Fig. 3.17.

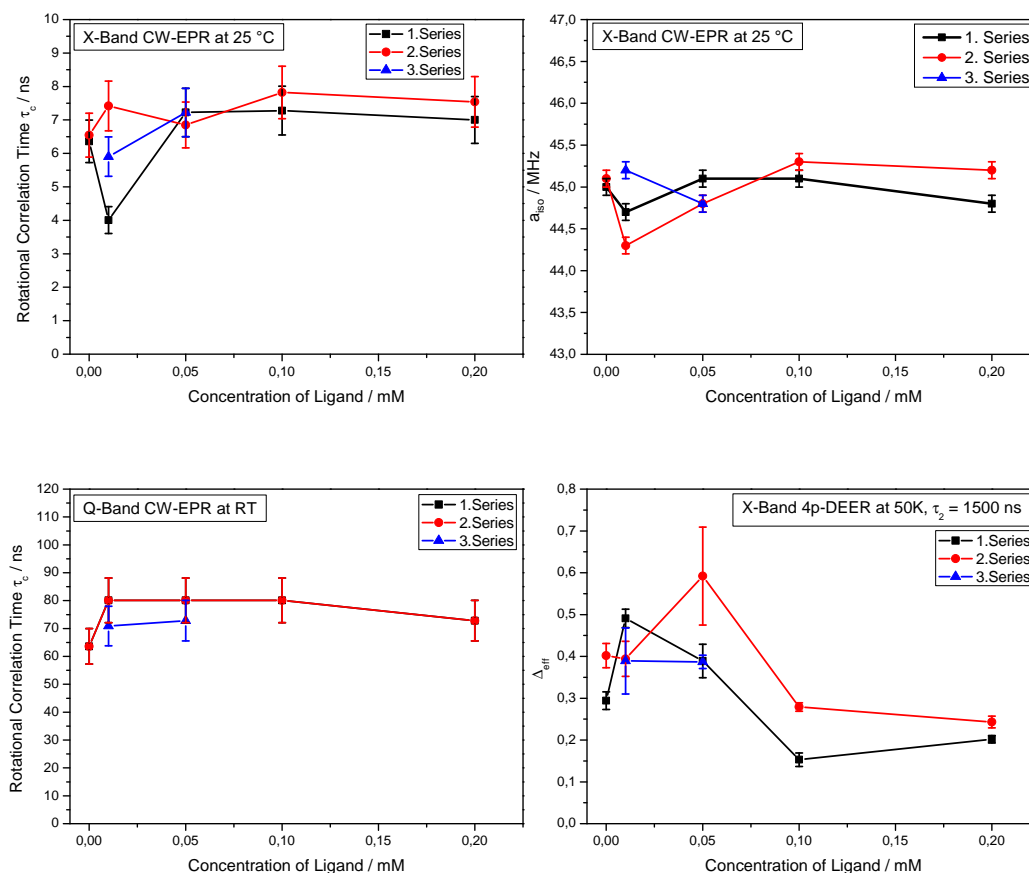


Figure 3.17. – Influence of Ligand X on α -Synuclein A19C. Shown are the rotational correlation times of X-band CW-EPR spectroscopy (upper left), a_{iso} -values of X-band CW-EPR (upper right), rotational correlation times of Q-band CW-EPR (bottom left), and Δ_{eff} (bottom right) in X-band DEER with respect to the ligand concentration. Measurements were carried with 0.2 mM α -Synuclein + 1.5 mM POPG in 20 mM phosphate + 20 % glycerol. Note that the τ_c -values of the first and the second series coincide at Q-band frequencies.

A first observation of α -Synuclein A19C leads to the conclusion that drastic changes of the parameters a_{iso} and τ_c at X-band, as well as Δ_{eff} within the different series are often found in the samples, where the ligand concentration is very low. This is a very interesting finding, because one would expect that higher concentrations of a ligand would lead to significant changes and not the very low ones where the ratio of protein and ligand are 4:1 and 20:1, respectively.

When observing the rotational correlation time extracted from spectral simulation in X-band CW-EPR, it is interesting that a very low ligand concentration of 0.01 mM shows a different behavior for all measurement series, whereas τ_c for all other ligand concentrations are nearly of the same magnitude when the error bars are taken into account. A decrease of τ_c as it is observed for the first and the third series would indicate a more fast rotation of the spin label. In the second series, τ_c is a bit higher compared to the measurement without the ligand, indicating that here the spin label is rotating more slowly. Changes can also be observed in the a_{iso} -values, which indicate a nonpolar environment since the value is decreasing, observable especially in the first and the second series. Interestingly, measurements of 0.01 mM ligand concentrations show a variability, whereas the a_{iso} -values for the other ligand concentrations are all within the same range.

The modulation depth of 4p-DEER increases at low ligand concentrations. The modulation depth is correlated to the number of coupled spins (see Eq. 1.43) so that a higher modulation depth is also indicating a higher number of coupled spins, i.e. the spin label of different monomers are getting more close and thus more compact on the liposome (see also Tab. 3.10).

This results indicate that the position 19 is probably becoming more compact upon interaction of the protein with the Ligand X. In the initial measurement it was assumed that the position 19 may be slightly incorporated into the membrane. Depending on the orientation of the spin label, this stronger compactness does not necessarily affect the mobility of the label. If this is the case, some motional freedom and therefore a variability in parameters may be observed. This would explain the differences of the τ_c -value in X-band CW-EPR. Interestingly, τ_c of Q-band CW-EPR shows higher values. However, when taking the error bars into account, the values are within the same range so that upon getting more compact, the rotation is only slightly hindered compared to the measurement without the ligand. Another possible scenario may be that upon getting more compact the position 19 might be slightly contorted at this low ligand concentration, but this contortion may not always be the case. This may also explain the variability of the parameters and that sometimes, dependent on the orientation of the label, rotation is a bit faster and sometimes it is a bit hindered.

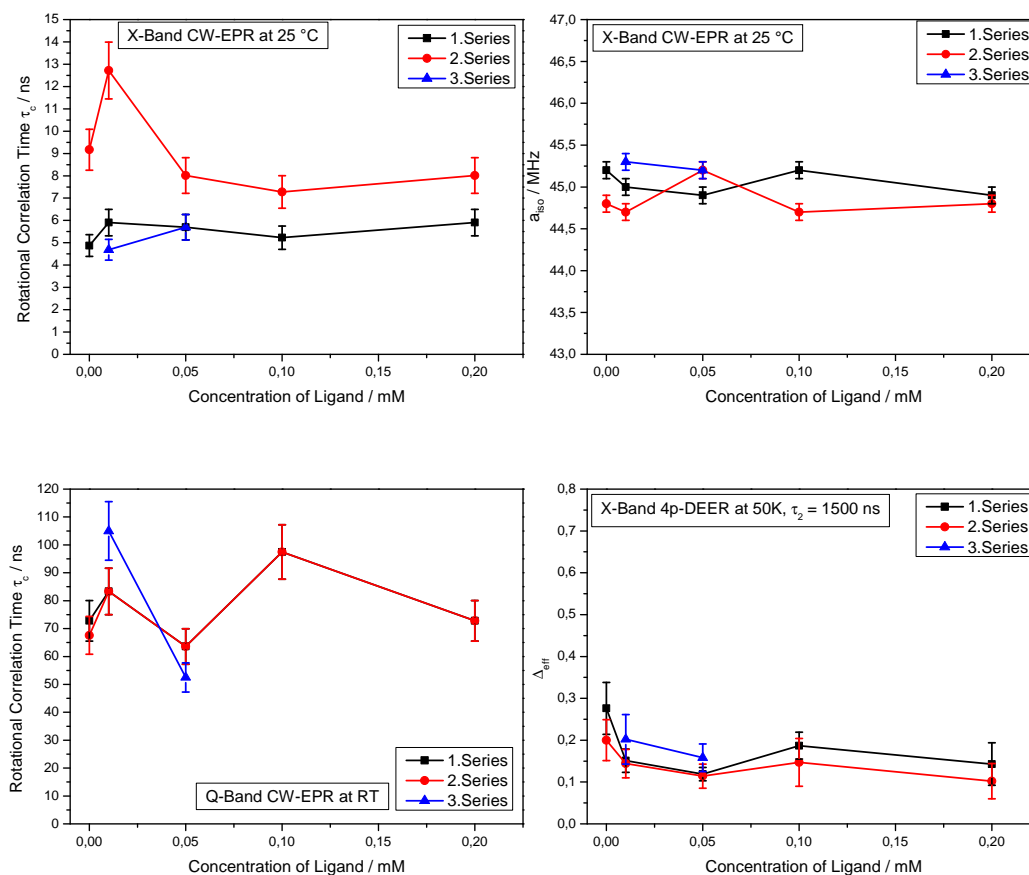


Figure 3.18. – Influence of Ligand X on α -Synuclein G41C. Shown are the rotational correlation times of X-band CW-EPR spectroscopy (upper left), a_{iso} -values of X-band CW-EPR (upper right), rotational correlation times of Q-band CW-EPR (bottom left), and Δ_{eff} (bottom right) in X-band DEER with respect to the ligand concentration. Measurements were carried with 0.2 mM α -Synuclein + 1.5 mM POPG in 20 mM phosphate + 20 % glycerol.

Compared to α -Synuclein A19C the position 41 shows an opposed behavior, see Fig. 3.18. τ_c of X-band CW-EPR as well as Q-band CW-EPR is increased at low ligand concentrations compared to the measurement without the ligand. In the initial measurements the τ_c -value in X-band CW-EPR has also been high so that this position is bound to the liposome.

Low ligand concentrations thus may lead to a slight increase in hindering the rotation of the spin label. However, compared to the position 19, Δ_{eff} from 4p-DEER of the low

ligand concentrations are slightly decreasing so that this position is not getting more compact but shows some flexibility. Again, it has to be pointed out that this position is within the linker region in the postulated horseshoe structure of α -Synuclein. It may be that this region becomes more loose upon interaction with the ligand, but if the spin label is aligned towards the membrane this may explain the higher rotational correlation times (in Q-band even at 0.1 mM ligand concentration) and the lower modulation depths (see also Tab. 3.11). The flexibility of this position can also be observed in the varied a_{iso} -values.

0.2 mM α -Synuclein G41C + 1.5 mM POPG + Ligand X in 20 mM Phosphate + 20 % Glycerol (4p-DEER)			
α -Synuclein G41C	Dimensions	Δ_{eff}	Coupled Spins
0 mM Ligand X	2	0.320 0.227 -	1.74 1.53 -
0.01 mM Ligand X	2	0.170 0.133 0.184	1.36 1.37 1.37
0.05 mM Ligand X	2	0.122 0.118 0.181	1.25 1.31 1.41
0.1 mM Ligand X	2	0.203 0.157 -	1.44 1.34 -
0.2 mM Ligand X	2	0.179 0.122 -	1.38 1.30 -

Table 3.11. – DEER parameters of 0.2 mM α -Synuclein G41C and 1.5 mM POPG + Ligand X in buffer. The coupled spins were calculated using Eq. 1.43 and a λ -value of 0.52. Values are listed for all three measurement series in one column and are separated by a line.

Significant changes upon addition of the ligand in very low concentrations are also observed for α -Synuclein A53C, see Fig. 3.19. However, in this case also the addition of 0.1 mM Ligand X shows a higher τ_c -value at X-band CW-EPR spectroscopy, especially in the second series. Changes in a_{iso} are very small so that it can be assumed that the polarity of the environment of the spin label is not changed. Δ_{eff} is again, like in α -Synuclein A19C, increasing at the low ligand concentrations, indicating a more compactness of the protein upon addition of the ligand.

A slight change in τ_c can also be observed at Q-band CW-EPR at low ligand concentrations of the first and the second series. If the τ_c -values of the the low ligand concentrations of the 3rd series in X- and Q-band, respectively, are compared, the same trend is observed, but it is stronger formed in Q-band. This trend of an increasing τ_c -value from 0.01 mM to 0.05 mM ligand concentration can be observed in all CW data of the position 53. Since the second helix, where this position is located, is not as strongly

bound to a membrane like the first one [72], a more compactness may also here not necessarily affect the motion of the label.

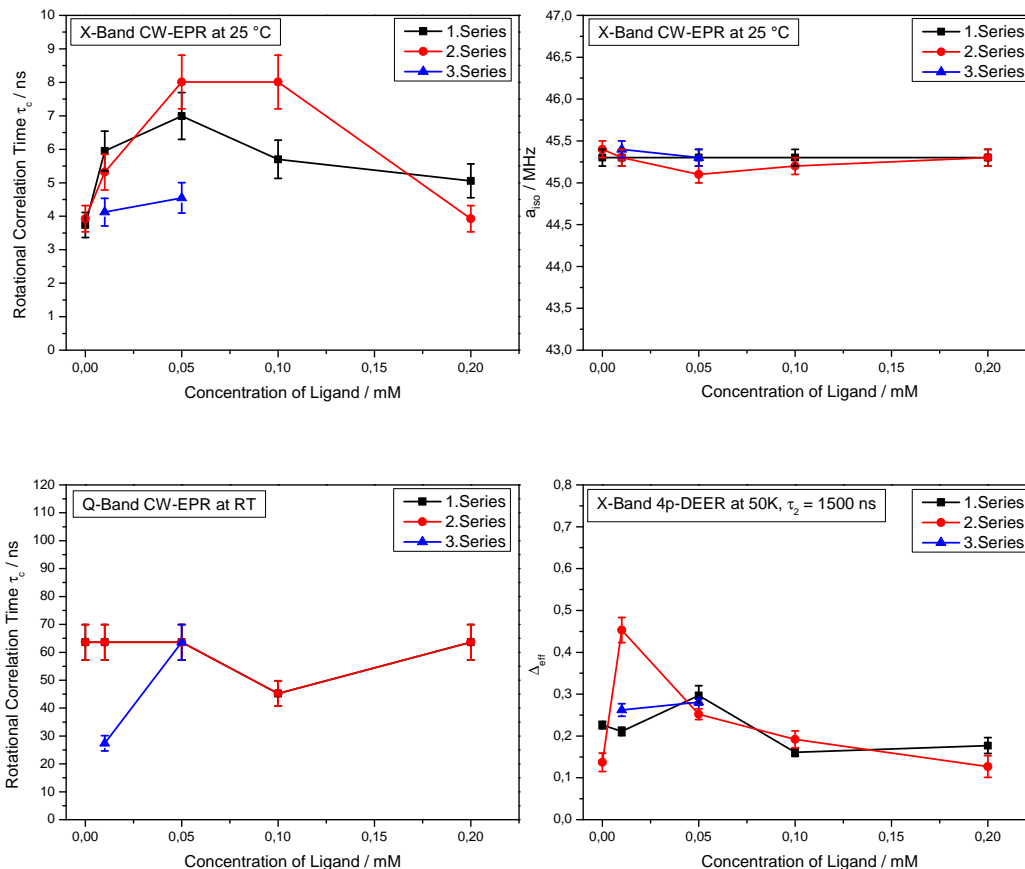


Figure 3.19. – Influence of Ligand X on α -Synuclein A53C. Shown are the rotational correlation times of X-band CW-EPR spectroscopy, a_{iso} -values of X-band CW-EPR, rotational correlation times of Q-band CW-EPR, and Δ_{eff} in X-band DEER with respect to the ligand concentration. Measurements were carried with 0.2 mM α -Synuclein + 1.5 mM POPG in 20 mM phosphate + 20 % glycerol. Note that the τ_c -values of the first and the second series coincide at Q-band frequencies.

0.2 mM α -Synuclein A53C + 1.5 mM POPG + Ligand X in 20 mM Phosphate + 20 % Glycerol (4p-DEER)			
α -Synuclein G41C	Dimensions	Δ_{eff}	Coupled Spins
0 mM Ligand X	3	0.228 0.152 -	1.50 1.30 -
0.01 mM Ligand X	3	0.211 0.474 0.269	1.45 2.19 1.59
0.05 mM Ligand X	3	0.313 0.261 0.283	1.72 1.55 1.62
0.1 mM Ligand X	3	0.168 0.206 -	1.35 1.43 -
0.2 mM Ligand X	3	0.191 0.145 -	1.41 1.29 -

Table 3.12. – DEER parameters of 0.2 mM α -Synuclein A53C and 1.5 mM POPG + Ligand X in buffer. The coupled spins were calculated using Eq. 1.43 and a λ -value of 0.52. Values are listed for all three measurement series in one column and are separated by a line.

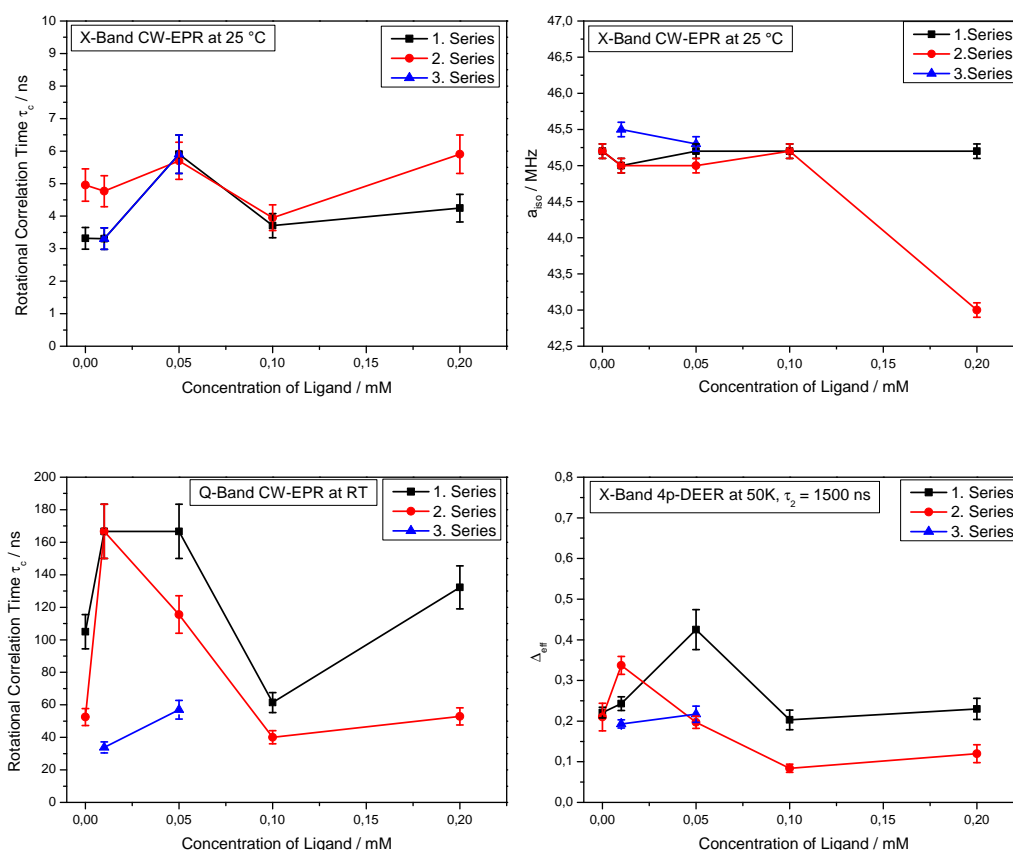


Figure 3.20. – Influence of Ligand X on α -Synuclein K80C. Shown are the rotational correlation times of X-band CW-EPR spectroscopy, a_{iso} -values of X-band CW-EPR, rotational correlation times of Q-band CW-EPR, and Δ_{eff} in X-band DEER with respect to the ligand concentration. Measurements were carried with 0.2 mM α -Synuclein + 1.5 mM POPG in 20 mM phosphate + 20 % glycerol.

0.2 mM α -Synuclein K80C + 1.5 mM POPG + Ligand X in 20 mM Phosphate + 20 % Glycerol (4p-DEER)			
α -Synuclein K80C	Dimensions	Δ_{eff}	Coupled Spins
0 mM Ligand X	3	0.211 0.219 -	1.46 1.43 -
0.01 mM Ligand X	3	0.255 0.348 0.198	1.57 1.76 1.41
0.05 mM Ligand X	3	0.424 0.204 0.210	2.06 1.43 1.42
0.1 mM Ligand X	3	0.211 0.081 -	1.46 1.17 -
0.2 mM Ligand X	3	0.245 0.135 -	1.54 1.26 -

Table 3.13. – DEER parameters of 0.2 mM α -Synuclein K80C and 1.5 mM POPG + Ligand X in buffer. The coupled spins were calculated using Eq. 1.43 and a λ -value of 0.52. Values are listed for all three measurement series in one column and are separated by a line.

For the position K80C significant changes upon addition of Ligand X are observed at the very low concentrations of the ligand, see Fig. 3.20. τ_c in X-band CW-EPR is a bit decreasing for 0.01 mM ligand concentration, but for the 0.05 mM ligand concentration nearly the same value is observed for all three measurement series. The same trend, i.e. a higher τ_c -value at the low ligand concentrations, is also observed at Q-band frequencies so that it can be assumed that the spin label is rotating slower. Changes in a_{iso} are more subtle, with a slight decreasing of the value, however the value for the 0.2 mM ligand concentration in the second series is significantly reduced.

Interestingly, Δ_{eff} in 4p-DEER shows an increasing value in the first and third series as well, whereas the value of 0.05 mM ligand concentration is again a bit lower. When checking the number of coupled spins (Tab. 3.13), it is obvious that for the low ligand concentration the protein is again more compact organized on the liposome. Again it can be assumed that this compactness does not necessarily affect the rotation of the spin label much as can be seen in the different trends of τ_c . α -Synuclein as a protein may still be quite flexible and is not interacting with the liposome always in the same manner.

α -Synuclein E104C shows a partially different behavior within the different measurement series (see Fig. 3.21 and Tab. 3.14). For the low ligand concentrations τ_c in X-band CW-EPR is slightly increasing in the first and second series, whereas in the third series, it is slightly decreasing from 0.01 mM to 0.05 mM ligand concentration. Interestingly, the rotation of the spin label in the first series at a ligand concentration of 0.1 mM seems to be slower. Changes in a_{iso} also show decreasing values from no ligand to a concentration of 0.1 mM. However, τ_c in Q-band CW-EPR behaves opposite compared to X-band CW-EPR. Interesting to observe is that Δ_{eff} of the first series looks the same as in α -Synuclein G41C with decreasing values, but opposite in the second and the third series.

This somewhat different results may be due to the position 104 being part or at least in the border region of the C-terminal domain that remains unstructured even when the N-terminal part is bound to the liposome. Thus, there may be a large flexibility of the protein and therefore depending on the orientation of the spin label the rotation may be altered. The dipolar coupling of the electron spins may thus also show a large variability in every sample.

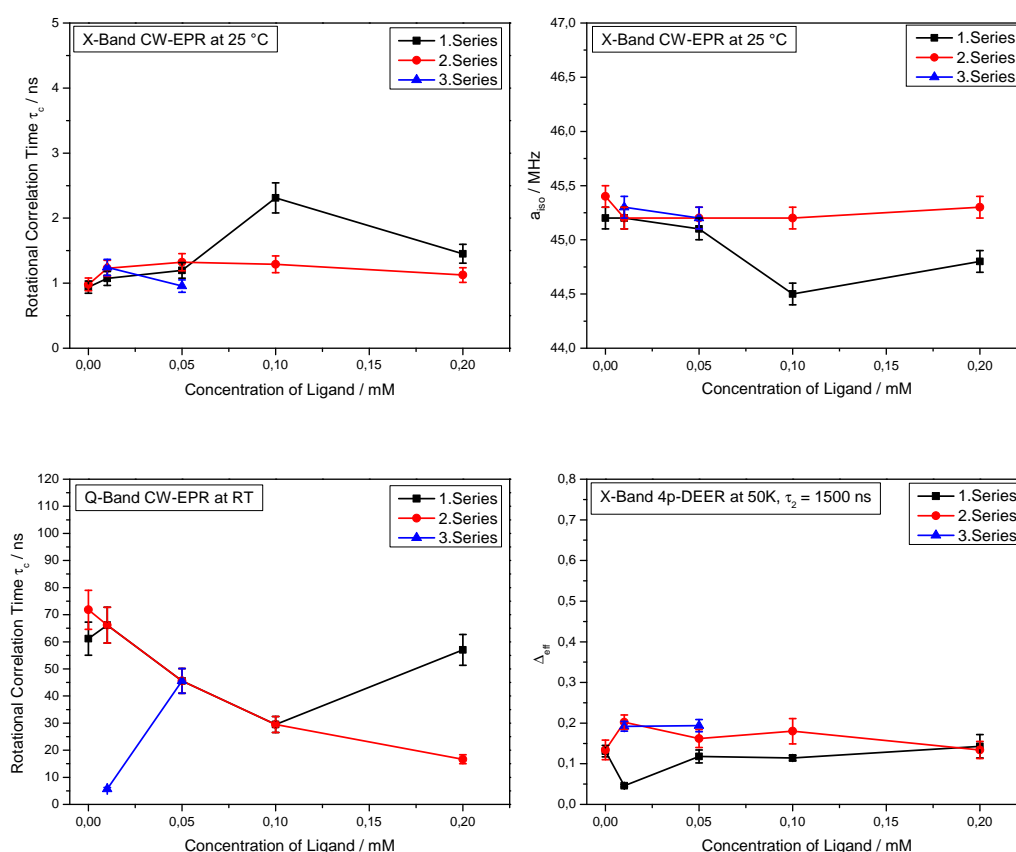


Figure 3.21. – Influence of Ligand X on α -Synuclein E104C. Shown are the rotational correlation times of X-band CW-EPR spectroscopy, a_{iso} -values of X-band CW-EPR, rotational correlation times of Q-band CW-EPR, and Δ_{eff} in X-band DEER with respect to the ligand concentration. Measurements were carried with 0.2 mM α -Synuclein + 1.5 mM POPG in 20 mM phosphate + 20 % glycerol.

0.2 mM α -Synuclein E104C + 1.5 mM POPG + Ligand X in 20 mM Phosphate + 20 % Glycerol (4p-DEER)			
α -Synuclein E104C	Dimensions	Δ_{eff}	Coupled Spins
0 mM Ligand X	3	0.140 0.151 -	1.29 1.30 -
0.01 mM Ligand X	3	0.044 0.214 0.197	1.09 1.42 1.41
0.05 mM Ligand X	3	0.129 0.177 0.204	1.26 1.35 1.43
0.1 mM Ligand X	3	0.119 0.202 -	1.24 1.42 -
0.2 mM Ligand X	3	0.158 0.148 -	1.33 1.30 -

Table 3.14. – DEER parameters of 0.2 mM α -Synuclein E104C and 1.5 mM POPG + Ligand X in buffer. The coupled spins were calculated using Eq. 1.43 and a λ -value of 0.52. Values are listed for all three measurement series in one column and are separated by a line.

How the different concentrations of the Ligand X affect the EPR parameters (CW and DEER) at the different labeling positions, is shown in Figs. 3.22-3.25:

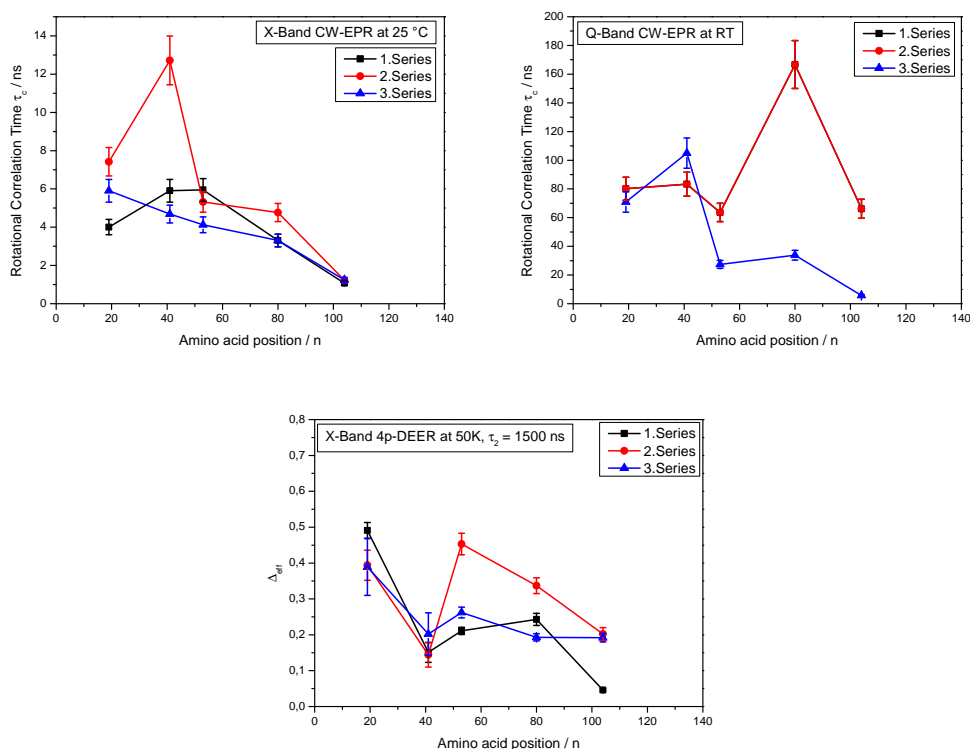


Figure 3.22. – Influence of 0.01 mM Ligand X on the different labeling positions. Shown are the rotational correlation times of X-band CW-EPR spectroscopy (upper left), rotational correlation times of Q-band CW-EPR (upper right), and Δ_{eff} (bottom) in X-band DEER with respect to the labeling position. Note that the τ_c -values of the first and the second series coincide at Q-band frequencies.

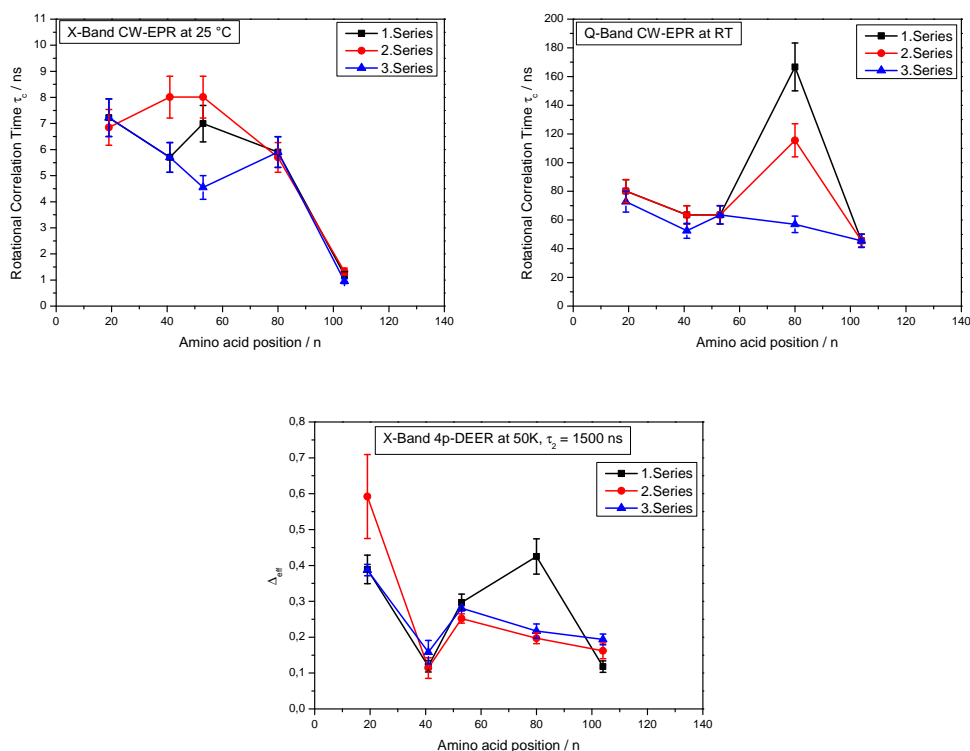


Figure 3.23. – Influence of 0.05 mM Ligand X on the different labeling positions.

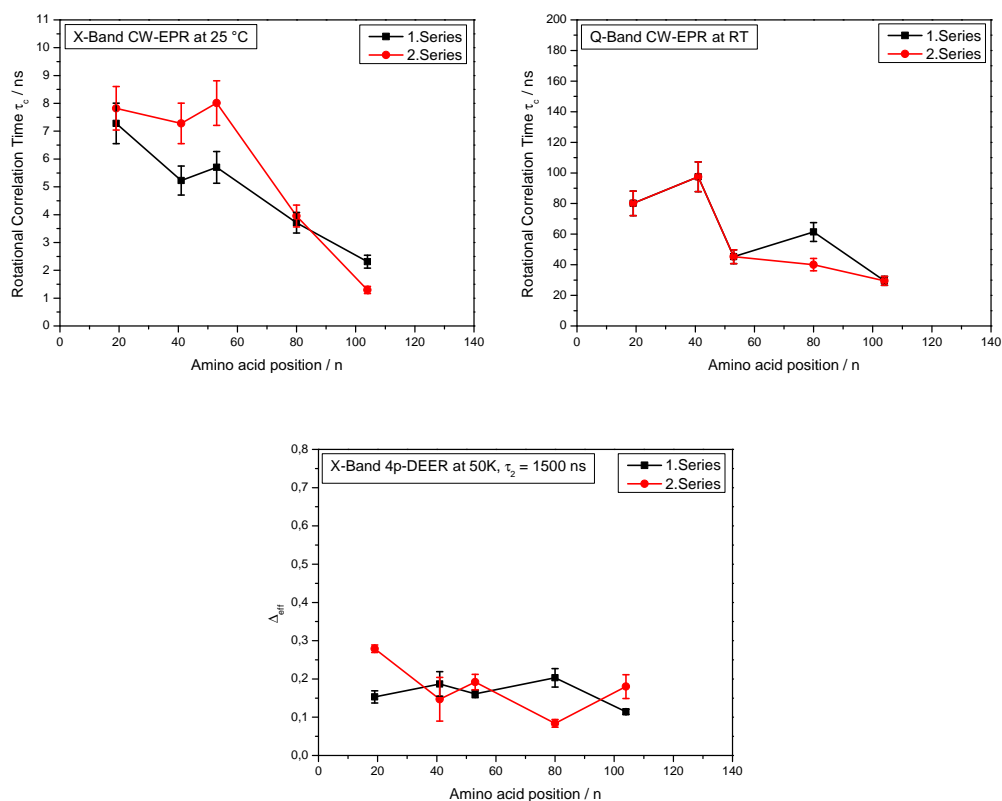


Figure 3.24. – Influence of 0.1 mM Ligand X on the different labeling positions.

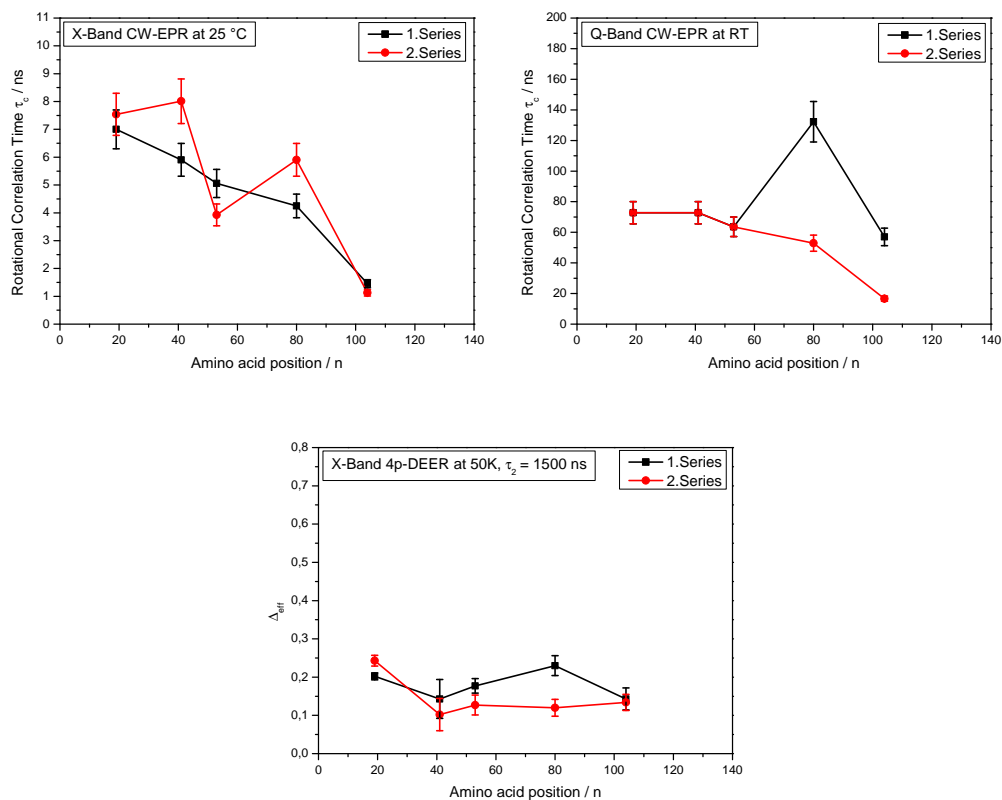


Figure 3.25. – Influence of 0.2 mM Ligand X on the different labeling positions.

The general trend Δ_{eff} for all ligand concentrations observed in 4p-DEER is, that at all labeling positions that are strongly bound to the liposome (like position 19, 53, and 80) show a higher value, whereas the positions with a more conformational flexibility show a lower Δ_{eff} -value.

Monitoring the rotational correlation times τ_c of both, X-band and Q-band CW-EPR, an interesting observation is, that the general trend of a decreasing value at X-band and a slight decreasing value at Q-band is still present. However, some labeling positions show a high variability. This variability is often found in the position 41, but also in positions 53 and 80, which are located in the second helix of the predicted horseshoe-structure, known to be a bit less bound to the liposome.

To sum up the different results from the measurements of 0.2 mM α -Synuclein + 1.5 mM POPG at different ligand concentrations, it can be assumed that the ligand interacts the strongest with the protein at low concentrations between 0.01 mM and 0.05 mM, respectively. The ligand is moreover often affecting the labeling positions that are known to interact strongly with the membrane. 4p-DEER data suggest that the ligand leads to a more compact protein on the membrane. Moreover, when the general trends of the different EPR measurements are compared to each other, no significant differences can be observed regarding the use DMSO or buffer used for the ligand dilution.

In 2010, Drescher et al. [139] published two proposed structures of lipid-bound dimers of α -Synuclein. The models, which take the horseshoe structure as the best model into account, were based upon DEER measurements. With these models the results from the ligand measurements can be demonstrated, see Fig. 3.26. Upon addition of the ligand, the labeling positions 19, 53, and 80 get in closer contact with their respective labeling position on the other dimer, which is especially observed as a higher Δ_{eff} -value and thus a higher number of coupled spins. Since position 41 is located within the linker region of the two helices, this position may possess some conformational flexibility. Moreover, it may also be that when the helices are more pressed together, the rather flexible linker region may orient itself outwards, which would explain the opposite behavior of position 41 compared to 19, 53, and 80.

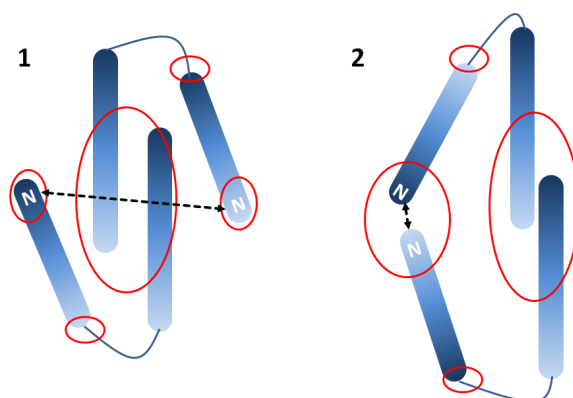


Figure 3.26. – Two proposed models of lipid-bound α -Synuclein. The models take the horseshoe structure into account. Shown in red are the regions that were examined during the ligand measurements. The cartoon is based upon [139]. The black arrows show the shorter and the longer distance between the N-terminal regions of two α -Synuclein monomers assembled as a lipid-bound dimer [139].

In the work of Drescher et al. [139], α -Synuclein was labeled at the position 18, whereas in this work here position 19 was measured. Principally it should be possible to some extent to compare the obtained distances. Drescher et al. [139] found a shorter distance of 2.2/2.4 nm (model vs. DEER) between the two α -Synuclein monomers at the position 18, which corresponds to model 2 in Fig. 3.26, and a longer distance of 4.3/4.2 nm (model vs. DEER) (model 1).

These shorter and longer distances were also obtained in this work when DEER data were analyzed with the DEERAnalysis software package [122]. Another distance of about 3 nm was also observed here, which may stem from the interaction of two different dimers. The distance distributions of the three measurement series of α -Synuclein A19C are shown in Fig. 3.28. A suggested model structure which shows how the dimers could be assembled on the liposome to yield a 3 nm distance distribution between two N-terminal domains of position 19 is shown in Fig. 3.27.

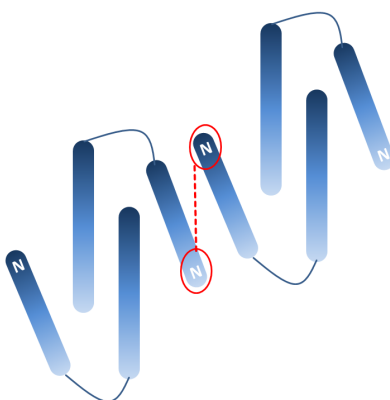


Figure 3.27. – Hypothetical model of the assembly of two lipid-bound α -Synuclein dimers to yield a 3 nm distance distribution between two N-terminal domains of position 19.

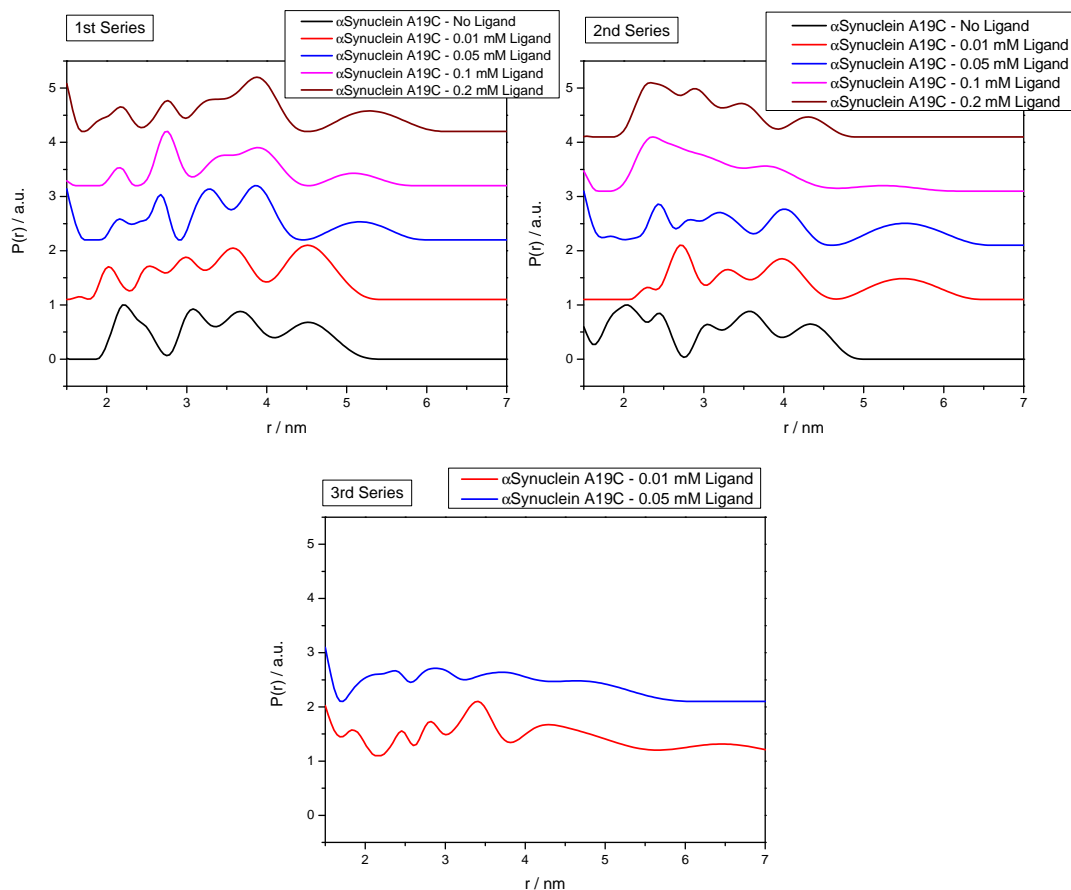


Figure 3.28. – Influence of Ligand X on α -Synuclein A19C - DEER distance distributions. A shorter distance of about 2 nm (model 2) and about 4 nm (model 1) is obtained. The distance of about 3 nm may stem from different dimers interacting with each other. To some extent the compacting of the protein upon interaction with the ligand can also be observed in the distance distributions. Tikhonov regularization for the distance distribution was conducted with the background position at the last third of the time trace, therefore at 1000ns.

3.1.2. Film Balance Measurements

Although the exact physiological function of α -Synuclein is still not clear, Vargas et al. [58] could recently show that the protein was associated with synaptic vesicles throughout the synaptic terminal. Moreover, due to the 11 residue binding motif in the N-terminal domain, which is also a feature of the exchangeable apolipoproteins - a class of proteins that interact with lipids - it was hypothesized that α -Synuclein can

also interact with phospholipids [66]. Due to this fact and the finding that α -Synuclein has a higher affinity to interact with curved membranes, many EPR and NMR studies were based on measurements with either SDS micelles or liposomes (SUVs and LUVs) of different composition.

Besides studying the membrane-bound state of α -Synuclein, another part of this work was to examine the affinity to different phospholipids, especially of a mixture that resembles the composition of a synaptic vesicle (SV) [141], using the monolayer technique.

3.1.2.1. Adsorption of α -Synuclein to the Air/Water-Interface

Before conducting adsorption experiments to examine the affinity of α -Synuclein to different phospholipid monolayers, the surface activity at the pure air/water interface was assessed. This is also an important step to determine the optimal amount of protein to be injected into the aqueous subphase underneath the phospholipid monolayer in subsequent experiments.

For this measurement a Langmuir film trough was filled with buffer (20 mM phosphate, 100 mM NaCl, pH 7.4). After adjusting the optimal fluid level, different amounts of a 0.8 mM α -Synuclein WT solution were injected with a Hamilton syringe into the aqueous phase. During these adsorption experiments a small metal orb was used to allow for a proper mixing of the subphase.

The measurement consisted of a time-dependent observation of the surface pressure. In the case of α -Synuclein the protein is already highly surface-active at the air/water-interface alone, as seen in Fig. 3.29. Even for very small trough concentrations (about 80 nM) the protein shows a saturation behavior. For a better comparison of the different measurements the surface pressure at a time of 10.000 s (~ 2.7 h) was read out via the Origin software and plotted against the injected amount of protein. An optimal amount for further measurements is thus 1 μ l of a 0.8 mM WT solution (80 nM trough concentration), see Fig. 3.30.

α -Synuclein was shown to be highly surface-active even at the pure air/water-interface as a trough-concentration of about 80 nM is already sufficient to have a saturation behavior. Since the protein is an IDP and contains thus "disorder-promoting" polar amino acids, especially a large amount of lysines in its N-terminal domain, those can interact with the polar aqueous subphase.

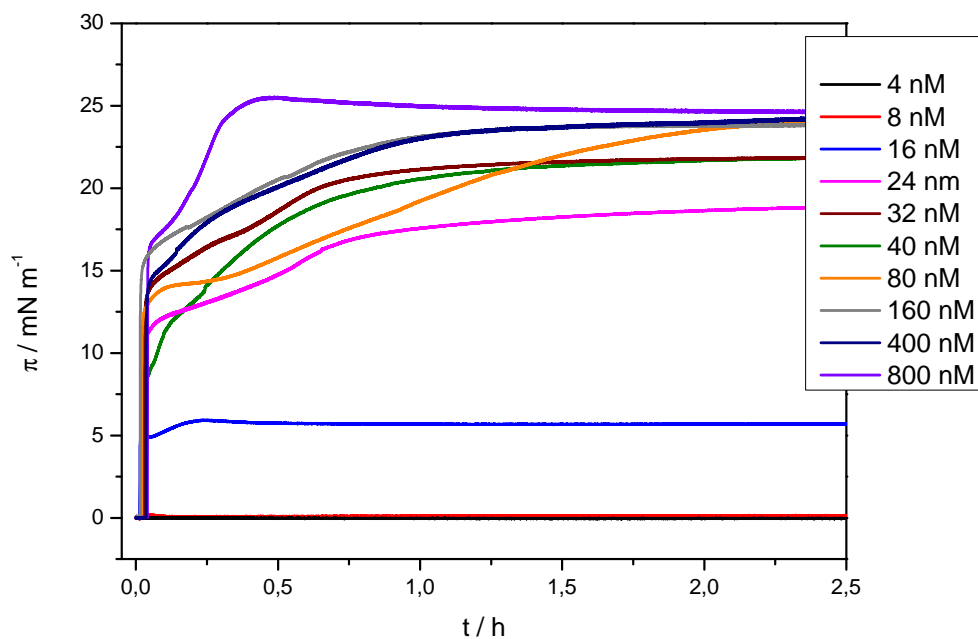


Figure 3.29. – Adsorption isotherms of α -Synuclein at the pure air/water-interface: Different amounts of an α -Synuclein WT solution (0.8 mM stock solution) were injected into the subphase (20 mM phosphate, 100 mM NaCl, pH 7.4) to obtain a wide range of trough concentrations.

3.1.2.2. Compression Isotherms of Phospholipids

Fig. 3.31 shows the compression isotherms of the different phospholipids used in this work. For a better comparison the phospholipids with a charged head group and the neutral phospholipids are shown separately.

As already stated in Fig. 1.17, p. 33, phospholipids with unsaturated fatty acid chains show only the liquid-expanded state and further compression will lead to the collapse of the monolayer. This behavior can clearly be seen in the compression isotherms of the pure phospholipids POPG and POPS (black and red curves, respectively). Both of these lipids possess the saturated 16:0 (palmitic acid) and the unsaturated 18:1 (oleic acid) fatty acids and differ only in the head groups.

The lipids from natural source (porcine brain) do not contain lipids of a specific saturation degree. They consist rather of a mixture of different fatty acids, but the same head

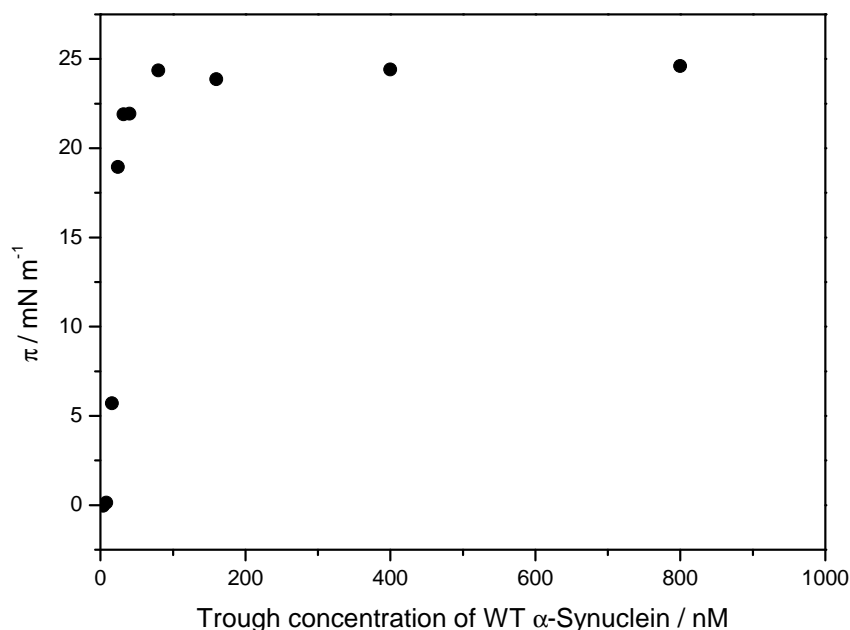


Figure 3.30. – The surface pressure for every adsorption isotherm of Fig. 3.29 is determined at a time of about 2.7 h and plotted against the amount of α -Synuclein injected into the subphase.

group. The characteristics of the brain lipids used are listed in the appendix A.1.11, p. 180. It is obvious that also the compression isotherms of BrainPC, BrainPS, BrainPE, and BrainSM show only the liquid-expanded state upon compression, since lipids with a high percentage of unsaturated fatty acids are present.

The characteristics that can further be obtained from the compression isotherm is the lift-off of the curve, i.e. the point where the molecules start to interact with each other and are forced to align themselves. The respective lift-off areas per molecule have been read out at a surface pressure of 1 mN/m. In the case of POPG the lift-off is about $136 \text{ \AA}^2/\text{molecule}$. Moreover, the collapse of the film can be read out which occurs at an area of about $62 \text{ \AA}^2/\text{molecule}$ and a surface pressure of about 42 mN/m for POPG. The area of the lift-off and of the collapse for the other phospholipids are listed in Tab. 3.15. Differences in the lift-off are mainly due to varying space requirements of the fatty acid chains, which is clearly obvious by comparing POPG and POPS, where the lift-off

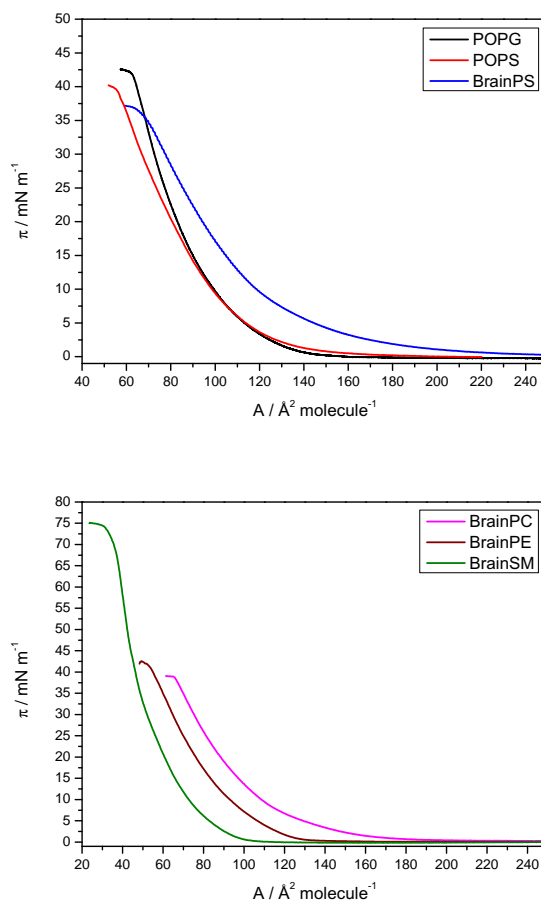


Figure 3.31. – Compression isotherms (at 20 °C) of different phospholipids used in this work.

area is of the same magnitude in both isotherms. The slight differences in the areas per molecule of the lift-off and at the collapse of the film are probably because of the different head group and therefore a slightly different packing of the phospholipids.

Synaptic Vesicle Composition As already stated, a lipid mix that resembles the composition of a synaptic vesicle was measured. This composition is based on a publication by Takamori et al. [141]. The same mix was also prepared without cholesterol. The mixes were prepared with the brain lipids of porcine brain. Both compositions are

Characteristic Data of the Compression Isotherms			
Phospholipid	Lift-Off A [Å ² /molecule]	Collapse A [Å ² /molecule]	Collapse π [mN/m]
POPG	136	62	42
POPS	145	55	40
Brain PS	203	64	37
Brain PC	170	65	39
Brain PE	125	51	42
Brain SM	97	31	74
SV Comp.	74	33	40
SV Comp. w/o Cholesterol	131	53	40

Table 3.15. – Characteristic data of the compression isotherms of the phospholipids used in this work.

listed in Tab. 3.16.

Composition of the SV Mix		
Lipid [mol-%]	SV Mix	SV Mix w/o Cholesterol
Brain PC	20	37
Brain PE	24	43
Brain SM	4	7
Brain PS	7	13
Cholesterol	45	0

Table 3.16. – Composition of the SV mix. Shown is the composition of the SV mixed based upon [141] as well as the same mix without cholesterol.

Fig. 3.32 shows the compression isotherms of the SV composition, as well as the composition without cholesterol, respectively. Both isotherms show only the liquid-expanded state due to the amount of unsaturated fatty acid chains of the porcine brain phospholipids. The most striking feature is the difference in the area per molecule of the lift-off and of the collapse of the monolayer. This can be explained by the condensing effect of cholesterol upon lipids in the fluid state [142]. Upon the presence of cholesterol the area per molecule is decreased compared to the areas when cholesterol is absent [143]. When checking the compression isotherm of the SV composition, it was not clear if another phase transition occurs between 33 and 24 $\text{\AA}^2/\text{molecule}$. An epi-fluorescence microscopy study was carried out to shed light on this matter. Since this measurement is not directly related to the initial scope of the project to gain information about the influence of Ligand X, the results of this study are shown in the appendix A.1.12, p. 180. It can be concluded that the collapse of the SV-Mix monolayer occurs at about 33 $\text{\AA}^2/\text{molecule}$.

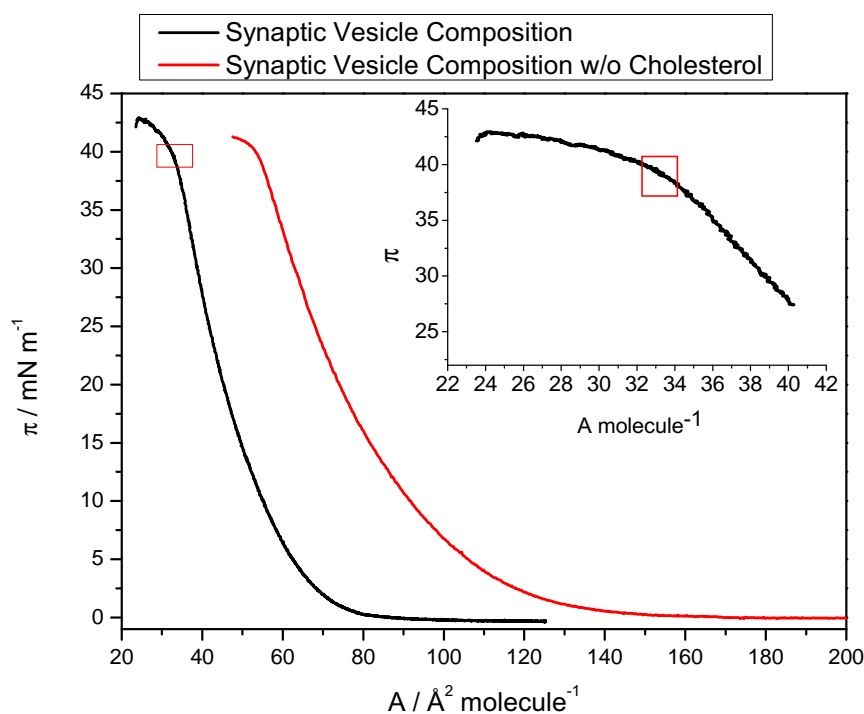


Figure 3.32. – Compression isotherms of the SV composition at 20 °C. Shown are the isotherms for the composition as stated in [141], as well as the same composition without cholesterol.

3.1.2.3. Adsorption of α -Synuclein to Phospholipid Monolayers

Adsorption experiments were carried out as stated in Fig. 1.18. The Langmuir film trough was filled with buffer (20 mM phosphate, 100 mM NaCl, pH 7.4) and adjusted to the optimal fluid level. Then the respective phospholipid, which was dissolved in chloroform/methanol, was spread onto the aqueous subphase to different surface pressures. It was desired that the initial surface pressures have a difference of about 5 mN/m. When the monolayer was stable, which was usually after 30 min to 60 min, α -Synuclein WT solution was injected underneath the phospholipid monolayer. The amount of protein to be injected was 1 μ l of 0.8 mM WT solution, as already shown in chapter 3.1.2.1, p. 75, resulting in a final trough concentration of 80 nM.

Fig. 3.33 shows the adsorption experiments of α -Synuclein to the monolayers POPG and POPS, respectively. Since the EPR measurements of this work were conducted with POPG liposomes, it was of interest to gain knowledge about the affinity of the protein for the phospholipids via film balance measurements. As already expected from the primary sequence of α -Synuclein and its many lysine residues in the N-terminal domain, the protein has a high affinity for lipids with negatively charged head groups. This can clearly be seen in the increase of the lateral surface pressure upon injection of the protein in the subphase underneath the monolayer. PG is only found in bacteria and the mammalian analogue of the charged head group is PS, so a similar measurement was conducted with POPS. It is also obvious by comparing the compression isotherms of the respective phospholipids and the adsorption isotherms that the phospholipid monolayers are in a liquid-expanded state with no phase transition at 20 °C, which is also the case for all other phospholipids and the SV mix used.

When looking closely at the adsorption isotherms it is furthermore evident, that the increase in surface pressure $\Delta\pi$ decreases with increasing initial surface pressures. As a consequence, when $\Delta\pi$ is plotted against the initial surface pressure a linear plot with a negative slope is obtained. From this linear plot two characteristic values can be calculated. First the already described maximum insertion pressure (see Fig. 1.18, p. 35), and secondly the synergy, which was introduced by Boisselier et al. [144].

The synergy can be calculated as: Synergy = Slope + 1. A positive synergy indicates a favorable binding of a protein to a monolayer, whereas a negative synergy indicates an unfavorable binding.

The adsorption isotherms for the brain lipids are shown in Fig. 3.34 and for the SV composition in Fig. 3.35, p. 84.

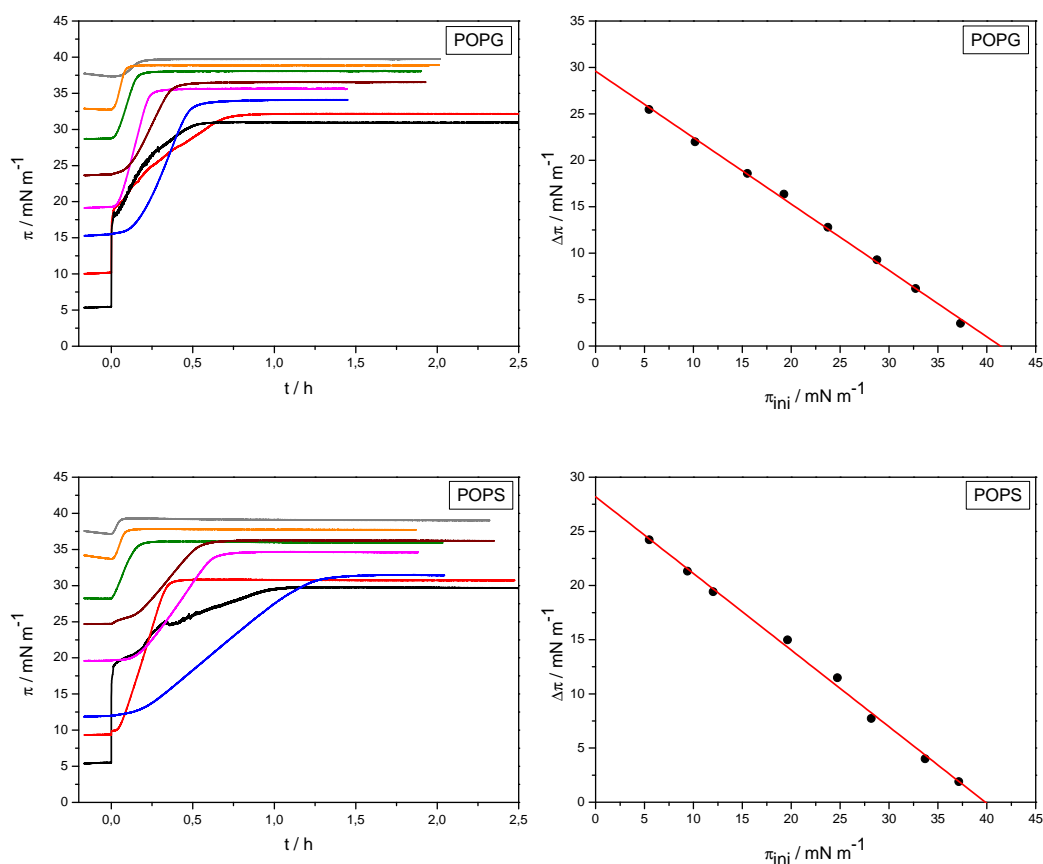


Figure 3.33. – Adsorption experiments and MIP determination of α -Synuclein to POPG and POPS monolayer at 20 °C.

The fitting parameters of the adsorption experiments as well as the calculated maximum insertions pressures and the synergy values are summarized in Tab. 3.17.

Parameters of the adsorption experiments of α -Synuclein to different monolayers					
Lipids	Intercept a [mN m ⁻¹]	Slope b	R ²	MIP [mN m ⁻¹]	Synergy
POPG	29.6 ± 0.30	-0.71 ± 0.01	0.998	41.7 ± 1.01	0.29 ± 0.01
POPS	28.2 ± 0.40	-0.71 ± 0.02	0.996	39.7 ± 1.68	0.29 ± 0.01
Brain PC	24.2 ± 0.28	-0.82 ± 0.02	0.998	29.5 ± 1.06	0.18 ± 0.02
Brain PE	23.9 ± 0.48	-0.75 ± 0.03	0.993	31.9 ± 1.92	0.25 ± 0.03
Brain PS	27.1 ± 0.50	-0.69 ± 0.02	0.993	39.3 ± 1.86	0.31 ± 0.02
Brain SM	23.8 ± 0.62	-0.66 ± 0.03	0.991	36.1 ± 2.58	0.34 ± 0.03
SV Comp.	24.8 ± 0.55	-0.93 ± 0.04	0.993	26.7 ± 1.74	0.07 ± 0.04
SV Comp. w/o Cholesterol	24.7 ± 0.89	-0.75 ± 0.04	0.984	32.9 ± 2.94	0.25 ± 0.04

Table 3.17. – Parameters of the adsorption experiments of α -Synuclein to different monolayers.

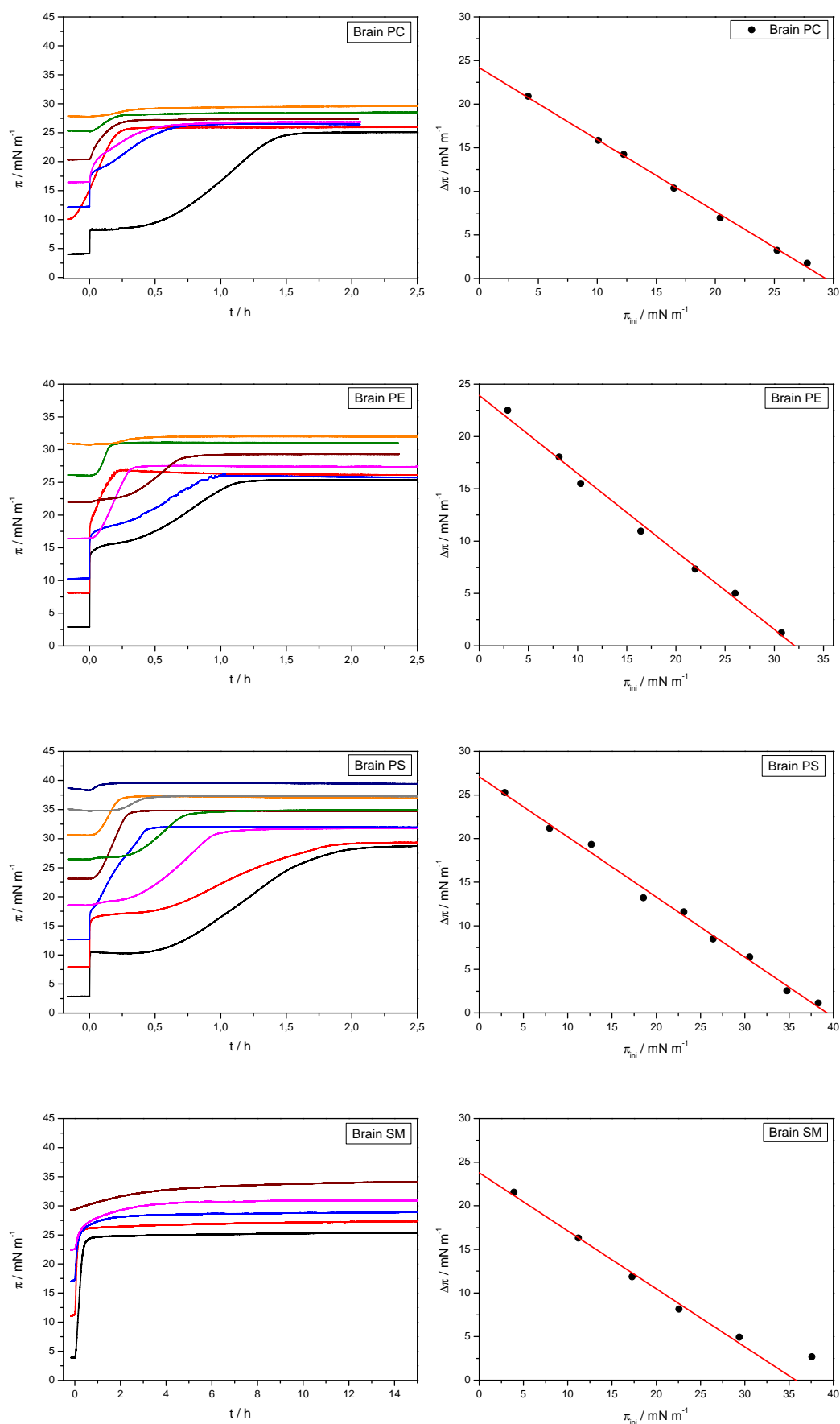


Figure 3.34. – Adsorption experiments and MIP determination of α -Synuclein to mono-layers of brain lipids at 20 °C.

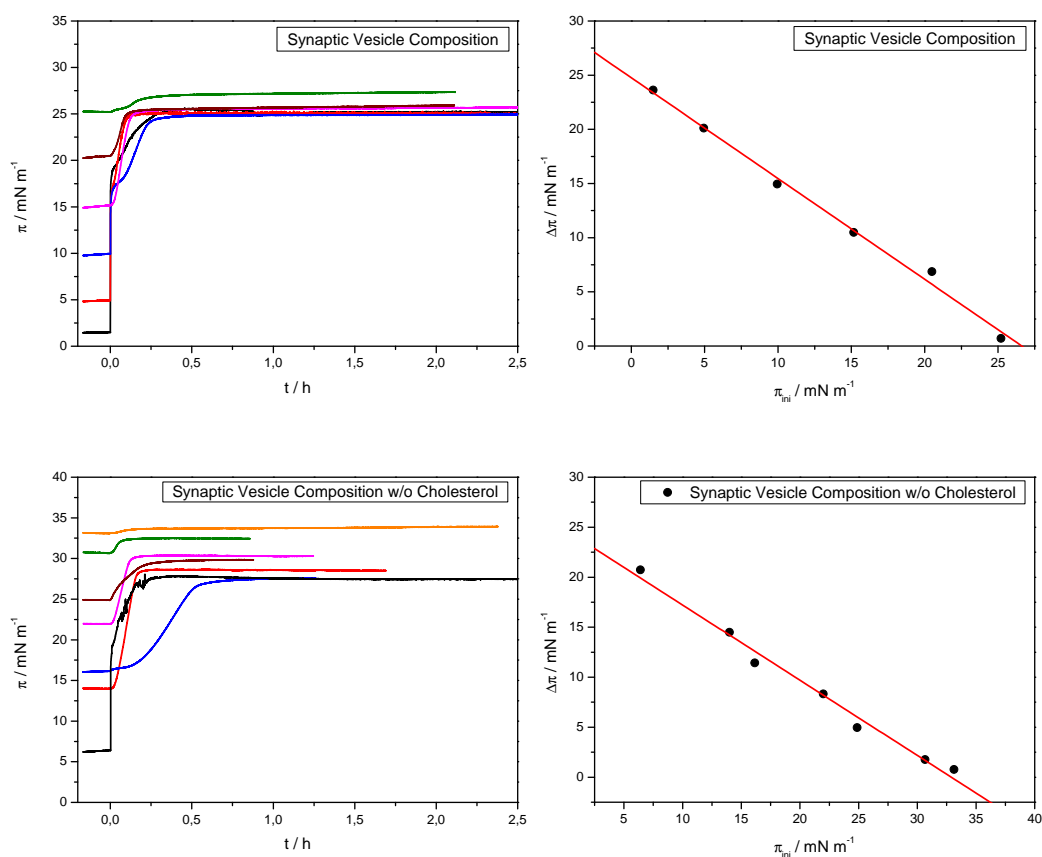


Figure 3.35. – Adsorption experiments and MIP determination of α -Synuclein to mono-layers of the SV compositions with and without cholesterol at 20 °C.

It can clearly be seen that the affinity of α -Synuclein to phospholipids with negatively charged head groups (POPS, POPG, and BrainPS) yields relatively high MIP values of about 40 mN/m. These values are higher compared to that of the membrane lateral pressure of 30 mN/m so that it can be concluded that the protein interacts strongly with those phospholipids. A strong interaction can also be seen by looking at the synergy values of about 0.30 (> 0) and the $\Delta\pi_0$ (the intercept a). Boisselier et al. [144] stated that when $\Delta\pi_0$ is equal to the protein surface activity the protein will likely interact with the polar head group, but not protrude more deeply. A higher value would indicate a more deep insertion. The surface activity of α -Synuclein was about 25 mN/m (see Fig. 3.29, p. 76). Thus, PG, PS, and BrainPS show slightly higher values compared to the neutral head groups.

The maximum insertion pressures for the phospholipids with neutral head groups show MIP values of about 30 mN/m, which is the lateral pressure found for many membrane-binding proteins [145]. Also the synergy values are decreased to values of about 0.18 - 0.25.

Interestingly BrainSM shows a different behavior compared to the other phospholipids with neutral head groups. The insertion of α -Synuclein takes a much longer time until the saturation plateau is reached. Taking the linear part of the $\Delta\pi$ vs. π_{ini} into account the MIP is about 36 mN/m. The synergy value is the highest of all measured phospholipids, however $\Delta\pi_0$ is below the surface activity of α -Synuclein 25 mN/m.

The most surprising result is that the MIP decreases to a value under 30 mN/m and a respective synergy of 0.07 in the adsorption experiments of α -Synuclein to monolayers of the SV composition. This value would indicate that α -Synuclein is very weakly interacting with synaptic vesicles. The MIP value of the SV composition without cholesterol is higher. However, due to the missing 45 mol-% cholesterol, the content of serine is also higher. α -Synuclein, which is negatively charged at pH 7.4 (charge about -9.7, calculated with the Prot Pi tool [146]) sees thus more positive charges, which would indicate that the interaction is primarily an electrostatic one.

Another explanation of this effect could stem from a certain function of cholesterol itself, which has been published more recently by Nakamura et al. [147]. They conducted experiments with liposomes composed of *E. coli* polar phospholipids as well as PC liposomes. In both cases cholesterol blocked the spontaneous insertion of a protein mutant of the Pf3 major coat protein. This protein is a protein of the bacteriophage Pf3 and is stored in the inner membrane of the infected cell [148]. A complete blockage was achieved with a cholesterol content of about 35 mol-% in the case of liposomes of *E. coli* polar phospholipids and in the case of PC liposomes the insertion decreased with increasing cholesterol content when cholesterol was present to about 20 mol-% [147]. The SV composition used here has a cholesterol content of 45 mol-% so that it is likely that the decrease of the MIP stems from the presence of cholesterol. Interestingly in the same study by Nakamura et al. [147] it has also been shown that the presence of sphingomyelin enhanced the spontaneous insertion in liposomes of *E. coli* polar phospholipids, whereas this effect has not been observed in PC liposomes. However, it is striking that the MIP of the adsorption and the overall behavior of α -Synuclein to a pure

BrainSM monolayer was somewhat different compared to other neutral phospholipids especially BrainPC, which also contains the choline head group and therefore may be explained by this enhancing effect to some extent.

3.1.2.4. Adsorption of α -Synuclein to Phospholipid Monolayers (Influence of Ligand X)

The influence of the Ligand X and if it affects the affinity of α -Synuclein to membranes was also assessed via film balance measurements. Since EPR measurements were conducted with POPG liposomes, film balance measurements were also carried out only with POPG and out of interest with the SV composition.

At first the surface activity of the ligand at the pure air/water interface was determined. For this measurement the trough was filled with buffer (20 mM phosphate, 100 mM NaCl, pH 7.4). After adjusting the optimal fluid level the Ligand X was injected in the same amount as used in later measurements. Since in the EPR measurements a drastic effect of the Ligand could be seen at concentrations of 0.05 mM Ligand X and 0.2 mM α -Synuclein (molar ratio ligand:protein 1:4), film balance measurements were carried out with this molar ratio and also with a 1:1 molar ratio. No surface activity of Ligand X can be seen on buffer alone and on POPG and SV mix films, see Fig. 3.36.

The adsorption experiments of α -Synuclein and the Ligand X have been conducted in a similar manner as the adsorption experiments with α -Synuclein alone. The respective phospholipid (POPG or the SV composition), have been spread up to several different surface pressures π . At the same time α -Synuclein was incubated with the Ligand X on a thermomixer, as stated in the experimental part, see p. 121. After injection of the protein/ligand-mixture into the aqueous subphase, the adsorption isotherms were recorded. Again, the MIP and synergy values were determined from the plot of $\Delta\pi$ against the initial pressure, see Fig. 3.37.

In general the ligand does not seem to affect the affinity of α -Synuclein very strongly. The MIP values for a POPG monolayer are still at about 40 mN/m and also the synergy values are close together. Slight changes can be observed in the SV composition. However, when checking the errors of the parameters, also in this case, the MIP and synergy values are close together. The large changes that have been detected with the EPR measurements can not be observed with the film balance technique. Thus, the ligand

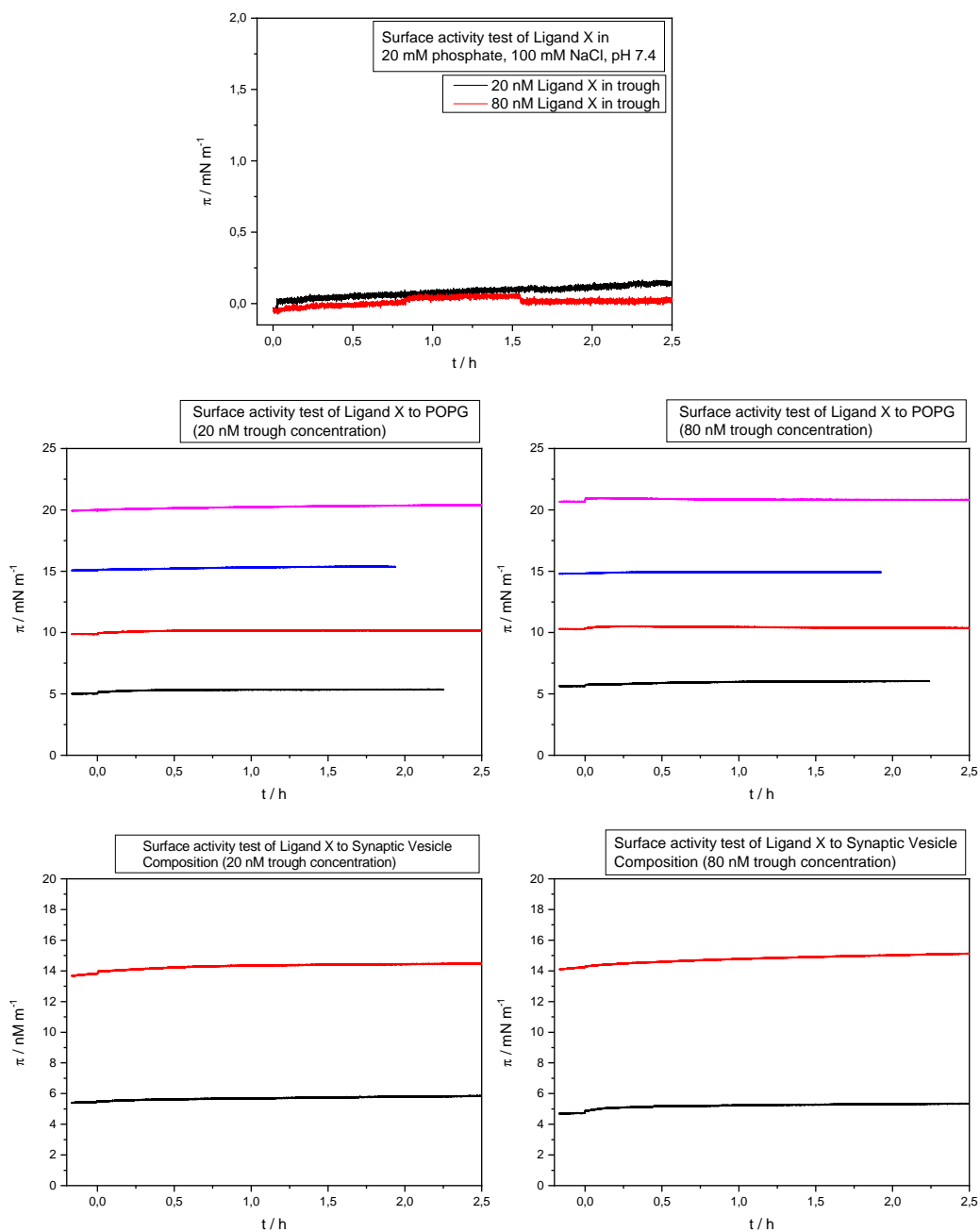


Figure 3.36. – Adsorption isotherms of Ligand X at the pure air/water-interface and POPG and SV composition at 20 °C. Amounts of Ligand X injected were the same as used in following film balance measurements.

interacts without changing the binding affinity of the protein to membranes.

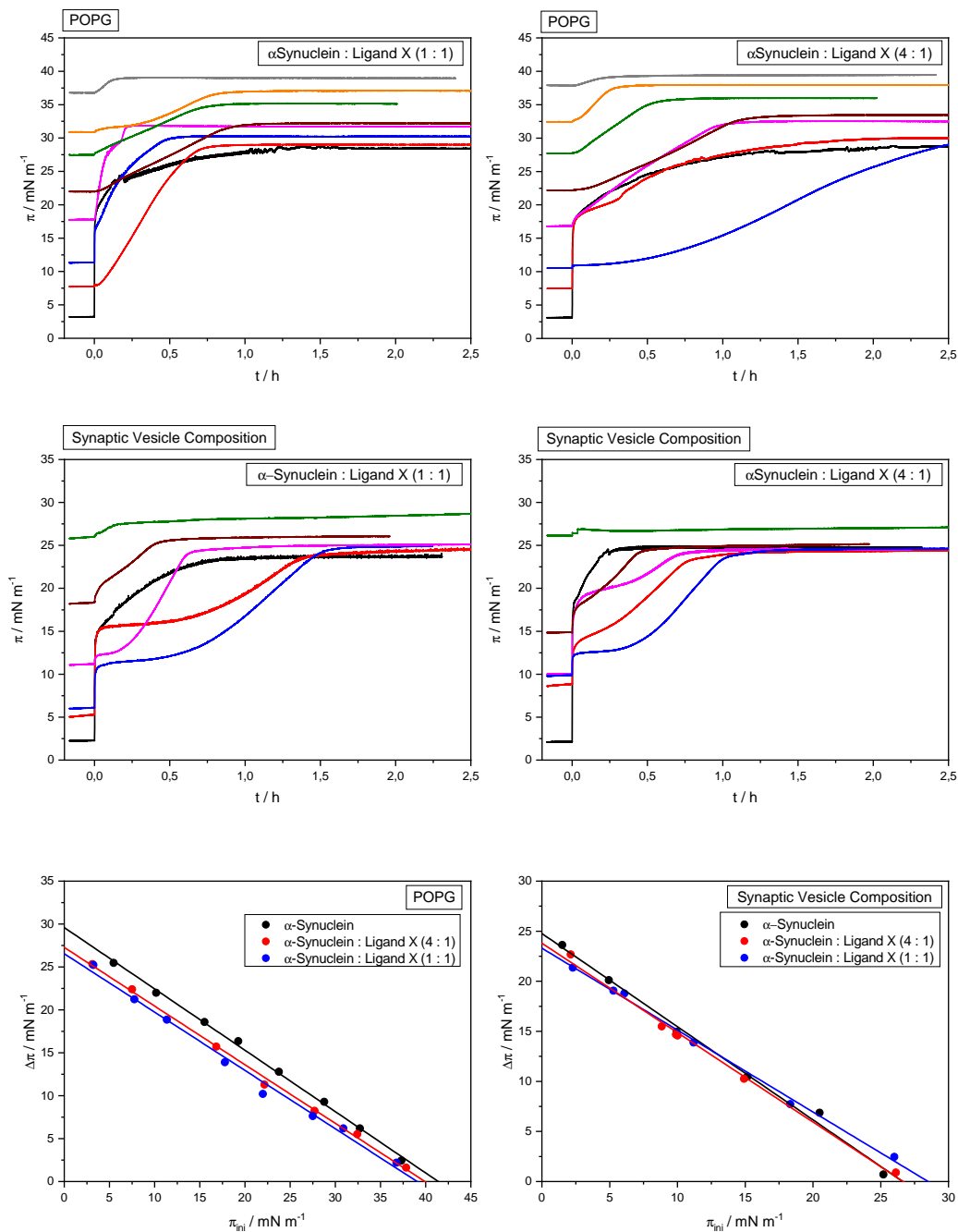


Figure 3.37. – Adsorption experiments and MIP determination of α -Synuclein incubated with Ligand X to monolayers of POPG and SV composition at 20 °C. Shown are the adsorption isotherms and the linear plots of $\Delta\pi$ against the injection pressure. For a better comparison the linear plot of α -Synuclein without the Ligand is also shown.

Parameters of the adsorption experiments of α -Synuclein to different monolayers					
Lipid / Ligand X	Intercept a [mN m ⁻¹]	Slope b	R ²	MIP [mN m ⁻¹]	Synergy (Slope + 1)
POPG / No Ligand	29.6 ± 0.30	-0.71 ± 0.01	0.998	41.7 ± 1.01	0.29 ± 0.01
POPG / 20 nM	27.3 ± 0.35	-0.68 ± 0.01	0.997	40.1 ± 1.10	0.32 ± 0.01
POPG / 80 nM	26.5 ± 0.58	-0.68 ± 0.03	0.990	39.0 ± 2.57	0.32 ± 0.03
SV / No Ligand	24.8 ± 0.55	-0.93 ± 0.04	0.993	26.7 ± 1.74	0.07 ± 0.04
SV / 20 nM	23.8 ± 0.42	-0.89 ± 0.03	0.994	26.7 ± 1.37	0.11 ± 0.03
SV / 80 nM	23.3 ± 0.31	-0.82 ± 0.02	0.996	28.4 ± 1.07	0.18 ± 0.02

Table 3.18. – Parameters of the adsorption experiments of α -Synuclein to different monolayers. A trough concentration of 20 nM for the Ligand X corresponds to the molar ratio 4:1 (α -Synuclein:Ligand), 80 nM corresponds to the molar ratio 1:1 (α -Synuclein:Ligand).

3.2. HPRG

Another part of this work was to purify the Histidine-Proline-rich Glycoprotein HPRG from rabbit serum. First, the more recent purification strategies based upon metal chelate affinity chromatography (IMAC) and subsequent size exclusion chromatography (SEC) or anion exchange chromatography (AEC) were tested. However, it was soon discovered that a large amount of serum albumin eluted also from the IMAC column. Serum albumin could not be successfully removed via SEC or AEC. The respective information about both, SEC and AEC, as well as gel pictures are shown in the appendix, see Ch. A.2, p. 183. In the following section a new approach, the purification via preparative gel electrophoresis, will be presented and discussed.

3.2.1. Cobalt Affinity Chromatography

The first step of the purification method was identical to the strategy that was described by Patel et al. [130]. Metal chelate affinity chromatography is usually utilized for the purification of recombinant proteins with a 6×His-tag. As the name of the protein indicates, HPRG contains many histidine amino acid residues of which half of them are located in the central histidine-rich region [89]. Therefore, HPRG contains a kind of a natural His-tag and metal chelate affinity chromatography can be used. This chromatography method is generally carried out with nickel ions, which have a greater

capacity for his-tagged proteins, albeit with lower specificity. On the other hand, cobalt has a lower capacity, but a higher specificity so that the protein that elutes from the column may be more pure. In case of HPRG, cobalt affinity chromatography may thus be the better choice, however both cobalt and nickel led to a co-purification of serum albumin (see Figs. 3.40 and A.25 (p. 183)). The general principle of the metal chelate affinity chromatography is shown in Fig. 3.38 for Ni-NTA, a tetradentate chelating agarose resin. The Co-NTA agarose resin used in this work interacts similarly.

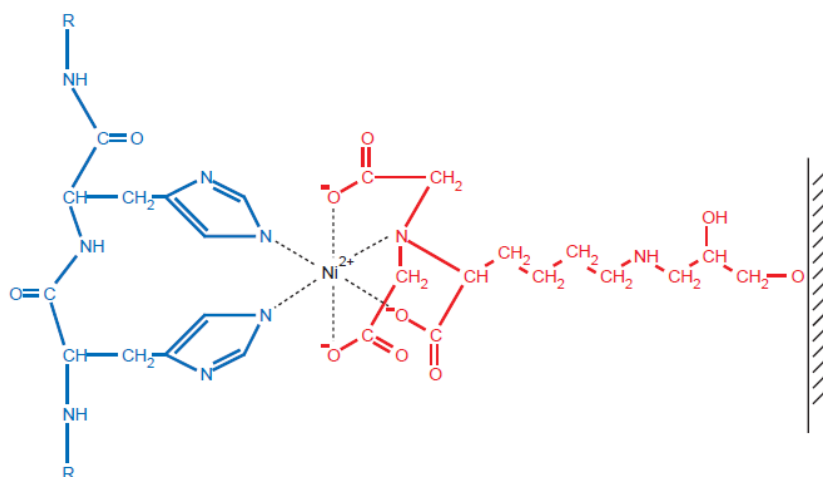


Figure 3.38. – Scheme of the interaction of histidine residues with Ni-NTA. Nitrilotriacetic acid (NTA) occupies four of the six ligand binding sites in the coordination sphere of nickel, so that the remaining two sites can interact with the histidines of a His-tag [149]. Ni-NTA itself is coupled to the Sepharose CL-6B. Scheme taken from [149].

Cobalt affinity chromatography was carried out as explained in the experimental part in Ch. 5.3.3, p. 125. Buffer compositions were the same as published by Patel et al. [130]. 20 mM imidazole was added to the binding buffer when HPRG was incubated with Co-NTA in order to prevent unspecific binding to the column. This amount of imidazole was also added to the washing buffer 1 for the same reason. Non-specifically bound proteins could be washed off the column with 80 mM imidazole (washing buffers 2 and 3). In washing buffer 2 the sodium chloride content was increased to 500 mM to dissociate ionic interactions. Finally, the protein was eluted with 500 mM imidazole [130].

This procedure is based upon the structural similarity of imidazole and histidine. Histi-

dine possesses an imidazole ring and both, imidazole and histidine, compete for the cobalt binding site, see Fig. 3.39. The imidazole ring of the histidine residues interacts with Co-NTA groups of the column material. However, imidazole itself can also bind to the cobalt ions and therefore disrupts the binding of proteins that contain a few isolated histidine residues. This is why the binding buffer and the washing buffers 1 and 2 contained a low content of imidazole so that unspecific binding could be successfully suppressed. His-tagged proteins can still bind to the column under these conditions. The column is washed with all the washing buffers until no further protein is washed off. Elution of the his-tagged protein can be achieved by increasing the imidazole content. Imidazole and histidine residues are then no longer competing for the binding site and the his-tagged protein is finally washed off [149].

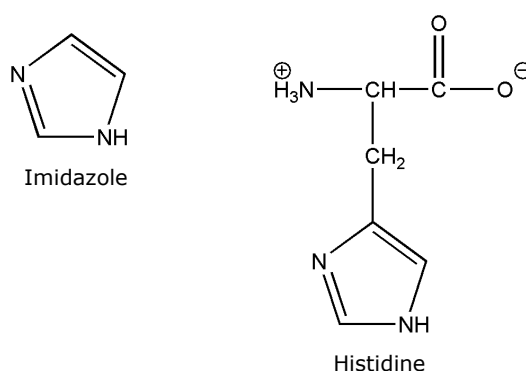


Figure 3.39. – Structures of imidazole and histidine. Histidine itself consists of an imidazole ring so that both of them can compete for the metal binding site in IMAC.

The elution fractions of cobalt affinity chromatography were analyzed via SDS-PAGE in Laemmli sample buffer as stated in the experimental part of this work, but without reducing agents and no thermal denaturation (see Ch. 5.3.2, p. 124). This electrophoretic conditions were the same as in the following preparative gel electrophoresis step for a better comparison. The respective SDS gel is shown in Fig. 3.40.

HPRG migrates on a SDS gel at approximately 90 kDa under reducing conditions [82] in contrast to Wakabayashi [79] where it is stated that the molecular weight of mammalian HPRG proteins is of the size about 70 kDa. This behavior on SDS gels can be explained by the fact that HPRG is a glycoprotein. According to literature [110], glycoproteins are not as strongly loaded with SDS as other proteins and thus migrate slower. Even

when working under non-reducing conditions, HPRG still seems to be migrating at approximately 90 kDa.

Another band is visible on both gels, which corresponds to serum albumin. Serum albumin migrates differently on SDS gels depending on the electrophoretic conditions, i.e. if the samples are reduced with either DTT or β -Mercaptoethanol, or if the samples are not reduced. Under reducing conditions serum albumin migrates at the apparent size of 67 kDa, whereas under non-reducing conditions it migrates at the apparent size of about 54 kDa [150, 151]. This is the reason why preparative gel electrophoresis can be successfully used to purify HPRG and to get rid of the serum albumin impurity. It was not possible to separate both proteins via SEC and AEC, but since they separate on a SDS gel, HPRG could be purified correspondingly.

The elution fractions of cobalt affinity chromatography containing HPRG were concentrated using centricons (10.000 MWCO or 30.000 MWCO, Amicon Ultra, Merck Millipore, Darmstadt, Germany). Afterwards the concentration of the protein solution was determined via BCA Assay (Ch. 5.3.1.2, p. 123).

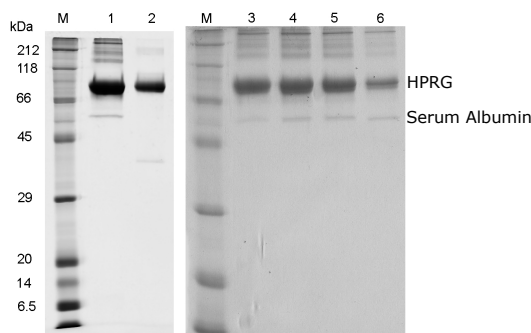


Figure 3.40. – SDS-PAGE of cobalt affinity chromatography elution fractions. The elution fractions of two cobalt affinity chromatography runs are shown. HPRG migrates at approximately 90 kDa, serum albumin at approximately 54 kDa under non-reducing conditions. Marker: ProteinMarker III (AppliChem, Darmstadt, Germany)

3.2.2. Preparative Gel Electrophoresis

The preparative gel electrophoresis based upon Hauer et al. [152] was carried out as explained in Ch. 5.3.4, p. 126.

The gel size for preparative gel electrophoresis was chosen to 20 x 20 cm (“Midi”) so that a higher amount of the protein could be loaded onto the gel. To avoid overloading, 0.5 - 1 mg of the concentrated cobalt affinity chromatography elution fraction was loaded onto a 10 % separating gel. Electrophoresis conditions were non-reducing to guarantee that the five disulfide bridges of rabbit HPRG [89] were not reduced as they may not fold back correctly.

The staining of the preparative gel was chosen to be a negative staining. Thus, the background of the gel, and not the protein itself was stained. This was achieved by the negative zinc-imidazole staining procedure [153]. This method is based upon the different binding of salts. Protein-bound salts (i.e. SDS or zinc) are chemically less active than free salts in the gel. The precipitation of an insoluble salt is slower in the regions of the gel where proteins are located, whereas the zinc dodecyl sulfate can precipitate in the background. Therefore, the protein remains translucent and the background is stained white [154]. The resulting gel picture of a negative stained preparative gel as obtained in this work is shown in Fig. 3.41. The respective band corresponding to HPRG was cut out of the gel and sliced into small pieces. The protein was then electro-eluted from the gel pieces with standard SDS running buffer as explained in Ch. 5.3.4, p. 128.

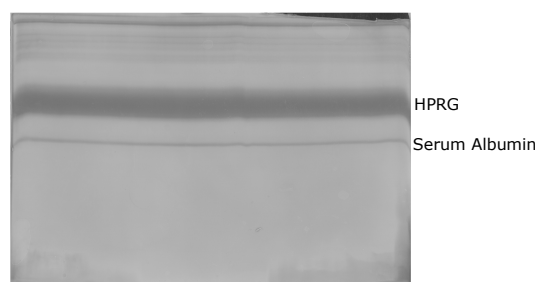


Figure 3.41. – Zinc-imidazole stained preparative gel of HPRG. HPRG and serum albumin (thin line underneath the HPRG band) are clearly separated on the gel. The thick band corresponding to HPRG was cut out.

To remove SDS and buffer salts from electrophoresis and electro-elution, a reversed-phase HPLC (RP-HPLC) was carried out at RT as explained in Ch. 5.3.4, p. 130. In contrast to “normal”-phase HPLC, in RP-HPLC the stationary phase of the column is nonpolar, consisting of hydrophobic alkyl chains, whereas the mobile phase is polar. Thus, in a RP-HPLC polar substances, like proteins, will be effectively eluted. The

column used in this work was a C3 column. In general, columns with short alkyl chains are used for proteins, whereas longer alkyl chains are used for the purification of peptides. Since in RP-HPLC compounds are separated by their hydrophobic character, a larger protein may possess more hydrophobic amino acids and can therefore better interact with the column so that a shorter alkyl chain length may be advantageous [155]. Elution of HPRG was achieved by the acetonitrile-water gradient as shown in Tab. 5.12, p. 130. A small amount of 0.05 % TFA was added because acids improve the chromatographic peak shape [155]. The gradient used in this work is based upon Hauer et al. [152]; the sudden jump from 43 % to 60 % acetonitrile from 20.0 min to 20.3 min allows to focus the eluting protein to just a few fractions. Afterwards, elution fractions containing HPRG were pooled and lyophilized (Alpha 2-4 LD Plus, Martin Christ Gefriertrocknungsanlagen GmbH, Osterode am Harz, Germany).

When the lyophilized HPRG fractions were dissolved in PBS-buffer and a SDS-PAGE was repeatedly carried out, no peak corresponding to serum albumin was visible anymore (see Fig. 3.42).

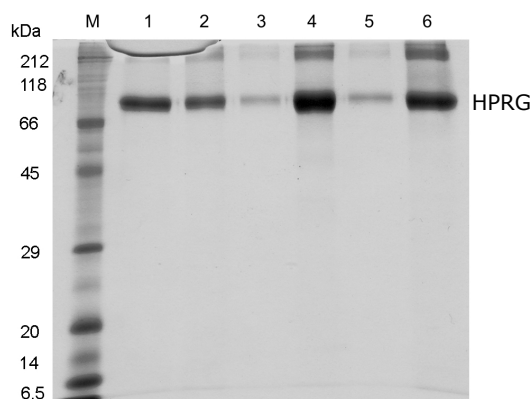


Figure 3.42. – Coomassie-stained SDS-PAGE of lyophilized HPRG fractions reconstituted in PBS-buffer. The band corresponding to HPRG is clearly visible, no further impurity corresponding to serum albumin can be detected.

It is noteworthy that this preparative gel purification step could not be successfully conducted without the use of SDS. Gel electrophoresis worked under native conditions. However, when the electro-elution was carried out in the following step, no protein was eluted from the gel slices. This indicates that the amount of SDS was necessary to effectively elute the protein out of the gel slices.

SDS usually denatures the protein under electrophoretic conditions. However, in standard SDS-PAGE protocols it is written that a *thermic denaturation* of proteins in SDS sample buffer should be carried out. In this work this thermic denaturation was not done to avoid complete denaturation. As already mentioned before, glycosylated proteins are not that strongly loaded with SDS and with the intrinsic disordered content of HPRG it is possible that the protein is hardly affected by the use of SDS. However, it is important to consider the use of SDS for later binding studies or studies of the protein structure. To characterize the isolated HPRG regarding the secondary structure, a CD measurement has been conducted, see Ch. 3.2.5, p. 102.

3.2.3. Recovery

The overall yield of rabbit HPRG during cobalt affinity chromatography was about 30 % in case the plasma concentration of HPRG is correctly determined to 900 mg/l as stated in Borza et al. [82]. Human HPRG isolated from plasma as stated in Patel et al. [130], whose buffer composition was used in this work, yielded about 56 % in the first step. No significant loss of protein should be expected from preparative gel electrophoresis and subsequent electro-elution so that the yield was >90 %. However, it has to be kept in mind that the elution fractions of cobalt affinity chromatography that were loaded onto the gel contained impurities, as e.g. serum albumin, which of course were also affecting the result of the BCA assay and therefore the amount of protein that was loaded onto the gel.

The recovery after RP-HPLC was estimated to exceed 80 %.

3.2.4. Mass Spectrometry

Mass spectrometry measurements and all corresponding data analyses were carried out by Angelika Schierhorn from the *Serviceeinheit für Massenspektrometrie* at the University of Halle (see Ch. 5.3.5, p. 130). Accessible information comprises the purity, correct amino acid sequence, molecular weight, as well as the glycosylation pattern. The results of the nanoLC-ESI-MS/MS, i.e. tryptic and Asp-N-digest before and after PNGase F treatment, are shown in the Appendix. Likewise, original MALDI data before PNGase F treatment and after PNGase F treatment are also shown in the Appendix, see

Ch. A.2.2, pp. 185.

3.2.4.1. Purity

The high purity of HPRG purified by preparative gel electrophoresis could be confirmed by mass spectrometry. The results of nanoLC-ESI-MS/MS from the digest of lyophilized HPRG with trypsin, a serine protease, before PNGase F treatment were analyzed with the BiopharmaLynx software as stated in Ch. 5.3.5, p. 130. Fig. 3.43 shows the ESI-MS/MS results of these data and the respective matches. The contamination with rabbit serum albumin was only about 1 %.

nanoLC-ESI-MS/MS Result of the Lyophilized HPRG after Preparative Gel Electrophoresis (Tryptic Digest)

Accession	Entry	Description	mW (Da)	pI (pH)	PLGS Score	Peptides	Theoretical Peptides	Coverage (%)	Precursor RMS Mass Error (ppm)	Products	Modified Peptides	Products RMS Mass Error (ppm)	Products RMS RT Error (min)	Amount (fmol)	Amount (ngrams)
HRG_RABIT	Q28640	Histidine-rich glycoprotein (Fragment)	58840	7,23	21141	56	36	53,2319	1,5146	765	0	5,5339	0,019741	4499,55	268,2554
ALBU_RABIT	P49065	Serum albumin OS=Oryctolagus cuniculus	68865	5,8	1340	26	55	49,0132	0,8856	205	0	10,0398	0,026945	51,253	3,6341
A1AF_RABIT	P23035	Alpha-1-antitrypsin OS=Oryctolagus cuniculus	45838	5,81	156,9	7	28	21,0654	8,308	47	0	12,7009	0,026782	10,3	0,4742

Figure 3.43. – Purity of rabbit HPRG purified by preparative gel electrophoresis.

3.2.4.2. Amino Acid Sequence

As already stated in the introduction part of this work, the amino acid sequence of rabbit HPRG was first published in 1996 by Borza et al. [82]. However, Ronca and Raggi [89] published a new sequence based upon a prediction of the transcribed RNA sequence in 2015. When the results of the tryptic data (see Figs. A.28 and A.29, p. 185) were compared against both published sequences, the later published sequence showed a better match (51.7 % coverage (“old”) vs. 62.2 % (“new”) (see Fig. 3.44). Since the MS data were in better agreement with the sequence XP_008264798.1 published in 2015, the following MS results were interpreted with this more recent sequence.

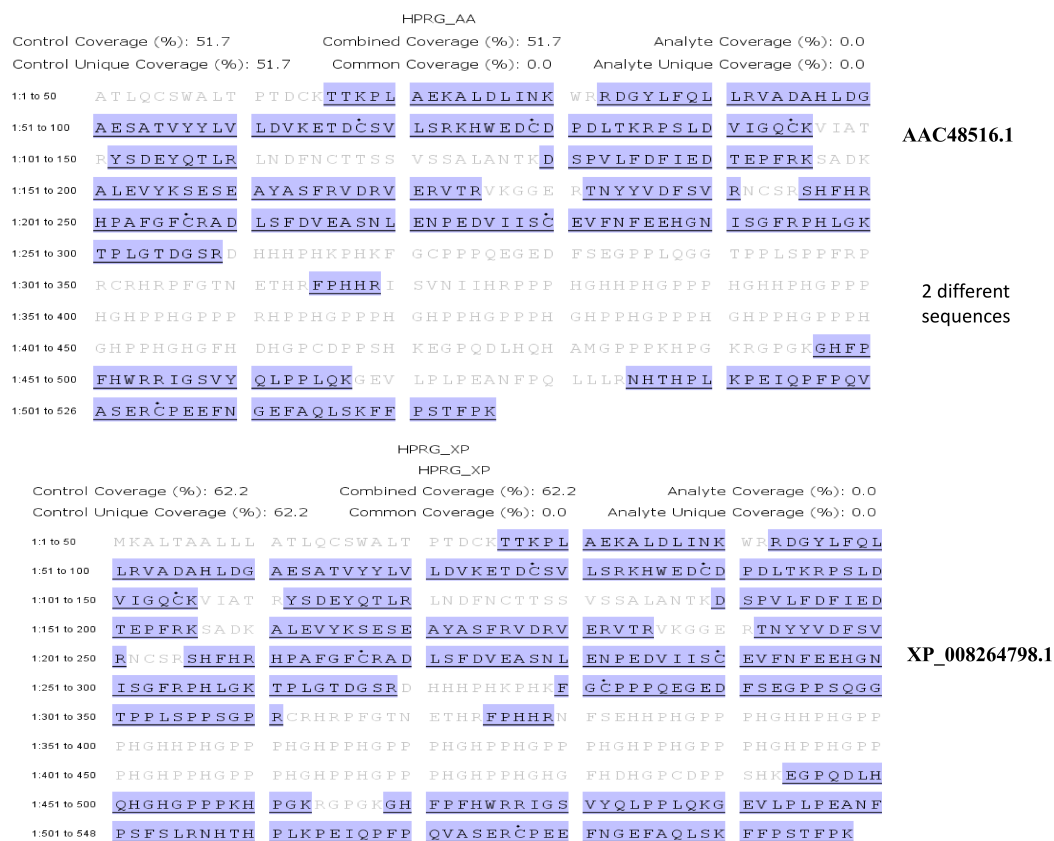


Figure 3.44. – Comparison of the coverage of the tryptic digest of both published rabbit HPRG sequences. Screenshot obtained from Ms. Schierhorn.

To obtain more information about the correct amino acid sequence, a further digest with Asp-N was carried out. Asp-N is a protease which cleaves peptide bonds at the N-terminal site of aspartic acid residues.

Furthermore, it was possible to remove the glycans of the glycoprotein HPRG via an enzymatic digestion with PNGase F. This enzyme effectively cleaves N-linked oligosaccharides between the innermost GlcNAc and asparagines. When the results of the tryptic and the Asp-N digests before PNGase F treatment, as well as after PNGase F treatment were combined, coverage with the XP_008264798.1 sequence was even higher (about 80 %), see Fig. 3.45.

MS data of the N-terminal peptides (amino acids 3-24 of the tryptic digest and 1-22 of the Asp-N digest) were missing. However, *de novo sequencing* of an unmatched peptide

with $m/z = 834.40$ led to the sequence $\text{LTPTDC}_{\text{mod}}\text{K}$, matching amino acids 19-25 of the HPRG sequence (see Fig. A.35, p. 194).

```

1  MKALTAALLL  ATLQCSWALT  PTDCYTKTKPL  AEKALDLINK  WRRDGYLFQL  LRVADAHLDG
61  AESATVYYLV  LDVKETDCSV  LSRKHWEDCD  PDLTKRPSLD  VIGQCKVIAT  RYSDEYQTLR
121 LDNFNCTTSS  VSSALANTKD  SPVLDFDIED  TEPFRKSADK  ALEVYKSESE  AYASFRVDRV
181 ERVTRVKGGE  RTNYVDFSV  RNCRSRSHFHR  HPAFGFCRAD  LSFVDEASNL  ENPEDVIISC
241 EVFNFEHGN  ISGFRPHLGK  TPLGTDGSRD  HHHPHKPHKF  GCPPPQEGED  FSEGPPSQGG
301 TPPLSPPSGP  RCRHRPFGTN  ETHRFPHHRN  FSEHHHPHGPP  PHGHHPHGPP  PHGHHPHGPP
361 PHGHPPHGPP  PHGHPPHGPP  PHGHPPHGPP  PHGHPPHGPP  PHGHPPHGPP  PHGHPPHGPP
421 PHGHPPHGHH  FHDHGPCDFP  SHKEGPQDLH  QHGHGPPPKH  PGKRGPGKGH  FPFHWRRIGS
481 VYQLPPLQKG  EVLPLPEANE  PSFSLRNHTH  PLKPEIQPF  QVASERCPEE  FNGEFAQLSK
541 FFPSTFPK

```

Figure 3.45. – HPRG total sequence coverage. Total sequence coverage (79.6%) of the new rabbit HPRG sequence. Results from the trypsin and Asp-N digest before/after PNGase F treatment were combined. Turquoise: matched amino acids. Yellow: *de novo* sequenced peptide.

It is not surprising that the first 18 amino acids of rabbit HPRG (Fig. 3.45) could not be observed. HPRG is a plasma protein and needs to be secreted accordingly. Therefore, the first 18 amino acids are likely to be a part of the N-terminal signal sequence that is necessary for secretion via the secretory pathway. This signal sequence is usually cleaved during transport.

The central HRR could also not be found in the MS data due to the many histidines and prolines. This part does not possess restriction sites for proteases.

3.2.4.3. Molecular Weight

To obtain information about the molecular weight of rabbit HPRG, MALDI-TOF MS was carried out. Measurements were conducted before and after PNGase F treatment, respectively. The corresponding results are shown in Fig. 3.46 and are consistent with the published molecular weights for HPRG of different mammalian species [79]. The native glycoprotein exhibits a mass of 73 kDa and a mass of 62 kDa after treatment with PNGase F. The weight increase upon glycosylation of the protein amounts to about 11 kDa (ca. 15% of the total molecular weight).

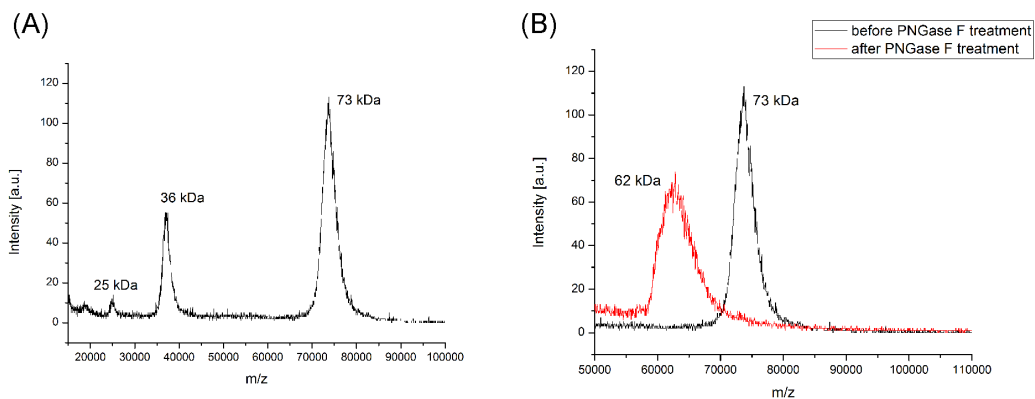


Figure 3.46. – MALDI-TOF MS spectra of purified rabbit HPRG. (A) MALDI-TOF MS spectrum of the purified rabbit HPRG before treatment with PNGase F. The purified protein has no major impurities. The peak at 73 kDa corresponds to the native glycoprotein. The peaks at 35 kDa and 25 kDa are the $[M+2H]^{2+}$ and $[M+2H]^{3+}$ ions. (B) MALDI-TOF MS spectrum of the purified rabbit HPRG before treatment with PNGase F (black) and after treatment with PNGase F (red).

3.2.4.4. Glycosylation Pattern

There are six theoretical N-linked glycosylation sites in the rabbit HPRG sequence. The respective motif of such a glycosylation is N-X-S/T, where X can be any amino acid except proline. These include: N-125, N-202, N-250, N-320, N-330, and N-507 as identified from the amino acid sequence of HPRG. When the nanoLC-ESI MS/MS results of the trypsin and Asp-N digests without PNGase F treatment were analyzed, glycopeptides of five of these glycosylation sites could be found. The only missing glycosylation site, N-330, belongs to the tryptic peptide 330-443 (MW 11883.5061 Da) and to the Asp-N peptide 290-432 (MW 15124.1251 Da). These were within the HRR, which was not detected in any of the digests at all.

The fragmentation of the glycopeptides was analyzed via ESI-MS/MS. Collision-induced fragmentation of glycopeptides mainly resulted in fragmentation of the sugar moieties, but not the peptide. The deglycosylated peptides were identified in the trypsin and Asp-N digests after PNGase F treatment (see Figs. A.31 and A.32, p. 190).

After deglycosylation with PNGase F the asparagine residue, to which the carbohydrate was attached, was changed to an aspartic acid residue (N/D-change). Thus, this site

could be identified as a glycosylation site. Moreover, a new cleavage site for Asp-N was created thereby. Therefore, in the Asp-N digest of the deglycosylated HPRG the new peptides 202-219 (MW 2243.9966 Da), 250-265 (MW 1694.9104 Da) and 250-269 (MW 2110.0918 Da) occurred.

For the N-glycosylation sites N-125, N-202, N-250, N-320 and N-507 no deglycosylated peptides were found in the trypsin and Asp- N digest without PNGase F treatment.

An example for the analysis of the glycan fragmentation of the HPRG glycopeptides during ESI-MS/MS is demonstrated in Fig. 3.47, where the fragmentation of the glycopeptide 507-526 NHTHPLKPEIQFPQVASER (glycosylation site N-507) is shown.

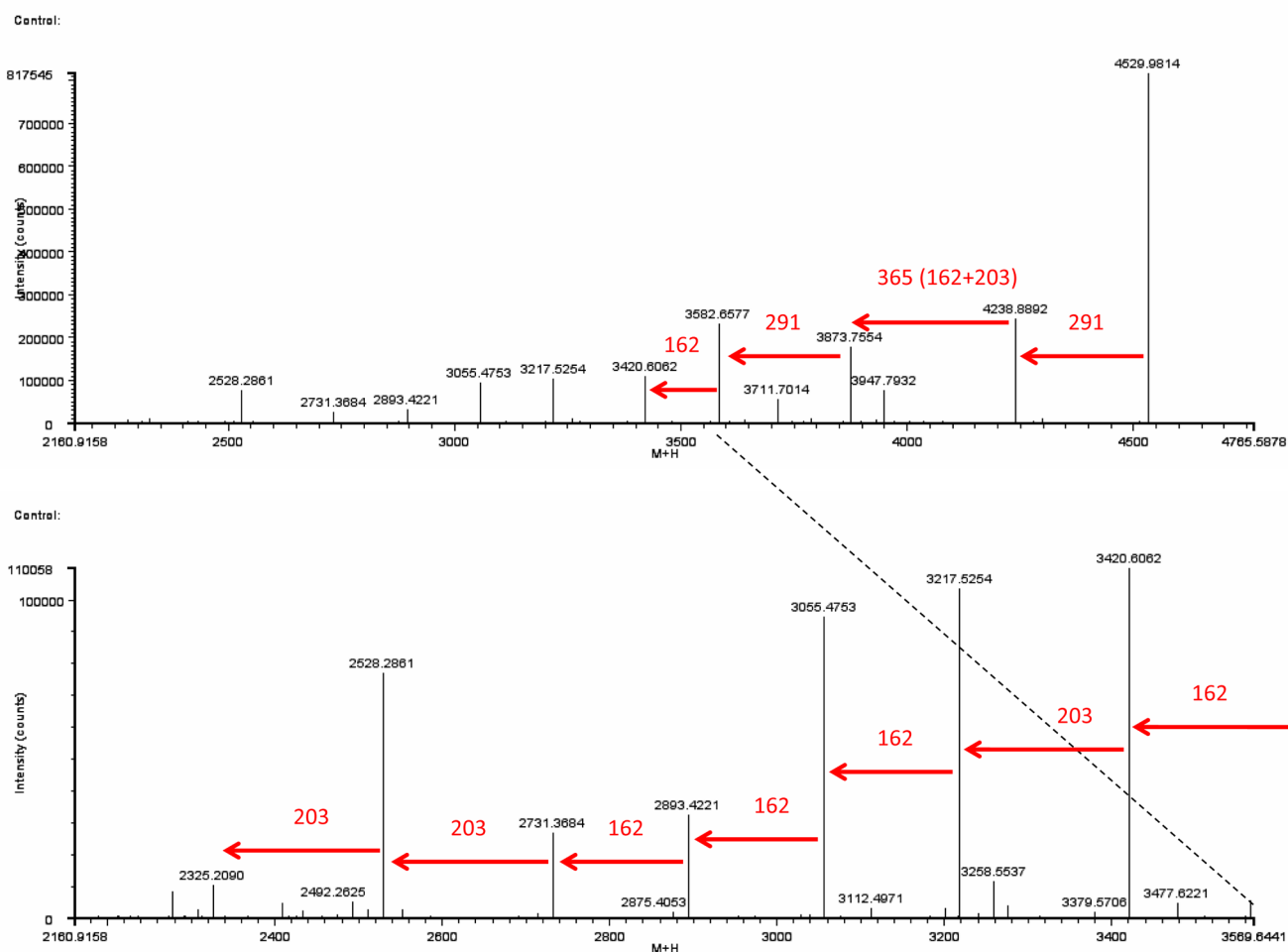


Figure 3.47. – Detail of the MS/MS-spectrum (deconvoluted to singly charged ions) of glycopeptide 507-526 NHTHPLKPEIQFPQVASER (trypsin digest) (glycosylation site N-507). The precursor ion m/z 4529.9814 was successively fragmented due to the loss of 2 NeuAc, 4 HexNAc and 5 Hex (glycan mass 2204.7724) Monosaccharid masses: NeuAc 291, HexNAc 203, Hex 162. Lower trace: Magnification of the range m/z 2160.9158-3569.6441 for a better comparison.

The peptide was found with a charge state of +4 ($m/z = 1133.2515$) and a retention time of 17.3 min. The MS/MS-spectrum was deconvoluted to singly charged ions. The precursor ion 4529.9814 ($[M+H]^+$) was successively fragmented due to the loss of NeuAc (291), followed by HexNAc (203) plus Hex (162), and again NeuAc (291). The glycan composition with 2 NeuAc, 4 HexNAc and 5 Hex ($m/z = 2204.7724$) indicates a complex type of N-linked glycan with a biantennary structure (Fig. 3.48). The difference between the measured mass of the glycopeptide and the mass of the glycan was 2324.1976 Da, which is in agreement with the molecular weight of the peptide 507-526, seen as a small singly charged fragment ion ($m/z = 2325.2346$) in the data.

This peptide could also be found with an additional triantennary glycan ($m/z = 2861.0$) at 17.7 min retention time and a molecular weight of 5185.2119 Da. The glycosylation sites N-250 and N-320 also possess these two complex glycan structures. The glycopeptides with triantennary N-glycan forms have increased retention times (0.3-0.4 min difference). The third negatively-charged NeuAc leads to tighter binding to the reversed phase material [156]. The proposed glycan structures mentioned above are shown schematically in Fig. 3.48.

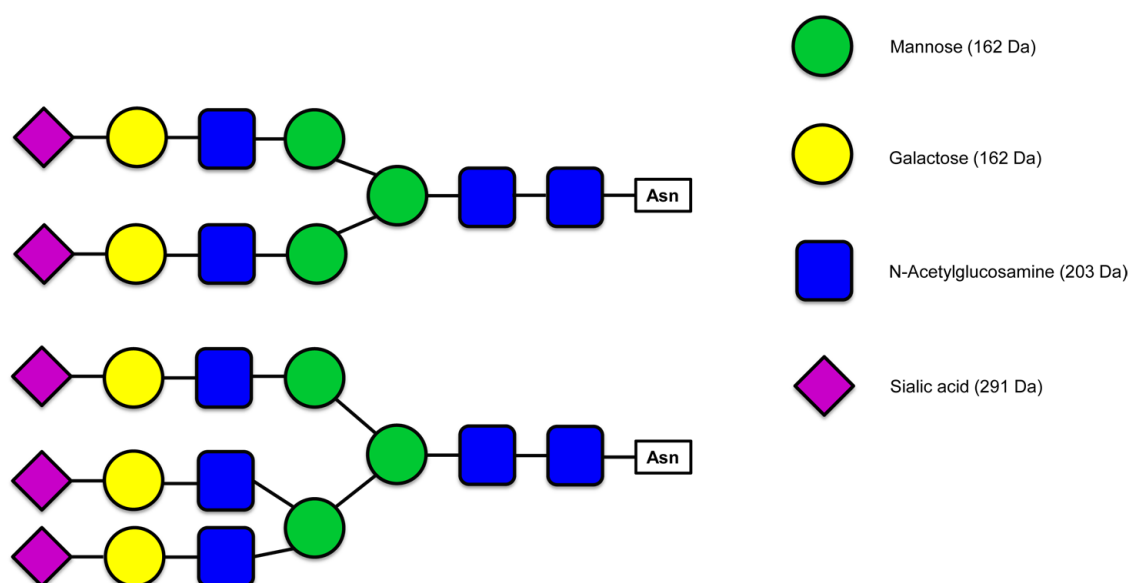


Figure 3.48. – Possible structures of the complex N-glycans of rabbit HPRG. Glycan symbols are according to the Essentials of Glycobiology/Consortium of Functional Glycomics [157].

The MS/MS spectra of the other glycopeptides can be found in the Appendix, see Figs. A.36 - A.40, pp. 194. A summary of all identified glycopeptides is shown in Tab. 3.19.

Glyco site	Digest	Glycan Composition	Start	End	Modification	RT (min)	Intensity (Counts)	Sequence	Observed GP Mass (Da)	Theoretical GP Mass (Da)	Error (ppm)
N-125	Trypsin	2*(NeuAc),4*(HexNac),5*(Hex)	121	139	CarbamidomethylC(1)	18.9	436622	LNDFN CTTSSVSSALANTK	4233.7261	4233.7146	-2.72
N-125	Asp-N	2*(NeuAc),4*(HexNac),5*(Hex)	123	139	CarbamidomethylC(1)	18.2	643631	DFN CTTSSVSSALANTK	4006.5920	4006.5876	-1.10
N-202	Asp-N	2*(NeuAc),4*(HexNac),5*(Hex)	197	219	CarbamidomethylC(2)	15.4	42206	DFSVRN CSRSFHRHHPAFGCRA	5052.0918	5052.0818	-1.98
N-250	Asp-N	3*(NeuAc),5*(HexNac),5*(Hex)	235	265	CarbamidomethylC(1)	22.1	19285	DVIISCEVFNFEHGN ISGFRPHLGKTPPLGT	6330.7212	6330.7088	-1.96
N-250	Asp-N	2*(NeuAc),4*(HexNac),5*(Hex)	235	269	CarbamidomethylC(1)	21.0	715358	DVIISCEVFNFEHGN ISGFRPHLGKTPPLGTDGSR	6089.6777	6089.6628	-2.45
N-250	Asp-N	2*(NeuAc),4*(HexNac),6*(Hex)	235	265	CarbamidomethylC(1)	21.8	284361	DVIISCEVFNFEHGN ISGFRPHLGKTPPLGT	5674.4956	5674.4812	-2.54
N-320	Trypsin	3*(NeuAc),5*(HexNac),6*(Hex)	314	324		12.6	148846	HRPFGTNETHR	4211.6631	4211.6541	-2.14
N-320	Trypsin	2*(NeuAc),4*(HexNac),5*(Hex)	314	324		12.3	897180	HRPFGTNETHR	3555.4302	3555.4265	-1.04
N-507	Trypsin	3*(NeuAc),5*(HexNac),6*(Hex)	507	526		17.7	346476	NHHTPLKPEI QPPFQVASER	5185.2119	5185.2026	-1.79
N-507	Trypsin	2*(NeuAc),4*(HexNac),5*(Hex)	507	526		17.3	2017335	NHHTPLKPEI QPPFQVASER	4528.9741	4528.9750	0.20

Table 3.19. – N-glycosylation mapping of rabbit HPRG obtained by nanoLC-ESI MS/MS.

3.2.5. CD Spectroscopy

In order to obtain information about the secondary structure of the lyophilized HPRG reconstituted in buffer, CD spectroscopy has been carried out (see Ch. 5.3.6, p. 132). Many buffer compounds (e.g. phosphate and Cl⁻ ions) strongly absorb light with shorter wavelengths. Therefore, the CD measurement was not carried out in PBS buffer, but in 10 mM phosphate, 50 mM NaCl at pH 7.4. With this buffer composition, the CD spectrum of HPRG could be obtained in the range of a range of 190 nm-250 nm.

The respective CD data were analyzed via the Dichroweb Tool [158, 159]. Fig. 3.49 shows the experimental CD spectrum of 0.69 mg/ml HPRG in a 0.1 mm cuvette. The concentration was obtained via Eq. 5.5, p. 122. Using the recently published amino acid sequence XP_008264798.1 (as explained in the previous chapter) an ϵ_{280} -value of $32150 M^{-1} cm^{-1}$ was calculated for rabbit HPRG.

The best fit was obtained when the CD spectrum was analyzed with the CONTIN algorithm [160, 161] in comparison to the reference data set 7 [162, 163]. The closest matching solution gave a content of 15.4 % α -helix, 24.1 % β -sheet, 18.4 % turns, and 42.1 % unordered structure. These results resemble of what is known about the protein having large amounts of disordered central regions, but ordered structure especially

in the N-terminal cystatin-like domain. Due to the non-reducing conditions during preparative gel electrophoresis, the disulfide bridges were kept intact and the overall structure of the protein can be considered to be preserved.

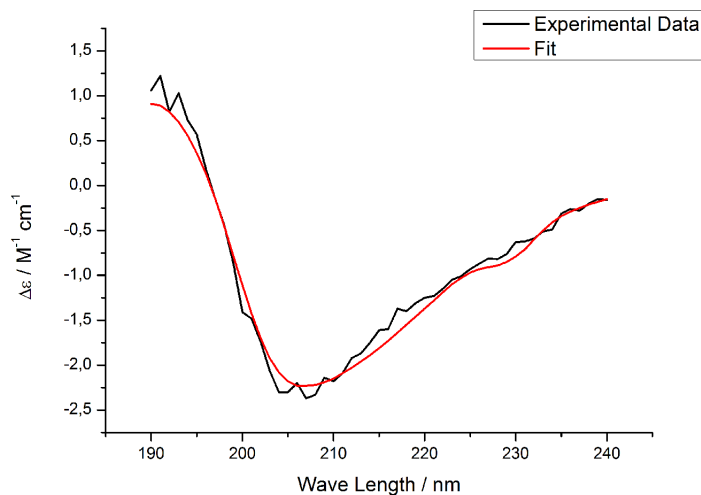


Figure 3.49. – Measured CD spectrum (black) and CONTIN Fit (red) [160, 161] in comparison to reference data set 7 [162, 163] of 0.69 mg/ml rabbit HPRG in 10 mM phosphate, 50 mM NaCl, pH 7.4 in a 0.1 mm cuvette. $\Delta\epsilon$ was calculated according to the recently published amino acid sequence XP_008264798.1. Thus the protein consists of 530 amino acid residues. With a molecular weight of 73 kDa, the mean residue weight is 138 Da.

The CD results also correspond well to the already published CD data of human HPRG [130]. However, the content of 3/10-helices or Poly-Pro-II helical structures could not be determined. To guarantee a proper analysis of 3/10-helices or Poly-Pro-II helices, CD data down to 176 nm are needed, which could not be obtained because the buffer also absorbs strongly at such low wavelengths. Measurements in the range of such low wavelengths would have led to increasing dynode voltage and correspondingly very poor signal to noise ratio. In this regard, reliable analyses of the data is not guaranteed.

4. Conclusion and Outlook

4.1. α -Synuclein

The membrane-bound state of α -Synuclein was examined by means of different EPR techniques and film balance measurements.

Initial EPR measurements with negatively charged POPG liposomes were in agreement with already published NMR data [67]. The N-terminal region of the protein (approximately amino acids 1–95) is bound to the liposome, whereas the C-terminal domain does not bind and remains unstructured in solution. The obtained data correspond well to the postulated horseshoe structure, where the two α -helices are connected by a linker around amino acids 38–44. Both helices seem to possess a different binding affinity, which can be explained by electrostatic interactions. The first helix consists of more cationic residues and thus the interaction with the negatively charged lipid is stronger [72]. Interestingly, the labeling position 41 showed a variability throughout the EPR measurements, which may be due to this position being a part of the, probably flexible, linker region of the horseshoe structure.

Additional CW-EPR measurements were conducted to assess the influence of 20% glycerol, which was needed as a cryoprotectant for the X-band Pulse-EPR measurements at a temperature of 50 K. This test was mainly conducted because glycerol led especially in Q-band CW-EPR to considerably broader peaks. Upon removal of glycerol, the labeling positions within the first helix were still strongly bound to the liposome, whereas the positions within the second helix consisted of much freely rotating components. Glycerol is a rather viscous liquid and thus it is to be assumed that it slows the rotation of the spin label in solution. Interestingly, labeling position 41 seems to be the only one that is not strongly affected by the removal of glycerol. Most strongly affected are the labeling positions of the second helix, which all show similar τ_c -values. Thus upon

removal of 20 % glycerol the contrast of τ_c is intensified and thus a better comparison is possible.

Film balance measurements were carried out to assess the affinity of α -Synuclein to different membrane monolayers. As expected, interaction was the strongest with negatively charged lipids like POPG, POPS, and Brain PS. Since α -Synuclein is assumed to interact with synaptic vesicles, a composition based upon Takamori et al. [141] was also tested. With just 7 mol-% Brain PS, the interaction became very weak. Thus if α -Synuclein interacts with synaptic vesicles it is likely that also this interaction is very weak. Synaptic vesicles possess also a high content (about 45 mol-%) of cholesterol. A more recent publication indicated that cholesterol blocks the spontaneous insertion of a protein to vesicles and therefore cholesterol interacts as a regulator, which might explain the weak interaction of α -Synuclein with this monolayer. It is likely that the insertion of proteins into membranes needs to be regulated to avoid negative effects.

The influence of a small molecule (Ligand X) of therapeutic interest, which could be a medical treatment for neurodegenerative diseases in the future, was also assessed by EPR measurements. Different concentrations of this ligand were added in the range from equimolar with respect to α -Synuclein (0.2 mM) down to 0.01 mM and compared to the measurement without the ligand. A very interesting finding was that the ligand led to the most drastic changes when it was added in very low concentration of 0.05 mM and 0.01 mM, respectively. This was surprising because one expects such strong effects when the concentration is higher. Moreover the labeling position, which were affected the most, are located in regions interacting strongly with the membrane (position 19, 53, and 80). Here, the ligand seems to compact the α -Synuclein monomers on the membrane, which can be seen in higher modulation depths and closer distances in 4p-DEER measurements.

Labeling position 41, which is located within the flexible linker region of the horseshoe structure and position 104, which is near, or probably already a part of the C-terminal domain, showed also some flexibility in this measurements.

No significant influence of the ligand was observed in film balance measurements to POPG and SV monolayers, indicating that the affinity of α -Synuclein to the membrane is not affected.

EPR measurements on vesicles that resemble synaptic vesicles have not been carried

out. Due to the small diameter of 40-50 nm and a high content of cholesterol, these vesicles are likely to be relatively unstable because of the strong curvature. Besides, corresponding measurements of the collaboration partner were also conducted on POPG liposomes with 100 nm.

4.2. HPRG

The purification of HPRG from rabbit serum according to more recent publications based upon metal chelate affinity chromatography followed by size exclusion chromatography or anion exchange chromatography, respectively, could not successfully be conducted [87, 130, 164]. A main problem was that also serum albumin was eluted of the metal chelate affinity chromatography column. Serum albumin could not successfully be separated from HPRG via the above stated chromatographic methods.

As it was noticed that the two proteins were separated during gel electrophoresis, a preparative gel electrophoresis method was carried out based upon Hauer et al. [152]. This was mainly due to the electrophoretic conditions used here, i.e. non-reducing, to avoid reducing the disulfide-bonds of HPRG. The migration of serum albumin is affected strongly depending on the electrophoretic conditions, whereas HPRG seems to be not affected at all.

When the preparative gel electrophoresis and subsequent electro-elution were carried out, especially the latter, did not work without the use of SDS. However during the sample preparation for electrophoresis no thermic denaturation was carried out in this work to avoid a possible complete denaturation of the protein. Besides, glycoproteins are not that strongly loaded with SDS as unglycosylated proteins. It was possible to obtain HPRG in high purity (only 1 % serum albumin impurity) as determined by mass spectrometry. However the use of SDS has to be kept in mind for further studies.

When the publication of the HPRG purification via preparative gel electrophoresis [164] was in review, another publication of the purification of the rabbit HPRG was published by Colwell et al. [165]. They also purified rabbit HPRG according to Patel et al. [130] and also found impurities after anion exchange chromatography. It is emphasized that Patel et al. purified HPRG from human serum or plasma, thus it might have worked for the human HPRG, however in the case of rabbit HPRG, this technique can not successfully

be applied. Colwell et al. stated that their preparation was more pure when a 25-50 % saturated ammonium sulfate precipitation is carried out. However, analysis was only conducted with SDS-PAGE.

An outlook for the further optimization of the purification of rabbit HPRG is to check whether a precipitation with saturated ammonium sulfate works and especially to carry out mass spectrometry measurements to compare the data of this work and the data of the precipitation step.

Further work with the purified rabbit HPRG are likely to be EPR measurements with the spin probing technique because the protein can not be labeled due to the disulfide bonds. Interesting EPR-active ligands would be Cu^{2+} and Cu(II)-Protoporphyrin IX as it is the copper-analogue of heme. Further ligands to check may be spin-labeled fatty acids because the protein is assumed to interact with phosphatidic acid [88].

Preliminary EPR measurements have been carried out by Selgar Henkel on peptides based on the HRR, and the two PRRs of rabbit HPRG [166]. However, these were based on the amino acid sequence as published in 1996 [82] and were obtained just prior to the publication by Ronca and Raggi [89]. It would be of big interest to generate peptides based on the recent published amino acid sequence and compare results of ligand measurements with those obtained for the full length protein.

5. Material and Methods

5.1. Materials

5.1.1. Chemicals

The chemicals used in this work were purchased from the following manufacturers:

Acetic acid	Sigma-Aldrich, St. Louis, USA
Acetonitrile (HPLC gradient grade)	Sigma-Aldrich, St. Louis, USA
Acrylamide Rotiphorese Gel 30 (37.5:1)	Carl Roth, Karlsruhe, Germany
Ammonium persulfat (APS)	AppliChem, Darmstadt, Germany
Bromophenol blue	AppliChem, Darmstadt, Germany
Chloroform (HPLC-grade)	Carl Roth, Karlsruhe, Germany
Disodium phosphate (p.a.)	Carl Roth, Karlsruhe, Germany
Dithiothreitol (DTT)	AppliChem, Darmstadt, Germany
Glycerol (86-88 % aqueous solution, p.a.)	Acros Organics, Geel, Belgium
Glycine	Carl Roth, Karlsruhe, Germany
Helium Lasal 4	Air Liquide, Paris, France
Hellmanex III	Hellma, Müllheim, Germany
Hydrochlorid acid (1M solution)	Fisher Scientific, Schwerte, Germany
Imidazole	Carl Roth, Karlsruhe, Germany
Isopropanol	Carl Roth, Karlsruhe, Germany
Isopentane ($\leq 99\%$)	Carl Roth, Karlsruhe, Germany
Methanol (HPLC-grade)	Carl Roth, Karlsruhe, Germany
Potassium chloride (p.a.)	Carl Roth, Karlsruhe, Germany
Potassium dihydrogen phosphate (p.a.)	Carl Roth, Karlsruhe, Germany
RotiBlue	Carl Roth, Karlsruhe, Germany

Sodium chloride (p.a.)	Carl Roth, Karlsruhe, Germany
Sodium dihydrogen phosphate (p.a.)	Carl Roth, Karlsruhe, Germany
Sodium dodecyl sulfate (SDS)	Carl Roth, Karlsruhe, Germany
Sodium hydroxide (1M solution)	Fisher Scientific, Schwerte, Germany
TEMED	AppliChem, Darmstadt, Germany
Trifluoroacetic acid	Sigma-Aldrich, St. Louis, USA
Tris	Carl Roth, Karlsruhe, Germany
Zinc sulfate heptahydrate	Carl Roth, Karlsruhe, Germany

5.1.2. Biological Reagents

For the purification of rabbit HPRG, preservative free rabbit serum (C12SBZ) was obtained from Bio-Rad AbD Serotec (Bio-Rad, Hercules, USA).

For minimizing proteolytic degradation during purification of rabbit HPRG via metal chelate affinity chromatography, a protease inhibitor was added (Inhibitor Cocktail Tissue, Carl Roth, Karlsruhe, Germany) according to the manufacturer's instructions.

Cobalt Affinity Chromatography was carried out with PureCube Co-NTA Agarose (Cube Biotech, Monheim, Germany).

5.1.3. Phospholipids

For film balance measurements the phospholipid 1-palmitoyl-2-oleoyl-*sn*-glycero-3-phosphoglycerol (POPG) was purchased from Genzyme Pharmaceuticals (Liestal, Switzerland). 1-palmitoyl-2-oleoyl-*sn*-glycero-3-phosphatidylserine (POPS) and the brain lipids from porcine brain (PC, PE, PS, SM) were purchased from Avanti Polar Lipids (Alabaster, USA). Cholesterol was purchased from Genzyme Pharmaceuticals (Liestal, Switzerland).

The respective phospholipids were prepared in HPLC-grade chloroform and methanol solutions.

5.1.4. Reagents and Buffer Compositions

Buffer / Reagent	Composition
20 mM phosphate (α -Synuclein)	5.2 mmol NaH ₂ PO ₄ 14.7 mmol Na ₂ HPO ₄ 100 mmol NaCl ad 1000 ml H ₂ O _{dd} pH 7.4
PBS buffer (HPRG)	8.0 g NaCl 0.2 g KCl 1.78 g Na ₂ HPO ₄ · H ₂ O 0.27 g KH ₂ PO ₄ ad 1000 ml
10x SDS-PAGE Running Buffer	250 mM Tris 1 920 mM Glycin 1 % (w/v) SDS
4x SDS-PAGE Sample Buffer	500 mM Tris 10 % (w/v) SDS 30 % (v/v) Glycerol (40 mM DTT) pH 6.8 10-15 drops of 0.1 % bromophenol blue
SDS-PAGE Stacking Gel Buffer	1 g SDS 15.5 g Tris ad 250 ml H ₂ O _{dd} pH 6.8
SDS-PAGE Separating Gel Buffer	1 g SDS 45.5 g Tris ad 250 ml H ₂ O _{dd} pH 8.8

SDS-PAGE Fixing Solution	40 % Methanol (400 ml) 10 % Acetic acid (100 ml) 500 ml H ₂ O _{dd}
Cobalt Affinity Chromatography Washing Buffer 1	50 mM NaH ₂ PO ₄ 50 mM NaCl 20 mM Imidazole pH 7.4
Cobalt Affinity Chromatography Washing Buffer 2	50 mM NaH ₂ PO ₄ 500 mM NaCl 80 mM Imidazole pH 7.4
Cobalt Affinity Chromatography Washing Buffer 3	50 mM NaH ₂ PO ₄ 150 mM NaCl 80 mM Imidazole pH 7.4
Cobalt Affinity Chromatography Elution Buffer	50 mM NaH ₂ PO ₄ 150 mM NaCl 500 mM Imidazole
SDS-Imidazole solution for Protein Staining	200 mM Imidazole 0.1 % (w/v) SDS
Electro-Elution Buffer	1X SDS-PAGE Running Buffer (40 ml) 2 % SDS (10 ml 10 % SDS)

Table 5.2. – Buffer compositions.

All buffers and samples were prepared in ultra-pure water (termed as H₂O_{dd} in this work). Ultra-pure water was obtained by the Milli-Q System (Merck Millipore, Darmstadt, Germany) and exhibited a conductivity of about 0.055 μ S/cm and a TOC (total organic carbon) value of about 4 ppm.

5.2. Methods (α -Synuclein)

5.2.1. Electron Paramagnetic Resonance

5.2.1.1. X-Band CW-EPR Spectroscopy

X-band CW-EPR spectroscopy was carried out on a benchtop spectrometer (MiniScope MS400, Magnettech GmbH, Berlin, Germany) at a frequency of about 9.43 GHz. The temperature was adjusted with the Temperature Controller H03 (Magnettech GmbH, Berlin, Germany). The exact frequency of the measurement was recorded by a frequency counter (Racal Dana, Model 2101, Neu-Isenburg, Germany). The experimental parameters of the measurement are listed in Tab. 5.3.

Experimental Parameters of X-band CW-EPR spectroscopy	
Center Field [G]	3360
Sweep Width [G]	120
Modulation Amplitude [G]	1
Microwave Attenuation [dB]	15
Sweep Time [s]	60
Scans	10

Table 5.3. – Experimental parameters of X-band CW-EPR spectroscopy on a benchtop X-band spectrometer.

5.2.1.2. Q-Band CW-EPR Spectroscopy

Q-band CW-EPR spectroscopy was carried out at a frequency of about 34 GHz with a Bruker EMX Plus spectrometer equipped with the magnet ER075, power supply ER083, ER05 SuperQ CW-EPR bridge, and the ER4123D CW-Resonator (Bruker, Karlsruhe, Germany). Spectra were recorded with the Xenon software provided by Bruker. The experimental parameters of the measurement are listed in Tab. 5.4.

Experimental Parameters of Q-band CW-EPR spectroscopy	
Center Field [G]	12140
Sweep Width [G]	200
Modulation Amplitude [G]	1
Modulation Frequency [kHz]	100
Microwave Attenuation [dB]	20
Conversion Time [ms]	20.50
Sweep Time [s]	41
Time Constant [ms]	5.12
Scans	20

Table 5.4. – Experimental parameters of Q-band CW-EPR spectroscopy.

5.2.1.3. Pulsed X-Band EPR Spectroscopy

Pulsed X-band EPR spectroscopy was carried out at a frequency of about 9.4 GHz with a Bruker Elexsys E580 spectrometer, equipped with a ER073 magnet, power supply ER081S, microwave bridge ESP 380-1010 and the MS3-ER4118K resonator (Bruker, Karlsruhe, Germany). Microwave pulses were amplified with a 1kW TWT Amplifier (Model 117, Applied Systems Engineering Inc., Fort Worth, USA) and applied pulses were visualized with the oscilloscope WaveJet 354 (Teledyne LeCroy, Chestnut Ridge, USA). The exact frequency was recorded with a frequency counter (model 5350B, Hewlett Packard Inc., Palo Alto, USA). The second microwave frequency necessary for DEER measurements was adjusted and fed into the systems with an oscilloscope (model OSC101-1012O and OSC101-1012P, Magnettech GmbH, Berlin, Germany).

Temperatures of 50 K were obtained with a closed-cycle cryostat consisting of a vacuum pump (model TMU-0710, Pfeiffer Vacuum Technology AG, Aßlar, Germany), a compressor (model ARS-4HW, Advanced Research Systems Inc., Macungie, USA) and a temperature controller (model 331, Lake Shore Cryotrics Inc., Carson, USA). The closed-cycle cryostat system was equipped with helium (Lasal 4, purity ≥ 99.996 Vol.-%, Air Liquide, Paris, France). Spectra were recorded with the Xep software provided by Bruker.

Pulsed X-band EPR measurements were carried out on stock-frozen solutions. These glass solutions are obtained from supercooling the respective protein sample in buffer and additional 20 % glycerol. In this vitrification process the sample is at first submerged in supercooled isopentane and then put into liquid nitrogen. Prior to vitrification the sample was filled in a 3 mm outer diameter quartz tube and put into the sample holder. After the vitrification process, the sample holder was put into the resonator at a temperature of 50 K in a helium reverse flow. The resonator was coupled to Q-values of about 200-300.

Prior to the 4p-DEER experiment an ESE spectrum was measured in order to obtain the respective field positions for the observer and the pump frequencies, respectively (see Fig. 1.11, p. 25). According to Fig. 1.10, p. 23 the $\pi/2$ -pulse was set to 16 ns, the π -pulse to 32 ns, τ was set to 200 ns.

For the 4p-DEER experiment the time t was varied, whereas $\tau_1 = 200$ ns and $\tau_2 = 1500$ ns were kept constant (see Fig. 1.11, p. 25). Note that for the measurement of α -Synuclein S129C a τ_2 of 2500 ns was used. The pulse length of the observer $\pi/2$ and π pulses

were set to 32 ns, the π pump pulse was set to 12 ns. Proton modulation was cancelled out by addition of eight time traces of variable τ_1 by starting with $\tau_1 = 200$ ns and then incrementing by $\Delta\tau_1 = 8$ ns. Usually 1000-1500 scans were averaged.

Data analysis of the DEER measurements was conducted with DEERAnalysis2015, which runs on MatLab [122].

5.2.1.4. Simulation of CW-EPR Spectra

The CW-EPR spectra obtained at X- and Q-band frequencies, respectively, were analyzed by spectral simulation with the EasySpin program package [167]. EasySpin is an open source package and runs on MatLab. Simulation of EPR spectra was carried out in a manual procedure with the implemented chili-function of EasySpin in the slow-motion regime which utilizes the stochastic Liouville equation for solving the Schrödinger equation [168]. The theory of slow-tumbling of nitroxides was developed by Schneider and Freed [169]. For the spectral simulations, the B-field offset was manually corrected in the respective simulation file.

The simulation parameters that can be extracted are the hyperfine splitting tensor \mathbf{A} , and the isotropic hyperfine splitting constant a_{iso} , as well as the diffusion tensor \mathbf{D} and the g -values to some extent (especially in Q-band CW-EPR measurements). g_{iso} can be extracted as follows:

$$g_{\text{iso}} = \frac{1}{3}(g_{xx} + g_{yy} + g_{zz}) . \quad (5.1)$$

The hyperfine splitting constant is calculated as follows:

$$a_{\text{iso}} = \frac{1}{3}(A_{xx} + A_{yy} + A_{zz}) . \quad (5.2)$$

The diffusion tensor \mathbf{D} is related to the rotational correlation time τ_c with the expression:

$$\tau_c = \frac{1}{6 \cdot \sqrt[3]{D_{xx} \cdot D_{yy} \cdot D_{zz}}} . \quad (5.3)$$

5.2.1.5. EPR Sample Preparation

0.24 mM α -Synuclein + 2 mM POPG in 20 mM Phosphate + 20 % (v/v) Glycerol						
	α -Syn. A19C	α -Syn. G41C	α -Syn. A53C	α -Syn. K80C	α -Syn. E104C	α -Syn. S129C
α -Synuclein Stock [mM]	0.8	0.76	0.5	0.8	0.8	0.47
Protein [μ l]	19.8	20.5	25.2	19.8	19.8	25.9
POPG (4 mg/ml stock) [μ l]	26.4	25.7	21.0	26.4	26.4	20.3
20 % Glycerol [μ l]	13.8	13.8	13.8	13.8	13.8	13.8

Table 5.5. – Pipetting scheme of 0.24 mM α -Synuclein + 2 mM POPG and additional 20 % (v/v) glycerol for the initial EPR measurements.

0.24 mM α -Synuclein + 2 mM POPG in 20 mM Phosphate w/o Glycerol						
	α -Syn. A19C	α -Syn. G41C	α -Syn. A53C	α -Syn. K80C	α -Syn. E104C	α -Syn. S129C
α -Synuclein Stock [mM]	0.8	0.76	0.5	0.52	0.8	0.47
Protein [μ l]	9.9	10.3	12.6	12.4	9.9	12.9
POPG (4 mg/ml stock) [μ l]	13.2	12.8	10.5	10.7	13.2	10.2
Buffer [μ l]	6.9	6.9	6.9	6.9	6.9	6.9

Table 5.6. – Pipetting scheme of 0.24 mM α -Synuclein + 2 mM POPG w/o glycerol for the initial EPR measurements.

The respective volumes of protein solution and POPG for the initial measurement of 0.24 mM α -Synuclein + 2 mM POPG had to be adjusted via the protein/POPG-ratio due to the low concentration of α -Synuclein S129C. The samples for the initial measurements were prepared according to Tables 5.5 and 5.6, respectively. After addition of all compounds, the sample tubes had been inverted and were allowed to incubate for about 30 min at RT.

For the EPR measurements with the Ligand X the sample concentration was changed to 0.2 mM α -Synuclein and 1.5 mM POPG (1.2 mg/ml in agreement with the collaboration partner (Research group of Prof. R. Konrat from University of Vienna)). Ligand X was received as a 20 mM stock solution in DMSO.

At first the protein, buffer, and the ligand were added to the sample tube. The tube was

then shaken on a thermomixer (4 °C, 300 rpm, Thermomixer C, Eppendorf, Hamburg, Germany) for about an hour to allow for proper mixing. Afterwards, the liposome as well as glycerol were added, the tube was inverted and allowed to incubate for about 30 min at RT.

0.2 mM α -Synuclein + 1.5 mM POPG + Ligand X (0.2 mM) in 20 mM Phosphate with 20 % (v/v) Glycerol					
	α -Syn. A19C	α -Syn. G41C	α -Syn. A53C	α -Syn. K80C	α -Syn. E104C
α -Synuclein Stock [mM]	0.8 / 0.82	0.76 / 1.0	0.5 / 1.1	0.8 / 0.52	0.8
Protein [μ l]	15.0 / 14.6	15.8 / 12.0	24.0 / 10.9	15.0 / 23.1	15.0
POPG (4 mg/ml stock) [μ l]	18.0	18.0	18.0	18.0	18.0
Ligand X [μ l]	0.6	0.6	0.6	0.6	0.6
Glycerol [μ l]	13.8	13.8	13.8	13.8	13.8
Buffer [μ l]	12.6 / 13.0	11.8 / 15.6	3.6 / 16.7	12.6 / 4.5	12.6

Table 5.7. – Pipetting scheme of 0.2 mM α -Synuclein + 1.5 mM POPG + 0.2 mM Ligand X.

0.2 mM α -Synuclein + 1.5 mM POPG + Ligand X (0.1 mM) in 20 mM Phosphate with 20 % (v/v) Glycerol					
	α -Syn. A19C	α -Syn. G41C	α -Syn. A53C	α -Syn. K80C	α -Syn. E104C
α -Synuclein Stock [mM]	0.8 / 0.82	0.76 / 1.0	0.5 / 1.1	0.8 / 0.52	0.8
Protein [μ l]	15.0 / 14.6	15.8 / 12.0	24.0 / 10.9	15.0 / 23.1	15.0
POPG (4 mg/ml stock) [μ l]	18.0	18.0	18.0	18.0	18.0
Ligand X [μ l]	0.3	0.3	0.3	0.3	0.3
Glycerol [μ l]	13.8	13.8	13.8	13.8	13.8
Buffer [μ l]	12.9 / 13.3	12.1 / 15.9	3.9 / 17.0	12.9 / 4.8	12.9

Table 5.8. – Pipetting scheme of 0.2 mM α -Synuclein + 1.5 mM POPG + 0.1 mM Ligand X.

0.2 mM α -Synuclein + 1.5 mM POPG + Ligand X (0.05 mM) in 20 mM Phosphate with 20 % (v/v) Glycerol					
	α -Syn. A19C	α -Syn. G41C	α -Syn. A53C	α -Syn. K80C	α -Syn. E104C
α -Synuclein Stock [mM]	0.8 / 0.82	0.76 / 1.0	0.5 / 1.1	0.8 / 0.52	0.8
Protein [μ l]	15.0 / 14.6	15.8 / 12.0	24.0 / 10.9	15.0 / 23.1	15.0
POPG (4 mg/ml stock) [μ l]	18.0	18.0	18.0	18.0	18.0
1 mM Ligand X [μ l]	3.0	3.0	3.0	3.0	3.0
Glycerol [μ l]	13.8	13.8	13.8	13.8	13.8
Buffer [μ l]	10.2 / 10.6	9.4 / 13.2	1.2 / 14.3	10.2 / 2.1	10.2

Table 5.9. – Pipetting scheme of 0.2 mM α -Synuclein + 1.5 mM POPG + 0.05 mM Ligand X.

0.2 mM α -Synuclein + 1.5 mM POPG + Ligand X (0.01 mM) in 20 mM Phosphate with 20 % (v/v) Glycerol					
	α -Syn. A19C	α -Syn. G41C	α -Syn. A53C	α -Syn. K80C	α -Syn. E104C
α -Synuclein Stock [mM]	0.8 / 0.82	0.76 / 1.0	0.5 / 1.1	0.8 / 0.52	0.8
Protein [μ l]	15.0 / 14.6	15.8 / 12.0	24.0 / 10.9	15.0 / 23.1	15.0
POPG (4 mg/ml stock) [μ l]	18.0	18.0	18.0	18.0	18.0
0.2 mM Ligand X [μ l]	3.0	3.0	3.0	3.0	3.0
Glycerol [μ l]	13.8	13.8	13.8	13.8	13.8
Buffer [μ l]	10.2 / 10.6	9.4 / 13.2	1.2 / 14.3	10.2 / 2.1	10.2

Table 5.10. – Pipetting scheme of 0.2 mM α -Synuclein + 1.5 mM POPG + 0.01 mM Ligand X.

The solution of 20 mM Ligand X in DMSO is diluted for the measurements of the low concentrations 0.01 mM and 0.05 mM to avoid pipetting very small volumes. For the first and the second series, dilution is conducted in the same solvent DMSO. In the third series, dilution is conducted in the buffer (20 mM phosphate, 100 mM NaCl, pH 7.4, see Tab. 5.2, p. 112). In all cases the ligand dilution is incubated on a thermomixer for about an hour.

5.2.2. Film Balance Measurements

5.2.2.1. Detection of Compression Isotherms

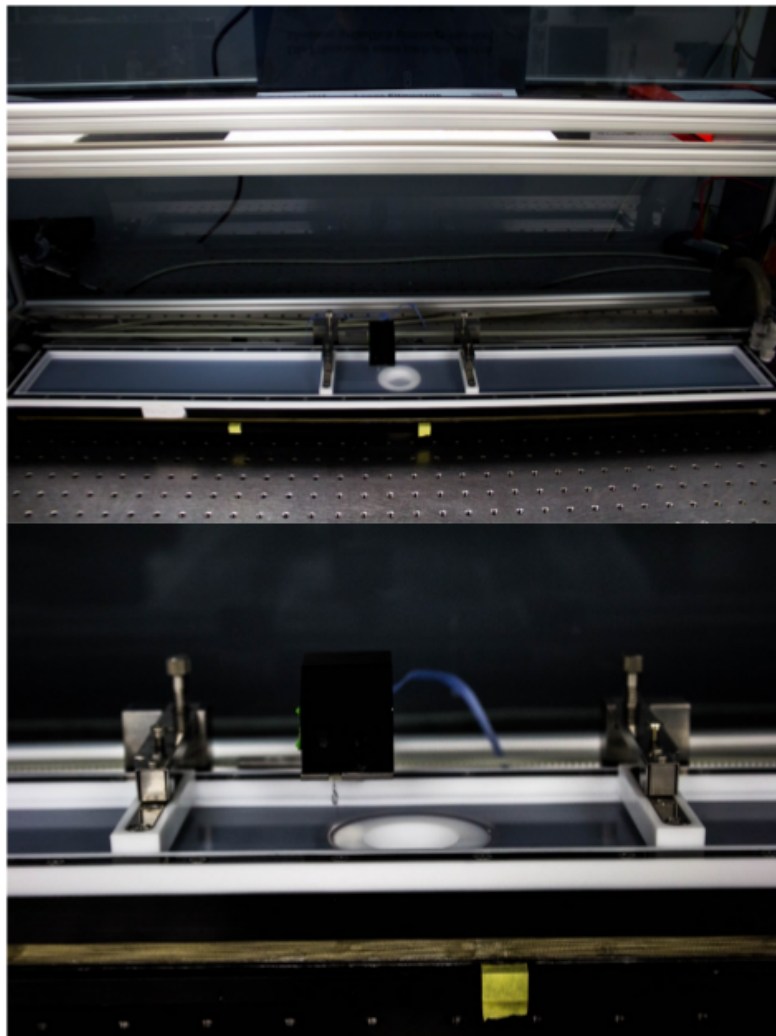


Figure 5.1. – Home-built Langmuir film trough for recording compression isotherms.

The compression isotherms of the phospholipids were recorded with a home-built Langmuir film trough (Riegler & Kirstein, Berlin, Germany), which is shown in Fig. 5.1. The isotherms could be measured by continuously decreasing the area between the two movable barriers. To maintain a steady temperature of the aqueous subphase, the trough was connected to a thermostat (Haake F3, Thermo Haake, Karlsruhe, Germany),

which was set to 20 °C throughout this work. Moreover, the trough was placed in a plastic hood that prevented perturbations of dust and also air draft. Surface pressures were measured by means of a Wilhelmy plate, which had to be calibrated to the surface pressure of water (72.8 mN/m) and air (0 mN/m) as reference points.

Prior to the measurement the trough was rinsed with ultra-pure water. If the water did not properly roll off from the Teflon trough, washing with a Hellmanex III solution had to be conducted. In this case it was necessary that the trough was rinsed at least seven times with ultra-pure water in order to completely remove the detergent.

For the measurement the trough was filled with buffer (α -Synuclein: 20 mM phosphate, 100 mM NaCl, pH 7.4) and adjusted to the optimal fluid level via the tip of a Hamilton syringe. The respective phospholipid in chloroform (and usually a bit methanol) was spread onto the aqueous subphase. The organic solvent was evaporated for about 10 minutes and the measurement was started with a compression speed of $2 \text{ \AA}^2 \text{ molecule}^{-1} \text{ min}^{-1}$. The software for the measurement was also provided by Riegler & Kirstein. Data from the compression isotherms were analyzed via the Origin 8.0 software (Origin Lab Corporation, Northampton, USA).

5.2.2.2. Detection of Adsorption Isotherms

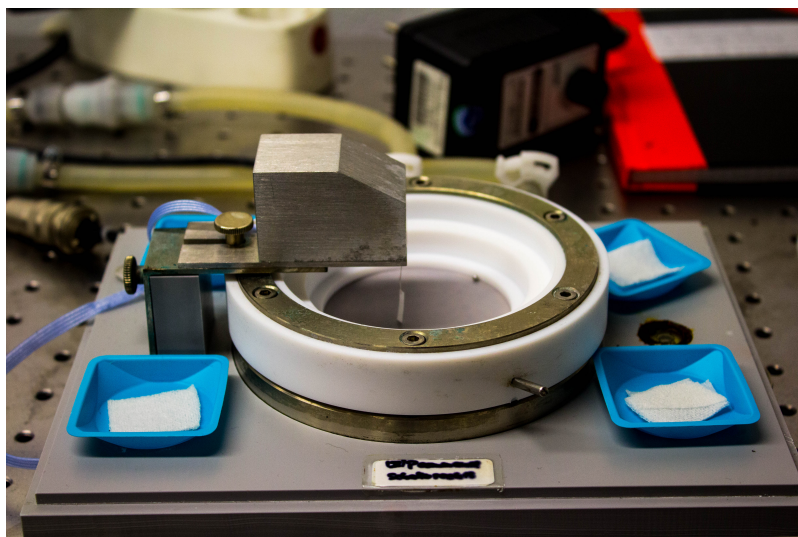


Figure 5.2. – Home-built Langmuir film trough for recording adsorption isotherms.

Adsorption isotherms were measured in a home-built Langmuir film trough (Riegler & Kirstein, Berlin, Germany), which is shown in Fig. 5.2. The dimensions of the trough were 6 cm in diameter and 0.3 cm in height. To maintain a steady temperature of the aqueous subphase, the trough was connected to a thermostat (Haake F6, Thermo Haake, Karlsruhe, Germany), which was set to 20 °C throughout this work. The trough was also placed in a plastic hood to prevent perturbations of dust and air draft. Since measurements usually run longer than those of the compression isotherms it was also important to guarantee that the humidity was constant. The latter was achieved by placing four small basins filled with water inside the plastic hood. During the measurement the aqueous subphase was stirred by using a magnetic stirrer underneath the trough, where in the trough itself a small metal orb was placed. The surface pressure was measured by means of a Wilhelmy plate, which had to be calibrated to the surface pressure of water (72.8 mN/m) and air (0 mN/m) as reference points.

For the measurement the trough was filled with buffer (α -Synuclein: 20 mM phosphate, 100 mM NaCl, pH 7.4) and adjusted to the optimal fluid level via the tip of a Hamilton syringe. The respective phospholipid in chloroform (+ usually a bit methanol) was spread onto the aqueous subphase to the desired surface pressure. After stabilization of the phospholipid monolayer (at least 30 min), α -Synuclein was injected through a channel at the side above the bottom of the trough. The desired trough concentration of α -Synuclein was 80 nM. When the measurement was finished, the trough had to be thoroughly cleaned with a Hellmanex III solution and rinsed with water at least seven times.

The adsorption isotherm was recorded by a software which was also provided by Riegler & Kirstein. Data of the adsorption isotherms were analyzed via the Origin 8.0 software (Origin Lab Corporation, Northampton, USA).

5.2.2.3. Preparation of Samples for the Ligand Measurements

In order to guarantee a proper mixing of α -Synuclein and Ligand X for the film balance adsorption experiments it was necessary to incubate the samples. To obtain a trough concentration of 20 nM and 80 nM for the ligand, respectively, it was necessary to dilute the 20 mM stock solution 100-fold in the α -Synuclein buffer. The solution was incubated for about 1 hour on a thermomixer at 4 °C.

For the 1:4 (Ligand:Protein) measurement, 1 μl of the 0.8 mM WT α -Synuclein stock was incubated with 1 μl of the prepared ligand dilution and 8 μl α -Synuclein buffer for 1 hour on a thermomixer at 4 °C.

The 1:1 (Ligand:Protein) measurement was prepared with 1 μl of the 0.8 mM WT α -Synuclein stock and 4 μl of the prepared ligand solution together with 5 μl α -Synuclein buffer and was also incubated for 1 hour on a thermomixer at 4 °C.

Finally, after 1 hour and when the already spread lipid film was stable, the incubated 10 μl samples were injected into the trough underneath the lipid monolayer.

5.3. Methods (HPRG)

5.3.1. Determination of Protein Concentration

5.3.1.1. UV/Vis-Spectroscopy

The concentration of a protein in solution can be determined via UV/Vis-spectroscopy at a wavelength of 280 nm. The aromatic amino acids tryptophan and tyrosine, as well as phenylalanine, absorb at this wavelength. Cystine also contributes to the absorption of a protein at a wavelength of 280 nm [170]. The maximum of absorption of tryptophan is at 279 nm and therefore contributes to most of the A_{280} -absorption. The absorption maxima of tyrosine and phenylalanine are located at 275 nm and 257 nm, respectively [110].

The absorption value is defined by the Lambert-Beer law:

$$A_{280} = \epsilon \cdot c \cdot d , \quad (5.4)$$

where ϵ is the molar absorption coefficient [$\text{M}^{-1}\text{cm}^{-1}$], c is the protein concentration [M], and d is the path length [cm]. If the amino acid sequence of a protein is available, ϵ can be calculated according to the relation [170]:

$$\epsilon_{280} = 5500 \cdot nW + 1490nY + 62.5 \cdot nC , \quad (5.5)$$

where W is the number of tryptophans, Y is the number of tyrosines, and C is the number of Cysteines.

Note that only cystines contribute to the absorption of a protein, i.e. disulfide bonds, so that only those cysteine residues have to be taken into account that form disulfide bonds in the calculation of ϵ .

The samples were measured in a precision cell (Hellma Suprasil Quartz cuvette, Sigma Aldrich, St. Louis, USA) at 280 nm (Agilent 8453 UV/Vis Spectroscopy System, Agilent Technologies, Santa Clara, USA).

5.3.1.2. BCA Assay

The bicinchoninic acid (BCA) assay is another method for determining the protein concentration of a solution. This assay is based upon a reduction of Cu^{2+} to Cu^+ by the peptide bonds of the protein and a subsequent formation of a chelate complex of two bicinchoninic acid molecules and one Cu^+ ion. The chelate complex is of purple color and has its absorption maximum at 562 nm. The quantification limit is between 0.1 - 1 $\mu\text{g}/\text{ml}$ [110].

The BCA assay was carried out with the *PierceTM BCA Protein Assay Kit* (Thermo Fisher, Scientific, Waltham, USA) according to the manufacturer's instructions. The standards and the protein samples were pipetted as follows:

BCA Assay: BSA Standards				
Standard Number	BSA Solution [μl] $c = 250 \mu\text{g}/\text{ml}$	$\text{H}_2\text{O}_{\text{dd}}$ [μl]	BCA [μl]	$\mu\text{g BSA}/\text{Sample}$
1 (Blank)	0	100	900	0
2	10	90	900	2.5
3	20	80	900	5.0
4	30	70	900	7.5
5	40	60	900	10.0
6	50	50	900	12.5
7	60	40	900	15.0
8	70	30	900	17.5

BCA Assay: Protein Samples			
Dilution	Protein Solution [μl]	$\text{H}_2\text{O}_{\text{dd}}$ [μl]	BCA [μl]
1:50	20	80	900
1:100	10	90	900
1:200	5	95	900

For larger dilution factors 5 μl protein solution + 95 μl $\text{H}_2\text{O}_{\text{dd}}$ was mixed, 50 μl of this sample were taken, diluted with another 50 μl $\text{H}_2\text{O}_{\text{dd}}$ + 900 μl BCA, yielding a 1:400 dilution.

A 1:1000 dilution was achieved by mixing 10 μl protein solution + 990 μl $\text{H}_2\text{O}_{\text{dd}}$, taking 100 μl of this sample + 900 μl BCA.

The samples were heated at 65 $^{\circ}\text{C}$ for 10 min. After cooling on ice they were subsequently measured at 562 nm (Agilent 8453 UV/Vis Spectroscopy System, Agilent Technologies, Santa Clara, USA).

5.3.2. Polyacrylamide Gel Electrophoresis

The Polyacrylamide Gel Electrophoresis (PAGE) is based upon the migration of charged molecules in an electric field. Depending on the net charge and different sizes of the respective molecules, a spatial separation can be obtained.

To separate protein mixtures, the SDS-PAGE (Sodium Dodecyl Sulfate-PAGE), as introduced by Laemmli [171], is widely used. It is a discontinuous electrophoretic technique and consists of two different gels: the stacking gel and the separating gel. In SDS-PAGE the protein samples are prepared in sample buffer, which contains the anionic detergent SDS. SDS covers the intrinsic charge of the protein and therefore the proteins are present as polyanions. The samples are heated to 95 $^{\circ}\text{C}$ so that the tertiary and the secondary structures are disrupted by loss of the hydrogen bonds. Furthermore, a reducing agent like β -Mercaptoethanol or dithiothreitol (DTT) can be added to reduce disulfide bonds. SDS-PAGE is often used to control the purity of a protein sample and/or estimation of the molecular weight of a protein. For the latter a molecular weight marker is additionally loaded onto the gel, which contains proteins with well-known sizes.

SDS-PAGE was carried out with the Mini-PROTEAN System and the PowerPac Basic Power Supply (Bio Rad, Hercules, USA). The compositions for a 12 % SDS-PAGE separating gel and a 4.5 % stacking gel are listed in the following table.

Gel Compositions (SDS-PAGE)		
	Separating Gel 12 %	Stacking Gel [μ l] 4.5 %
H ₂ O _{dd} [ml]	5.25	3
Separating Gel Buffer [ml]	3.75	0
Stacking Gel Buffer [ml]	0	1.25
Acrylamide 30 % [ml]	6	0.75
APS 10 % [μ l]	75	30
TEMED [μ l]	30	10

For SDS-PAGE the Protein Marker III (6.5 - 200 kDa) (AppliChem, Darmstadt, Germany) was used. The molecular masses of this marker are: 212, 118, 66, 45, 29, 20, 14, and 6.5 kDa. The voltage was set to 100-200 V for electrophoresis. After incubating the gel with SDS-PAGE fixing solution for about an hour, the gels were stained overnight with Coomassie Brilliant Blue G250 (RotiBlue, Carl Roth, Karlsruhe, Germany) staining solution.

5.3.3. Cobalt Affinity Chromatography

Rabbit HPRG was purified from preservative free rabbit serum (AbD Serotec, Bio Rad, Hercules, USA). To avoid multiple thawing and freezing cycles, aliquots were made.

For preventing proteolytic degradation, the cobalt affinity chromatography was carried out in a cold room at 4 °C. 10 ml of serum aliquots were thawed and then incubated with 1 ml of PureCube Co-NTA Agarose (Cube Biotech, Monheim, Germany). Unspecific binding to the column material was prevented by adding of 20 mM imidazole to this mixture. Further proteolytic degradation was inhibited by supplying this mixture with a protease inhibitor cocktail (Inhibitor cocktail tissue, Carl Roth, Germany) according to the manufacturer's instructions.

After incubation of one to two hours, the suspension was transferred onto a column and was washed sequentially with washing buffers 1-3. When no further protein was washed from the column, HPRG was eluted with 500 mM imidazole.

Elution fractions were analyzed via SDS-PAGE. HPRG-containing fractions were concentrated (10.000 or 30.000 MWCO, Amicon Ultra, Merck Millipore, Darmstadt, Germany) and the concentration was determined via a BCA assay.

5.3.4. Preparative Gel Electrophoresis

The gel chambers for preparative gel electrophoresis were custom-made. Glass plates with the dimension 20 x 20 cm and a thickness of 4 mm were used. Furthermore, glass plates with a notch of 16 x 2 cm and a thickness of 4 mm were used. The 1.5 mm spacer was of the dimension 20 x 1 x 0.15 cm. The separation gel was of the size of about 18 x 15 x 0.15 cm and the stacking gel was about 18 x 2 x 0.15 cm. The gel chamber is shown in Fig. 5.3.

The cathodic buffer tank is filled with ca. 500 ml 1x SDS-PAGE running buffer and the anodic tank with ca. 250 ml 1x SDS-PAGE running buffer. The whole apparatus for preparative gel electrophoresis is shown in Fig. 5.4. Sample slots can be generated with an inverted mounted comb. However, it is also possible (as is was done in this work) to overlay the poured stacking gel with a layer of isopropanol (as it is done after pouring the separation gel). But it is important to remove the isopropanol completely before the sample is loaded onto the stacking gel. The compositions for the separating and the stacking gel are listed in Tab. 5.11.

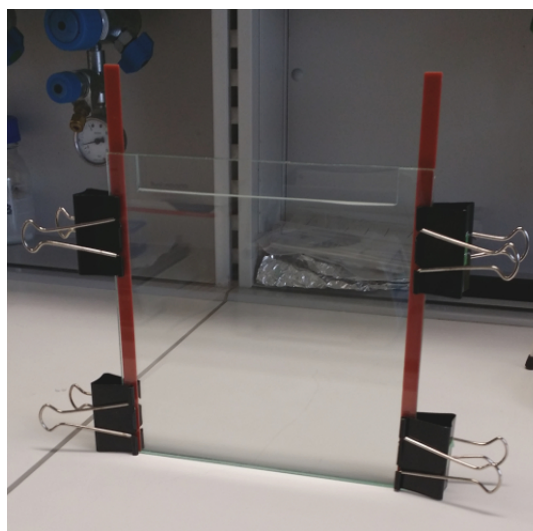


Figure 5.3. – Gel chamber for preparative gel electrophoresis.

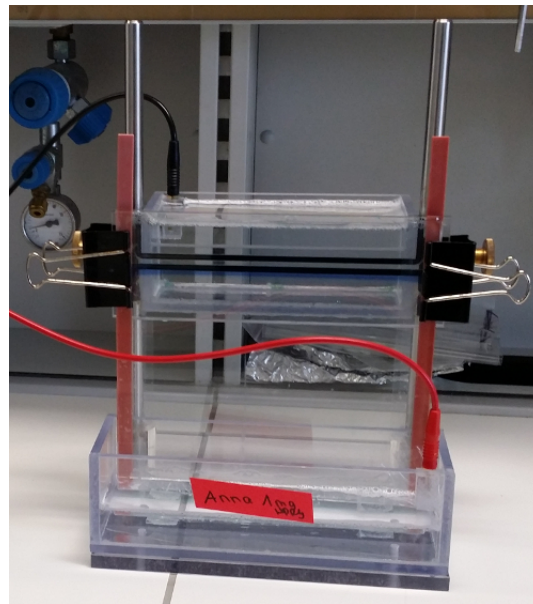


Figure 5.4. – Preparative gel electrophoresis apparatus. The upper cathodic tank and the lower anodic tank are filled with 1x SDS-PAGE running buffer.

Gel Compositions (Preparative Gel Electrophoresis)		
	Separating Gel 10 % (1.5 mm Spacer)	Stacking Gel [μ l] 4.5 % (1.5 mm Spacer)
H ₂ O _{dd} [ml]	19.5	10.425
2 M Tris, pH 8.8 [ml]	12.0	0
1 M Tris, pH 6.8 [ml]	0	1.875
Acrylamide 30 % [ml]	16.0	2.5
10 % SDS [μ l]	480	150
10 % APS [μ l]	225	75
TEMED [μ l]	22.5	7.5

Table 5.11. – Preparative gel composition. Calculation for different thicknesses, e.g. a 1 mm spacer can be conducted by dividing the respective volume of the 1.5 mm spacer by 1.5.

0.5-1.0 mg of HPRG from the concentrated cobalt affinity chromatography elution fraction was diluted in Laemmli sample buffer without any reducing agents. The thermic denaturation was also not carried out. Gels were run overnight at RT without further cooling at a constant voltage of 60-70 V (the current is about 30 mA in the beginning and about 8 mA when the run is complete). If the dye front has not completely migrated

to the anodic site the next morning, the voltage can be risen up to 200 V. About 1500 $V \cdot h$ are needed for the migration of the dye front to the anodic site. This means that if the current was set to 1500 V, the dye front would migrate to the anodic site within one hour. However, high voltages lead to an increase in temperature of the respective running buffer, so that the voltage should not be set to too high values.

The protein gel bands were visualized with non-fixing zinc-imidazole staining [153]. At first, the gel was shortly rinsed in H_2O_{dd} . After pouring out the water, the gel was incubated for 20 min with the SDS-imidazole solution for protein staining. Subsequent to removing this solution, the gel was incubated with 0.2 mM $ZnSO_4$ in H_2O_{dd} until all bands were visible (after about 30 s). The staining reaction was stopped by removing the zinc solution and the gel was shortly rinsed with H_2O_{dd} .

The band corresponding to HPRG was recovered and cut into small pieces. Afterwards, electro-elution was carried out in custom-made chambers, that correspond to the “bridge-type electro-eluter” [172]. They possess a Serva dialysis membrane with a molecular weight cut-off of 3.5 kDa (see Fig. 5.5).



Figure 5.5. – Electro-elution chamber. Gel slices are filled into the broad side of the chamber. The chamber is then filled with electro-elution buffer so that the whole chamber including the bridge is filled to guarantee a current flow.

The gel slices were placed in the broad part of the electro-elution chamber that was filled with electro-elution buffer on the cathodic site. It has to be taken care that the

bridge is also filled with buffer, otherwise there will be no current flow. The electro-elution running trough (Fig. 5.6) was filled with 1x SDS-PAGE running buffer and the electro-elution chambers were positioned so, that the protein was eluted to the anodic side.

Electro-elution was carried out on 70 V at RT overnight for about 15 hours. Afterwards, HPRG was collected from the anodic side of the chamber via a plain-tipped syringe to avoid causing damage to the membrane. The membrane was also washed a few times with buffer to remove residual protein. The purified protein was then stored at 4 °C.

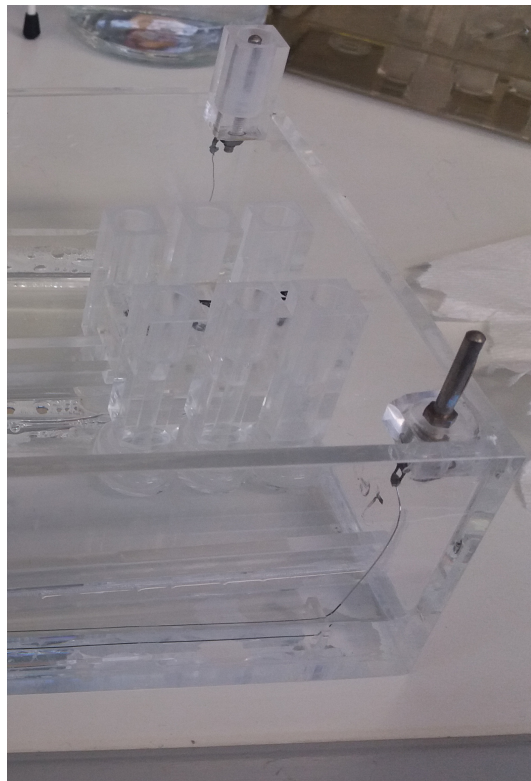


Figure 5.6. – Electro-elution apparatus. The electro-elution chambers are placed in a trough filled with 1x SDS-PAGE running buffer. Cables were connected so, that the protein was eluted to the anodic side.

To remove buffer salts and SDS from the electro-elution fractions, the protein was applied to a reversed-phase HPLC (column EC 125/4 Nucleosil 500-5 C3-PPN, Macherey & Nagel; flow rate 1 ml/min; detection wave length: 220 nm) and eluted with an acetonitrile-water gradient. Fractions were collected after 19 min. HPRG eluted at

about 23 – 24 min from the column. The fractions containing HPRG were lyophilized (Alpha 2-4 LD Plus, Martin Christ Gefriertrocknungsanlagen GmbH, Osterode am Harz, Germany). The applied acetonitrile-water gradient is shown in Tab. 5.12.

Acetonitrile-Water Gradient		
Time [min]	Solvent A [%]	Solvent B [%]
0 - 6	90.0	10.0
6 - 7	90.0-70.0	10.0-30.0
7 - 20	70.0-57.0	30.0-43.0
20 - 20.3	57.0-40.0	43.0-60.0
20.3 - 25.0	40.0	60.0
25.0 - 27.0	40.0-10.0	60.0-90.0
27.0 - 30.0	10.0	90.0
30.0 - 32.0	10.0-90.0	90.0-10.0
32.0 - 40.0	90.0	10.0

Table 5.12. – Acetonitrile-water gradient applied to the reversed phase HPLC to purify HPRG from buffer salts and SDS after preparative gel electrophoresis (solvent A: water + 0.05 % TFA; solvent B: acetonitrile + 0.05 % TFA). The sudden jump from 43 % to 60 % acetonitrile from 20.0 min to 20.3 min focuses the protein to few elution fractions.

5.3.5. Mass Spectrometry

Mass spectrometry was carried out by Ms. Angelika Schierhorn at the *Serviceeinheit für Massenspektrometrie* at the University of Halle.

For mass spectrometry analysis 50 µg of lyophilized HPRG were dissolved in 50 mM NH₄HCO₃ buffer and 0.1 % ProteaseMAXTM Surfactant (Promega, Madison, USA) was added according to the manufacturer's instructions. A small fraction of this preparation was used for determination of the molecular weight of HPRG by MALDI-MS.

To alkylate the cysteine residues, the protein was reduced with 0.5 M DTT (Sigma-Aldrich, St. Louis, USA) for 20 min at 56 °C. After incubation with 0.55 M iodoacetamide (Sigma-Aldrich, St. Louis, USA) for 15 min in the dark, an overnight incubation with trypsin (Promega, Madison, USA) and Asp-N (Promega, Madison, USA), respectively, was started.

To further analyze the protein regarding the glycosylation sites, the carbohydrates were removed in a parallel preparation via treatment with PNGase F (Promega, Madison,

USA) for 4 hours at 37°C. 0.1 % ProteaseMAX™ Surfactant was added according to the manufacturer's instructions. A small fraction of this preparation was again used for determination of the molecular weight by MALDI-MS.

This preparation of deglycosylated HPRG was also digested overnight with trypsin and Asp-N at RT, respectively.

For MALDI-TOF-MS analysis 1 µl of a solution of 2,5-dihydroxy-benzoic acid in methanol (7 mg/100 µl) was mixed with 1 µl protein solution. 1 µl of this mixture was deposited on a stainless steel target. The protein spectra were recorded with an Ultraflex-II TOF/TOF mass spectrometer (Bruker Daltonic, Bremen, Germany) equipped with MALDI source, nitrogen laser, LIFT cell for fragment ion post-acceleration and a gridless ion reflector. The software Flex Control 3.0, Flex Analysis 3.0 and Biotoools 3.0 were used to operate the instrument and analyze the data. For external calibration a protein calibration mixture was used (Bruker Daltonics, Bremen, Germany).

For ESI-QTOF-MS/MS measurements the peptide solution was injected into a nanoACQUITY UPLC system (Waters Co., Milford, USA) equipped with a binary solvent manager, sample manager, a heating and a trapping module. 2 µl were injected via "microliter pickup" mode and desalted on-line through a symmetry C18 180 µm x 20 mm precolumn. The peptides were separated on a 100 µm x 100 mm analytical RP column (1.7 µm BEH 130 C18, Waters Co., Milford, USA) using a typical UPLC gradient from 3.0 % to 33.0 % over 15 min. The respective mobile phases were 0.1 % formic acid in water and 0.1 % formic acid in acetonitrile. The column was connected to an SYNAPT® G2 HDMS-mass spectrometer (Waters Co., Milford, USA), which is a hybrid quadrupole tandem time-of-flight (Q-TOF) mass spectrometer, equipped with Tri-wave ion guides that trap and separate ions by ion mobility (Waters Co., Milford, USA). Data were acquired in LC/MS^E mode, switching between low and elevated energy on alternate scans. Subsequent correlation of precursor and product ions could be achieved upon using retention time alignment. BiopharmaLynx (1.3.2, Waters Co., Milford, USA) was used to analyze the obtained MS and MS/MS data. Proteomics researches were conducted with ProteinLynx GlobalSERVER™ using SwissProt database.

5.3.6. Circular Dichroism

Circular Dichroism (CD) is a technique to determine information about the secondary structure of a protein. CD is based upon the different absorption of left-handed and right-handed circularly polarized light by chiral molecules. The different secondary structural elements of a protein generate characteristic CD spectra. For example α -helical proteins have negative bands at 222 nm and 208 nm and a positive band at 193 nm [173, 174]. Proteins with (antiparallel) β -sheets have a negative band at 218 nm and a positive band at 195 nm. Disordered proteins (random coils) have a low ellipticity above 210 nm and a negative band near 195 nm (see Fig. 5.7) [173, 175, 176].

Thus, information about the secondary structure of a protein is found as the sum of the characteristic individual CD spectra from each type of secondary structure present in the protein [158]. There are several software and web tools available that utilize reference databases of CD spectra of proteins whose crystal structures are known. Therefore, an estimation of the content of secondary structures of the measured protein is possible. In this work, CD spectra were analyzed with the Dichroweb Tool [158, 159].

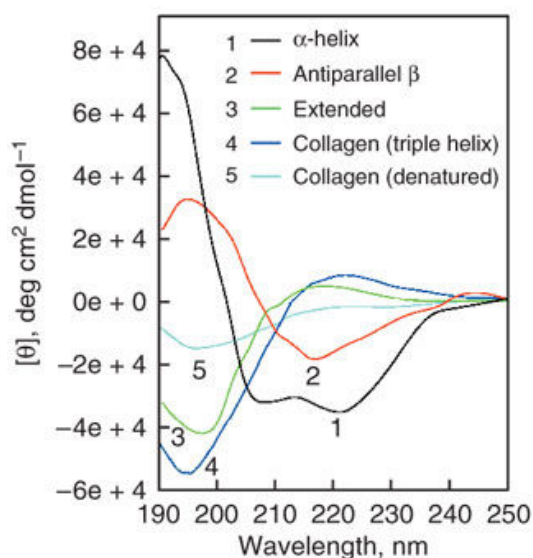


Figure 5.7. – Characteristic CD spectra of secondary structures. Taken from [173].

CD measurements were performed on a Jasco J-810 CD spectrometer (Jasco, Easton, USA) at 20 °C. The wavelength range was set to values where the dynode voltage did not exceed 600 V (190 – 250 nm). Measurements were carried out in 10 mM phosphate, 50

mM NaCl, pH 7.4) in a 0.1 mm cuvette, 60 scans were averaged. The sample volume was 50 μ l.

References

- [1] Emil Fischer. Einfluss der Configuration auf die Wirkung der Enzyme. *Ber. Dtsch. Chem. Ges.*, 27(3):2985–2993, 1894. doi: 10.1002/cber.18940270364.
- [2] D. E. Koshland. Application of a theory of enzyme specificity to protein synthesis. *PNAS*, 44(2):98–104, 1958.
- [3] Peter E. Wright and H. Jane Dyson. Intrinsically Unstructured Proteins: Re-assessing the Protein Structure-Function Paradigm. *J. Mol. Biol.*, 293(2):321–331, 1999. doi: 10.1006/jmbi.1999.3110.
- [4] A. Keith Dunker and Zoran Obradovic. The protein trinity—linking function and disorder. *Nat. Biotechnol.*, 19:805–806, 2001. doi: 10.1038/nbt0901-805.
- [5] John C. Kendrew, G. Bodo, Howard M. Dintzis, R.G. Parrish, Harold Wyckoff, and David C. Phillips. A three-dimensional model of the myoglobin molecule obtained by x-ray analysis. *Nature*, 181(4610):662–666, 1958.
- [6] Vladimir N. Uversky and A. Keith Dunker. Understanding protein non-folding. *Biochim. Biophys. Acta, Proteins Proteomics*, 1804(6):1231–1264, 2010. doi: 10.1016/j.bbapap.2010.01.017.
- [7] Klaus Gast, Hilde Damaschun, Klaus Eckert, Kai Schulze-Forster, H. Rainer Maurer, Marlies Müller-Frohne, Dietrich Zirwer, Jan Czarnecki, and Gregor Damaschun. Prothymosin α : A Biologically Active Protein with Random Coil Conformation. *Biochemistry*, 34(40):13211–13218, 1995. doi: 10.1021/bi00040a037.
- [8] Tanguy Chouard. Structural biology: Breaking the protein rules. *Nature*, 471: 151–153, 2011. doi: 10.1038/471151a.

- [9] Natasha S. Latysheva, Tilman Flock, Robert J. Weatheritt, Sreenivas Chavali, and M. Madan Babu. How do disordered regions achieve comparable functions to structured domains? *Protein Sci.*, 24(6):909–922, 2015. doi: 10.1002/pro.2674.
- [10] Francois-Xavier Theillet, Lajos Kalmar, Peter Tompa, Kyou-Hoon Han, Philipp Selenko, A. Keith Dunker, Gary W. Daughdrill, and Vladimir N. Uversky. The alphabet of intrinsic disorder: I. Act like a Pro: On the abundance and roles of proline residues in intrinsically disordered proteins. *Intrinsically Disord. Proteins*, 1(1):e24360–1–e24360–13, 2013. doi: 10.4161/idp.24360.
- [11] Vladimir N. Uversky. What does it mean to be natively unfolded? *FEBS J.*, 269(1): 2–12, 2002. doi: 10.1046/j.0014-2956.2001.02649.x.
- [12] Vladimir N. Uversky. Intrinsically disordered proteins from A to Z. *Int. J. Biochem. Cell Biol.*, 43(8):1090–1103, 2011. doi: 10.1016/j.biocel.2011.04.001.
- [13] A. Keith Dunker, Marc S. Cortese, Pedro Romero, Lilia M. Iakoucheva, and Vladimir N. Uversky. Flexible nets: The roles of intrinsic disorder in protein interaction networks. *FEBS J.*, 272(20):5129–5148, 2005. doi: 10.1111/j.1742-4658.2005.04948.x.
- [14] H. Jane Dyson and Peter E. Wright. Intrinsically unstructured proteins and their functions. *Nat. Rev. Mol. Cell Biol.*, 6(3):197–208, 2005. doi: 10.1038/nrm1589.
- [15] Lilia M. Iakoucheva, Celeste J. Brown, J. David Lawson, Zoran Obradović, and A.Keith Dunker. Intrinsic Disorder in Cell-signaling and Cancer-associated Proteins. *J. Mol. Biol.*, 323(3):573–584, 2002. doi: 10.1016/S0022-2836(02)00969-5.
- [16] Swasti Raychaudhuri, Sucharita Dey, Nitai P. Bhattacharyya, and Debashis Mukhopadhyay. The Role of Intrinsically Unstructured Proteins in Neurodegenerative Diseases. *PLOS ONE*, 4(5):e5566, 2009. doi: 10.1371/journal.pone.0005566.
- [17] Michel Goedert. Alpha-Synuclein and Neurodegenerative Diseases. *Nat. Rev. Neurosci.*, 2:492–501, 2001. doi: 10.1038/35081564.
- [18] James Parkinson. An Essay on the Shaking Palsy. *J. Neuropsychiatry Clin. Neurosci.*, 14(2):223–236, 1817.

- [19] Friedrich H. Lewy. Paralysis agitans. I. Pathologische Anatomie. *Handbuch der Neurologie*, 3(2):920–933, 1912.
- [20] Constantin Trétiakoff. *Contribution à l'étude de l'anatomie pathologique du locus niger de Soemmering avec quelques déductions relatives à la pathogénie des troubles du tonus musculaire et de la maladie de Parkinson*. PhD thesis, University of Paris, 1919.
- [21] Andrew J. Lees, Marianna Selikhova, Luiz Augusto Andrade, and Charley Duyckaerts. The Black Stuff and Konstantin Nikolaevich Tretiakoff. *Mov. Disord.*, 23(6):777–783, 2008. doi: 10.1002/mds.21855.
- [22] Mihael H. Polymeropoulos, Joseph J. Higgins, Lawrence I. Golbe, William G. Johnson, Susan E. Ide, Giuseppe Di Iorio, Giuseppe Sanges, Edward S. Stenroos, Lana T. Pho, Alejandro A. Schaffer, Alice M. Lazzarini, Robert L. Nussbaum, and Roger C. Duvoisin. Mapping of a Gene for Parkinson's Disease to Chromosome 4q21-q23. *Science*, 274(5290):1197–1199, 1996.
- [23] Mihael H. Polymeropoulos, Christian Lavedan, Elisabeth Leroy, Susan E. Ide, Anindya Dehejia, Amalia Dutra, Brian Pike, Holly Root, Jeffrey Rubenstein, Rebecca Boyer, Edward S. Stenroos, Settara Chandrasekharappa, Aglaia Athanassiadou, Theodore Papapetropoulos, William G. Johnson, Alice M. Lazzarini, Roger C. Duvoisin, Giuseppe Di Iorio, Lawrence I. Golbe, and Robert L. Nussbaum. Mutation in the α -Synuclein Gene Identified in Families with Parkinson's Disease. *Science*, 276(5321):2045–2047, 1997. doi: 10.1126/science.276.5321.2045.
- [24] Lawrence I. Golbe, Giuseppe Di Iorio, Vincenzo Bonavita, Douglas C. Miller, and Roger C. Duvoisin. A Large Kindred with Autosomal Dominant Parkinson's Disease. *Ann Neurol.*, 27(3):276–282, 1990. doi: 10.1002/ana.410270309.
- [25] Maria Grazia Spillantini, Marie Luise Schmidt, Virginia M.-Y. Lee, John Q. Trojanowski, Ross Jakes, and Michel Goedert. α -Synuclein in Lewy bodies. *Nature*, 388:839–840, 1997. doi: 10.1038/42166.
- [26] Maria Grazia Spillantini, R. Anthony Crowther, Ross Jakes, Masato Hasegawa, and Michel Goedert. α -Synuclein in filamentous inclusions of Lewy bodies from

- Parkinson's disease and dementia with Lewy bodies. *PNAS*, 95(11):6469–6473, 1998.
- [27] Makoto Hashimoto and Eliezer Masliah. Alpha-Synuclein in Lewy Body Disease and Alzheimer's Disease. *Brain Pathol.*, 9(4):707–720, 1999. doi: 10.1111/j.1750-3639.1999.tb00552.x.
- [28] Kazunari Sekiyama, Yoshiki Takamatsu, Masaaki Waragai, and Makoto Hashimoto. Role of genomics in translational research for Parkinson's disease. *Biochem. Biophys. Res. Commun.*, 452(2):226–235, 2014. doi: 10.1016/j.bbrc.2014.06.028.
- [29] Christine Klein and Ana Westenberger. Genetics of Parkinson's Disease. *Cold Spring Harb. Perspect. Med.*, 2(1):a008888, 2012. doi: 10.1101/cshperspect.a008888.
- [30] Rejko Krüger, Wilfried Kuhn, Thomas Müller, Dirk Voitalla, Manuel Graeber, Sigfried Kösel, Horst Przuntek, Jörg T. Epplen, Ludger Schols, and Olaf Riess. Ala30Pro mutation in the gene encoding α -Synuclein in Parkinson's disease. *Nat. Genet.*, 18:106–108, 1998. doi: 10.1038/ng0298-106.
- [31] Juan J. Zarranz, Javier Alegre, Juan C. Gómez-Esteban, Elena Lezcano, Raquel Ros, Israel Ampuero, Lídice Vidal, Janet Hoenicka, Olga Rodriguez, Begoña Atarés, Verónica Llorens, Estrella Gomez Tortosa, Teodoro del Ser, David G. Muñoz, and Justo G. de Yebenes. The new mutation, E46K, of α -Synuclein Causes Parkinson and Lewy Body Dementia. *Ann. Neurol.*, 55(2):164–173, 2004. doi: 10.1002/ana.10795.
- [32] Silke Appel-Cresswell, Carles Vilarino-Guell, Mary Encarnacion, Holly Sherman, Irene Yu, Brinda Shah, David Weir, Christina Thompson, Chelsea Szu-Tu, Joanne Trinh, Jan O. Aasly, Alex Rajput, Ali H. Rajput, A. Jon Stoessl, and Matthew J. Farrer. Alpha-Synuclein p.H50Q, a Novel Pathogenic Mutation for Parkinson's Disease. *Mov. Disord.*, 28(6):811–813, 2013. doi: 10.1002/mds.25421.
- [33] Aoife P. Kiely, Yasmine T. Asi, Eleanna Kara, Patricia Limousin, Helen Ling, Patrick Lewis, Christos Proukakis, Niall Quinn, Andrew J. Lees, John Hardy, Tamas Revesz, Henry Houlden, and Janice L. Holton. α -Synucleinopathy associated with G51D

- SNCA* mutation: a link between Parkinson's disease and multiple system atrophy? *Acta Neuropathol.*, 125(5):753–769, 2013. doi: 10.1007/s00401-013-1096-7.
- [34] Suzanne Lesage, Mathieu Anheim, Franck Letournel, Luc Bousset, Aurélie Honoré, Nelly Rozas, Laura Pieri, Karine Madiona, Alexandra Dürr, Ronald Melki, Christophe Verny, Alexis Brice, and for the French Parkinson's Disease Genetics Study Group. G51D α -Synuclein Mutation Causes a Novel Parkinsonian-Pyramidal Syndrome. *Ann Neurol.*, 73(4):459–471, 2013. doi: 10.1002/ana.23894.
- [35] Petra Pasanen, Liisa Myllykangas, Maija Siitonen, Anna Raunio, Seppo Kaakkola, Jukka Lyytinen, Pentti J. Tienari, Minna Pöyhönen, and Anders Paetau. A novel α -Synuclein mutation A53E associated with atypical multiple system atrophy and Parkinson's disease-type pathology. *Neurobiol. Aging*, 35(9):2180.e1–2180.e5, 2014. doi: 10.1016/j.neurobiolaging.2014.03.024.
- [36] Hiroyo Yoshino, Makito Hirano, A. Jon Stoessl, Yoko Imamichi, Aya Ikeda, Yuanzhe Li, Manabu Funayama, Ikuko Yamada, Yusaku Nakamura, Vesna Sossi, Matthew J. Farrer, Kenya Nishioka, and Nobutaka Hattori. Homozygous alpha-Synuclein p.A53V in familial Parkinson's disease. *Neurobiol. Aging*, 57:248.e7–248.e12, 2017. doi: 10.1016/j.neurobiolaging.2017.05.022.
- [37] Marie-Christine Chartier-Harlin, Jennifer Kachergus, Christophe Roumier, Vincent Mouroux, Xavier Douay, Sarah Lincoln, Clotilde Levecque, Lydie Larvor, Joris Andrieux, Mary Hulihan, Nawal Waucquier, Luc Defebvre, Philippe Amouyel, Matthew Farrer, and Alain Destée. α -Synuclein locus duplication as a cause of familial Parkinson's disease. *The Lancet*, 364(9440):1167–1169, 2004. doi: 10.1016/S0140-6736(04)17103-1.
- [38] A. B. Singleton, M. Farrer, J. Johnson, A. Singleton, S. Hague, J. Kachergus, M. Hulihan, T. Peuralinna, A. Dutra, R. Nussbaum, S. Lincoln, A. Crawley, M. Hanson, D. Maraganore, C. Adler, M. R. Cookson, M. Muentner, M. Baptista, D. Miller, J. Blancato, J. Hardy, and K. Gwinn-Hardy. α -Synuclein Locus Triplication Causes Parkinson's Disease. *Science*, 302(5646):841, 2003. doi: 10.1126/science.1090278.
- [39] Owen A. Ross, Adam T. Braithwaite, Lisa M. Skipper, Jennifer Kachergus, Mary M. Hulihan, Frank A. Middleton, Kenya Nishioka, Julia Fuchs, Thomas Gasser,

- Demetrius M. Maraganore, Charles H. Adler, Lydie Larvor, Marie-Christine Chartier-Harlin, Christer Nilsson, J. William Langston, Katrina Gwinn, Nobutaka Hattori, and Matthew J. Farrer. Genomic Investigation of α -Synuclein Multiplication and Parkinsonism. *Ann Neurol.*, 63(6):743–750, 2008. doi: 10.1002/ana.21380.
- [40] Shinsuke Fujioka, Kotaro Ogaki, Pawel M. Tacik, Ryan J. Uitti, Owen A. Ross, and Zbigniew K. Wszolek. Update on novel familial forms of Parkinson's disease and multiple system atrophy. *Parkinsonism Relat. Disord.*, 20(1):S29–S34, 2014. doi: 10.1016/S1353-8020(13)70010-5.
- [41] Dorota Hoffman-Zacharska, Dariusz Kozirowski, Owen A. Ross, Michał Milewski, Jarosław Poznański, Marta Jurek, Zbigniew K. Wszolek, Alexandra Soto-Ortolaza, Jarosław Sławek, Piotr Janik, Zygmunt Jamrozik, Anna Potulska-Chromik, Barbara Jasińska-Myga, Grzegorz Opala, Anna Krygowska-Wajs, Krzysztof Czyżewski, Dennis W. Dickson, Jerzy Bal, and Andrzej Friedman. Novel A18T and pA29S substitutions in α -synuclein may be associated with sporadic Parkinson's disease. *Parkinsonism Relat. Disord.*, 19(11):1057–1060, 2013. doi: 10.1016/j.parkreldis.2013.07.011.
- [42] L Maroteaux, JT Campanelli, and RH Scheller. Synuclein: a Neuron-Specific Protein Localized to the Nucleus and Presynaptic Nerve Terminal. *J. Neurosci.*, 8(8):2804–2815, 1988.
- [43] K Uéda, H Fukushima, E Masliah, Y Xia, A Iwai, M Yoshimoto, D A Otero, J Kondo, Y Ihara, and T Saitoh. Molecular cloning of cDNA encoding an unrecognized component of amyloid in Alzheimer disease. *PNAS*, 90(23):11282–11286, 1993.
- [44] Ross Jakes, Maria Grazia Spillantini, and Michel Goedert. Identification of two distinct synucleins from human brain. *FEBS Letters*, 345(1):27–32, 1994. doi: 10.1016/0014-5793(94)00395-5.
- [45] Shigeo Nakajo, Kazuhiko Tsukada, Kumiko Omata, Yasuharu Nakamura, and Kazuyasu Nakaya. A new brain-specific 14-kda protein is a phosphoprotein. *Eur. J. Biochem.*, 217(3):1057–1063, 1993. doi: 10.1111/j.1432-1033.1993.tb18337.x.

- [46] Hongjun Ji, Yiliang E. Liu, Tongli Jia, Mingsheng Wang, Jingwen Liu, Guowei Xiao, Benjamin K. Joseph, Craig Rosen, and Y. Eric Shi. Identification of a Breast Cancer-specific Gene, BCSG1, by Direct Differential cDNA Sequencing. *Cancer Res.*, 57(4):759–764, 1997.
- [47] Julia M. George. The Synucleins. *Genome Biol.*, 3(1):reviews3002.1, 2001. doi: 10.1186/gb-2001-3-1-reviews3002.
- [48] Euijung Jo, JoAnne McLaurin, Christopher M. Yip, Peter St. George-Hyslop, and Paul E. Fraser. α -Synuclein Membrane Interactions and Lipid Specificity. *J. Biol. Chem.*, 275(44):34328–34334, 2000. doi: 10.1074/jbc.M004345200.
- [49] Christian Lavedan. The Synuclein Family. *Genome Res.*, 8:871–880, 1998. doi: 10.1101/gr.8.9.871.
- [50] David F. Clayton and Julia M. George. Synucleins in Synaptic Plasticity and Neurodegenerative Disorders. *J. Neurosci. Res.*, 58(1):120–129, 1999.
- [51] Julia M. George, Hui Jin, Wendy S. Woods, and David F. Clayton. Characterization of a Novel Protein Regulated during the Critical Period for Song Learning in the Zebra Finch. *Neuron*, 15(2):361–372, 1995. doi: 10.1016/0896-6273(95)90040-3.
- [52] John M. Jenco, Andrew Rawlingson, and Brenda Daniels Andrew J. Morris. Regulation of Phospholipase D2: Selective Inhibition of Mammalian Phospholipase D Isoenzymes by α - and β -Synucleins. *Biochemistry*, 37(14):4901–4909, 1998. doi: 10.1021/bi972776r.
- [53] William C. Colley, Tsung-Chang Sung, Richard Roll, John Jenco, Scott M. Hammond, Yelena Altshuller, Dafna Bar-Sagi, Andrew J. Morris, and Michael A. Frohman. Phospholipase D2, a distinct phospholipase D isoform with novel regulatory properties that provokes cytoskeletal reorganization. *Curr. Biol.*, 7(3):191–201, 1997. doi: 10.1016/S0960-9822(97)70090-3.
- [54] Elizabeth R. Middleton and Elizabeth Rhoades. Effects of Curvature and Composition on α -Synuclein Binding to Lipid Vesicles. *Biophys. J.*, 99(7):2279–2288, 2010. doi: 10.1016/j.bpj.2010.07.056.

- [55] Christopher H. Westphal and Sreeganga S. Chandra. Monomeric Synucleins Generate Membrane Curvature. *J. Biol. Chem.*, 288:1829–1840, 2013. doi: 10.1074/jbc.M112.418871.
- [56] Jacqueline Burré, Manu Sharma, Theodoros Tsetsenis, Theodoros Tsetsenis, Mark R. Etherton, and Thomas C. Südhof. α -Synuclein Promotes SNARE-Complex Assembly in Vivo and in Vitro. *Science*, 329(5999):1663–1667, 2010. doi: 10.1126/science.1195227.
- [57] Karina J. Vargas, Sachin Makani, Taylor Davis, Christopher H. Westphal, Pablo E. Castillo, and Sreeganga S. Chandra. Synucleins Regulate the Kinetics of Synaptic Vesicle Endocytosis. *J. Neurosci.*, 34(28):9364–9376, 2014. doi: 10.1523/JNEUROSCI.4787-13.2014.
- [58] Karina J. Vargas, Nikolas Schrod, Taylor Davis, Ruben Fernandez-Busnadiego, Yumiko V. Taguchi, Ulrike Laugks, Vladan Lucic, and Sreeganga S. Chandra. Synucleins Have Multiple Effects on Presynaptic Architecture. *Cell Rep.*, 18(1):161–173, 2017. doi: 10.1016/j.celrep.2016.12.023.
- [59] Hilal A. Lashuel, Cassia R. Overk, Abid Oueslati, and Eliezer Masliah. The many faces of α -Synuclein: from structure and toxicity to therapeutic target. *Nat. Rev. Neurosci.*, 14:38–48, 2013. doi: 10.1038/nrn3406.
- [60] Todd Logan, Jacob Bendor, Chantal Toupin, Kurt Thorn, and Robert H Edwards. α -Synuclein promotes dilation of the exocytotic fusion pore. *Nat. Neurosci.*, 20(5):681–689, 2017. doi: 10.1038/nn.4529.
- [61] Dennis J Selkoe. Showing transmitters the door: synucleins accelerate vesicle release. *Nat. Neurosci.*, 20(5):629–631, 2017. doi: 10.1038/nn.4551.
- [62] Toshiko Shibayama-Imazu, Ikuko Okahashi, Kumiko Omata, Shigeo Nakajo, Hidehiko Ochiai, Yasumitsu Nakai, Tokiko Hama, Yasuharu Nakamura, and Kazuyasu Nakaya. Cell and tissue distribution and developmental change of neuron specific 14 kDa protein (phosphoneuroprotein 14). *Brain Res.*, 622(1):17–25, 1993. doi: 10.1016/0006-8993(93)90796-P.

- [63] Michael C. Irizarry, Tae-Wan Kim, Megan McNamara, Rudolph E. Tanzi, Julia M. George, David F. Clayton, and Bradley T. Hyman. Characterization of the Precursor Protein of the Non-A β Component of Senile Plaques (NACP) in the Human Central Nervous System. *J. Neuropathol. Exp. Neurol.*, 55(8):889–895, 1996. doi: 10.1097/00005072-199608000-00004.
- [64] George J. Siegel, Bernard W. Agranoff, R. Wayne Albers, Stephen K. Fisher, and Michael D. Uhler, editors. *Basic Neurochemistry, 6th edition*. Lippincott-Raven, Philadelphia, 1999.
- [65] Jere P. Segrest, Hans De Loof, Jan G. Dohlman, Christie G. Brouillette, and G. M. Anantharamaiah. Amphipathic Helix Motif: Classes and Properties. *Proteins*, 8(2):103–117, 1990. doi: 10.1002/prot.340080202.
- [66] W. Sean Davidson, Ana Jonas, David F. Clayton, and Julia M. George. Stabilization of α -Synuclein Secondary Structure upon Binding to Synthetic Membranes. *J. Biol. Chem.*, 273(16):9443–9449, 1998. doi: 10.1074/jbc.273.16.9443.
- [67] David Eliezer, Esin Kutluay, Robert Bussell, and Gillian Browne. Conformational Properties of α -Synuclein in its Free and Lipid-associated States. *J. Mol. Biol.*, 307(4):1061–1073, 2001. doi: 10.1006/jmbi.2001.4538.
- [68] Tobias S. Ulmer, Ad Bax, Nelson B. Cole, and Robert L. Nussbaum. Structure and Dynamics of Micelle-bound Human α -Synuclein. *J. Biol. Chem.*, 280(10):9595–9603, 2005. doi: 10.1074/jbc.M411805200.
- [69] Igor Dikiy and David Eliezer. Folding and misfolding of alpha-synuclein on membranes. *Biochim. Biophys. Acta, Biomembr.*, 1818(4):1013–1018, 2012. doi: 10.1016/j.bbamem.2011.09.008.
- [70] Sreeganga Chandra, Xiaocheng Chen, Josep Rizo, Reinhard Jahn, and Thomas C. Südhof. A Broken α -Helix in Folded α -Synuclein. *J. Biol. Chem.*, 278(17):15313–15318, 2003. doi: 10.1074/jbc.M213128200.
- [71] Marco Bortolus, Fabio Tombolato, Isabella Tessari, Marco Bisaglia, Stefano Mammi, Luigi Bubacco, Alberta Ferrarini, and Anna Lisa Maniero. Broken Helix in Vesicle and Micelle-Bound α -Synuclein: Insights from Site-Directed Spin

- Labeling-EPR Experiments and MD Simulations. *J. Am. Chem. Soc.*, 130(21): 6690–6691, 2008. doi: 10.1021/ja8010429.
- [72] Malte Drescher, Gertjan Veldhuis, Bart D. van Rooijen, Sergey Milikisyants, Vinod Subramaniam, and Martina Huber. Antiparallel Arrangement of the Helices of Vesicle-Bound α -Synuclein. *J. Am. Chem. Soc.*, 130(25):7796–7797, 2008. doi: 10.1021/ja801594s.
- [73] Christine C. Jao, Ani Der-Sarkissian, Jeannie Chen, and Ralf Langen. Structure of membrane-bound α -synuclein studied by site-directed spin labeling. *PNAS*, 101(22):8331–8336, 2004. doi: 10.1073/pnas.0400553101.
- [74] Christine C. Jao, Balachandra G. Hegde, Jeannie Chen, Ian S. Haworth, and Ralf Langen. Structure of membrane-bound α -synuclein from site-directed spin labeling and computational refinement. *PNAS*, 105(50):19666–19671, 2008. doi: 10.1073/pnas.0807826105.
- [75] Elka R. Georgieva, Trudy F. Ramlall, Peter P. Borbat, Jack H. Freed, and David Eliezer. Membrane-Bound α -Synuclein Forms an Extended Helix: Long-Distance Pulsed ESR Measurements Using Vesicles, Bicelles, and Rodlike Micelles. *J. Am. Chem. Soc.*, 130(39):12856–12857, 2008. doi: 10.1021/ja804517m.
- [76] Adam J. Trexler and Elizabeth Rhoades. α -Synuclein Binds Large Unilamellar Vesicles as an Extended Helix. *Biochemistry*, 48(11):2304–2306, 2009. doi: 10.1021/bi900114z.
- [77] Marta Robotta, Patrick Braun, Bart van Rooijen, Vinod Subramaniam, Martina Huber, and Malte Drescher. Direct Evidence of Coexisting Horseshoe and Extended Helix Conformations of Membrane-Bound Alpha-Synuclein. *ChemPhysChem*, 12(2):267–269, 2011. doi: 10.1002/cphc.201000815.
- [78] Allison L Jones, Mark D Hulett, and Christopher R Parish. Histidine-rich glycoprotein: A novel adaptor protein in plasma that modulates the immune, vascular and coagulation systems. *Immunol. Cell. Biol.*, 83:106–118, 2005. doi: 10.1111/j.1440-1711.2005.01320.x.

- [79] Sadao Wakabayashi. *Int. Rev. Cell. Mol. Biol.*, chapter New Insights into the Functions of Histidine-Rich Glycoprotein, pages 467–493. Academic Press, 2013. doi: 10.1016/B978-0-12-407696-9.00009-9.
- [80] Heinz Haupt and Norbert Heimburger. Humanserumproteine mit hoher Affinität zu Carboxymethylcellulose, I, Isolierung von Lysozym, C1q und zwei bisher unbekanntem α -Globulinen. *Hoppe-Seyler's Z Physiol Chem*, 353:1125–1132, 1972. doi: 10.1515/bchm2.1972.353.2.1125.
- [81] Norbert Heimburger, Heinz Haupt, Theodor Kranz, and Siegfried Baudner. Humanserumproteine mit hoher Affinität zu Carboxymethylcellulose, II. Physikalisch-chemische und immunologische Charakterisierung eines histidinreichen 3,8S- α 2-Glykoproteins (CM-Protein I). *Hoppe-Seyler's Z. Physiol. Chem.*, 353, 1972. doi: 10.1515/bchm2.1972.353.2.1133.
- [82] Dorin-Bogdan Borza, Fred M. Tatum, and William T. Morgan. Domain Structure and Conformation of Histidine-Proline-Rich Glycoprotein. *Biochemistry*, 35(6): 1925–1934, 1996. doi: 10.1021/bi952061t.
- [83] Takehiko Koide and Shoji Odani. Histidine-rich glycoprotein is evolutionarily related to the cystatin superfamily: Presence of two cystatin domains in the n-terminal region. *FEBS Letters*, 216(1):17–21, 1987. doi: 10.1016/0014-5793(87)80748-2.
- [84] Chunsik Lee, Erik Bongcam-Rudloff, Christian Sollner, Willi Jahnen-Dechent, and Lena Claesson-Welsh. Type 3 cystatins; fetuins, kininogen and histidine-rich glycoprotein. *Front. Biosci.*, 14:2911–2922, 2009.
- [85] Bart C. Hennis, Moniek P.M. de Maat, Paul H. A Quax, Elizabeth J. le Clercq, Johan Kuiper, and Cornelius Kluft. Evaluation of sites of synthesis of the histidine-rich glycoprotein. *Thromb. Haemost.*, 65(884):Abstract 660, 1991.
- [86] Takehiko Koide, Donald Foste, Shinji Yoshitake, and Earl W. Davie. Amino Acid Sequence of Human Histidine-Rich Glycoprotein Derived from the Nucleotide Sequence of Its cDNA. *Biochemistry*, 25(8):2220–2225, 1986.

- [87] Omar Kassar, Stephen A. McMahon, Rory Thompson, Catherine H. Botting, James H. Naismith, and Alan J. Stewart. Crystal structure of histidine-rich glycoprotein N2 domain reveals redox activity at an interdomain disulfide bridge: implications for angiogenic regulation. *Blood*, 123:1948–1955, 2014. doi: 10.1182/blood-2013-11-535963.
- [88] Ivan K. H. Poon, Kruti K. Patel, David S. Davis, Christopher R. Parish, and Mark D. Hulett. Histidine-rich glycoprotein: the Swiss Army knife of mammalian plasma. *Blood*, 117(7):2093–2101, 2011. doi: 10.1182/blood-2010-09-303842.
- [89] Francesca Ronca and Antonio Raggi. Structure-function relationships in mammalian histidine-proline-rich glycoprotein. *Biochimie*, 118:207–220, 2015. doi: 10.1016/j.biochi.2015.09.024.
- [90] Takehiko Koide, Shoji Odani, and Teruo Ono. The N-terminal sequence of human plasma histidine-rich glycoprotein homologous to antithrombin with high affinity for herapin. *FEBS Letters*, 141(2):222–224, 1982. ISSN 0014-5793. doi: 10.1016/0014-5793(82)80052-5.
- [91] L. L. Leung. Interaction of histidine-rich glycoprotein with fibrinogen and fibrin. *J. Clin. Invest.*, 77(4):1305–1311, 1986. doi: 10.1172/JCI112435.
- [92] Henri R Lijnen, Marc Hoylaerts, and Desire Collen. Isolation and Characterization of a Human Plasma Protein with Affinity for the Lysine Binding Sites in Plasminogen. Role in the Regulation of Fibrinolysis and Identification as Histidine-rich Glycoprotein. *J. Biol. Chem.*, 255(21):10214–10222, 1980.
- [93] Ivan K. H. Poon, Anna-Karin Olsson, Mark D. Hulett, and Christopher R. Parish. Regulation of histidine-rich glycoprotein (HRG) function via plasmin-mediated proteolytic cleavage. *Biochem J*, 424(1):27–37, November 2009. doi: 10.1042/BJ20090794.
- [94] Philip A. Klenotic, Ping Huang, Juan Palomo, Balveen Kaur, Erwin G. Van Meir, Michael A. Vogelbaum, Maria Febbraio, Candece L. Gladson, and Roy L. Silverstein. Histidine-Rich Glycoprotein Modulates the Anti-Angiogenic Effects of Vasculostatin. *Am. J. Pathol.*, 176(4):2039–2050, 2010. doi: 10.2353/ajpath.2010.090782.

- [95] Ronit Simantov, Maria Febbraio, René Crombie, Adam S. Asch, Ralph L. Nachman, and Roy L. Silverstein. Histidine-rich glycoprotein inhibits the antiangiogenic effect of thrombospondin-1. *J. Clin. Invest.*, 107(1):45–52, 2000. doi: 10.1172/JCI9061.
- [96] R. Simantov, M. Febbraio, and R. L. Silverstein. The antiangiogenic effect of thrombospondin-2 is mediated by CD36 and modulated by histidine-rich glycoprotein. *Matrix Biol.*, 24(1):27–34, 2005. doi: 10.1016/j.matbio.2004.11.005.
- [97] Nick N. Gorgani, Christopher R. Parish, Simon B. Easterbrook Smith, and Joseph G. Altin. Histidine-Rich Glycoprotein Binds to Human IgG and C1q and Inhibits the Formation of Insoluble Immune Complexes. *Biochemistry*, 36(22):6653–6662, 1997. doi: 10.1021/bi962573n.
- [98] William T. Morgan. Human serum histidine-rich glycoprotein. I. Interactions with heme, metal ions and organic ligands. *Biochim. Biophys. Acta, Protein Struct.*, 535(2):319–333, 1978. doi: 10.1016/0005-2795(78)90098-3.
- [99] Masanao Katagiri, Ken Tsutsui, Toshio Yamano, Yasutsugu Shimonishi, and Fumihide Ishibashi. Interaction of heme with a synthetic peptide mimicking the putative heme-binding site of histidine-rich glycoprotein. *Biochem. Biophys. Res. Commun.*, 149(3):1070–1076, 1987. doi: 10.1016/0006-291X(87)90517-1.
- [100] K. Tsutsui and G. C. Mueller. A protein with multiple heme-binding sites from rabbit serum. *J. Biol. Chem.*, 257(7):3925–3931, 1982.
- [101] William T. Morgan. Interactions of the Histidine-rich Glycoprotein of Serum with Metals. *Biochemistry*, 20(5):1054–1061, 1981. doi: 10.1021/bi00508a002.
- [102] Alan J. Stewart, Claudia A. Blindauer, and Peter J. Sadler. Plasma fatty acid levels may regulate the zn^{2+} -dependent activities of histidine-rich glycoprotein. *Biochimie*, 91(11):1518–1522, 2009. doi: 10.1016/j.biochi.2009.08.002.
- [103] Dorin-Bogdan Borza and William T. Morgan. Histidine-Proline-rich Glycoprotein as a Plasma pH Sensor: MODULATION OF ITS INTERACTION WITH GLYCOSAMINOGLYCANS BY pH AND METALS. *J. Biol. Chem.*, 273(10):5493–5499, 1998. doi: 10.1074/jbc.273.10.5493.

- [104] Allison L. Jones, Mark D. Hulett, and Christopher R. Parish. Histidine-rich Glycoprotein Binds to Cell-surface Heparan Sulfate via Its N-terminal Domain following Zn^{2+} Chelation. *J. Biol. Chem.*, 279(29):30114–30122, 2004. doi: 10.1074/jbc.M401996200.
- [105] Victoria Rydengård, Anna-Karin Olsson, Matthias Mörgelin, and Artur Schmidtchen. Histidine-rich glycoprotein exerts antibacterial activity. *FEBS Journal*, 274(2):377–389, 2007. doi: 10.1111/j.1742-4658.2006.05586.x.
- [106] Walther Gerlach and Otto Stern. Der experimentelle Nachweis der Richtungsquantelung im Magnetfeld. *Zeitschrift für Physik*, 9:349–352, 1922.
- [107] John A. Weil and James R. Bolton. *Electron Spin Resonance - Elementary Theory and Practical Applications*. Wiley, 2007.
- [108] A. Abragam and M. H. L. Pryce. Theory of the nuclear hyperfine structure of paramagnetic resonance spectra in crystals. *Proc. R. Soc. Lond. A*, 205(1080): 135–153, 1951. doi: 10.1098/rspa.1951.0022.
- [109] Arthur Schweiger and Gunnar Jeschke. *Principles of pulse electron paramagnetic resonance*. Oxford University Press, 2001.
- [110] Friedrich Lottspeich and Joachim W. Engels. *Bioanalytik*. Springer Spektrum, 2012.
- [111] Victor Chechik, Emma Carter, and Damien Murphy. *Electron Paramagnetic Resonance*. Oxford University Press, 2016.
- [112] Gunnar Jeschke. DEER Distance Measurements on Proteins. *Annu. Rev. Phys. Chem.*, 63(1):419–446, 2012. doi: 10.1146/annurev-physchem-032511-143716.
- [113] Julia Holterhues. *Analyse der Signalweiterleitung im spinmarkierten sensorischen Rhodopsin/Transducer-Komplex mittels zeitaufgelöster ESR-Spektroskopie*. PhD thesis, Universität Osnabrück, 2009.
- [114] Paolo Rossi, G. V. T. Swapna, Yuanpeng J. Huang, James M. Aramini, Clemens Anklin, Kenith Conover, Keith Hamilton, Rong Xiao, Thomas B. Acton, Asli

- Ertekin, John K. Everett, and Gaetano T. Montelione. A microscale protein NMR sample screening pipeline. *J. Biomol. NMR*, 46:11–22, 2010. doi: 10.1007/s10858-009-9386-z.
- [115] O. Hayes Griffith and A. S. Waggoner. Nitroxide Free Radicals: Spin Labels for Probing Biomolecular Structure. *Acc. Chem. Res.*, 2(1):17–24, 1969. doi: 10.1021/ar50013a003.
- [116] E. L. Hahn. Spin Echoes. *Phys. Rev.*, 80(4):580–594, 1950.
- [117] Gunnar Jeschke and Yevhen Polyhach. Distance measurements on spin-labelled biomacromolecules by pulsed electron paramagnetic resonance. *Phys. Chem. Chem. Phys.*, 9(16):1895–1910, 2007. doi: 10.1039/B614920K.
- [118] A. D. Milov, A. B. Ponomarev, and Yu. D. Tsvetkov. Electron-electron double resonance in electron spin echo: Model biradical systems and the sensitized photolysis of decalin. *Chem. Phys. Lett.*, 110(1):67–72, 1984. doi: 10.1016/0009-2614(84)80148-7.
- [119] M. Pannier, S. Veit, A. Godt, G. Jeschke, and H. W. Spiess. Dead-Time Free Measurement of Dipole-Dipole Interactions between Electron Spins. *J. Magn. Reson.*, 142(2):331–340, 2000. doi: 10.1006/jmre.1999.1944.
- [120] Gunnar Jeschke. Distance Measurements in the Nanometer Range by Pulse EPR. *ChemPhysChem*, 3(11):927–932, 2002. doi: 10.1002/1439-7641(20021115)3:11<927::aid-cphc927>3.0.co;2-q.
- [121] Olav Schiemann and Thomas Prisner. Long-range distance determinations in biomacromolecules by EPR spectroscopy. *Q. Rev. Biophys.*, 40:1–53, 2007. doi: 10.1017/S003358350700460X.
- [122] G. Jeschke, V. Chechik, P. Ionita, A. Godt, H. Zimmermann, J. Banham, C. R. Timmel, D. Hilger, and H. Jung. Deeranalysis2006—a comprehensive software package for analyzing pulsed eldor data. *Appl. Magn. Reson.*, 30(3):473–498, 2006. doi: 10.1007/BF03166213.

- [123] Félix M. Goñi. The basic structure and dynamics of cell membranes: An update of the Singer–Nicolson model. *Biochim. Biophys. Acta, Biomembr.*, 1838(6):1467–1476, 2014. doi: <http://dx.doi.org/10.1016/j.bbamem.2014.01.006>.
- [124] Lukas Buehler. *Cell Membranes*. Garland Science, 2015.
- [125] S. J. Singer and G. L. Nicolson. The Fluid Mosaic Model of the Structure of Cell Membranes. *Science*, 175(4023):720–731, 1972. doi: <http://dx.doi.org/10.1126/science.175.4023.720>.
- [126] Roland Winter and Frank Noll. *Methoden der Biophysikalischen Chemie*. Teubner Studienbücher, 1998.
- [127] A. Kerth. *Infrarot-Reflexions-Absorptions-Spektroskopie an Lipid-, Peptid- und Flüssigkristallfilmen an der Luft/Wasser-Grenzfläche*. PhD thesis, Martin-Luther-Universität Halle-Wittenberg, 2003.
- [128] Régine Maget-Dana. The monolayer technique: a potent tool for studying the interfacial properties of antimicrobial and membrane-lytic peptides and their interactions with lipid membranes. *Biochim. Biophys. Acta, Biomembr.*, 1462(1):109–140, 1999. doi: [10.1016/S0005-2736\(99\)00203-5](https://doi.org/10.1016/S0005-2736(99)00203-5).
- [129] Alfred Blume. A comparative study of the phase transitions of phospholipid bilayers and monolayers. *Biochim. Biophys. Acta, Biomembr.*, 557(1):32–44, 1979. doi: [10.1016/0005-2736\(79\)90087-7](https://doi.org/10.1016/0005-2736(79)90087-7).
- [130] K. Patel Kruti, H. Poon Ivan K., H. Talbo Gert, A. Perugini Matthew, L. Taylor Nicole, J. Ralph Troy, J. Hoogenraad Nicholas, and D. Hulett Mark. New Method for Purifying Histidine-rich Glycoprotein from Human Plasma Redefines its Functional Properties. *IUBMB Life*, 65(6):550–563, 2013. doi: [10.1002/iub.1168](https://doi.org/10.1002/iub.1168).
- [131] Ivan K. H. Poon, Mark D. Hulett, and Christopher R. Parish. Histidine-rich glycoprotein is a novel plasma pattern recognition molecule that recruits IgG to facilitate necrotic cell clearance via FcγRI on phagocytes. *Blood*, 2010. doi: [10.1182/blood-2009-07-234013](https://doi.org/10.1182/blood-2009-07-234013).

- [132] Christian Altenbach, Sabine L. Flitsch, H. Gobind Khorana, and Wayne L. Hubbell. Structural Studies on Transmembrane Proteins. 2. Spin Labeling of Bacteriorhodopsin Mutants at Unique Cysteines. *Biochemistry*, 28(19):7806–7812, 1989. doi: 10.1021/bi00445a042.
- [133] Peter Borbat, Trudy F. Ramlall, Jack H. Freed, and David Eliezer. Inter-Helix Distances in Lysophospholipid Micelle-Bound α -Synuclein from Pulsed ESR Measurements. *J. Am. Chem. Soc.*, 128(31):10004–10005, 2006. doi: 10.1021/ja063122l.
- [134] Malte Drescher, Frans Godschalk, Gertjan Veldhuis, Bart D. van Rooijen, Vinod Subramaniam, and Martina Huber. Spin-Label EPR on α -Synuclein Reveals Differences in the Membrane Binding Affinity of the Two Antiparallel Helices. *ChemBioChem*, 9(15):2411–2416, 2008. doi: 10.1002/cbic.200800238.
- [135] Martin Plato, Heinz-Jürgen Steinhoff, Christopf Wegener, Jens T. Törring, Anton Savitsky, and Klaus Möbius. Molecular orbital study of polarity and hydrogen bonding effects on the g and hyperfine tensors of site directed no spin labelled bacteriorhodopsin. *Mol. Phys.*, 100(23):3711–3721, 2002. doi: 10.1080/00268970210166246.
- [136] Derek Marsh. Spin-Label EPR for Determining Polarity and Proticity in Biomolecular Assemblies: Transmembrane Profiles. *Appl. Magn. Reson.*, 37:435–454, 2010. doi: 10.1007/s00723-009-0078-3.
- [137] Greta Pifat-Mrzljak, editor. *Supramolecular Structure and Function 8*, chapter Multi-Frequency EPR Spectroscopy Studies of the Structure and Conformational Changes of Site-Directed Spin Labelled Membrane Proteins, pages 145–177. Springer, Boston, MA, 2004. ISBN 978-0-306-48661-6. doi: 10.1007/0-306-48662-8_10.
- [138] Gunnar Jeschke. *DeerAnalysis2013.2 User Manual*. ETH Zürich, 2013.
- [139] Malte Drescher, Bart D. van Rooijen, Gertjan Veldhuis, Vinod Subramaniam, and Martina Huber. A Stable Lipid-Induced Aggregate of α -Synuclein. *J. Am. Chem. Soc.*, 132(12):4080–4082, 2010. doi: 10.1021/ja909247j.

- [140] Tsutomu Arakawa, Yoshiko Kita, and Serge N. Timasheff. Protein precipitation and denaturation by dimethyl sulfoxide. *Biophys. Chem.*, 131(1):62–70, 2007. doi: 10.1016/j.bpc.2007.09.004.
- [141] Shigeo Takamori, Matthew Holt, Katinka Stenius, Edward A. Lemke, Mads Grønborg, Dietmar Riedel, Henning Urlaub, Stephan Schenck, Britta Brügger, Philippe Ringle, Shirley A. Müller, Burkhard Rammner, Frauke Gräter, Jochen S. Hub, Bert L. De Groot, Gottfried Mieskes, Yoshinori Moriyama, Jürgen Klingauf, Helmut Grubmüller, John Heuser, Felix Wieland, and Reinhard Jahn. Molecular Anatomy of a Trafficking Organelle. *Cell*, 127(4), 2006. doi: <http://dx.doi.org/10.1016/j.cell.2006.10.030>.
- [142] John R. Silvius. Role of cholesterol in lipid raft formation: lessons from lipid model systems. *Biochim. Biophys. Acta, Biomembr.*, 1610(2):174–183, 2003. doi: 10.1016/S0005-2736(03)00016-6.
- [143] R.A. Demel, L. L. M. van Deenen, and B. A. Pethica. Monolayer interactions of phospholipids and cholesterol. *Biochim. Biophys. Acta, Biomembr.*, 135(1):11–19, 1967.
- [144] Élodie Boisselier, Philippe Calvez, Éric Demers, Line Cantin, and Christian Salesse. Influence of the Physical State of Phospholipid Monolayers on Protein Binding. *Langmuir*, 28(25):9680–9688, 2012. doi: 10.1021/la301135z.
- [145] Philippe Calvez, Sylvain Bussi eres,  Eric Demers, and Christian Salesse. Parameters modulating the maximum insertion pressure of proteins and peptides in lipid monolayers. *Biochimie*, 91(6):718–733, 2009. doi: 10.1016/j.biochi.2009.03.018.
- [146] URL <https://www.protpi.ch>.
- [147] Shota Nakamura, Sonomi Suzuki, Hiroaki Saito, and Ken-ichi Nishiyama. Cholesterol blocks spontaneous insertion of membrane proteins into liposomes of phosphatidylcholine. *J. Biochem.*, 163(4):313–319, 2018. doi: 10.1093/jb/mvx083.
- [148] Alexander B. Meijer, Ruud B. Spruijt, Cor J. A. M. Wolfs, and Marcus A. Hemminga. Membrane Assembly of the Bacteriophage Pf3 Major Coat Protein. *Biochemistry*, 39(20):6157–6163, 2000. doi: 10.1021/bi992972t.

- [149] QIAGEN. *The QIAexpressionist - A handbook for high-level expression and purification of 6xHis-tagged proteins*, 5th edition edition, 2003.
- [150] H. F. Lodish and N. Kong. The secretory pathway is normal in dithiothreitol-treated cells, but disulfide-bonded proteins are reduced and reversibly retained in the endoplasmic reticulum. *J. Biol. Chem.*, 268(27):20598–20605, 1993.
- [151] I. Miller, M. Teinfalt, M. Leschnik, R. Wait, and M. Gemeiner. Nonreducing two-dimensional gel electrophoresis for the detection of Bence Jones proteins in serum and urine. *Proteomics*, 4(1):257–260, 2004. doi: 10.1002/pmic.200300546.
- [152] René Steffen Hauer, René Schlesier, Kathleen Heilmann, Julia Dittmar, Mario Jakob, and Ralf Bernd Klösgen. Enough is enough: TatA demand during Tat-dependent protein transport. *Biochim. Biophys. Acta, Mol. Cell. Res.*, 1833(5): 957–965, 2013. doi: 10.1016/j.bbamcr.2013.01.030.
- [153] Lila Castellanos-Serra, Wilfredo Proenza, Vivian Huerta, Robert L. Moritz, and Richard J. Simpson. Proteome analysis of polyacrylamide gel-separated proteins visualized by reversible negative staining using imidazole-zinc salts. *Electrophoresis*, 20:732–737, 1999. doi: 10.1002/(SICI)1522-2683(19990101)20:4/5<732::AID-ELPS732>3.0.CO;2-Q.
- [154] Simpson RJ. Zinc/Imidazole procedure for visualization of proteins in gels by negative staining. *CSH Protoc.*, 2007. doi: 10.1101/pdb.prot4701.
- [155] Andrew Guzzetta. *Reverse Phase HPLC Basics for LC/MS*, 2001. URL <http://www.ionsource.com/tutorial/chromatography/rphplc.htm>.
- [156] Benlian Wang, Yaroslav Tsybovsky, Krzysztof Palczewski, and Mark R. Chance. Reliable Determination of Site-Specific In Vivo Protein N-Glycosylation Based on Collision-Induced MS/MS and Chromatographic Retention Time. *J. Am. Soc. Mass Spectrom. Chem.*, 25(5):729–741, 2014. doi: 10.1007/s13361-013-0823-6.
- [157] Ajit Varki, Richard D Cummings, Jeffrey D Esko, Hudson H Freeze, Pamela Stanley, Carolyn R Bertozzi, Gerald W Hart, and Marilyn E Etzler, editors. *Essentials of Glycobiology*. Cold Spring Harbor, 2009.

- [158] Lee Whitmore and B. A. Wallace. DICHROWEB, an online server for protein secondary structure analyses from circular dichroism spectroscopic data. *Nucleic Acids Res.*, 32:W668–W673, 2004. doi: 10.1093/nar/gkh371.
- [159] Lee Whitmore and B. A. Wallace. Protein Secondary Structure Analyses from Circular Dichroism Spectroscopy: Methods and Reference Databases. *Biopolymers*, 89(5):392–400, 2008. doi: 10.1002/bip.20853.
- [160] Stephen W. Provencher and Juergen Gloeckner. Estimation of Globular Protein Secondary Structure from Circular Dichroism. *Biochemistry*, 20(1):33–37, 1981.
- [161] Ivo H. M. van Stokkum, Hans J. W. Spoelder, Michael Bloemendal, Rienk van Grondelle, and Frans C. A. Groen. Estimation of Protein Secondary Structure and Error Analysis from Circular Dichroism Spectra. *Anal. Biochem.*, 191(1):110–118, 1990. doi: 10.1016/0003-2697(90)90396-Q.
- [162] Narasimha Sreerama and Robert W. Woody. Estimation of Protein Secondary Structure from Circular Dichroism Spectra: Comparison of CONTIN, SELCON, and CDSSTR Methods with an Expanded Reference Set. *Anal. Biochem.*, 287(2): 252–260, 2000. doi: 10.1006/abio.2000.4880.
- [163] Narasimha Sreerama, Sergei Yu. Venyaminov, and Robert W. Woody. Estimation of Protein Secondary Structure from Circular Dichroism Spectra: Inclusion of Denatured Proteins with Native Proteins in the Analysis. *Anal. Biochem.*, 287(2): 243–251, 2000. doi: 10.1006/abio.2000.4879.
- [164] Anna Katharina Weyrauch, Mario Jakob, Angelika Schierhorn, Ralf Bernd Klösgen, and Dariush Hinderberger. Purification of rabbit serum histidine-proline-rich glycoprotein via preparative gel electrophoresis and characterization of its glycosylation patterns. *PLOS ONE*, 12(9):e0184968, 2017. doi: 10.1371/journal.pone.0184968.
- [165] Mathia Colwell, Najma Ahmed, and Ralph Butkowski. Detection of histidine-rich glycoprotein and fibrinogen with nickel-enzyme conjugates: Purification of rabbit HRG. *Anal. Biochem.*, 525:67–72, 2017. doi: 10.1016/j.ab.2017.02.013.

- [166] Selgar Henkel. Untersuchungen an Histidin- und Prolinreichen Peptiden mittels ESE-, ESEEM- und HYSCORE-Spektroskopie. Master's thesis, Martin-Luther-Universität Halle -Wittenberg, Naturwissenschaftliche Fakultät II, Institut für Chemie, 2016.
- [167] Stefan Stoll and Arthur Schweiger. EasySpin, a comprehensive software package for spectral simulation and analysis in EPR. *J. Magn. Reson. Resonance*, 178(1): 42–55, 2006. doi: 10.1016/j.jmr.2005.08.013.
- [168] Stefan Stoll and Arthur Schweiger. EasySpin: Simulating cw ESR spectra. *Biol. Magn. Reson.*, 27:299–321, 2007.
- [169] David J. Schneider and Jack H. Freed. Calculating Slow Motional Magnetic Resonance Spectra. In *Spin Labeling: Theory and Applications*, pages 1–76. Springer US, 1989. doi: 10.1007/978-1-4613-0743-3_1.
- [170] C. Nick Pace, Felix Vajdos, Lanette Fee, Gerald Grimsley, and Theronica Gray. How to measure and predict the molar absorption coefficient of a protein. *Protein Sci.*, 4(11):2411–2423, 1995. doi: 10.1002/pro.5560041120.
- [171] U. K. Laemmli. Cleavage of Structural Proteins during the Assembly of the Head of Bacteriophage T4. *Nature*, 227:680–685, 1970. doi: 10.1038/227680a0.
- [172] Holger Seelert and Frank Krause. Preparative isolation of protein complexes and other bioparticles by elution from polyacrylamide gels. *Electrophoresis*, 29: 2617–2636, 2008. doi: 10.1002/elps.200800061.
- [173] Norma J. Greenfield. Using circular dichroism spectra to estimate protein secondary structure. *Nat. Protoc.*, 1:2876–2890, 2007. doi: 10.1038/nprot.2006.202.
- [174] G. Holzwarth and P. Doty. The Ultraviolet Circular Dichroism of Polypeptides. *J. Am. Chem. Soc.*, 87(2):218–228, 1965.
- [175] Norma J. Greenfield and Gerald D. Fasman. Computed circular dichroism spectra for the evaluation of protein conformation. *Biochemistry*, 8(10):4108–4116, 1969.

- [176] S. Y. Venyaminov, I. A. Baikalov, Z. M. Shen, C. S. C. Wu, and J. T. Yang. Circular Dichroic Analysis of Denatured Proteins: Inclusion of Denatured Proteins in the Reference Set. *Anal. Biochem.*, 214(1):17–24, October 1993. ISSN 0003-2697.
- [177] Jörg Reichenwallner. *EPR Spectroscopic Characterization of Solution Dynamics of Albumins and Albumin-inspired, Self-organizing Compounds*. PhD thesis, Martin-Luther-Universität Halle-Wittenberg, 2018.

A. Appendix

A.1. α -Synuclein

A.1.1. Influence of Ligand X - X-Band CW-EPR - 1st Series

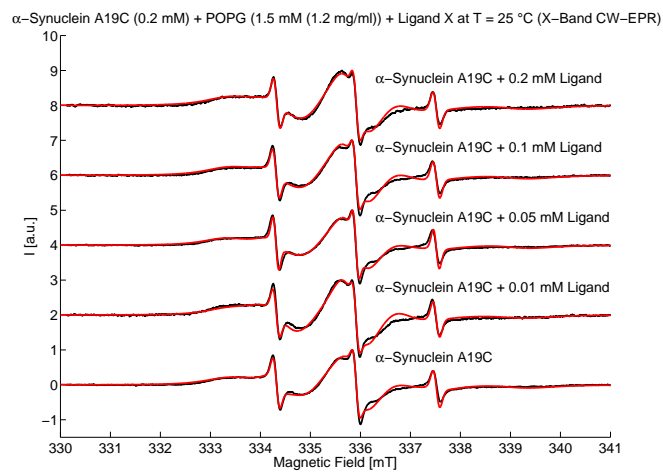


Figure A.1. – Measured spectra (black) and simulations (red) of 0.2 mM α -Synuclein A19C and 1.5 mM POPG in buffer (X-band CW-EPR) + Ligand X (1st Series).

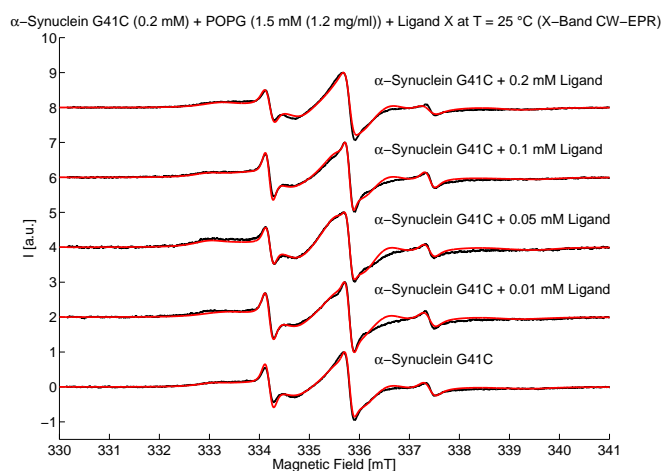


Figure A.2. – Measured spectra (black) and simulations (red) of 0.2 mM α -Synuclein G41C and 1.5 mM POPG in buffer (X-band CW-EPR) + Ligand X (1st Series).

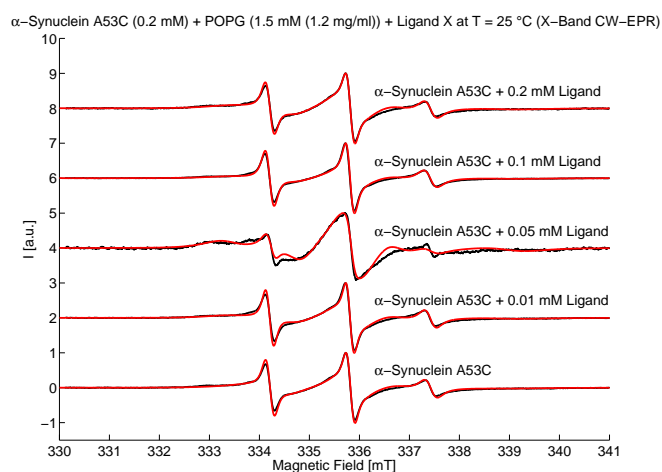


Figure A.3. – Measured spectra (black) and simulations (red) of 0.2 mM α -Synuclein A53C and 1.5 mM POPG in buffer (X-band CW-EPR) + Ligand X (1st Series).

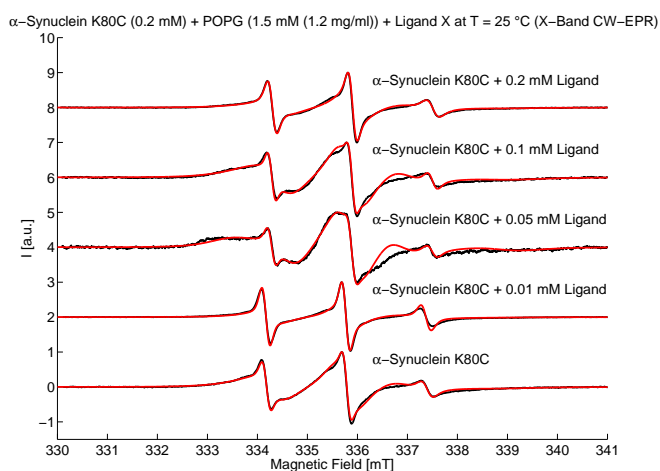


Figure A.4. – Measured spectra (black) and simulations (red) of 0.2 mM α -Synuclein K80C and 1.5 mM POPG in buffer (X-band CW-EPR) + Ligand X (1st Series).

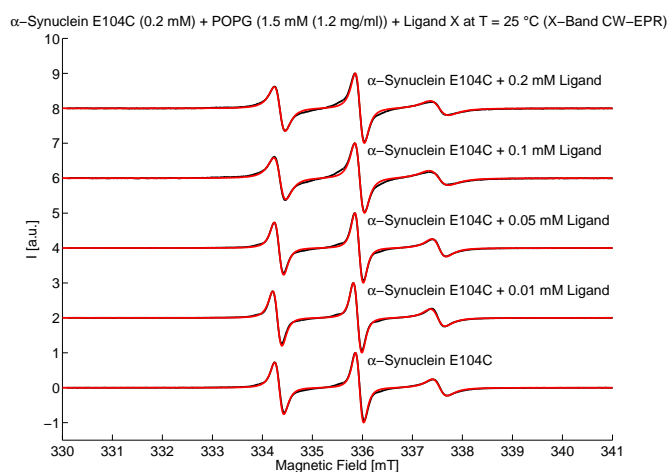


Figure A.5. – Measured spectra (black) and simulations (red) of 0.2 mM α -Synuclein E104C and 1.5 mM POPG in buffer (X-band CW-EPR) + Ligand X (1st Series).

0.2 mM α -Synuclein + 1.5 mM POPG in 20 mM Phosphate + 20 % Glycerol + Ligand X (X-band CW-EPR); 1st Series				
α -Synuclein	Ligand X [mM]	Slow Comp. [%] / τ_c [ns]	Intermediate Comp. [%] / τ_c [ns]	Fast Comp. [%] / τ_c [ns]
A19C	0	91 / 6.360	7 / 1.568	2 / 0.040
A19C	0.2	85 / 7.000	13 / 3.180	2 / 0.066
A19C	0.1	83 / 7.280	15 / 3.732	2 / 0.050
A19C	0.05	83 / 7.223	15 / 4.016	2 / 0.056
A19C	0.01	34 / 8.299	64 / 4.006	2 / 0.064
G41C	0	15 / 18.771	75 / 4.873	10 / 0.830
G41C	0.2	25 / 10.095	65 / 5.904	10 / 0.774
G41C	0.1	25 / 22.527	68 / 5.228	7 / 0.656
G41C	0.05	25 / 20.999	70 / 5.700	5 / 0.659
G41C	0.01	3 / 22.527	87 / 5.904	10 / 0.917
A53C	0	0 / -	75 / 3.739	25 / 0.761
A53C	0.2	0 / -	78 / 5.058	22 / 0.917
A53C	0.1	0 / -	65 / 5.700	35 / 1.558
A53C	0.05	0 / -	93 / 6.994	7 / 1.396
A53C	0.01	0 / -	77 / 5.948	23 / 0.745
K80C	0	0 / -	90 / 3.318	10 / 0.638
K80C	0.2	0 / -	75 / 4.246	25 / 1.182
K80C	0.1	0 / -	95 / 3.709	5 / 0.405
K80C	0.05	0 / -	96 / 5.904	4 / 0.538
K80C	0.01	0 / -	75 / 3.307	25 / 0.435
E104C	0	0 / -	0 / -	100 / 0.938
E104C	0.2	0 / -	0 / -	100 / 1.425
E104C	0.1	0 / -	0 / -	100 / 2.312
E104C	0.05	0 / -	0 / -	100 / 1.197
E104C	0.01	0 / -	0 / -	100 / 1.073

Table A.1. – Percentages and rotational correlation times τ_c of the different components extracted from spectral simulation (X-band CW-EPR) of α -Synuclein + Ligand X (1st Series).

A.1.2. Influence of Ligand X - X-Band CW-EPR - 2nd Series

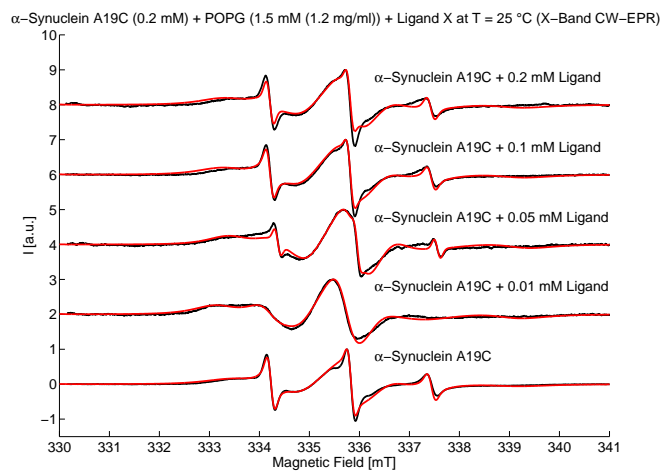


Figure A.6. – Measured spectra (black) and simulations (red) of 0.2 mM α -Synuclein A19C and 1.5 mM POPG in buffer (X-band CW-EPR) + Ligand X (2nd Series).

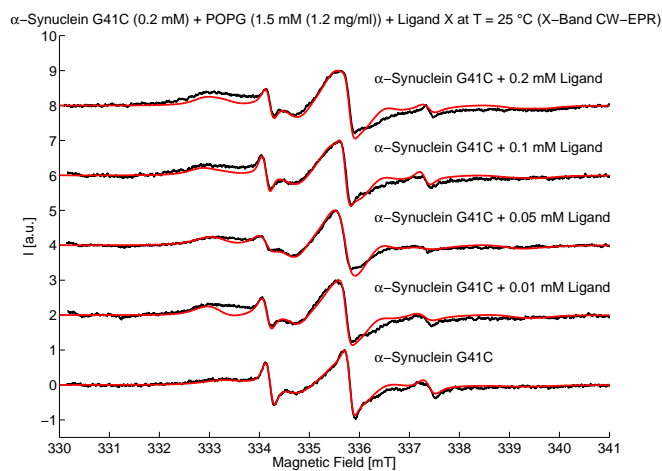


Figure A.7. – Measured spectra (black) and simulations (red) of 0.2 mM α -Synuclein G41C and 1.5 mM POPG in buffer (X-band CW-EPR) + Ligand X (2nd Series).

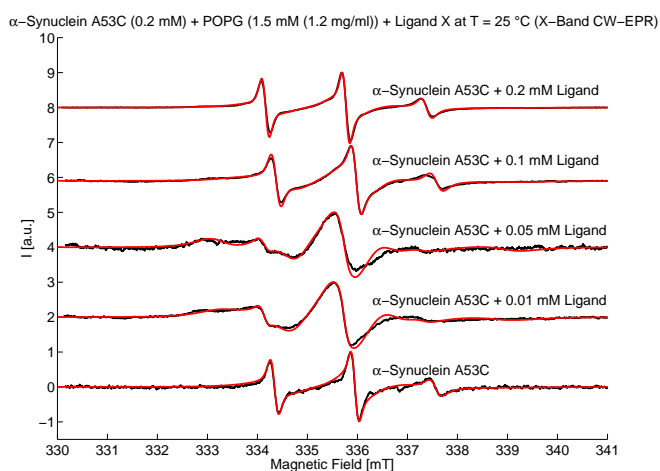


Figure A.8. – Measured spectra (black) and simulations (red) of 0.2 mM α -Synuclein A53C and 1.5 mM POPG in buffer (X-band CW-EPR) + Ligand X (2nd Series).

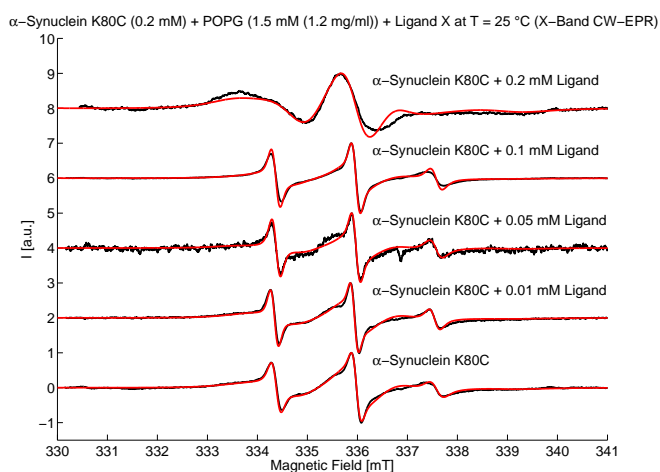


Figure A.9. – Measured spectra (black) and simulations (red) of 0.2 mM α -Synuclein K80C and 1.5 mM POPG in buffer (X-band CW-EPR) + Ligand X (2nd Series).

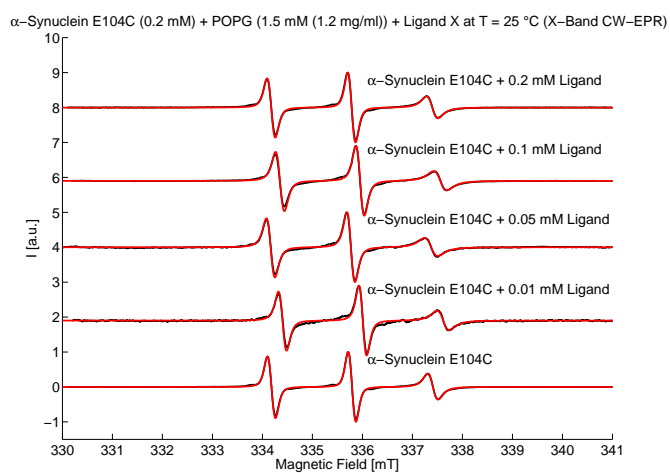


Figure A.10. – Measured spectra (black) and simulations (red) of 0.2 mM α -Synuclein E104C and 1.5 mM POPG in buffer (X-band CW-EPR) + Ligand X (2nd Series).

0.2 mM α -Synuclein + 1.5 mM POPG in 20 mM Phosphate + 20 % Glycerol + Ligand X (X-band CW-EPR); 2nd Series				
α -Synuclein	Ligand X [mM]	Slow Comp. [%] / τ_c [ns]	Intermediate Comp. [%] / τ_c [ns]	Fast Comp. [%] / τ_c [ns]
A19C	0	90 / 6.547	6 / 1.432	4 / 0.211
A19C	0.2	90 / 7.540	7 / 2.705	3 / 0.232
A19C	0.1	90 / 7.822	7 / 1.877	3 / 0.223
A19C	0.05	91 / 6.851	8 / 2.437	1 / 0.049
A19C	0.01	85 / 7.418	15 / 2.397	0 / -
G41C	0	15 / 9.500	75 / 9.172	10 / 0.620
G41C	0.2	20 / 83.333	75 / 8.012	5 / 0.676
G41C	0.1	25 / 45.240	70 / 7.280	5 / 0.459
G41C	0.05	9 / 20.999	83 / 8.012	8 / 1.456
G41C	0.01	9 / 83.333	81 / 12.719	10 / 0.930
A53C	0	0 / -	75 / 3.926	25 / 0.627
A53C	0.2	0 / -	75 / 3.926	25 / 0.578
A53C	0.1	0 / -	81 / 8.012	19 / 0.717
A53C	0.05	0 / -	95 / 8.012	5 / 2.262
A53C	0.01	0 / -	95 / 5.317	5 / 1.425
K80C	0	0 / -	83 / 4.956	17 / 1.159
K80C	0.2	0 / -	99 / 5.904	1 / 3.307
K80C	0.1	0 / -	77 / 3.952	23 / 0.556
K80C	0.05	0 / -	73 / 5.700	27 / 1.456
K80C	0.01	0 / -	85 / 4.767	15 / 1.490
E104C	0	0 / -	0 / -	100 / 0.981
E104C	0.2	0 / -	0 / -	100 / 1.125
E104C	0.1	0 / -	0 / -	100 / 1.291
E104C	0.05	0 / -	0 / -	100 / 1.323
E104C	0.01	0 / -	0 / -	100 / 1.228

Table A.2. – Percentages and rotational correlation times τ_c of the different components extracted from spectral simulation (X-band CW-EPR) of α -Synuclein + Ligand X (2nd Series).

A.1.3. Influence of Ligand X - X-Band CW-EPR - 3rd Series

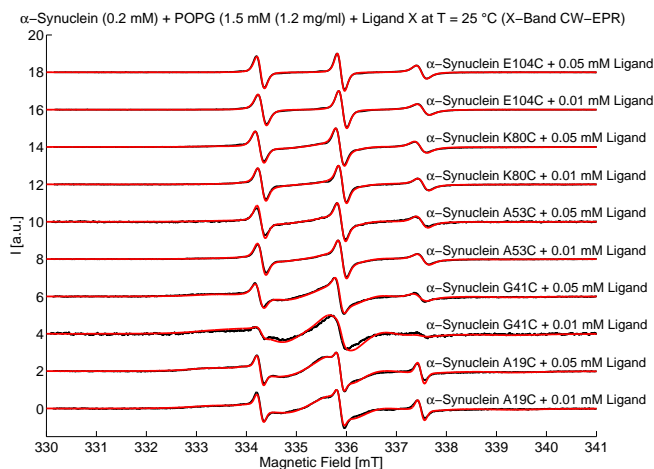


Figure A.11. – Measured spectra (black) and simulations (red) of 0.2 mM α -Synuclein and 1.5 mM POPG in buffer (X-band CW-EPR) + Ligand X (3rd Series).

0.2 mM α -Synuclein + 1.5 mM POPG in 20 mM Phosphate + 20 % Glycerol + Ligand X (X-band CW-EPR); 3rd Series				
α -Synuclein	Ligand X [mM]	Slow Comp. [%] / τ_c [ns]	Intermediate Comp. [%] / τ_c [ns]	Fast Comp. [%] / τ_c [ns]
A19C	0.05	70 / 7.223	27 / 4.016	3 / 0.076
A19C	0.01	88 / 5.904	9 / 2.343	3 / 0.060
G41C	0.05	20 / 9.172	65 / 5.700	15 / 0.950
G41C	0.01	10 / 11.969	87 / 4.686	3 / 0.801
A53C	0.05	0 / -	70 / 4.548	30 / 0.528
A53C	0.01	0 / -	70 / 4.124	30 / 0.710
K80C	0.05	0 / -	60 / 5.904	40 / 0.667
K80C	0.01	0 / -	60 / 3.307	40 / 0.613
E104C	0.05	0 / -	0 / -	100 / 0.956
E104C	0.01	0 / -	0 / -	100 / 1.242

Table A.3. – Percentages and rotational correlation times τ_c of the different components extracted from spectral simulation (X-band CW-EPR) of α -Synuclein + Ligand X (3rd Series).

A.1.4. Influence of Ligand X - X-Band CW-EPR - Simulation Parameters

0.2 mM α -Synuclein + 1.5 mM POPG + Ligand X in 20 mM Phosphate + 20 % Glycerol (X-band CW EPR)				
Sample α -Syn.	Ligand [mM]	g_{iso}	a_{iso} [MHz]	τ_c [ns]
A19C	0	2.0057 2.0056 -	45.0 45.1 -	6.360 6.547 -
A19C	0.2	2.0057 2.0055 -	44.8 45.2 -	7.000 7.540 -
A19C	0.1	2.0057 2.0057 -	45.1 45.3 -	7.280 7.822 -
A19C	0.05	2.0057 2.0057 2.0057	45.1 44.8 44.8	7.223 6.851 7.223
A19C	0.01	2.0058 2.0057 2.0056	44.7 44.3 45.2	4.006 7.418 5.904
G41C	0	2.0056 2.0056 -	45.2 44.8 -	4.873 9.172 -
G41C	0.2	2.0055 2.0059 -	44.9 44.8 -	5.904 8.012 -
G41C	0.1	2.0058 2.0057 -	45.2 44.7 -	5.228 7.280 -
G41C	0.05	2.0057 2.0058 2.0056	44.9 45.2 45.2	5.700 8.012 5.700
G41C	0.01	2.0057 2.0058 2.0057	45.0 44.7 45.3	5.904 12.719 4.686
A53C	0	2.0057 2.0056 -	45.3 45.4 -	3.739 3.926 -
A53C	0.2	2.0057 2.0057 -	45.3 45.3 -	5.058 3.926 -
A53C	0.1	2.0057 2.0056 -	45.3 45.2 -	5.700 8.012 -
A53C	0.05	2.0056 2.0056 2.0058	45.3 45.1 45.3	6.994 8.012 4.548
A53C	0.01	2.0057 2.0056 2.0057	45.3 45.3 45.4	5.948 5.317 4.124
K80C	0	2.0056 2.0056 -	45.2 45.2 -	3.318 4.956 -
K80C	0.2	2.0056 2.0057 -	45.2 43.0 -	4.246 5.904 -
K80C	0.1	2.0057 2.0057 -	45.2 45.2 -	3.709 3.952 -
K80C	0.05	2.0058 2.0056 2.0057	45.2 45.0 45.3	5.904 5.700 5.904
K80C	0.01	2.0056 2.0056 2.0057	45.0 45.0 45.5	3.307 4.767 3.307
E104C	0	2.0057 2.0057 -	45.2 45.4 -	0.938 0.981 -
E104C	0.2	2.0058 2.0058 -	44.8 45.3 -	1.425 1.125 -
E104C	0.1	2.0058 2.0058 -	44.5 45.2 -	2.312 1.291 -
E104C	0.05	2.0057 2.0058 2.0057	45.1 45.2 45.2	1.197 1.323 0.956
E104C	0.01	2.0058 2.0058 2.0057	45.2 45.2 45.3	1.073 1.228 1.242

Table A.4. – X-band CW-EPR simulation parameters of 0.2 mM α -Synuclein + 1.5 mM POPG + Ligand X + 20 % glycerol in buffer. Values are listed for all three measurement series in one column and are separated by a line.

A.1.5. Influence of Ligand X - Q-Band CW-EPR - 1st Series

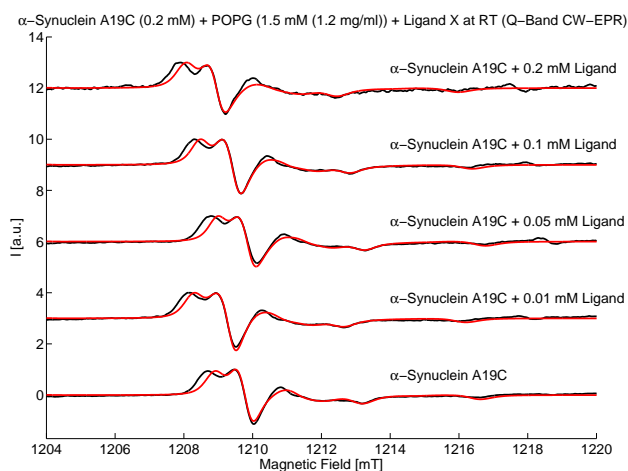


Figure A.12. – Measured spectra (black) and simulations (red) of 0.2 mM α -Synuclein A19C and 1.5 mM POPG in buffer (Q-band CW-EPR) + Ligand X (1st Series).

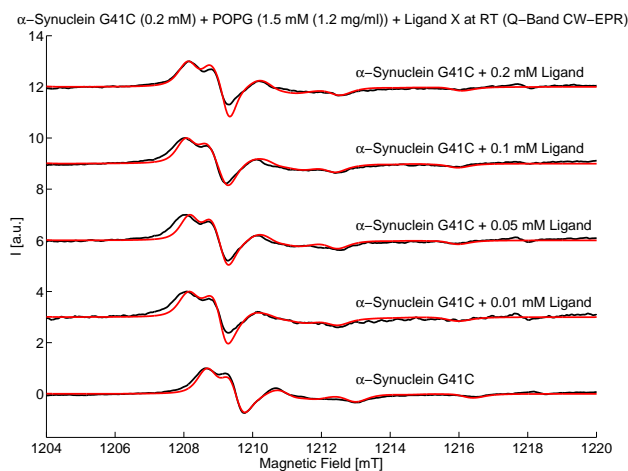


Figure A.13. – Measured spectra (black) and simulations (red) of 0.2 mM α -Synuclein G41C and 1.5 mM POPG in buffer (Q-band CW-EPR) + Ligand X (1st Series).

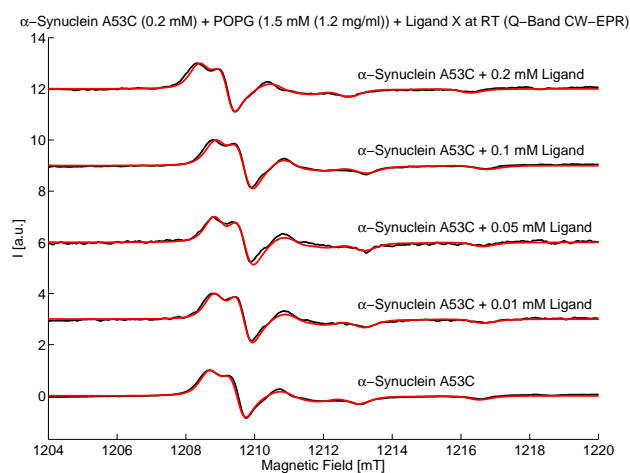


Figure A.14. – Measured spectra (black) and simulations (red) of 0.2 mM α -Synuclein A53C and 1.5 mM POPG in buffer (Q-band CW-EPR) + Ligand X (1st Series).

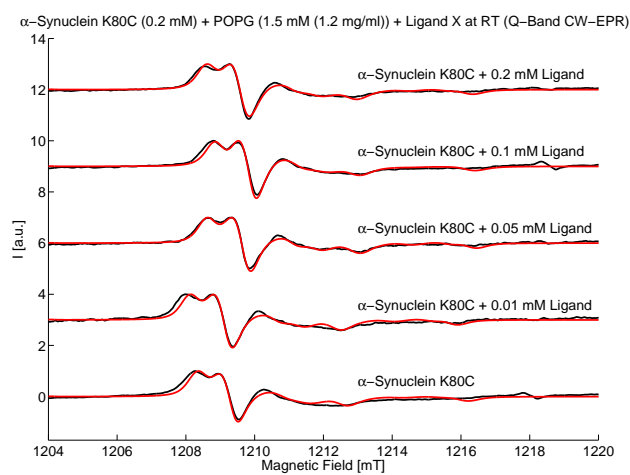


Figure A.15. – Measured spectra (black) and simulations (red) of 0.2 mM α -Synuclein K80C and 1.5 mM POPG in buffer (Q-band CW-EPR) + Ligand X (1st Series).

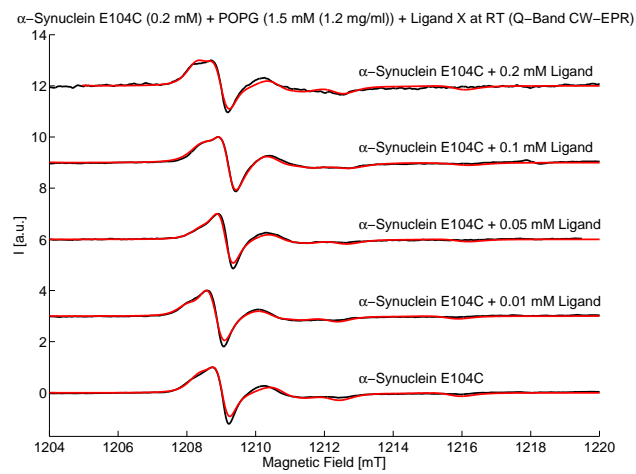


Figure A.16. – Measured spectra (black) and simulations (red) of 0.2 mM α -Synuclein E104C and 1.5 mM POPG in buffer (Q-band CW-EPR) + Ligand X (1st Series).

0.2 mM α -Synuclein + 1.5 mM POPG in 20 mM Phosphate + 20 % Glycerol + Ligand X (Q-band CW-EPR); 1st Series			
α -Synuclein	Ligand X [mM]	Slow Comp. [%] / τ_c [ns]	Fast Comp. [%] / τ_c [ns]
A19C	0	82 / 63.595	18 / 13.340
A19C	0.2	90 / 72.798	10 / 10.095
A19C	0.1	85 / 80.125	15 / 6.469
A19C	0.05	85 / 80.125	15 / 10.875
A19C	0.01	83 / 80.125	17 / 5.556
G41C	0	80 / 72.798	20 / 10.095
G41C	0.2	85 / 72.798	15 / 3.333
G41C	0.1	85 / 97.467	15 / 5.904
G41C	0.05	85 / 63.595	15 / 5.904
G41C	0.01	90 / 83.333	10 / 6.614
A53C	0	90 / 63.595	10 / 9.500
A53C	0.2	90 / 63.595	10 / 10.499
A53C	0.1	93 / 45.240	7 / 16.667
A53C	0.05	95 / 63.595	5 / 10.875
A53C	0.01	90 / 63.595	10 / 10.875
K80C	0	87 / 104.993	13 / 7.280
K80C	0.2	85 / 132.283	15 / 7.280
K80C	0.1	85 / 61.401	15 / 6.140
K80C	0.05	90 / 166.667	10 / 16.667
K80C	0.01	90 / 166.667	10 / 16.667
E104C	0	70 / 61.147	30 / 17.262
E104C	0.2	85 / 56.999	15 / 18.771
E104C	0.1	80 / 29.518	20 / 6.420
E104C	0.05	60 / 45.546	40 / 16.667
E104C	0.01	65 / 66.142	35 / 17.954

Table A.5. – Percentages and rotational correlation times τ_c of the different components extracted from spectral simulation (Q-band CW-EPR) of α -Synuclein + Ligand X (1st Series).

A.1.6. Influence of Ligand X - Q-Band CW-EPR - 2nd Series

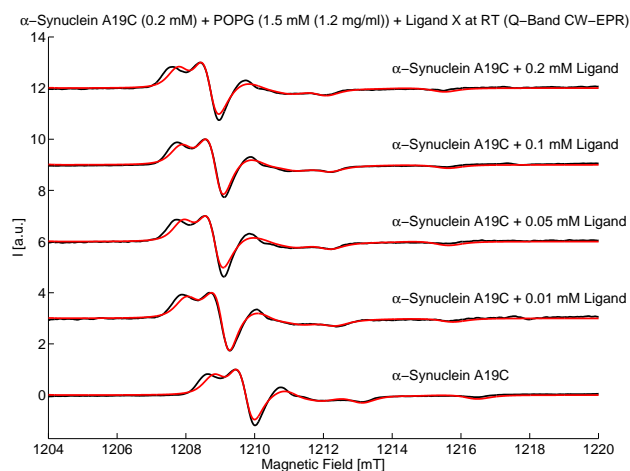


Figure A.17. – Measured spectra (black) and simulations (red) of 0.2 mM α -Synuclein A19C and 1.5 mM POPG in buffer (Q-band CW-EPR) + Ligand X (2nd Series).

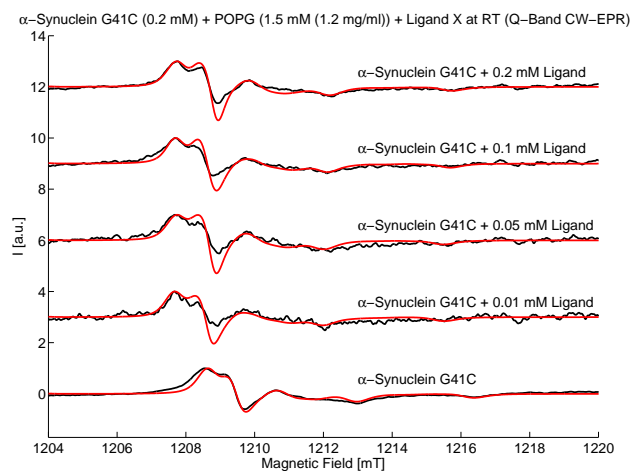


Figure A.18. – Measured spectra (black) and simulations (red) of 0.2 mM α -Synuclein G41C and 1.5 mM POPG in buffer (Q-band CW-EPR) + Ligand X (2nd Series).

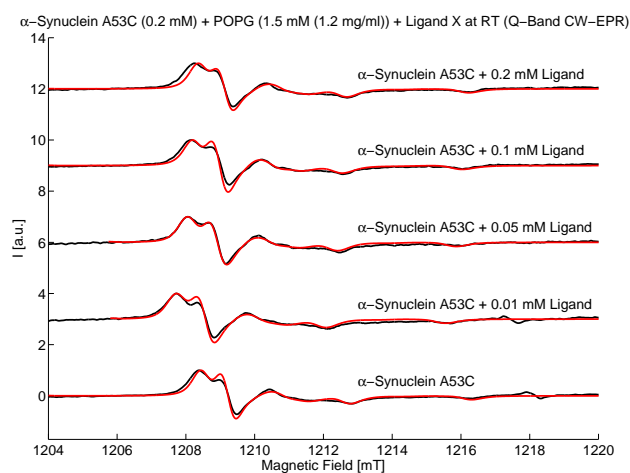


Figure A.19. – Measured spectra (black) and simulations (red) of 0.2 mM α -Synuclein A53C and 1.5 mM POPG in buffer (Q-band CW-EPR) + Ligand X (2nd Series).

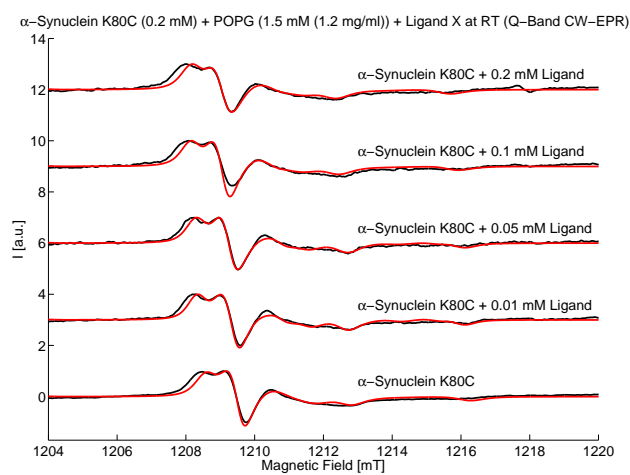


Figure A.20. – Measured spectra (black) and simulations (red) of 0.2 mM α -Synuclein K80C and 1.5 mM POPG in buffer (Q-band CW-EPR) + Ligand X (2nd Series).

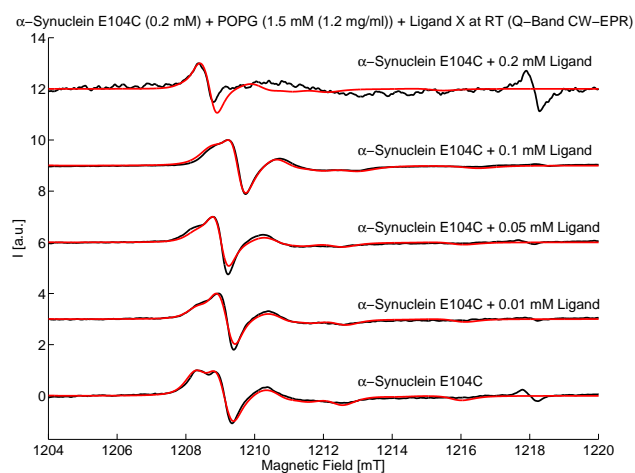


Figure A.21. – Measured spectra (black) and simulations (red) of 0.2 mM α -Synuclein E104C and 1.5 mM POPG in buffer (Q-band CW-EPR) + Ligand X (2nd Series).

0.2 mM α -Synuclein + 1.5 mM POPG in 20 mM Phosphate + 20 % Glycerol + Ligand X (Q-band CW-EPR); 2nd Series			
α -Synuclein	Ligand X [mM]	Slow Comp. [%] / τ_c [ns]	Fast Comp. [%] / τ_c [ns]
A19C	0	84 / 63.595	16 / 32.489
A19C	0.2	82 / 72.798	18 / 10.095
A19C	0.1	82 / 80.125	18 / 6.469
A19C	0.05	85 / 80.125	15 / 10.875
A19C	0.01	84 / 80.125	16 / 5.556
G41C	0	85 / 67.580	15 / 4.686
G41C	0.2	85 / 72.798	15 / 3.333
G41C	0.1	85 / 97.467	15 / 5.904
G41C	0.05	80 / 63.595	20 / 5.904
G41C	0.01	90 / 83.333	10 / 6.614
A53C	0	90 / 63.595	10 / 9.500
A53C	0.2	90 / 63.595	10 / 10.499
A53C	0.1	88 / 45.240	12 / 16.667
A53C	0.05	95 / 63.595	5 / 10.875
A53C	0.01	90 / 63.595	10 / 10.875
K80C	0	80 / 52.497	20 / 7.280
K80C	0.2	89 / 52.913	11 / 7.280
K80C	0.1	88 / 40.062	12 / 6.140
K80C	0.05	91 / 115.560	9 / 10.499
K80C	0.01	90 / 166.667	10 / 16.667
E104C	0	85 / 71.814	15 / 16.667
E104C	0.2	20 / 38.520	80 / 16.667
E104C	0.1	80 / 29.518	20 / 6.420
E104C	0.05	60 / 45.546	40 / 16.667
E104C	0.01	65 / 66.142	35 / 17.954

Table A.6. – Percentages and rotational correlation times τ_c of the different components extracted from spectral simulation (Q-band CW-EPR) of α -Synuclein + Ligand X (2nd Series).

A.1.7. Influence of Ligand X - Q-Band CW-EPR - 3rd Series

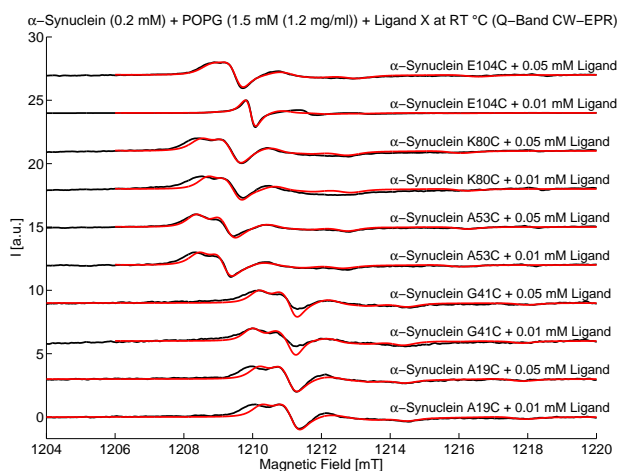


Figure A.22. – Measured spectra (black) and simulations (red) of 0.2 mM α -Synuclein and 1.5 mM POPG in buffer (Q-band CW-EPR) + Ligand X (3rd Series).

0.2 mM α -Synuclein + 1.5 mM POPG in 20 mM Phosphate + 20 % Glycerol + Ligand X (Q-band CW-EPR); 3rd Series			
α -Synuclein	Ligand X [mM]	Slow Comp. [%] / τ_c [ns]	Fast Comp. [%] / τ_c [ns]
A19C	0.05	90 / 72.798	10 / 22.527
A19C	0.01	90 / 70.882	10 / 22.527
G41C	0.05	85 / 52.497	15 / 5.904
G41C	0.01	90 / 104.993	10 / 3.852
A53C	0.05	95 / 63.595	5 / 10.875
A53C	0.01	90 / 27.402	10 / 13.228
K80C	0.05	90 / 56.999	10 / 16.667
K80C	0.01	90 / 33.790	10 / 22.527
E104C	0.05	81 / 45.546	19 / 16.667
E104C	0.01	15 / 66.142	85 / 5.700

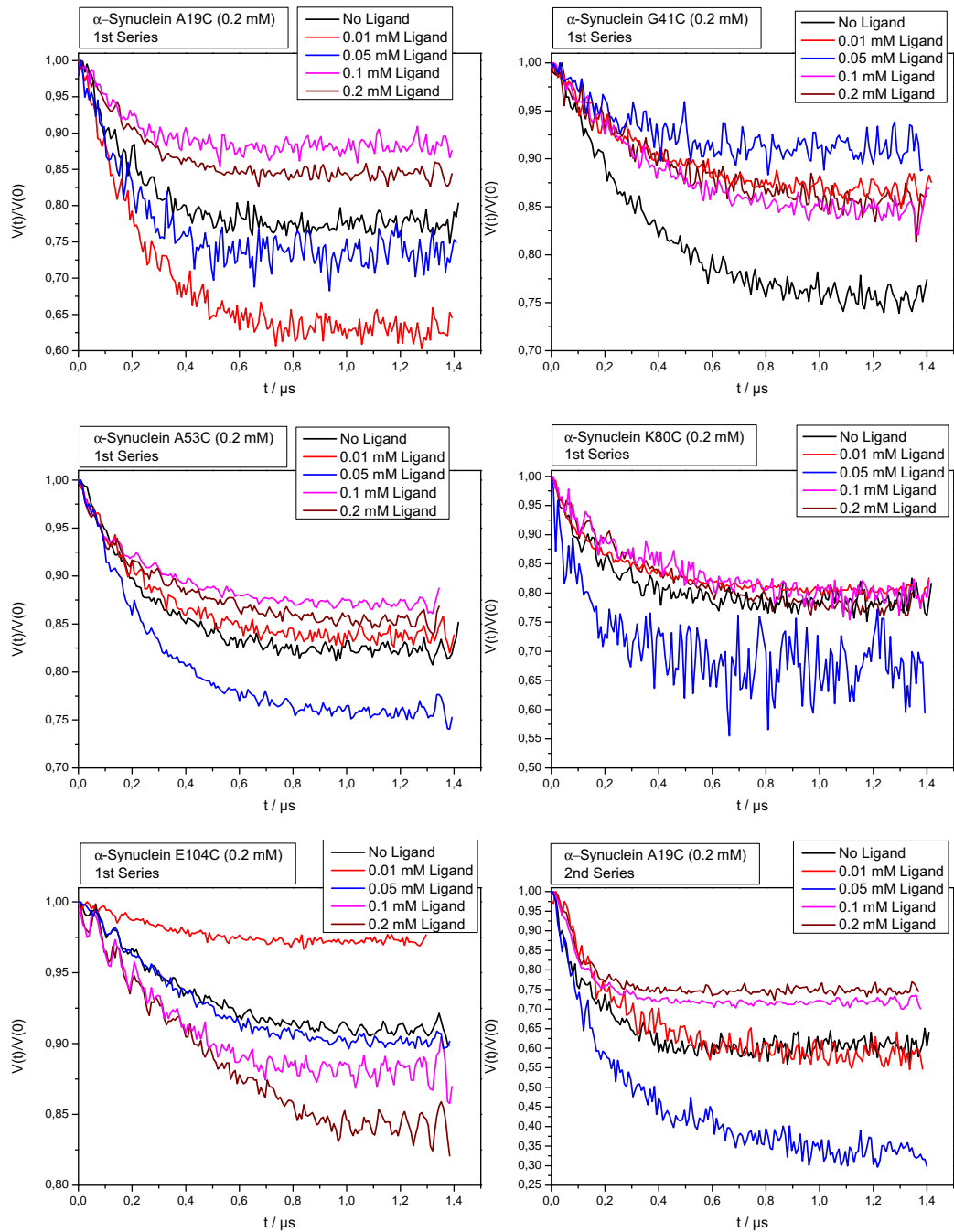
Table A.7. – Percentages and rotational correlation times τ_c of the different components extracted from spectral simulation (Q-band CW-EPR) of α -Synuclein + Ligand X (3rd Series).

A.1.8. Influence of Ligand X - Q-Band CW-EPR - Simulation Parameters

0.2 mM α -Synuclein + 1.5 mM POPG + Ligand X in 20 mM Phosphate + 20 % Glycerol (Q-band CW EPR)					
Sample	Ligand [mM]	g_{xx}	g_{zz}	A_{zz} [MHz]	τ_c [ns]
α -Syn. A19C	0	2.0090 2.0090 -	2.0029 2.0028 -	98.0 95.5 -	63.595 63.595 -
α -Syn. A19C	0.2	2.0090 2.0090 -	2.0028 2.0029 -	100.3 98.0 -	72.798 72.798 -
α -Syn. A19C	0.1	2.0090 2.0090 -	2.0028 2.0028 -	101.0 98.0 -	80.125 80.125 -
α -Syn. A19C	0.05	2.0090 2.0090 2.0090	2.0030 2.0029 2.0029	100.5 98.0 98.0	80.125 80.125 72.798
α -Syn. A19C	0.01	2.0090 2.0090 2.0090	2.0028 2.0028 2.0029	101.0 97.5 98.0	80.125 80.125 70.882
α -Syn. G41C	0	2.0090 2.0090 -	2.0028 2.0027 -	97.0 97.0 -	72.798 67.580 -
α -Syn. G41C	0.2	2.0090 2.0090 -	2.0027 2.0026 -	101.0 101.0 -	72.798 72.798 -
α -Syn. G41C	0.1	2.0090 2.0090 -	2.0030 2.0028 -	101.0 101.0 -	97.467 97.467 -
α -Syn. G41C	0.05	2.0090 2.0090 2.0090	2.0029 2.0029 2.0028	100.0 99.0 100.0	63.595 63.595 52.497
α -Syn. G41C	0.01	2.0090 2.0090 2.0090	2.0029 2.0029 2.0029	100.0 100.0 98.0	83.333 83.333 104.993
α -Syn. A53C	0	2.0090 2.0090 -	2.0029 2.0028 -	100.5 100.5 -	63.595 63.595 -
α -Syn. A53C	0.2	2.0090 2.0090 -	2.0029 2.0029 -	101.0 101.0 -	63.595 63.595 -
α -Syn. A53C	0.1	2.0090 2.0090 -	2.0026 2.0026 -	100.0 100.0 -	45.240 45.240 -
α -Syn. A53C	0.05	2.0090 2.0090 2.0090	2.0028 2.0028 2.0028	98.0 98.0 99.0	63.595 63.595 63.595
α -Syn. A53C	0.01	2.0090 2.0090 2.0090	2.0028 2.0028 2.0027	99.0 99.0 99.8	63.595 63.595 27.402
α -Syn. K80C	0	2.0090 2.0090 -	2.0030 2.0030 -	99.0 99.0 -	104.993 52.497 -
α -Syn. K80C	0.2	2.0090 2.0090 -	2.0030 2.0030 -	95.0 95.0 -	132.283 52.913 -
α -Syn. K80C	0.1	2.0090 2.0090 -	2.0030 2.0027 -	95.0 99.0 -	61.401 40.062 -
α -Syn. K80C	0.05	2.0090 2.0090 2.0090	2.0029 2.0028 2.0029	95.0 96.0 95.0	166.667 115.560 56.999
α -Syn. K80C	0.01	2.0090 2.0090 2.0090	2.0030 2.0030 2.0029	95.0 95.0 98.0	166.667 166.667 33.790
α -Syn. E104C	0	2.0090 2.0090 -	2.0034 2.0031 -	101.8 98.5 -	61.147 71.814 -
α -Syn. E104C	0.2	2.0090 2.0084 -	2.0029 2.0025 -	101.8 99.0 -	56.999 16.667 -
α -Syn. E104C	0.1	2.0090 2.0090 -	2.0025 2.0025 -	101.8 101.8 -	29.518 29.518 -
α -Syn. E104C	0.05	2.0090 2.0090 2.0090	2.0029 2.0029 2.0029	102.5 102.5 102.5	45.546 45.546 45.546
α -Syn. E104C	0.01	2.0090 2.0090 2.0084	2.0029 2.0030 2.0029	100.5 99.5 95.5	66.142 66.142 5.700

Table A.8. – Q-band CW-EPR simulation parameters of 0.2 mM α -Synuclein + 1.5 mM POPG + Ligand X + 20 % glycerol in buffer. Values are listed for all three measurement series in one column and are separated by a line.

A.1.9. Influence of Ligand X - DEER Time Traces



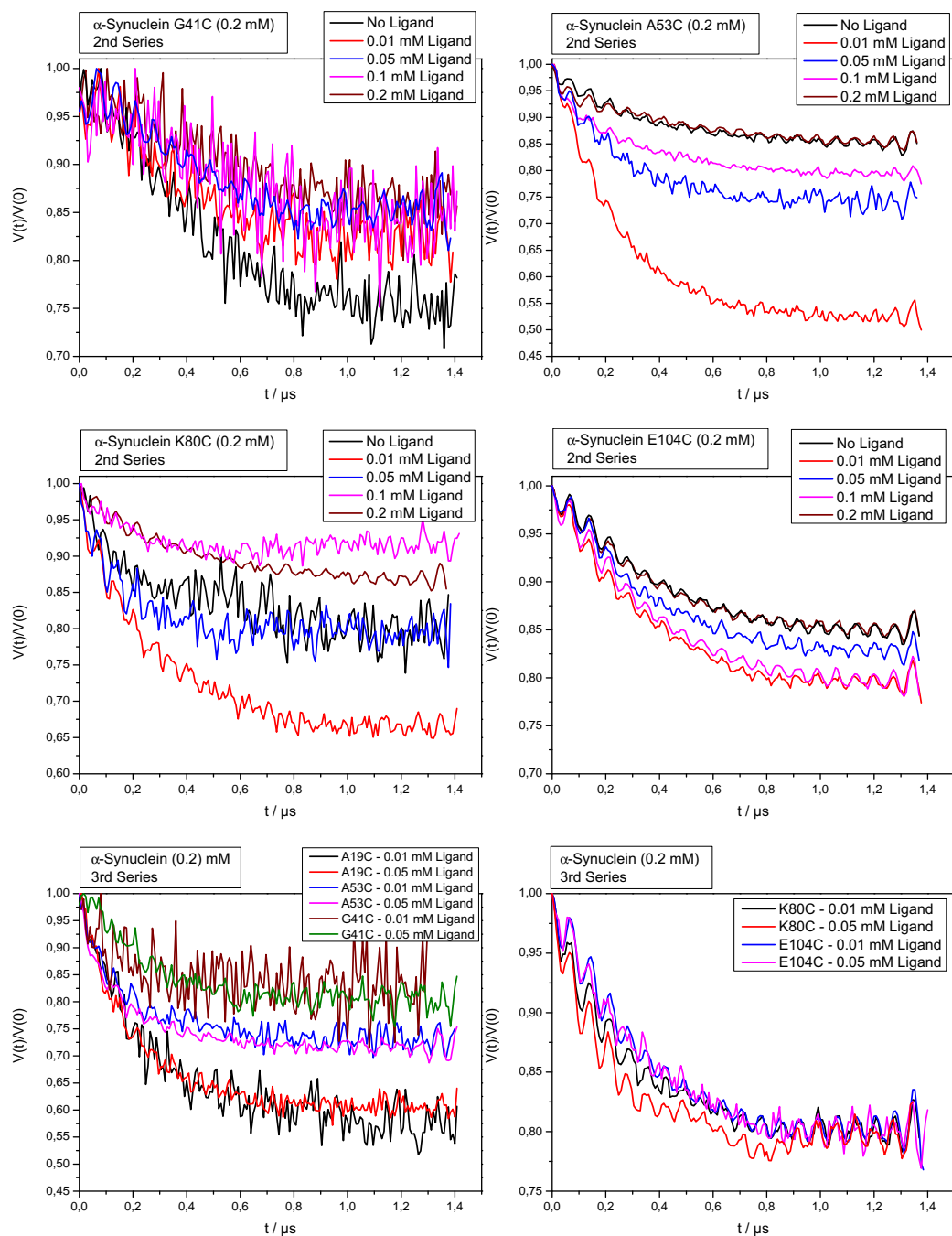


Figure A.23. – Influence of Ligand X on α -Synuclein (DEER Time Traces).

A.1.10. Scaling of Δ_{eff}

When the α -Synuclein measurements of the first series with the Ligand X were carried out, the π pump pulse at the pump frequency had to be set to a length of 32 ns due to spectrometer issues. With the pump pulse length of 12 ns no inversion of the signal could be obtained. Measurement and analysis of the few respective data worked, however when checking a reference biradical measurement, it was obvious that the λ -factor of 0.52 retains, but the measured modulation depths are significantly lower indicating an inferior excitation.

In the case of the few measurements where this spectrometer issue applied, a scaling of the modulation depths has been carried out. However it is strongly emphasized that this is just for the sake of a better comparison between the different ligand series and results should be treated with care.

The biradical measured was the “ruler 3” [120], which was newly prepared by Reichenwallner [177] and termed as “Biradical 2”.

“Biradical 2”			
	Pump Pulse [ns]	Δ	Coupled Spins
1	12	0.311	1.73
2	32	0.229	1.50
3	32	0.251	1.55

Table A.9. – DEER Parameters of the “Biradical 2”

The average value of Δ of the two biradical measurements with the 32 ns pump pulse is 0.240. The value of the 12 ns pump pulse measurement of 0.311 is thus 1.3 times higher. Modulation depths of the ligand measurements where this use of the longer pump pulse was the case are thus scaled by a factor of 1.3 for a better comparison. The affected measurements of the first series are: α -Synuclein A19C, G41C, and A53C completely, furthermore α -Synuclein K80C + 0.01 mM Ligand X and α -Synuclein K80C + 0.05 mM Ligand X as well as α -Synuclein E104C, α -Synuclein E104C + 0.01 mM Ligand X and α -Synuclein E104C + 0.05 mM Ligand X.

A.1.11. Fatty acid distribution of Porcine Brain Lipids

Fatty acid distribution of Porcine Brain Lipids				
Fatty acids	Brain PC [%]	Brain PS [%]	Brain PE [%]	Brain SM [%]
14:0	0.3	0	0	0
14:1	0	0	0	0
16:0	30.6	0	3.7	2.0
16:1	0.9	0	0.6	0
18:0	16.5	42.0	15.9	50.0
18:1	33.3	30.0	24.1	0
18:2	1.1	0	0.4	0
18:3	0	0	0	0
20:0	0	0	0	5.0
20:1	0.8	0	2.3	0
20:2	0	0	0.6	0
20:3	0.2	0	0.6	0
20:4	3.1	2	18.6	0
22:0	0	0	0	7.0
22:1	0	0	0.5	0
22:6	0.6	11.0	11.5	0
24:0	0	0	0	5.0
24:1	0	0	0	21.0
Unknown	12.8	15.0	21.1	10.0

Table A.10. – Fatty acid distribution of Porcine Brain Lipids. Shown is the percentage of the different fatty acids in commercially available porcine brain lipids. Values were taken from the Avanti Polar Lipids website from where the lipids were purchased.

A.1.12. Epi-Fluorescence Microscopy

Epi-Fluorescence Microscopy was carried out to determine whether the synaptic vesicle composition shows a phase transition. This technique combines a home-built Langmuir monolayer trough (Riegler & Kirstein, Berlin, Germany) for determination of compression isotherms and the fluorescence microscopy (Axio Scope.A1 Vario Microscope, Carl Zeiss MicroImaging, Jena, Germany). The trough is again placed in a plastic hood to prevent perturbations of dust and also air draft. Moreover, the trough is placed on a x-y-z-table (Märzhäuser, Wetzlar, Germany) to be able to move the monolayer surface (x-y-z motion control, Ludl Electronic Products, Hawthorne, USA). To

maintain a steady temperature of the aqueous subphase, the trough is connected to a thermostat (Haake DC30-K10, ThermoFisher Scientific, Waltham, USA), which was set to 20 °C. Furthermore the microscope comprises a HXP 120C lamp (Kübler Codix, Villingen-Schwenningen, Germany), a long distance EC-Epiplan NEOFLUAR-objective (magnification 50x) and different filter sets for excitation and detection. For the measurement in this work the fluorescence label Rhodamin-DHPE was added to the SV mix to about 5 mol-%. The label prefers the expanded phase, which appears bright, whereas the condensed domains appear dark. The filter set used is the Fs 20 (excitation band-pass BP 546/12 nm, beam splitter FT 560 nm, emission band-pass BP575-640nm). The images were recorded with a CCD camera (ImageEM C9100-13, Hamamatsu, Herrsching, Germany). Data acquisition was accomplished with the AxioVision software (Carl Zeiss MicroImaging, Jena, Germany).

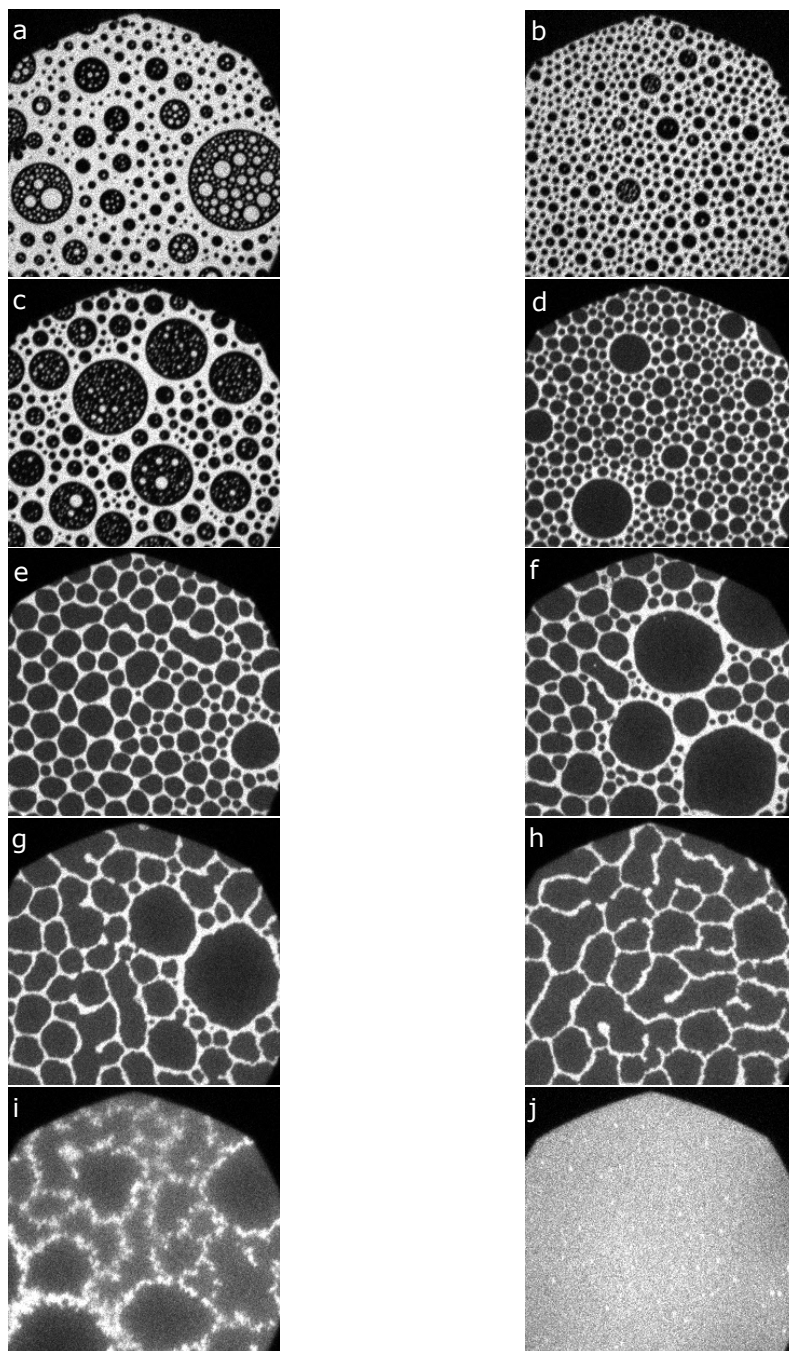


Figure A.24. – Epi-Fluorescence Images of the Synaptic Vesicle Composition. a: gaseous phase ($A = 112 \text{ \AA}^2/\text{molecule}$); b: near Lift-Off ($A = 77 \text{ \AA}^2/\text{molecule}$); c,d: liquid-expanded phase (48 and $39 \text{ \AA}^2/\text{molecule}$, respectively; e-i: condensed phases are getting bigger (area about $39\text{-}33 \text{ \AA}^2/\text{molecule}$), j: after film collapse at about $32 \text{ \AA}^2/\text{molecule}$

A.2. HPRG

A.2.1. Alternative Purification Approaches of HPRG

More recent purification approaches of HPRG were based on nickel affinity chromatography and size exclusion chromatography, as published by Kassar et al. [87] and on cobalt affinity chromatography and anion exchange chromatography as published by Patel et al. [130]. Fig. A.25 shows elution fractions of the purification of rabbit serum HPRG with nickel affinity chromatography, which was carried out as published by Kassar et al. [87]. As expected, besides HPRG also serum albumin elutes from the column.

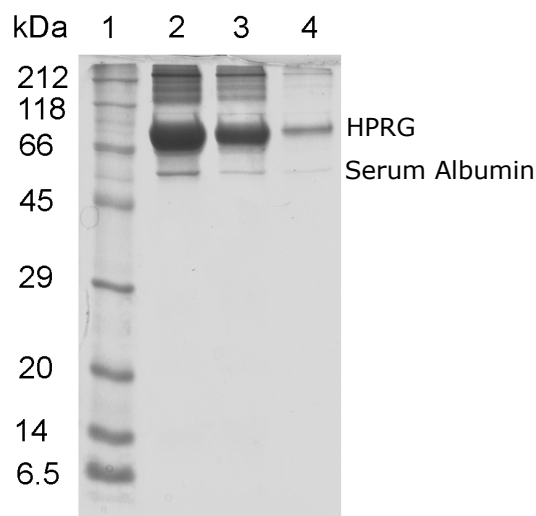


Figure A.25. – Coomassie-stained SDS-gel of nickel affinity chromatography. Three consecutive elution fractions of nickel affinity chromatography (His Trap HP, GE Healthcare) are shown in lanes 2, 3, and 4. HPRG was eluted with 400 mM imidazole, as described by Kassar et al. [87]. As expected, besides HPRG also serum albumin is found in the elution fractions.

Separation of HPRG and serum albumin could not be achieved by gel filtration with a Superdex 200 column, see Fig. A.26 and also not via anion exchange chromatography, see Fig. A.27.

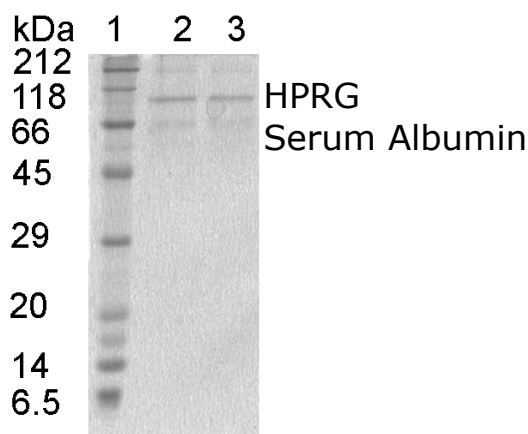


Figure A.26. – Coomassie-stained reducing SDS-gel of gel filtration. SDS-PAGE of gel filtration (Superdex 200 10/300 GL, GE Healthcare). There is a fragment visible at the marker height (lane 1) of BSA. The size exclusion chromatography column was equilibrated with 25 mM phosphate, 154 mM NaCl, pH 7.4. The sample applied to the column was the elution fraction of the cobalt affinity chromatography.

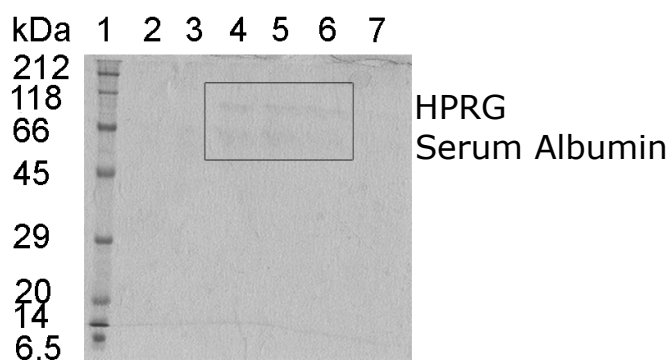


Figure A.27. – Coomassie-stained reducing SDS-gel of anion exchange chromatography. SDS-PAGE of elution fractions from anion exchange chromatography (Hi Trap Q FE, GE Healthcare). Yields are very low in lane 4, 5, and 6. A fragment running at the marker height (lane 1) of BSA is visible. For the anion exchange, the cobalt affinity chromatography elution sample was diluted in 20 mM Tris, pH 8.5. The column was washed with the same buffer and HPRG eluted with 20 mM Tris, 500 mM NaCl, pH 8.5.

A.2.2. Mass Spectrometry Data

nanoLC-ESI-MS/MS Results from the Tryptic Digest of HPRG before PNGase F treatment
Comparison against Sequence AAC48516.1

Peptide	Start	End	Modifiers	Calculated Peptide Mass (Da)	RT (Min)	m/z	Charge State	Observed Peptide Mass (Da)	Intensity (Counts)	Control Mass Error (ppm)
TTKPLAEK	16	23		886,5124	12,1	444,2635	2	886,5112	42338	-1,4
TTKPLAEK	16	23		886,5124	23,5	444,2659	2	886,5116	2883	4,1
ALDLINK	24	30		785,4647	17,3	393,7396	2	785,4633	601471	-1,8
RDGYLFQLLR	33	42		1279,7037	21,1	427,5753	3	1279,7021	720377	-1,3
DGYLFQLLR	34	42		1123,6025	22,8	562,8091	2	1123,6023	644488	-0,2
VADAHLDGAESATVYLVLV										
DVK	43	64		2348,1899	22,1	783,7374	3	2348,1882	1478884	-0,7
VADAHLDGAESATVYLVLV										
DVK	43	64		2348,1899	23,1	783,7377	3	2348,1892	382318	-0,3
ETDCSVLSR	65	73	Carbamidomethyl C(1)	1065,4761	14,8	533,7456	2	1065,4753	664889	-0,8
KHWEDCDPDLTK	74	85	Carbamidomethyl C(1)	1542,6772	14,5	515,2334	3	1542,6764	864719	-0,5
HWEDCDPDLTK	75	85	Carbamidomethyl C(1)	1414,5824	15,5	708,2985	2	1414,5812	86202	-0,8
RPSLDVIGQCK	86	96	Carbamidomethyl C(1)	1271,6656	16,2	636,8399	2	1271,6639	814365	-1,3
YSDEYQTLR	102	110		1173,5303	15,4	587,7729	2	1173,5299	1000655	-0,3
DSPVLFDFIEDTEPFRK	130	146		2053,9995	23,3	685,6752	3	2054,0017	1408052	1,1
DSPVLFDFIEDTEPFR	130	145		1925,9047	23,5	963,9623	2	1925,9087	612002	2,1
DSPVLFDFIEDTEPFRK	130	146		2053,9995	22,5	685,6752	3	2054,0017	1990	1,1
ALEVYK	151	156		721,401	15,3	361,7086	2	721,4014	424748	0,6
ALEVYKSESEAYASFR	151	166		1848,8894	18,1	617,3039	3	1848,8878	1680	-0,9
ALEVYKSESEAYASFR	151	166		1848,8894	23,6	925,4567	2	1848,8975	1111	4,4
SESEAYASFR	157	166		1145,4989	15,8	573,7573	2	1145,4987	1001702	-0,2
VDRVER	167	172		772,4191	11,4	387,2174	2	772,4189	2460	-0,3
VTR	173	175		374,2278	13,4	375,2355	1	374,2276	6455	-0,5
TNYVDFSVR	182	191		1262,5931	19,1	632,3041	2	1262,5923	1026489	-0,6
SFHFR	196	200		682,33	5,3	342,1735	2	682,3311	3761	1,6
HPAFGFCR	201	208	Carbamidomethyl C(1)	990,4494	16	496,232	2	990,4482	453444	-1,2
ADLSFDVEASNLENPEDVIIS										
CEVFNFEHGHISGFRPHLG										
K	209	250	Carbamidomethyl C(1)	4731,2188	23,1	947,2527	5	4731,2236	11417	1
TPLGTDGSR	251	259		902,4457	13,4	452,2311	2	902,4463	571687	0,7
FPHHR	315	319		692,3506	11,4	347,1825	2	692,3491	6162	-2,2
FPHHR	315	319		692,3506	10,1	347,1825	2	692,3491	4455	-2,2
GHFPFHWR	447	454		1082,5199	17,6	361,8481	3	1082,5206	94881	0,6
RIGSVYQLPPLQK	455	467		1497,8667	18,4	500,2966	3	1497,8661	94964	-0,4
IGSVYQLPPLQK	456	467		1341,7656	19,1	671,8901	2	1341,7643	1612751	-1
NHHTPLKPEIQFPQVASER	485	504		2324,2026	17	582,0579	4	2324,2	27835	-1,1
CPEEFNGEFAQLSK	505	518	Carbamidomethyl C(1)	1654,7297	18,7	552,5845	3	1654,7297	13569	0
CPEEFNGEFAQLSK	505	518	Carbamidomethyl C(1)	1654,7297	18,8	1655,7305	1	1654,7225	2708	-4,4
FFPSTFPK	519	526		969,496	19	485,7561	2	969,4963	1150300	0,3

Figure A.28. – nanoLC-ESI-MS/MS results from the tryptic digest of lyophilized HPRG before PNGase F treatment. Comparison against “old” sequence AAC48516.1 [82].

nanoLC-ESI-MS/MS Results from the Tryptic Digest of HPRG before PNGase F treatment
Comparison against Sequence XP_008264798.1

Protein	Peptide	Start	End	Modifiers	Calculated Peptide Mass (Da)	Control Mass Error (ppm)
HPRG_XP	TTKPLAEK	26	33		886,5124	-1,4
HPRG_XP	TTKPLAEK	26	33		886,5124	4,1
HPRG_XP	ALDLINK	34	40		785,4647	-1,8
HPRG_XP	DLINK	36	40		601,3435	-2
HPRG_XP	RDGYLFQLLR	43	52		1279,7037	-1,3
HPRG_XP	RDGYLFQ	43	49		879,4239	-0,7
HPRG_XP	RDGYL	43	47		604,2969	-1,7
HPRG_XP	RDGYLF	43	48		751,3653	-1,3
HPRG_XP	RDGYLFQL	43	50		992,5079	1
HPRG_XP	DGYLFQLLR	44	52		1123,6025	-0,2
HPRG_XP	VADAHLDGAESATVYYL VLDVK	53	74		2348,1899	-0,7
HPRG_XP	VADAHLDGAESATVYYL VLDVK	53	74		2348,1899	-0,3
HPRG_XP	VADAHLDGAESATVYYL VL	53	71		1987,989	1,1
HPRG_XP	ETDCSVLSR	75	83	Carbamidomethyl C(1)	1065,4761	-0,8
HPRG_XP	KHWEDCDPDLTK	84	95	Carbamidomethyl C(1)	1542,6772	-0,5
HPRG_XP	KHWEDCD	84	90	Carbamidomethyl C(1)	970,3604	1,2
HPRG_XP	HWEDCDPDLTK	85	95	Carbamidomethyl C(1)	1414,5824	-0,8
HPRG_XP	RPSLDVIGQCK	96	106	Carbamidomethyl C(1)	1271,6656	-1,3
HPRG_XP	RPSLDVI	96	102		780,4493	-0,3
HPRG_XP	RPSLDV	96	101		667,3653	-1,8
HPRG_XP	RPSLD	96	100		568,2969	-1,4
HPRG_XP	RPSLDVIG	96	103		837,4708	1,3
HPRG_XP	IGQCK	102	106	Carbamidomethyl C(1)	604,3003	-1,7
HPRG_XP	GQCK	103	106	Carbamidomethyl C(1)	491,2162	-1,8
HPRG_XP	YSDEYQTLR	112	120		1173,5303	-0,3
HPRG_XP	DSPVLFDFIEDTEPFRK	140	156		2053,9995	1,1
HPRG_XP	DSPVLFDFIEDTEPFR	140	155		1925,9047	2,1
HPRG_XP	DSPVLFDFIEDTEPFRK	140	156		2053,9995	1,1
HPRG_XP	ALEVYK	161	166		721,401	0,6

HPRG_XP	ALEVYKSESEAYASFR	161	176		1848,8894	-0,9
HPRG_XP	ALEVYKSESEAYASFR	161	176		1848,8894	4,4
HPRG_XP	EVYK	163	166		537,2798	-0,4
HPRG_XP	SESEAYASFR	167	176		1145,4989	-0,2
HPRG_XP	VDRVER	177	182		772,4191	-0,3
HPRG_XP	VTR	183	185		374,2278	-0,5
HPRG_XP	TNYVDFSVR	192	201		1262,5931	-0,6
HPRG_XP	SHFHR	206	210		682,33	1,6
HPRG_XP	HPAFGFCSR	211	218	Carbamidomethyl C(1)	990,4494	-1,2
HPRG_XP	ADLSFDVEASLENPED VIISCEVFNFEHGNISGF RPHLGK	219	260	Carbamidomethyl C(1)	4731,2188	1
HPRG_XP	TPLGTDGSR	261	269		902,4457	0,7
HPRG_XP	FGCPPPQEGEDFSEGPP SQGGTPPLSPSPGPR	280	311	Carbamidomethyl C(1)	3261,4673	-0,2
HPRG_XP	FGCPPPQEGEDFSEGPP SQGGTPPLSPSPGPR	280	311	Carbamidomethyl C(1)	3261,4673	1,4
HPRG_XP	FPHHR	325	329		692,3506	-2,2
HPRG_XP	FPHHR	325	329		692,3506	-2,2
HPRG_XP	EGPQDLHQHGHGPPPK	444	459		1729,8284	-1,4
HPRG_XP	EGPQDLHQHGHGPPPK HPGK	444	463		2149,0564	-0,5
HPRG_XP	PQDLHQHGHGPPPK	446	459		1543,7644	-0,8
HPRG_XP	DLHQHGHGPPPK	448	459		1318,6531	0,4
HPRG_XP	GHFPHWR	469	476		1082,5199	0,6
HPRG_XP	RIGSVYQLPPLQK	477	489		1497,8667	-0,4
HPRG_XP	RIGSVYQL	477	484		916,5131	-0,9
HPRG_XP	IGSVYQLPPLQK	478	489		1341,7656	-1
HPRG_XP	GEVLPPEANFPFSLSR	490	506		1871,9781	-0,4
HPRG_XP	NHHTPLKPEIQFPQVA SER	507	526		2324,2026	-1,1
HPRG_XP	HTHPLKPEIQFPQVASE R	508	526		2210,1597	-1,4
HPRG_XP	CPEEFNGEFAQLSK	527	540	Carbamidomethyl C(1)	1654,7297	0
HPRG_XP	CPEEFNGEFAQLSK	527	540	Carbamidomethyl C(1)	1654,7297	-4,4
HPRG_XP	FFPSTFPK	541	548		969,496	0,3
HPRG_XP	PSTFPK	543	548		675,3592	-1

Figure A.29. – nanoLC-ESI-MS/MS results from the tryptic digest of lyophilized HPRG before PNGase F treatment. Comparison against “new” sequence XP_008264798.1 [89].

nanoLC-ESI-MS/MS Results from the Asp-N Digest of HPRG before PNGase F treatment
Comparison against Sequence XP_008264798.1

Peptide	Start	End	Modifiers	Calculated Peptide Mass (Da)	RT (Min)	m/z	Charge State	Observed Peptide Mass (Da)	Intensity (Counts)	Mass Error (ppm)
DLINKWRRDGYLFQLLRVA	36	54		2375,3225	22,5	594,8384	4	2375,3218	44256	-0,3
DLINKWRR	36	43		1099,625	15,7	367,5497	3	1099,6252	7544	0,2
DGYLFQLLRVA	44	54		1293,7081	23,4	647,8627	2	1293,7095	7300	1,1
DGAESATVYVL	59	71		1399,6871	23,4	700,8526	2	1399,6893	72867	1,6
DCSVLSRKHWE	77	87	Carbamidomethyl C(1)	1415,6616	16,4	472,8969	3	1415,667	776268	3,8
DCSVLSRKHWE	77	87	Carbamidomethyl C(1)	1415,6616	15,4	472,8949	3	1415,6609	486583	-0,5
DPDLTKRPSL	90	99		1140,6139	15,4	571,3096	2	1140,6034	937	-9,2
DLTKRPSL	92	99		928,5342	15,4	465,2749	2	928,5339	19272	-0,3
DVIGQCKVIATRY	100	113	Carbamidomethyl C(1)	1608,8293	16,8	537,284	3	1608,8282	1033030	-0,7
DEYQTLRLN	114	122		1150,5619	17,4	576,2875	2	1150,5591	775118	-2,4
DSPVLF	140	145		676,3432	21,3	677,3501	1	676,3422	409436	-1,5
DFIE	146	149		522,2325	17,6	523,2389	1	522,231	194292	-2,9
DTEPFRKSA	150	158		1049,5142	13,5	525,7651	2	1049,5144	404656	0,2
EPFRKSA	152	158		833,4395	13,5	417,7278	2	833,4398	11062	0,4
EAYASFRV	170	177		941,4607	18	471,7373	2	941,4587	118199	-2,1
DLSF	220	223		480,222	19,5	481,2293	1	480,2214	219029	-1,2
DVIISC	235	240	Carbamidomethyl C(1)	705,3367	17,1	706,3416	1	705,3337	3620	-4,3
DHGPCDPPSHK	433	443		1188,4982	17,4	397,1762	3	1188,5048	899	5,6
DPPSHKEGPQ	438	447		1090,5043	10,9	546,2605	2	1090,5051	78022	0,7
DPPSHKEGPQ	438	447		1090,5043	12	546,2605	2	1090,5051	8102	0,7

Figure A.30. – nanoLC-ESI-MS/MS results from the Asp-N digest of lyophilized HPRG before PNGase F treatment. Comparison against “new” sequence XP_008264798.1 [89].

nanolC-ESI-MS/MS Results from the Tryptic Digest of HPRG after PNGase F treatment
Comparison against Sequence XP_008264798.1

Peptide	Start	End	Modifiers	Calculated Peptide Mass (Da)	RT (Min)	m/z	Charge State	Observed Peptide Mass (Da)	Intensity (Counts)	Mass Error (ppm)
TTKPLAEK	26	33		886,5124	12	444,2628	2	886,5097	23983	-3
ALDLINK	34	40		785,4647	17,1	393,7401	2	785,4644	406621	-0,4
DLINK	36	40		601,3435	17,1	602,351	1	601,343	23658	-0,8
RDGYLFQLLR	43	52		1279,7037	20,9	427,5751	3	1279,7014	669338	-1,8
RDGYLFQ	43	49		879,4239	20,9	440,7195	2	879,4232	15411	-0,8
RDGYL	43	47		604,2969	20,9	605,3033	1	604,2954	15349	-2,5
RDGYLF	43	48		751,3653	20,9	376,69	2	751,3641	14466	-1,6
RDGYLFQL	43	50		992,5079	20,9	497,2622	2	992,5086	8967	0,7
DGYLFQLLR	44	52		1123,6025	22,8	562,8092	2	1123,6025	222346	0
QLLR	49	52		528,3384	20,9	529,3452	1	528,3373	15349	-2,1
VADAHLDGAESATVYVLDVK	53	74		2348,1899	22	783,737	3	2348,1873	1249649	-1,1
VADAHLDGAESATVYVLDVK	53	74		2348,1899	23	783,7379	3	2348,1897	155559	-0,1
VADAHLDGAESATVYVLDVK	53	74		2348,1899	0,6	783,7372	3	2348,188	2191	-0,8
ETDCSVLSR	75	83	Carbamidomethyl C(1)	1065,4761	14,6	533,7455	2	1065,4751	441269	-0,9
KHWEDCDPDLTK	84	95	Carbamidomethyl C(1)	1542,6772	14,4	515,233	3	1542,675	532587	-1,4
KHWEDCD	84	90	Carbamidomethyl C(1)	970,3604	14,4	486,1881	2	970,3604	3899	0
KHWEDCDPDLTK	84	95	Carbamidomethyl C(1)	1542,6772	0,6	515,2336	3	1542,6769	2589	-0,2
HWEDCDPDLTK	85	95	Carbamidomethyl C(1)	1414,5824	15,3	708,298	2	1414,5802	79168	-1,6
RPSLDVIGQCK	96	106	Carbamidomethyl C(1)	1271,6656	16	636,8397	2	1271,6635	570554	-1,7
RPSLDVI	96	102		780,4493	16,1	391,2323	2	780,4488	35599	-0,6
RPSLDV	96	101		667,3653	16,1	668,3717	1	667,3638	31270	-2,2
RPSLD	96	100		568,2969	16,1	569,3036	1	568,2957	6769	-2,1
RPSLDVIG	96	103		837,4708	16,1	419,7438	2	837,4718	6026	1,2
YSDEYQTLR	112	120		1173,5303	15,3	587,7724	2	1173,5289	711336	-1,2
YSDEYQTLR	112	120		1173,5303	1,3	587,7725	2	1173,5291	779	-1
LNDFNCTSSVSSALANTK	121	139	Carbamidomethyl C(1),Deglycosylation of N(1)	2029,9263	18,6	1015,9696	2	2029,9233	855896	-1,5
LNDFNCTSSVSSALANTK	121	139	Carbamidomethyl C(1),Deglycosylation of N(1)	2029,9263	21,4	1015,9693	2	2029,9227	3873	-1,8
LNDFNCTSSVSSALA	121	136	Carbamidomethyl C(1),Deglycosylation of N(1)	1668,7301	18,6	835,3785	2	1668,7411	3125	6,6
DSPVLDFIEDTEPFRK	140	156		2053,9995	23,2	685,6737	3	2053,9973	768780	-1,1
DSPVLDFIEDTEPFR	140	155		1925,9047	23,4	963,9597	2	1925,9034	296587	-0,7
DSPVLDFIEDTEPFRK	140	156		2053,9995	0,6	685,6736	3	2053,9971	3715	-1,2
DSPVLDFIEDTEPFR	140	155		1925,9047	0,6	963,9586	2	1925,9012	2126	-1,8
PVLDFIEDTEPFRK	142	156		1851,9407	23,2	618,3206	3	1851,938	2772	-1,5

DFIEDTEPRFK	146	156		1395,667	23,3	1396,6818	1	1395,6738	1238	4,9
ALEVYK	161	166		721,401	15,1	361,708	2	721,4002	277183	-1,1
ALEVYKSESEAYASFR	161	176		1848,8894	17,9	617,3044	3	1848,8895	3386	0,1
EVVK	163	166		537,2798	15,1	538,2867	1	537,2788	20893	-1,9
SESEAYASFR	167	176		1145,4989	15,6	573,7563	2	1145,4967	674885	-1,9
SESEAYASFR	167	176		1145,4989	17,9	573,7573	2	1145,4987	5594	-0,2
SESEAYASFR	167	176		1145,4989	1,4	573,7565	2	1145,4972	856	-1,5
TNYVDFSVR	192	201		1262,5931	19	632,3034	2	1262,5909	819073	-1,7
SHFHR	206	210		682,33	5	342,1733	2	682,3308	1186	1,2
HPAFGFCR	211	218	Carbamidomethyl C(1)	990,4494	15,9	496,2319	2	990,448	238324	-1,4
ADLSFDVEASNLENPEDVIISCEV FNFEHGNISGFRPHLGK	219	260	Carbamidomethyl C(1),Deglycosylation of N(1)	4732,2026	23	947,4489	5	4732,2046	543359	0,4
TPLTGDGSR	261	269		902,4457	13,2	452,2303	2	902,4448	353662	-1
FGCPPPQEGEDFSEGGPPSQGGT PPLSPSGPR	280	311	Carbamidomethyl C(1)	3261,4673	18,3	1088,1628	3	3261,4646	926903	-0,8
FGCPPPQEGEDFSEGGPPSQGGT PPLSPSGPR	280	311	Carbamidomethyl C(1)	3261,4673	0,5	1088,165	3	3261,4714	2994	1,3
HRPFGTNETHR	314	324	Deglycosylation of N(1)	1351,6381	12,3	451,5537	3	1351,6372	305914	-0,7
FPHHR	325	329		692,3506	11,2	347,1825	2	692,3491	4120	-2,2
FPHHR	325	329		692,3506	9,9	347,1832	2	692,3505	1321	-0,1
EGPQDLHQHGHGPPPK	444	459		1729,8284	12,4	433,4644	4	1729,8257	612636	-1,6
EGPQDLHQHGHGPPPKHPGK	444	463		2149,0564	12	538,2704	4	2149,05	9985	-3
PQDLHQHGHGPPPK	446	459		1543,7644	12,4	386,9483	4	1543,7615	2008	-1,9
GHFPPHWR	469	476		1082,5199	17,2	361,8478	3	1082,5195	186230	-0,4
RIGSVYQLPPLQK	477	489		1497,8667	18,2	500,2963	3	1497,865	98886	-1,1
IGSVYQLPPLQK	478	489		1341,7656	19	671,8892	2	1341,7625	1189257	-2,3
GEVLPLEAFNPFSLR	490	506		1871,9781	22,9	936,9967	2	1871,9775	1208434	-0,3
GEVLPLEAFNPFSLRNHHTPL KPEIQFPQVASER	490	526	Deglycosylation of N(1)	4179,1543	21,3	836,8382	5	4179,1514	3906	-0,7
NHHTPLKPEIQFPQVASER	507	526	Deglycosylation of N(1)	2325,1865	17,4	582,3043	4	2325,1855	1687316	-0,4
NHHTPLKPEIQPF	507	519	Deglycosylation of N(1)	1539,7833	17,4	514,2695	3	1539,7847	3430	0,9
NHHTPLKPEIQFPQV	507	522	Deglycosylation of N(1)	1863,9631	17,4	466,9986	4	1863,9626	3032	-0,3
CPEEFNGEFAQLSK	527	540	Carbamidomethyl C(1)	1654,7297	18,6	828,369	2	1654,7222	485418	-4,5
CPEEFNGEFAQLSK	527	540	Carbamidomethyl C(1),Deglycosylation of N(1)	1655,7137	19,1	828,8645	2	1655,7131	241936	-0,4
CPEEFNGEFAQLSK	527	540	Carbamidomethyl C(1),Deglycosylation of N(1)	1655,7137	21,1	828,8666	2	1655,7174	5922	2,2
CPEEFNGEFAQLSK	527	540	Carbamidomethyl C(1),Deglycosylation of N(1)	1655,7137	0,6	828,8647	2	1655,7135	3180	-0,1
FFPSTFPK	541	548		969,496	18,8	485,7558	2	969,4957	964136	-0,3
PSTFPK	543	548		675,3592	18,8	676,3654	1	675,3575	21728	-2,5

Figure A.31. – nanoLC-ESI-MS/MS results from the tryptic digest of lyophilized HPRG after PNGase F treatment. Comparison against “new” sequence XP_008264798.1 [89].

nanoLC-ESI-MS/MS Results from the Asp-N Digest of HPRG after PNGase F treatment
Comparison against Sequence XP_008264798.1

Peptide	Start	End	Modifiers	Calculated Peptide Mass (Da)	RT (Min)	m/z	Charge State	Observed Peptide Mass (Da)	Intensity (Counts)	Mass Error (ppm)
DLINKWRRDGYLFQL LRVA	36	54		2375,3225	22,4	594,8384	4	2375,3218	5464	-0,3
DGAESATVYYLVL	59	71		1399,6871	23,3	700,8516	2	1399,6873	38402	0,1
ETDCSVLSRKHWE	75	87	Carbamidomethyl C(1)	1645,7518	15,3	549,5898	3	1645,7457	1349	-3,7
DCSVLSRKHWE	77	87	Carbamidomethyl C(1)	1415,6616	16,2	472,8968	3	1415,6665	430153	3,5
DCSVLSRKHWE	77	87	Carbamidomethyl C(1)	1415,6616	15,3	472,8943	3	1415,6591	117017	-1,8
DVIGQCKVIATRYIS	100	113	Carbamidomethyl C(1)	1608,8293	16,6	537,2825	3	1608,8237	674497	-3,5
DVIGQCKVIATRYISDE YQTLRLN	100	122	Carbamidomethyl C(1)	2741,3806	18,9	686,3531	4	2741,3809	6922	0,1
DVIGQCKVI	100	108	Carbamidomethyl C(1)	1012,5376	16,6	507,2757	2	1012,5356	3216	-2
DVIGQCKVIATRY	100	112	Carbamidomethyl C(1)	1503,7867	16,6	752,8989	2	1503,782	2207	-3,1
DVIGQCKV	100	107	Carbamidomethyl C(1)	899,4535	16,6	450,7334	2	899,451	1343	-2,8
IGQCKVIATRYIS	102	113	Carbamidomethyl C(1)	1394,734	16,6	698,3733	2	1394,7307	3026	-2,4
DEYQTLRLN	114	122		1150,5619	17,3	576,2875	2	1150,5592	463251	-2,3
DEYQTLRLNDFNCTT SSVSSALANTK	114	139	Carbamidomethyl C(1),Deglycosylation of N(2)	2936,3345	20,2	979,7865	3	2936,3357	21674	0,4
DFNCTTSSVSSALANT K	123	139	Carbamidomethyl C(1),Deglycosylation of N(1)	1802,7993	18	902,408	2	1802,8	11187	0,4
DSPVLF	140	145		676,3432	21,2	677,3496	1	676,3417	278693	-2,2
DFIE	146	149		522,2325	17,4	523,2392	1	522,2313	71535	-2,3
EDTEPFRKSA	149	158		1178,5568	18,3	590,2865	2	1178,5571	2695	0,3
DTEPFRKSA	150	158		1049,5142	13,4	525,7656	2	1049,5153	145467	1
EPFRKSA	152	158		833,4395	13,4	417,7279	2	833,44	4329	0,6
PFRKSA	153	158		704,397	13,4	353,2069	2	704,398	1307	1,4
DKALEVYKSES	159	169		1267,6295	14,5	634,8228	2	1267,6296	41842	0,1
DKALEVYKSE	159	168		1162,587	14,5	582,3002	2	1162,5846	1783	-2,1
EYKSESEAYASFRV	163	177		1763,8365	18	588,9534	3	1763,8364	6985	-0,1
EAYASFRV	170	177		941,4607	17,9	471,7379	2	941,46	50004	-0,7
DRVERVTRVKGGER NYV	178	196		2296,2036	14,2	575,0588	4	2296,2034	187196	-0,1
DRVERVTRVKGGER NYY	178	195		2179,1245	14,2	545,7892	4	2179,125	5635	0,2
DRVERVTRVKGGER NY	178	194		2016,0613	14,2	505,0242	4	2016,0651	1609	1,9
DLSF	220	223		480,222	19,4	481,2295	1	480,2216	111379	-0,8
DHHHPKPKHKFGCP PPQEGE	270	289	Carbamidomethyl C(1)	2367,0715	12,1	592,7751	4	2367,0686	162475	-1,2
DHHHPKPKHKFGCP PPQEG	270	288	Carbamidomethyl C(1)	2220,0183	12,1	556,0114	4	2220,0137	3069	-2,1
DHHHPKPKHKFGCP PPQE	270	287	Carbamidomethyl C(1)	2162,9968	12,1	541,7566	4	2162,9946	2552	-1
DFSEGPSPQGGT SPPSGPRCRHRPFGT N	290	320		3231,5269	16,7	808,8893	4	3231,5254	6044	-0,5
EGPPSQGGT GPRCRHRPFGT RFPHHRNFS	293	332	Carbamidomethyl C(1),Deglycosylation of N(2)	4487,1226	15,2	748,8615	6	4487,1211	178516	-0,3
DHGCPDPPSHKEGP Q	433	447	Carbamidomethyl C(1)	1656,6951	11,8	553,2386	3	1656,6919	331633	-1,9
DPPSHKEGPQ	438	447		1090,5043	10,4	546,2593	2	1090,5027	7258	-1,5
PPSHKEGPQ	439	447		975,4774	11,8	488,7454	2	975,4749	7357	-2,6

Figure A.32. – nanoLC-ESI-MS/MS results from the Asp-N digest of lyophilized HPRG after PNGase F treatment. Comparison against “new” sequence XP_008264798.1 [89] .

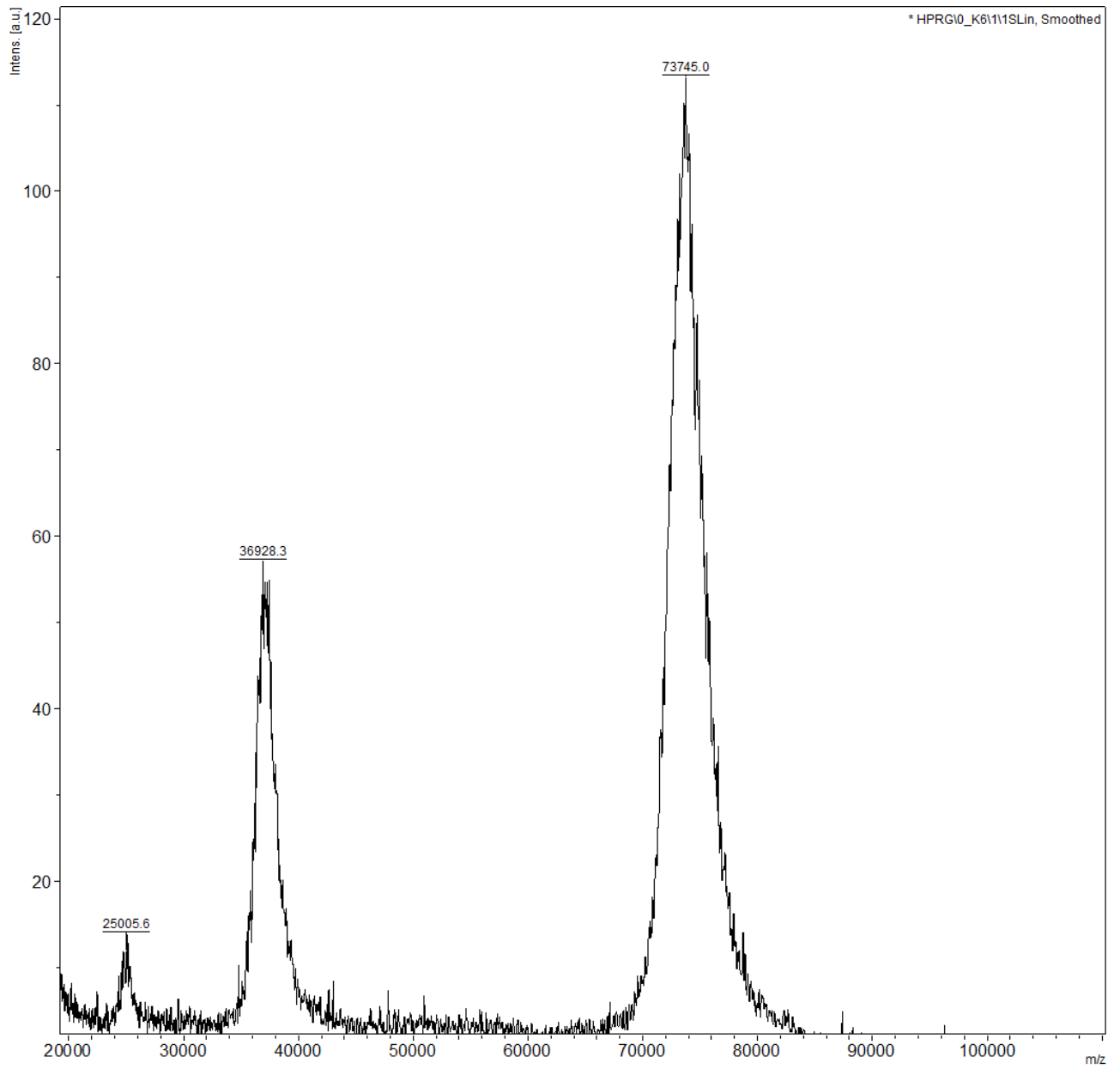


Figure A.33. – MALDI of lyophilized HPRG before PNGase F treatment.

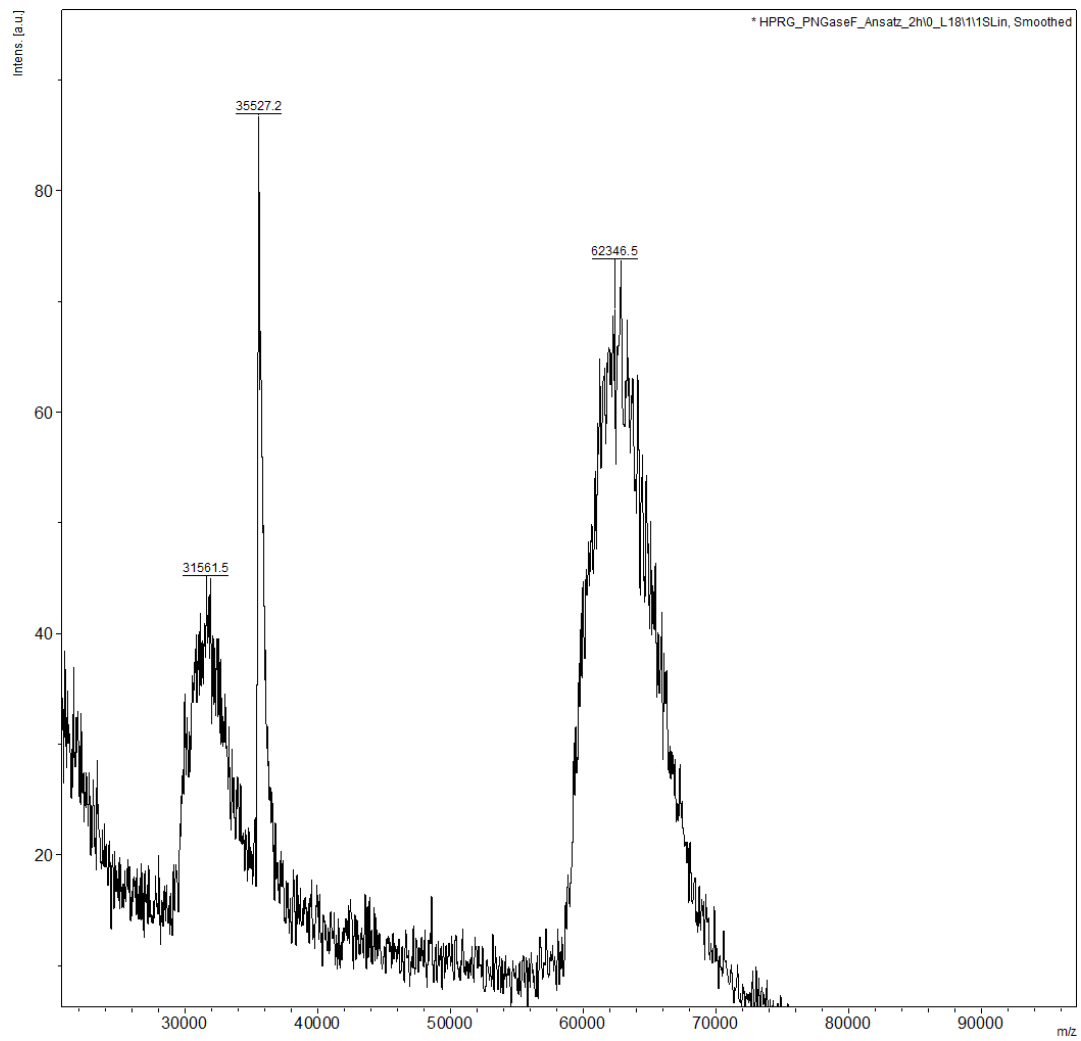


Figure A.34. – MALDI of lyophilized HPRG after PNGase F treatment.

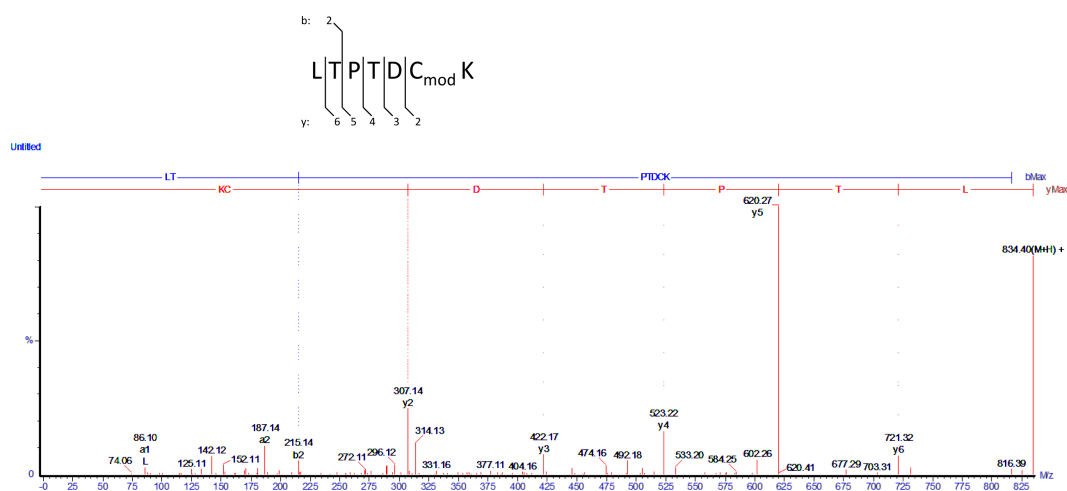


Figure A.35. – De novo sequencing of an unmatched peptide with m/z 834.10 led to the sequence LTPPTDC_{mod}K resembling the amino acids 19-25 of the HPRG sequence. According to [164].

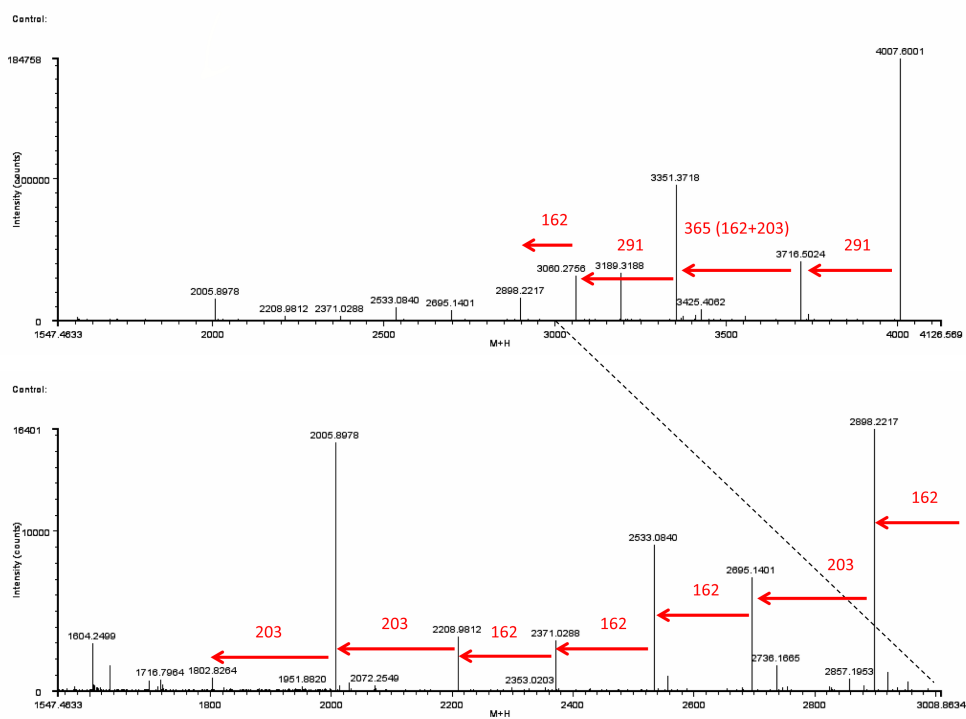


Figure A.36. – Detail of the MS/MS-spectrum (deconvoluted to singly charged ions) of glycopeptide 123-139 (Asp-N digest) (glycosylation site N-125). The precursor ion 4007.6001 ($[M+H]^+$) was successively fragmented due to the loss of 2 NeuAc, 4 HexNAc and 5 Hex (glycan mass 2204.7724) Monosaccharid masses: NeuAc 291, HexNAc 203, Hex 162. Lower trace: Magnification of the range m/z 1547.4633-3008.8634 for a better comparison.

Figure A.37

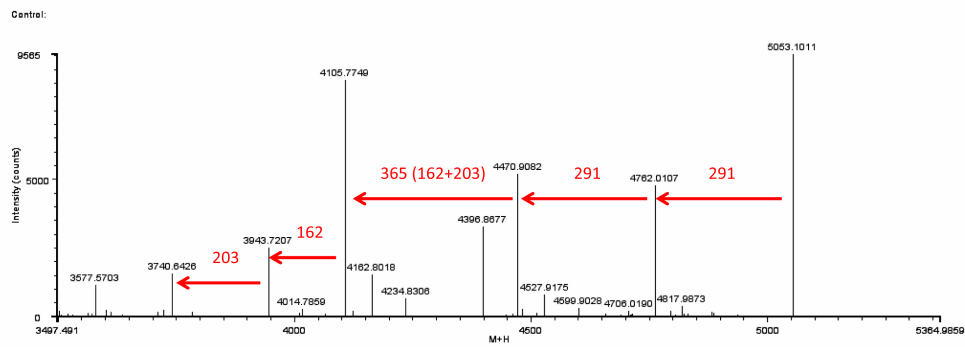


Figure A.37. – Detail of the MS/MS-spectrum (deconvoluted to singly charged ions) of glycopeptide 197-219 (Asp-N digest) (glycosylation site N-202). The precursor ion 5053.1011([M+H]⁺) was successively fragmented due to the loss of 2 NeuAc, 4 HexNac and 5 Hex (glycan mass 2204.7724) Monosaccharid masses: NeuAc 291, HexNac 203, Hex 162. Lower trace: Magnification of the range m/z 3497.4910-5364.9859 for a better comparison.

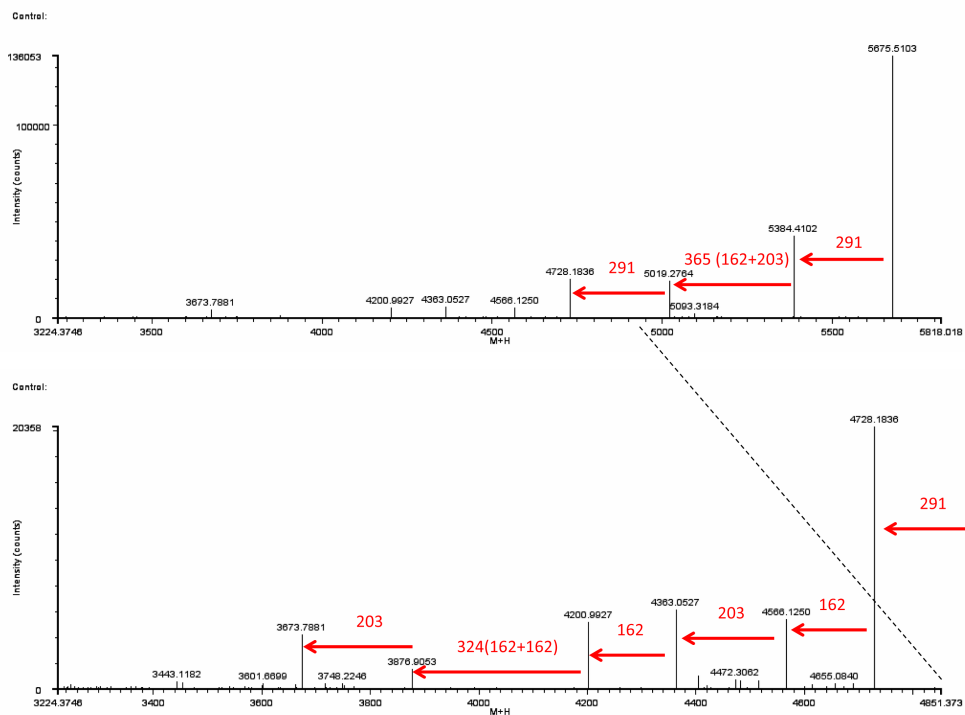


Figure A.38. – Detail of the MS/MS-spectrum (deconvoluted to singly charged ions) of glycopeptide 235-265 (Asp-N digest) (glycosylation site N-250). The precursor ion 5675.5103([M+H]⁺) was successively fragmented due to the loss of 2 NeuAc, 4 HexNAc and 5 Hex (glycan mass 2204.7724) Monosaccharid masses: NeuAc 291, HexNAc 203, Hex 162. Lower trace: Magnification of the range m/z 3224.3746-4851.3730 for a better comparison.

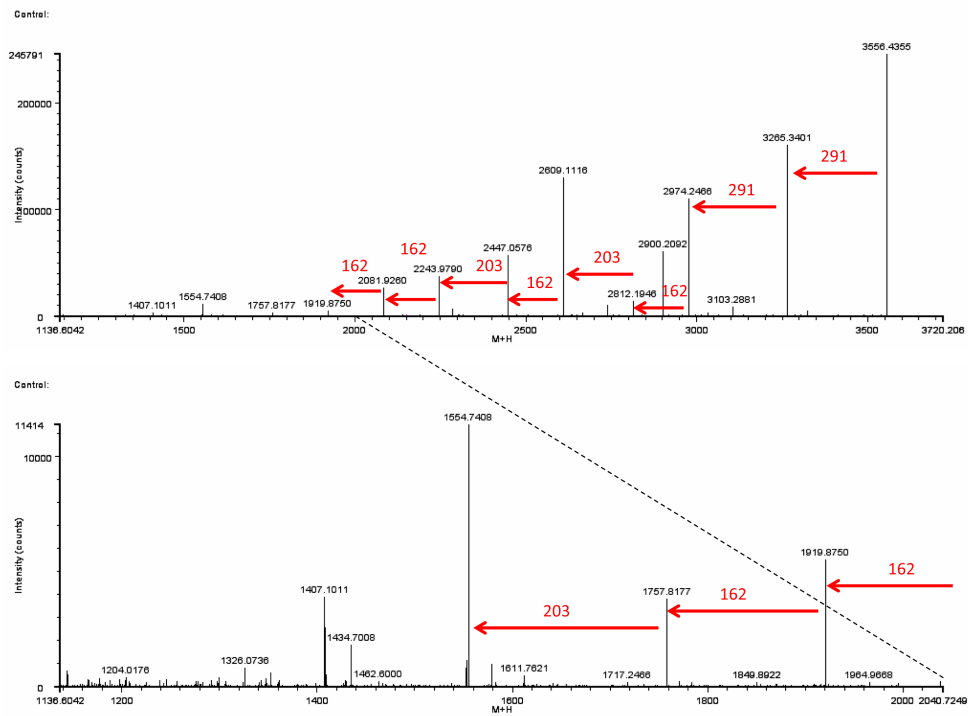


Figure A.39. – Detail of the MS/MS-spectrum (deconvoluted to singly charged ions) of glycopeptide 314-324 (trypsin digest) (glycosylation site N-320). The precursor ion 3556.4355($[M+H]^+$) was successively fragmented due to the loss of 2 NeuAc, 4 HexNAc and 5 Hex (glycan mass 2204.7724) Monosaccharid masses: NeuAc 291, HexNAc 203, Hex 162. Lower trace: Magnification of the range m/z 1136.6042-2040.7249 for a better comparison.

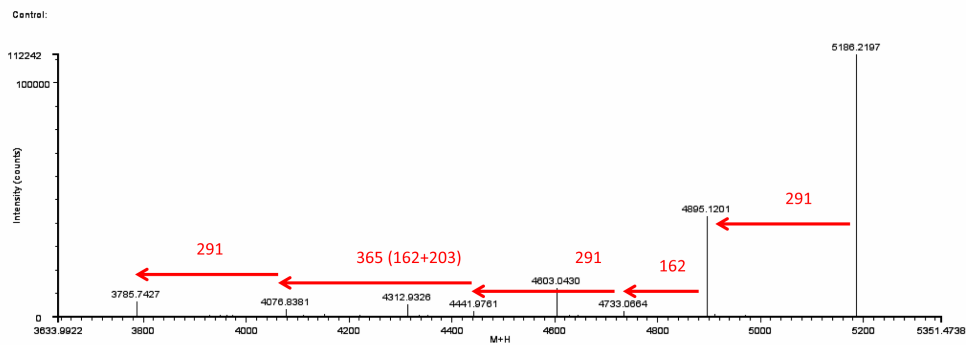


Figure A.40. – Detail of the MS/MS-spectrum (deconvoluted to singly charged ions) of glycopeptide 507-526 (trypsin digest) (glycosylation site N-507). The precursor ion 5186.2197($[M+H]^+$) was successively fragmented due to the loss of 3 NeuAc, 5 HexNAc and 6 Hex (glycan mass 2861.0000) Monosaccharid masses: NeuAc 291, HexNAc 203, Hex 162. Lower trace: Magnification of the range m/z 3633.9922-5351.4738 for a better comparison.

B. Acknowledgements

First of all I would like to thank my supervisor Prof. Dr. Dariush Hinderberger for accepting me into his group and for giving me the opportunity to work on two very interesting projects. I appreciate the guidance, helpful discussions as well as the granted freedom during the doctorate. I would also like to thank for the opportunity to present my results on several international conferences.

My sincere thanks also goes to Prof. Dr. Robert Konrat (University of Vienna) for the α -Synuclein cooperation, and Dr. Thomas Schwarz for supplying me regularly with the protein and the liposomes so that the measurements could be carried out.

The HPRG project could not have been accomplished without the support of Prof. Dr. Kirsten Bacia, who allowed me to work in her S1 lab. Furthermore, I thank also Dr. Sebastian Daum for the assistance during Äkta runs, and the research group of Prof. Bacia for a pleasant working atmosphere.

I would also like to thank Prof. Dr. Ralf-Bernd Klösgen for giving me the opportunity to test preparative gel electrophoresis for purification of HPRG in his lab when other techniques failed to purify the protein. A special gratitude goes to Dr. Mario Jakob for the continuous support regarding the preparative gel approach, for introducing me to this technique, showing me how to use the RP-HPLC and for answering all kind of questions. I also thank very much Birgit Kretschmann and the whole group of Prof. Klösgen for a pleasant working atmosphere.

A very special gratitude goes to my fellow co-workers for the introduction into new techniques: Dr. Andreas Kerth for introducing me to the film balance technique; Dr. Nadica Maltar-Strmecki (Ruđer Bošković Institute, Croatia), Dr. Haleh Hashemi Haeri and Jörg Reichenwallner for introducing me to the pulsed EPR-technique and for many helpful discussions.

Thanks are also directed to Heike Schimm, Stefanie Weber, and Andreas Lonitz for the

technical support, my former master student Selgar Henkel for his successful work on HPRG peptides, and the secretaries Luise Quil and Jessika Bohm for all kind of organizational aid.

I thank my fellow labmates of the Hinderberger group for the many helpful discussions and many enjoyable coffee rounds on friday mornings.

I also thank Angelika Schierhorn for the measurement of several mass spectrometry data and for the analysis of the carbohydrate structure of HPRG as well as Dr. Hauke Lilie for letting me measure the HPRG CD spectrum in his group.

Furthermore I would like to thank the former members of the Blume group for support and discussions regarding the film balance technique.

At last I would like to thank my family for the continuous support throughout the years.

C. Scientific Contributions

C.1. Publications

1. Weyrauch AK, Jakob M, Schierhorn A, Klösigen RB, and Hinderberger D. Purification of rabbit serum histidine-proline-rich glycoprotein via preparative gel electrophoresis and characterization of its glycosylation patterns. PLOS ONE, 12(9):e0184968, 2017. doi:10.1371/journal.pone.0184968.

C.2. Oral Contributions

- 27.09. - 06.10.2014 “EPR- and IRRAS studies on α -Synuclein”, 12th Greta Pifat-Mrzljak International School of Biophysics, Primosten, Croatia
- 18.07. - 22.07.2015 “EPR- and IRRAS studies on α -Synuclein”, 10th European Biophysics Congress, Dresden, Germany
- 23.07. - 28.07.2017 “EPR spectroscopy of peptides and proteins with intrinsic disorder” ISMAR 2017, Québec City, Canada

C.3. Poster Contributions

- 27.09. - 06.10.2014 12th Greta Pifat-Mrzljak International School of Biophysics, Primosten, Croatia
- 18.07. - 22.07.2015 10th European Biophysics Congress, Dresden, Germany
- 12.09. - 13.09.2016 Biennial Meeting of the GDCh-Division Macromolecular Chemistry, Halle (Saale), Germany
- 25.09. - 28.09.2016 Annual Meeting of the German Biophysical Society 2016, Erlangen, Germany

D. Curriculum Vitae

Personal Details

Name Anna Katharina Weyrauch
Date of Birth 03.09.1985
Place of Birth Kaiserslautern
Citizenship German

Education and Working Experience

- 11/2013 – 08/2018 **Doctorate: Chemistry**, *Martin Luther University Halle-Wittenberg*, Characterization of Proteins with Intrinsic Disorder in Solution and in Lipid Monolayers, Group of Prof. Dr. D. Hinderberger.
- 10/2006 – 06/2013 **Studies: Chemistry**, *Technical University Kaiserslautern*, Specialization: *Life Sciences in Chemistry*, Degree: Diploma (Final Grade: 1,2).
Thesis: *Generierung neuer SecB-Mutanten zur Untersuchung mittels ESR-Spektroskopie*, Group of Prof. Dr. W. Trommer
- 10/2005 – 07/2006 **Studies: Biology**, *Technical University Kaiserslautern*, Subject change after two semesters.
- 2005 **General Qualification for University Entrance**, *Gymnasium Weierhof am Donnersberg*.
- 2002-2005 **Gymnasium Weierhof am Donnersberg, Bolanden.**
- 1996-2005 **Gymnasium am Römerkastell, Alzey.**
- 1992-1996 **Grundschule Kriegsfeld, Kriegsfeld.**

Halle (Saale), 7.8.2018

Anna Weyrauch

E. Eidesstattliche Erklärung

Hiermit erkläre ich, dass ich die vorliegende Arbeit selbstständig und ohne fremde Hilfe verfasst, andere als die von mir angegebenen Quellen und Hilfsmittel nicht benutzt und die den benutzten Werken wörtlich oder inhaltlich entnommenen Stellen als solche kenntlich gemacht habe.

Diese Arbeit wurde an keiner anderen Universität oder Hochschule vorgelegt.

Halle (Saale), 7.8.2018

Anna Weyrauch